ISSN 2074-272X

науково-практичний журнал

2023/2

Електротехніка і Електромеханіка

Electrical Engineering & Electromechanics

Електричні машини та апарати
Електротехнічні комплекси та системи
Промислова електроніка
Електричні станції, мережі і системи

Журнал включено до найвищої категорії «А»
Переліку фахових видань України

З 2021 р. журнал індексується у Scopus

З 2015 р. журнал індексується
у Web of Science Core Collection:
Emerging Sources Citation Index

Electrical Engineering & Electromechanics

Scientific Journal was founded in 2002
Founder – National Technical University «Kharkiv Polytechnic Institute» (Kharkiv, Ukraine)

From no. 1 2021 Journal «Electrical Engineering & Electromechanics» is indexing in **Scopus** and from no. 1 2015 Journal is indexing in **Web of Science Core Collection: Emerging Sources Citation Index (ESCI)**.

Also included in DOAJ (Directory of Open Access Journals), in EBSCO's database, in ProQuest's databases – Advanced Technologies & Aerospace Database and Materials Science & Engineering Database, in Gale/Cengage Learning databases.

Editorial office address:
National Technical University «Kharkiv Polytechnic Institute», Kyrpychova Str., 2, Kharkiv, 61002, Ukraine
phones: +380 57 7076281, +380 67 3594696, **e-mail:** a.m.grechko@gmail.com (**Grechko O.M.)**

ISSN (print) 2074-272X
ISSN (online) 2309-3404

Printed 07 March 2023. Format 60 × 90 ⅛. Paper – offset. Laser printing. Edition 200 copies.
Printed by Printing house «Madrid Ltd» (18, Gudanova Str., Kharkiv, 61024, Ukraine)

Electrical Engineering & Electromechanics
Scientific Journal

no. 2, 2023

Table of Contents

Electrical Machines and Apparatus

Electrotechnical Complexes and Systems

Industrial Electronics

Power Stations, Grids and Systems

UDC 621.313 https://doi.org/10.20998/2074-272X.2023.2.01

J. Fan, Y. Lee

Dynamic measurement of magnetic characteristics of switched reluctance motor

Introduction. *Switched reluctance motor (SRM) is a type of electric motor featuring nonlinear magnetic characteristics. The flux linkage or inductance profile of SRM is usually required for the purpose of high control performance, and can be normally obtained through conventional static test by using DC or AC method when the rotor is locked.* ***Problem***. *However, it is not practical to use the conventional method of measurement when the specific apparatus for locking the rotor is unavailable. Besides, due to the magnetic nonlinearity of SRM, the saturation effect makes it difficult to obtain the saturated magnetic characteristics, and the conventional static AC test fails to address this problem.* ***Novelty***. *In this paper, a dynamic measurement method of the magnetization curves of SRM is proposed which allows the measurement take place while the motor is running with load.* ***Methodology***. *Based on the conventional static AC test, the proposed measurement handles the saturation problem successfully by introducing a DC offset in the high frequency AC voltage. Phase inductance with different rotor positions and currents can be obtained by analyzing simple equivalent circuit.* ***Practical value***. *Simulation is conducted in MATLAB/Simulink environment and the results have verified that the proposed dynamic measurement can effectively obtain the magnetic characteristics of SRM.* References 16, table 1, figures 6.
Key words: **magnetic characteristics, saturation, switched reluctance motor.**

Вступ. *Вентильний реактивний двигун (ВРД) є типом електродвигуна з нелінійними магнітними характеристиками. Профіль потокозчеплення або індуктивності ВРД зазвичай потрібний для забезпечення високої ефективності управління і зазвичай може бути отриманий за допомогою звичайних статичних випробувань з використанням постійного або змінного струму, коли ротор заблокований.* ***Проблема***. *Однак недоцільно використовувати традиційний метод вимірювання, коли відсутній спеціальний пристрій для блокування ротора. Крім того, через магнітну нелінійність ВРД ефект насичення ускладнює отримання насичених магнітних характеристик, і звичайне статичне випробування змінним струмом не вирішує цю проблему.* ***Новизна***. *У цій роботі пропонується метод динамічного вимірювання кривих намагнічування ВРМ, який дозволяє проводити вимірювання під час роботи двигуна з навантаженням.* ***Методологія*** *Пропонований вимір, заснований на звичайному статичному випробуванні змінним струмом, успішно вирішує проблему насичення за рахунок введення зміщення постійного струму у високочастотну змінну напругу. Фазна індуктивність при різних положеннях ротора та струмів може бути отримана шляхом аналізу простої еквівалентної схеми.* ***Практична цінність***. *Моделювання проводилося у MATLAB/Simulink, і результати підтвердили, що пропонованим динамічним вимірюванням можливо ефективно отримати магнітні характеристики ВРД.* Бібл. 16, табл. 1, рис. 6.
Ключові слова: **магнітні характеристики, насичення, вентильний реактивний двигун.**

Introduction. There is an increasing popularity of the adoption of the switched reluctance motor (SRM) in areas such as industrial and home applications in recent years [1-8]. SRM is also considered as a strong competitor in electric vehicles due to its simple structure, high efficiency and low cost [9, 10].

However, the doubly salient structure of SRM makes the magnetic circuit highly non-linear, i.e., the flux linkage or inductance of SRM not only varies with rotor position but also level of current [11]. In order to achieve high performance control such as position sensorless control and instantaneous torque control, magnetic characteristics of SRM should be obtained in advance [12, 13].

There are various ways of obtaining the magnetic characteristics of an SRM, such as performing finite element analysis in computer simulation program, and carrying out measurement in hardware platform. The widely used method of inductance measurement is the locked rotor test. By locking the rotor using a heavy clamping device and applying a short voltage pulse in the phase winding, and monitoring the phase voltage and phase current waveform using oscilloscope, flux linkage can be calculated via integration and inductance can then be obtained [14, 15]. The static measurement method is simple yet tedious and requires special clamping device which might not be available. Thus, dynamic measurement is recommended in [16], in which the inductance profile can be measured while the motor is running. The principle of the dynamic method resembles that of the static method, there is no need to lock the rotor in the former method however. An alternative method of inductance measurement is by using static AC test proposed in [14], the phase winding becomes a sinusoidal circuit and the inductance can be simply estimated by using the RMS value of phase voltage and phase current. However, the static AC test method has two major drawbacks, one is that the rotor still needs to be locked to exclude the effect of the rotor position on the variation of the inductance, another is that saturation is ignored thus the inductance obtained is only linear inductance, while SRM is normally working under deep saturated condition, the nonlinear magnetic characteristics is not yet present.

In this paper, dynamic inductance measurement for SRM is proposed. By using high-frequency and small AC signal with a DC offset, the slope of flux linkage curve can be obtained from the proposed method. The utilization of the DC offset can cover the region where the motor is even magnetically saturated. Compared with the static measurement method where the rotor of SRM is required to be locked by a clamp, the proposed dynamic method can be applied when the rotor is rotating, which is more practical when the special clamping device is not available. Simulation results are given to prove the effectiveness of the proposed measurement method.

Conventional static AC measurement. In static AC measurement method, the shaft of SRM is locked by a clamp, the rotor is thus not moving due to friction even when current is flowing in the phase winding. By applying AC voltage of which the amplitude is small such that the generated current is lower than the saturated current, the phase winding can be considered as a simple RL circuit in which the inductance is constant. Then the inductance of the phase winding can be obtained from voltage vs current test.

The voltage equation of a phase can be written as:

$$u = R \cdot i + \frac{\mathrm{d}\psi}{\mathrm{d}t}, \quad (1)$$

where u is the phase voltage; i is the phase current; R is the phase resistance; ψ is the phase flux linkage; t is the time.

Considering the aforementioned condition, (1) can be rewritten as:

$$u = R \cdot i + L \cdot \frac{\mathrm{d}i}{\mathrm{d}t}, \quad (2)$$

where L is the unvaried phase inductance. It should be noted that magnetic saturation is not consider in this equation.

The inductance can then be calculated as:

$$L\big|_{\theta=\theta_l} = \frac{1}{2 \cdot \pi \cdot f} \cdot \sqrt{\frac{U^2}{I^2} - R^2}, \quad (3)$$

where θ is the rotor position; θ_l is the rotor position where the rotor is locked; U is the RMS value of the applied AC voltage; I is the RMS value of the phase current; f is the frequency of the AC voltage.

By changing the clamped rotor position manually and repeating the above process, the linear inductance at different rotor position can be obtained.

However, the static AC test not only is tedious but also requires the clamping apparatus to lock the rotor which might not be available. Besides, the method is only capable of obtaining the unsaturated inductance, while the saturation is not yet present due to the nonlinearity, i.e., the inductance is no long constant when the current goes above the saturation point. The drawbacks of the static AC test method hamper the wide application of this method and make it less appealing compared with the static DC test.

Proposed dynamic AC measurement. In order to overcome the disadvantages in the static AC test, a dynamic AC test method is proposed in this paper. The test setup is shown in Fig. 1. Sensors are used for sensing phase voltage and phase current to be used in the calculation of the magnetic characteristics. Incremental encoder is adopted to obtain the rotor position. A DC offset is adding to the AC voltage source to encounter the unsolved saturated condition in the static AC test. The adoption of DC voltage has two main functions, one is to freely move the equilibrium point beyond saturated current, the other is to rotate the rotor.

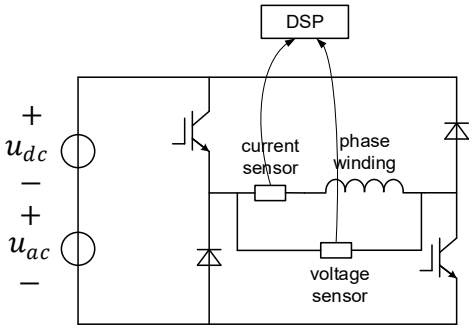

Fig. 1. Setup for magnetic characteristics measurement

Considering a short time of which the period is far longer than the cycle of the AC voltage, and during which the rotor barely rotates. In this condition, the rotor position can be considered constant. Assuming the current is reaching steady state and it will swing back and forth around the equilibrium point I_{dc} due to the existence of the AC component. By observing the flux linkage vs current curve of the particular rotor position in the vicinity of the equilibrium point, if the variation of the current is small enough, local linearization can be applied and the segment of the curve can be replaced by a linear line segment, as shown in Fig. 2.

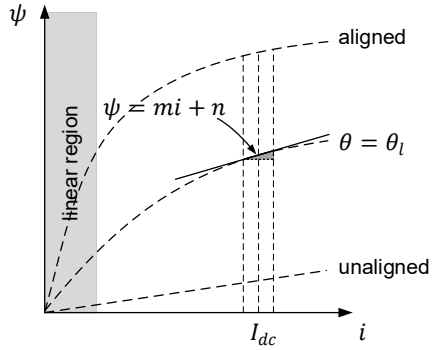

Fig. 2. Local linearization of flux linkage curve

The locally linearized curve can be expressed as:

$$\psi = m \cdot i + n, \quad (4)$$

where m and n are the coefficients of the linear line segment; m is the slope of the curve at the equilibrium point, which can be written as:

$$m = \frac{\mathrm{d}\psi}{\mathrm{d}i}\bigg|_{i=I_{dc}}. \quad (5)$$

By substituting (5) into (1), the voltage equation can be rewritten as:

$$u = R \cdot i + m \cdot \frac{\mathrm{d}i}{\mathrm{d}t}, \quad (6)$$

The coefficient m is also known as the dynamic inductance. Thus, the equivalent circuit of (6) can be constructed with a real resistor and an imaginary inductor in series connection as shown in Fig. 3,*a*. In the circuit shown in Fig. 3,*a*, superposition theorem is applicable. The circuit can be divided into two sub-circuits as shown in Fig. 3,*b* and Fig. 3,*c*, where only one voltage source is present in each sub-circuit. The current of the equilibrium point is determined by the DC voltage source, while the imaginary inductance can be obtained from the sub-circuit with the AC voltage source.

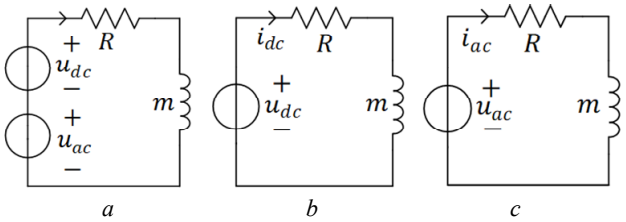

Fig. 3. *a* – equivalent circuit at equilibrium point; *b* – sub-circuit with DC voltage source; *c* – sub-circuit with AC voltage source

The current in the AC circuit can be obtained from performing Fast Fourier Transform (FFT) on the phase current and the slope of the flux linkage curve can still be calculated by (3). Once the slope is obtained for all the current, flux linkage can be calculated by performing integration. Then dividing the flux linkage by current can yield the inductance. By changing the DC voltage, the equilibrium current I_{dc} can be adjusted. Repeating the

above process at different equilibrium point, inductance profiles can be obtained.

It should be noted that the speed of the motor should be kept low enough to ensure that the current can reach the desired level and the circuit can reach steady state quickly. Thus, load torque should be properly tuned.

Simulation results and discussion. Simulation of the proposed dynamic measurement using an outer rotor SRM is carried out in MATLAB/Simulink environment. The parameters of the motor are listed in Table 1.

Table 1

Parameters of the outer rotor SRM

Parameter	Value
Number of phases	3
Pole combination	6/4
Stator outer radius	51 mm
Stator inner radius	20 mm
Stator yoke	15 mm
Stator pole arc	28°
Rotor outer radius	95 mm
Rotor inner radius	52 mm
Rotor yoke	15 mm
Rotor pole arc	32°
Stack length	50 mm
Turn number per pole	150

Two voltage sources in series connection supply power to the phase winding to run the motor. The AC voltage is kept at 1 V (magnitude) and 10 kHz, while the DC voltage is manually changed based on the need of equilibrium point. In order to know the magnetic characteristics under different current conditions, a 3 A linear step length is used. The required DC voltage u_{dc} is given by:

$$u_{dc} = R \cdot i_{dc}, \tag{7}$$

where i_{dc} = 3 A, 6 A, ..., 30 A; R = 2.56 Ω.

In order to verify the accuracy of the proposed dynamic measurement, finite element method (FEM) is adopted beforehand to obtain accurate flux linkage characteristics, and used to compare with the proposed method in simulation. The dynamic inductance calculated by FEM is represented by solid lines, while the one estimated from the proposed method is denoted by stars, as shown in Fig. 4.

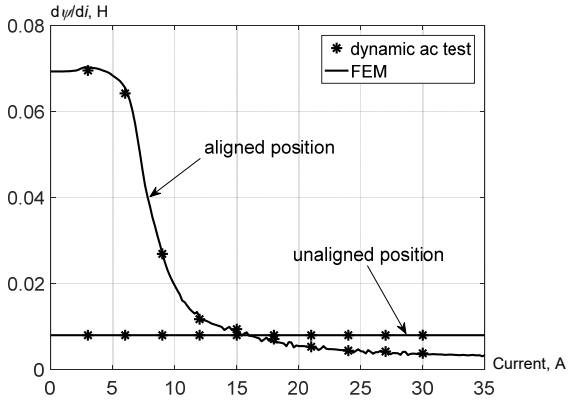

Fig. 4. Slope of flux linkage vs current curve at aligned and unaligned position obtained from the proposed dynamic AC measurement and FEM

Two typical positions, namely aligned position and unaligned position are presented in the figure. The characteristics at other rotor positions can also be obtained through the same process. The magnetic saturation point is at around 6 A. It can be found that the results given by the proposed method are in good agreement with that of FEM, no matter whether magnetic circuit is unsaturated or saturated, and no matter what the rotor position is. It should be noted that the large dynamic inductance change found in Fig. 4 is due to the outer rotor structure, which is uncommon in a conventional motor with an external stator.

In Fig. 5, the waveforms of phase voltage, phase current and rotor position are shown. The DC voltage is chosen as 61.4 V, thus the equilibrium current is 24 A, and it is well beyond the saturated current. The FFT result at aligned position is shown in Fig. 6, it can be found that the magnitude of the AC current caused by the AC voltage is 3.63 mA. By using (3), the estimated slope m of flux linkage curve is 4.40 mH, while the result obtained from FEM is 4.42 mH, of which the difference is less than 1 %. The simulation results show good accuracy when using the proposed measurement in both unsaturated region and saturated region.

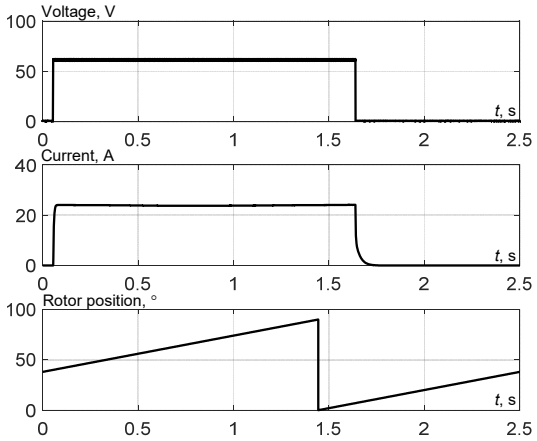

Fig. 5. Simulation waveforms when the current at equilibrium point is 24 A

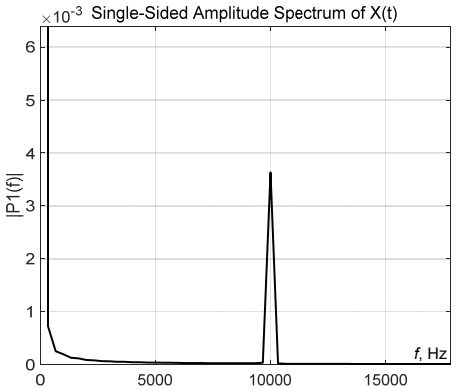

Fig. 6. FFT result at aligned position when the current at equilibrium point is 24 A

Conclusions. This paper proposes a dynamic measurement method of magnetic characteristics for SRM under both unsaturated and saturated conditions. The conventional lock-rotor test is not practical to implement if the specific apparatus used to lock the rotor is not available. Besides, the saturation effect is falsely ignored in the static AC test. The proposed method handles the nonlinear characteristics of SRM by introducing a DC offset in the high frequency AC voltage, and equivalent

circuit at equilibrium point is given by performing local linearization. By simply changing the DC offset, the proposed method can cover regions from magnetic unsaturation to saturation. The superposition theorem in electrical circuits is used to obtain the slope of flux linkage curves. Compared with the conventional static AC measurement, the proposed method does not require to lock the rotor. Besides, saturation effect is properly addressed. Simulation results show that the proposed dynamic measurement is effective in obtaining the magnetic characteristics of SRM.

Acknowledgement. This study was supported by Seoul National University of Science and Technology.

Conflict of interest. The authors declare that they have no conflicts of interest.

REFERENCES

1. Pan J.F., Cheung N.C., Gan W.C., Zhao S.W. A Novel Planar Switched Reluctance Motor for Industrial Applications. *IEEE Transactions on Magnetics*, 2006, vol. 42, no. 10, pp. 2836-2839. doi: https://doi.org/10.1109/TMAG.2006.879143.

2. Zhang T., Chen J., Zhu W. Suspension Performance Analysis on the Novel Hybrid Stator Type Bearingless Switched Reluctance Motor. *IEEE Transactions on Magnetics*, 2021, vol. 57, no. 6, pp. 1-4. doi: https://doi.org/10.1109/TMAG.2021.3064078.

3. Niguchi N., Hirata K.N., Takahara K., Suzuki H. Proposal of a New Coil Arrangement for a Four-Phase Switched Reluctance Motor. *IEEE Transactions on Magnetics*, 2021, vol. 57, no. 2, pp. 1-6. doi: https://doi.org/10.1109/TMAG.2020.3019082.

4. Chen H.-C., Wang W.-A., Huang B.-W. Integrated Driving/Charging/Discharging Battery-Powered Four-Phase Switched Reluctance Motor Drive With Two Current Sensors. *IEEE Transactions on Power Electronics*, 2019, vol. 34, no. 6, pp. 5019-5022. doi: https://doi.org/10.1109/TPEL.2018.2880259.

5. Chen H., Yu F., Yan W., Orabi M. Calculation and Analysis of Eddy-Current Loss in Switched Reluctance Motor. *IEEE Transactions on Applied Superconductivity*, 2021, vol. 31, no. 8, pp. 1-4. doi: https://doi.org/10.1109/TASC.2021.3091068.

6. Ahmad S.S., Narayanan G. Evaluation of DC-Link Capacitor RMS Current in Switched Reluctance Motor Drive. *IEEE Transactions on Industry Applications*, 2021, vol. 57, no. 2, pp. 1459-1471. doi: https://doi.org/10.1109/TIA.2020.3048637.

7. Zhu J., Cheng K.W.E., Xue X. Design and Analysis of a New Enhanced Torque Hybrid Switched Reluctance Motor. *IEEE Transactions on Energy Conversion*, 2018, vol. 33, no. 4, pp. 1965-1977. doi: https://doi.org/10.1109/TEC.2018.2876306.

8. Bibik O.V., Mazurenko L.I., Shykhnenko M.O. Formation of characteristics of operating modes of switched reluctance motors with periodic load. *Electrical Engineering & Electromechanics*, 2019, no. 4, pp. 12-16. doi: https://doi.org/10.20998/2074-272X.2019.4.02.

9. Kiyota K., Chiba A. Design of Switched Reluctance Motor Competitive to 60-kW IPMSM in Third-Generation Hybrid Electric Vehicle. *IEEE Transactions on Industry Applications*, 2012, vol. 48, no. 6, pp. 2303-2309. doi: https://doi.org/10.1109/TIA.2012.2227091.

10. Yang Z., Shang F., Brown I.P., Krishnamurthy M. Comparative Study of Interior Permanent Magnet, Induction, and Switched Reluctance Motor Drives for EV and HEV Applications. *IEEE Transactions on Transportation Electrification*, 2015, vol. 1, no. 3, pp. 245-254. doi: https://doi.org/10.1109/TTE.2015.2470092.

11. Lin Z., Reay D.S., Williams B.W., He X. Online Modeling for Switched Reluctance Motors Using B-Spline Neural Networks. *IEEE Transactions on Industrial Electronics*, 2007, vol. 54, no. 6, pp. 3317-3322. doi: https://doi.org/10.1109/TIE.2007.904009.

12. Gao H., Salmasi F.R., Ehsani M. Inductance Model-Based Sensorless Control of the Switched Reluctance Motor Drive at Low Speed. *IEEE Transactions on Power Electronics*, 2004, vol. 19, no. 6, pp. 1568-1573. doi: https://doi.org/10.1109/TPEL.2004.836632.

13. Yao S., Zhang W. A Simple Strategy for Parameters Identification of SRM Direct Instantaneous Torque Control. *IEEE Transactions on Power Electronics*, 2018, vol. 33, no. 4, pp. 3622-3630. doi: https://doi.org/10.1109/TPEL.2017.2710137.

14. Radimov N., Ben-Hail N., Rabinovici R. Inductance measurements in switched reluctance machines. *IEEE Transactions on Magnetics*, 2005, vol. 41, no. 4, pp. 1296-1299. doi: https://doi.org/10.1109/TMAG.2005.844835.

15. Peng Zhang, Cassani P.A., Williamson S.S. An Accurate Inductance Profile Measurement Technique for Switched Reluctance Machines. *IEEE Transactions on Industrial Electronics*, 2010, vol. 57, no. 9, pp. 2972-2979. doi: https://doi.org/10.1109/TIE.2010.2048831.

16. Ustun O. Measurement and Real-Time Modeling of Inductance and Flux Linkage in Switched Reluctance Motors. *IEEE Transactions on Magnetics*, 2009, vol. 45, no. 12, pp. 5376-5382. doi: https://doi.org/10.1109/TMAG.2009.2026897.

Received 22.07.2022
Accepted 13.12.2022
Published 07.03.2023

Jiayi Fan[1]*, Master's Degree,*
Yongkeun Lee[1]*, PhD, Professor,*
[1] Seoul National University of Science and Technology,
Seoul 01811, South Korea,
e-mail: fjy1510780466@163.com,
yklee@seoultech.ac.kr (Corresponding Author)

How to cite this article:
Fan J., Lee Y. Dynamic measurement of magnetic characteristics of switched reluctance motor. *Electrical Engineering & Electromechanics*, 2023, no. 2, pp. 3-6. doi: https://doi.org/10.20998/2074-272X.2023.2.01

UDC 621.313 https://doi.org/10.20998/2074-272X.2023.2.02

A.N. Patel

Slot opening displacement technique for cogging torque reduction of axial flux brushless DC motor for electric two-wheeler application

Introduction. *Reduction of cogging torque is the crucial design consideration of axial flux brushless DC (BLDC) motor, particularly for low-speed applications.* ***Aim****. The slot opening displacement technique is presented in this article to reduce cogging torque in axial flux BLDC motors suitable for electric two-wheeler applications.* ***Methods****. Double rotor single stator configuration of axial flux BLDC motor is the most suitable for such vehicular applications. Initially double rotor single stator 250 W, 150 rpm axial flux BLDC motor is designed with stator slot opening in middle position and considered as reference motor for further analysis. To evaluate the cogging torque profile of the reference motor 3D finite element modeling and analysis are performed. The design is enhanced by dividing all stator teeth into groups and displacing the slot openings of each group in opposite direction with respect to the adjacent group.* ***Results****. The influence of slot opening displacement on cogging torque is evaluated with finite element modeling and analysis. As cogging torque is reduced from 1.23 N·m to 0.63 N·m, the slot opening displacement technique is found to be effective in reducing cogging torque of axial flux BLDC motor.* References 26, table 2, figures 13.

Key words: **axial flux brushless DC motor, cogging torque, slot opening displacement, design improvement, finite element analysis.**

Вступ*. Зменшення зубчастого обертаючого моменту є важливим фактором при проектуванні безщіткових двигунів постійного струму (БЩДПС) з осьовим потоком, особливо для низькошвидкісних застосувань.* ***Мета****. У цій статті представлений метод зміщення отвору щілини для зменшення зубчастого моменту в БЩДПС з осьовим потоком, придатних для застосування в електричних двоколісних транспортних засобах.* ***Методи****. Конфігурація двигуна постійного струму з осьовим потоком з двома роторами та одним статором є найбільш підходящою для таких транспортних засобів. Початково спроєктований двороторний двигун БЩДПС з одним статором потужністю 250 Вт, 150 об/хв з осьовим потоком з отвором в статорному пазу в середньому положенні вважається еталонним двигуном для подальшого аналізу. Для оцінки профілю зубчастого обертаючого моменту еталонного двигуна виконується 3D-моделювання та аналіз методом скінченних елементів. Конструкція вдосконалена за рахунок поділу всіх зубів статора на групи та усунення пазових отворів кожної групи у протилежному напрямку по відношенню до сусідньої групи.* ***Результати****. Вплив зміщення отвору паза на зубчастий обертаючий момент оцінюється за допомогою моделювання та аналізу методом скінченних елементів. Оскільки зубчастий обертаючий момент зменшується з 1,23 Н·м до 0,63 Н·м, метод зміщення відкриття щілини виявився ефективним для зниження зубчастого обертаючого моменту двигуна БЩДПС з осьовим потоком.* Бібл. 26, табл. 2, рис. 13.

Ключові слова: **безщітковий двигун постійного струму з осьовим потоком, зубчастий обертаючий момент, зміщення отвору паза, удосконалення конструкції, аналіз методом скінченних елементів.**

Introduction. Permanent magnet (PM) brushless motors are extensively used in various applications as it has attractive features like high efficiency, compactness, wide speed range, and fast dynamic response. The development in high energy PM materials and semiconductor switching devices has been the key factor in volume applications of PM brushless motors [1, 2]. PM brushless motors are generally categorized according to magnetic flux path as permanent radial flux magnet motors and permanent axial flux magnet motors [3]. The magnetic flux sets in radial direction and exciting current flows in axial direction in radial flux PM motors while magnetic flux sets in axial direction and exciting current flows in radial direction in axial flux PM motors. The better performance of axial flux PM motors over radial flux PM motors has attracted a lot of attention. Axial flux PM motors offer superior performance in terms of high efficiency, high power density, better utilization of copper, adjustable air-gap, and flat shape [4]. Due to these noteworthy merits axial flux PM motors are popularly used in typical applications like electric vehicles, elevators, robotics, servo drives, aerospace equipments, torpedo, and etc. [5]. In torque quality sensitive applications, torque ripple is one of the most significant performance characteristics. Vibration and noise are exacerbated by high torque ripple. It is important to note that the effects of high torque ripple are more objectionable in low speed range. Performance enhancement with torque ripple reduction of axial flux PM motors is highly indispensable particularly in low speed applications like electric vehicles.

Cogging torque and commutating torque due to distorted current and back electromotive force (EMF) waveforms are two components of torque ripple. The former is derived from variation of field energy due to slot reluctance variation and the later is derived due to harmonics in current and back EMF [6]. Cogging torque has greater effect on vibration, noise and start up performance. PM motors have inherent cogging torque due to the presence of PMs and a slotted stator structure. Because of the interaction between slot reluctance variation and the magneto motive force of PMs, cogging torque is inevitable. To improve the overall performance of axial flux brushless DC (BLDC) motors, it is critical to reduce cogging torque. Cogging torque can be lowered through PM motor design changes, whereas commutation torque can be reduced through control technique changes. It is always preferable to reduce cogging torque with design improvement since any reform in control technique will lead to compromise in efficiency. As a result, the focus of this research is on cogging torque reduction in axial flux BLDC motors through design reform.

Several techniques have been introduced to reduce cogging torque of radial flux PM motors like skewing of stator slots, skewing of magnets, dual skewing, displacement of pole, shaping of magnet pole, shaping and/or notching of stator tooth, notching of magnets, variation of pole arc, stepped slot opening shift, and etc. [7-16]. Genetic algorithms based optimization is done by changing the rotor design in terms of the magnet thickness, pole span and shape of the magnets for cogging

torque reduction of permanent magnet synchronous motor [17]. Among them only few techniques are directly applicable to axial flux permanent motors. Implementation cost and manufacturability are important factors that decide the applicability of design reforms for cogging torque reduction of PM axial flux motors. In radial flux PM motors, skewing the stator slot is more practicable than in axial flux PM motors. With the twin notched design of a radial flux surface mounted PM motor, cogging torque is minimized by using less PM material [18]. An effective technique for cogging torque reduction in axial flux PM motors is magnet skewing [19]. It is important to note that axial thrust increases along with reduction in cogging torque due to magnet skewing [20]. Variation of magnet pole arc reduces cogging torque with compromise in average torque and quality of back EMF waveform. Dual skew magnet technique is better option for cogging torque reduction of yoke less and segmented armature (YASA) axial flux PM motors [21]. Slot opening variation reduced cogging torque by 52 % of flat shape axial flux PM motor with main dimensions of 180 mm and 27 mm [22]. PMs with a relative displacement reduce cogging torque. As magnets are moved from a symmetrical to an unsymmetrical position, flux leakage increases [5]. In comparison to sector magnets and cylindrical magnets, sinusoidally shaped magnets perform better. With stator side adjustments such as slot opening shape variation and skewed slot opening, the cogging torque of an axial flux machine can be lowered [23]. Cogging torque of axial flux BLDC motor can be reduced with magnet notching technique. Magnet notching results in to increased unit cost of PM pole and reduced mechanical strength particularly when thickness of magnet is less [24].

This work focuses on reducing the cogging torque of axial flux brushless motor, as it is an important factor to be considered during design. The techniques pertaining to cogging torque reduction of radial flux PM motors are not directly applicable to axial flux PM motors in majority. Manufacturability and cost of implementation govern the real applicability of these techniques. Manufacturable and low-cost techniques are highly desirable in this context. Skewing of rotor and/or stator is effective method for cogging torque reduction of axial flux PM motors. However, axial force generation and manufacturing difficulties are the limitations of stator skewing of axial flux PM motors. In order to preclude abovementioned limitations, this paper proposes the slot opening displacement technique for cogging torque reduction of axial flux BLDC motors. There is no deterioration of back EMF waveform with displacement of slot as center lines of slots remain unchanged in the proposed technique. This technique is practically implementable and does not incur any extra cost.

Cogging torque. Cogging torque is caused by interaction of PMs and stator teeth hence it is the inherent characteristic of PM motors. PMs are the source of magnetic flux and stator teeth are source of reluctance variation. Air-gap reluctance variation is periodic hence cogging torque is also periodic in nature. Cogging torque is present even if stator winding is unexcited hence it is also named as no current torque. Equation (1) expresses the cogging torque in fundamental form [25]:

$$T_{cog}\left(\phi_{pm},\theta_r\right)=-\frac{1}{2}\phi_{pm}^2\frac{\mathrm{d}R}{\mathrm{d}\theta_r}, \tag{1}$$

where ϕ_{pm}, R, θ_r are the air-gap flux, air-gap reluctance and rotor angle, respectively.

Due to the periodicity cogging torque may be represented by Fourier series. Summation of interaction of each edge of PM with slot opening is the cogging torque. Following equation expresses the cogging torque produced without skewing in BLDC motors. Saturation and magnetic leakage are assumed to be negligible:

$$T_{cog}=\sum_{k=1}^{\infty}T_{N_pk}\sin\left(N_pk\alpha\right), \tag{2}$$

where k is the order of harmonics; N_p is the number of cycles of cogging torque in a rotor revolution. It is given by least common multiplier of number of slots N_s, and number of poles p; α is the relative displacement between stator teeth and rotor; T_{Npk} is the coefficient produced due to Fast Fourier Transform (FFT) of the profile.

Above mentioned equation (2) is applied to each teeth obtain cogging torque. The total cogging torque is the sum of cogging torque caused by every stator teeth. N_pk in (2) must be integer times pole numbers p. Expressing ratio of N_pk to p as i, for an arbitrary teeth given by, its cogging torque becomes:

$$T_{scj}=\sum_{i=1}^{\infty}T_{sci}\sin pi\left(\alpha+\phi_j\right), \tag{3}$$

where T_{sci} is the Fourier coefficient; ϕ_j is the relative placement of the teeth j with reference teeth (teeth no. 1).

Hence, as per (3), total cogging torque can be calculated by adding all cogging torque components of all the N_s stator teeth:

$$T_{cog}=\sum_{j=1}^{N_s}\sum_{i=1}^{\infty}T_{sci}\sin pi\left(\alpha+\frac{2\pi}{N_s}\left(j-1\right)\right). \tag{4}$$

From (4), when p/N_s is an integer number, then irrespective of teeth number j, $\sin pi\left(\alpha+\frac{2\pi}{N_s}\left(j-1\right)\right)=\sin pi\alpha$. This shows that individual cogging torque developed by every stator teeth and the total cogging torque are cophasel. Hence, total cogging torque becomes N_s times the individual cogging torque and can be expressed as

$$T_{cog}=N_s\sum_{i=1}^{\infty}T_{sci}\sin pi\alpha, \tag{5}$$

cogging torque caused by different teeth is not in phase if p/N_s is not an integer. Then, it is difficult to simplify (4). Formation of a group of certain number of adjacent slots is required for solution. The groups are chosen on the basis that the cogging torque developed by various groups is cophasel. Therefore, the total cogging torque may be explicitly linked with the cogging torque of individual group directly.

Take λ adjacent slots (teeth) as one group then $\lambda = N_p/p$. From this, the number of groups will be n, where $n = N_sp/N_p$. For a certain teeth j, the cogging torque is given by (3). Equation (3) can be rewritten as

$$T_{sc_{gj}}=\sum_{i=1}^{\infty}T_{sci}\sin pi\left(\alpha+\frac{2\pi}{N_s}\left(j-1\right)\right). \tag{6}$$

The cogging torque generated by a particular group having λ teeth is the summation of the cogging torques developed by each teeth of this group and is given by:

$$T_{cog_g} = \sum_{j=1}^{\lambda} \sum_{i=1}^{\infty} T_{sci} \sin\left[pi\left(\alpha + \frac{2\pi}{N_s}(j-1) \right) \right]. \quad (7)$$

The simplification of (6) is as:

$$T_{cog_g} = \sum_{i=1}^{\infty} T_{sci} \frac{\sin \frac{p\lambda\pi i}{N_s}}{\sin \frac{p\pi i}{N_s}} \sin\left(pi\alpha + \frac{p\lambda\pi i}{N_s} - \frac{p\pi i}{N_s} \right). \quad (8)$$

As $p\lambda i/N_s$ in (8) is an integer number the $\sin(p\lambda\pi i/N_s)$ is 0. Hence, for certain harmonic index i only the cogging torque component will exist. Equation (8) can be simplified to these i values as

$$T_{cog_g} = \sum_{i=1}^{\infty} T_{sci} \lambda \sin pi\alpha \,. \quad (9)$$

Total cogging torque can be calculated by multiplying the cogging torque of single group given by (9) with number of groups (n) as:

$$T_{cog} = n \sum_{i=1}^{\infty} T_{sci} \lambda \sin pi\alpha \,. \quad (10)$$

Axial flux BLDC motor. 3D view of double rotor single stator axial flux motor considered in present work is shown in Fig. 1. Motor rating of 250 W, 150 rpm determined for electric two-wheeler application based on application needs and system dynamics. Application requirements include a laden vehicle weight of 150 kg, top speed of 25 km/h and acceleration of 0-25 km/h in 9 s.

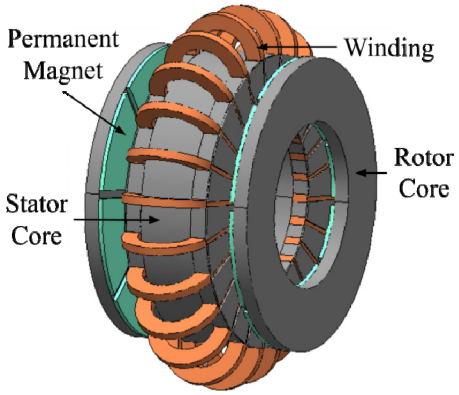

Fig. 1. Axial flux BLDC motor

Axial flux dual rotor single stator BLDC motor is designed with 48 stator slots and 16 rotor poles. Stator core is made of siliceous material of high relative permeability and laminated in order to reduce eddy current losses. Stator consists back to back ring type winding. Back-to-back ring type winding results in to short over hang. Rotor comprises rotor core and surface mount PMs. Rotor core is made of high relative permeability soft iron material. High energy NdFeB grade 50 type PM material is selected to obtain high power density and better overall performance of motor.

Design of motor is carried out based on various design variables like magnetic and electric loadings, current density, conductor packing factor, diametric ratio, number of slots/pole/phase, magnet fraction, permissible flux density in core section, and etc. Diametric ratio is assumed to be $\sqrt{3}$ to obtain optimum power density [26]. None of the cogging torque reduction technique is applied to the initially designed motor. Initially designed motor has slot openings in middle of slot and all stator teeth are symmetrically placed over the stator periphery. Initially designed motor is considered to be the reference motor for further analysis and performance comparison. Table 1 displays the important design parameters of reference motor.

Table 1

Design parameters of reference motor

Motor parameters	Value
Outer diameter, D_o	182 mm
Inner diameter, D_i	104 mm
Number of slots, N_s	48
Number of pole pair, p	16
Magnet length, L_m	2.7 mm
Length of air-gap, L_g	0.5 mm
Type of PM	NdFeB, Grade 50
PM remanence, B_r	1.2 T
Core material type	M19

According to the polarity of opposite PMs, a double rotor sandwiched stator axial flux motor can be classified as NN or NS. In a NN type motor, two opposite magnets have the same polarity, whereas two opposite magnets have opposite polarities in NS topology as shown in Fig. 2,*a*,*b* respectively.

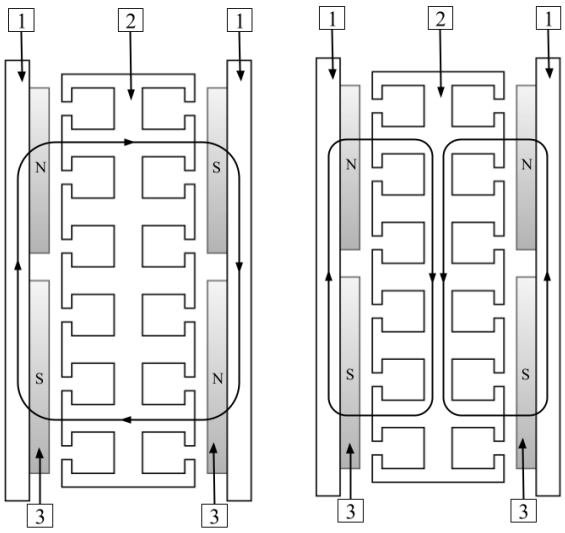

1 – rotor core; 2 – stator core; 3 – PM

Fig. 2. Flux path: (*a*) – NN topology; (*b*) – NS topology

This research work is focused on NN type axial flux PM motor. As shown in Fig. 2,*a* magnetic flux emanates from a PM, traverses the air-gap, travels through the stator core, and closes the circuit to the opposite polarity PM. Axial flux PM motors consist a disc type motor stator having a roll stacked structure including teeth, slots, and a back iron section. The tooth and the slot are formed to be apart from each other on both sides of a spiral wound ring-shaped laminated core along a circumference direction and the windings are inserted into the slots. Slots are created on spiral wound core with CNC laser cutting machines as per design calculation.

Figure 3 shows a rotor disc with 8 poles of PM material of the NdFeB type and Fig. 4 shows stator core of initially designed reference motor with slot openings in middle position and its close up view.

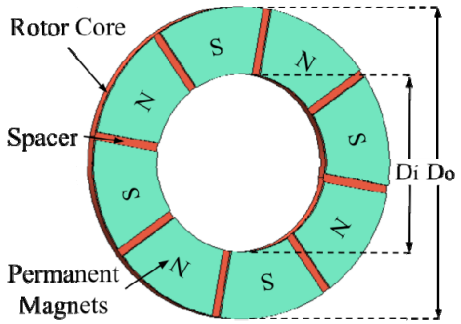

Fig. 3. Rotor disc of reference motor

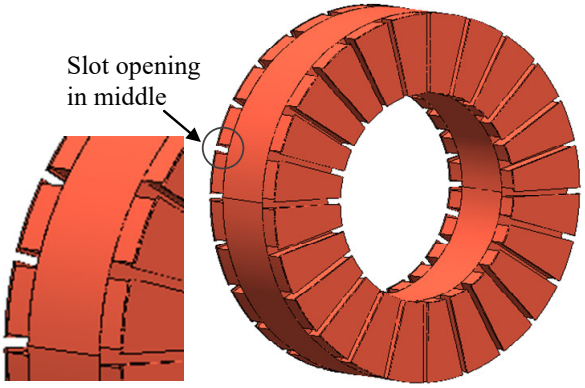

Fig. 4. Stator core of reference motor

3D modelling and simulation is required for accurate electromagnetic analysis of axial flux BLDC motor. 3D Finite Element Analysis (FEA) gives precise results considering geometric details and magnetic non-linearity. Complexity in modelling and considerable time for simulation are limitations of 3D modelling and simulation. Modelling and simulation is carried out with finite element software MagNet7.1 that is commercially available. According to the design outcome, a 3D model is created and appropriate materials are assigned. Tetrahedral elements are used to form the mesh, and boundary constraints are assigned. At different rotor position cogging torque is obtained with FEA. This technique is repeated until the final rotor position is obtained through incremental rotor position.

The cogging torque profile is plotted using the results of the cogging torque at different rotor positions. Variation of cogging torque with respect to rotor position is periodic in nature because of symmetrical structure of motor. Figure 5 illustrates the flow chart for the exercise to obtain cogging torque profile.

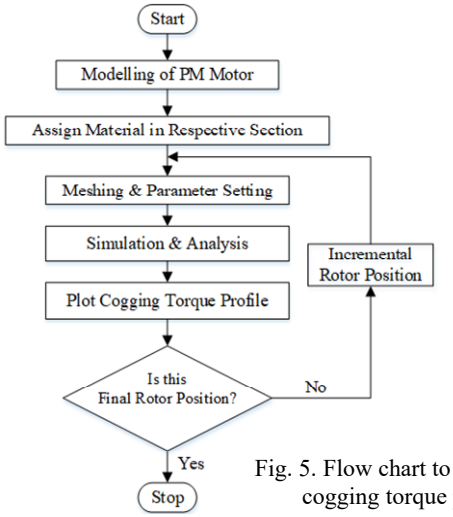

Fig. 5. Flow chart to obtain cogging torque profile

It is analysed that reference axial flux BLDC motor has 2.46 N·m peak to peak cogging torque as illustrated in Fig. 6.

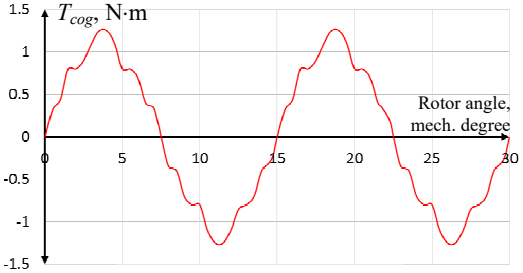

Fig. 6. Cogging torque profile of initially designed motor

Slot displacement technique. Various design strategies for cogging torque reduction of radial flux brushless motors can be found in archival literature. This section discusses techniques of axial flux BLDC motors' cogging torque reduction. Undesirable axial force is generated due to skewing of stator and/or rotor. The quality of back EMF gets deteriorated in conventional skewing because of decentralizing in winding function. Variation of pole arc adversely affect quality of back EMF waveform and average torque. Because of the interaction between air-gap flux and air-gap reluctance variation, cogging torque is produced in axial flux BLDC motors. By reducing air-gap reluctance variation, cogging torque can be reduced. This section presents modified structure based on displacement of stator slot openings. As there is no skewing or pole arc variation, the related demerits of those techniques are removed. Other performance parameters of proposed topology are in line with skewed motor. The displacement of slot openings results in smoothing air-gap reluctance variation. Because the slot openings are the main source of air-gap reluctance variation, it is important to displace only slot openings so as to obtain trapezoidal back EMF and less cogging torque. It is important to note that only slot openings are displaced keeping slot center lines fixed. Stator slots are grouped and slot openings are displaced in anti-clockwise and clockwise respectively in group as illustrated in Fig. 7,*b*. Figure 7,*a* represents reference design.

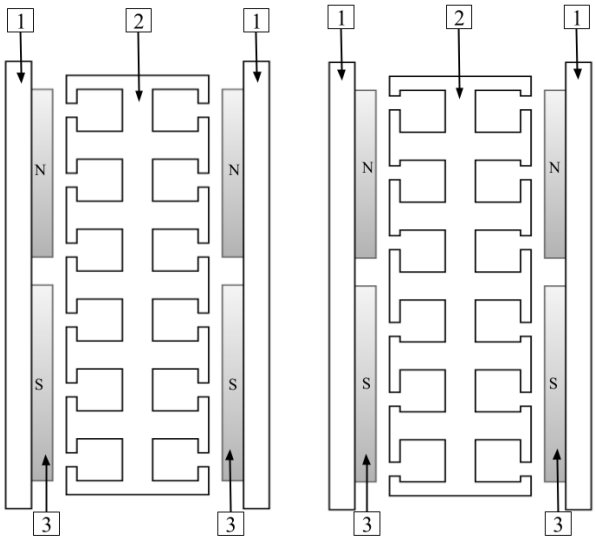

1 – rotor core; 2 – stator core; 3 – PM
Fig. 7. (*a*) – reference design of slot; (*b*) – improved slots with displaced openings

Figures 8,*a*,*b* illustrate modified stator core and its close up view with slot openings displaced by 0.75° in anti-

clockwise and clockwise respectively in group. It is important to note that only slot openings have been displaced keeping all other dimensions i.e. stator outer diameter, stator inner diameter, slot area, slot width, slot depth, and etc. same as initially designed reference motor.

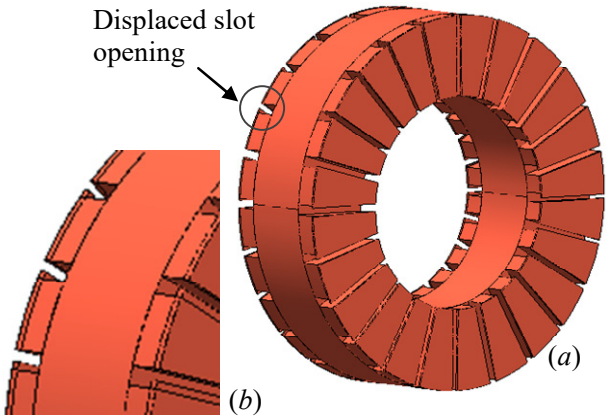

Fig. 8. (*a*) – improved stator core with shifted slot openings; (*b*) – improved stator core with shifted slot openings

Simulation and results. The slot opening displacement technique described in previous section is applied to reference axial flux PM motor having design details as per Table 1. The motor considered in present work has total 48 stator slots and number of slots on each side of rotor are 24. Each stator side has 8 groups of slots having 3 slots in each group. Slot openings of one group are displaced in clockwise direction while slot openings of adjacent group are displaced in anti-clockwise direction. Cogging torque developed by each group can be determined from (10). Due to displacement of stator slot openings in opposite direction, the cogging torque developed by adjacent group is not co-phasal hence combined cogging torque of two groups is reduced which leads to reduction of overall cogging torque. Axial flux permanent BLDC motors possess non-linear characteristic in addition to the leakage flux, fringing, manufacturing tolerances, and etc. Since FEA offer accurate and realistic results considering above-mentioned typical motor characteristics, to present effectiveness of proposed slot opening displacement technique 3D FEA has been performed. Cogging torque profile of reference motor and improved motor are displayed in Fig. 9.

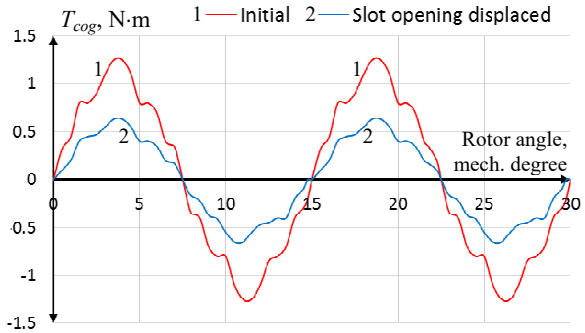

Fig. 9. Comparison between cogging torque profiles

As mentioned in Table 2 the reference axial flux BLDC motor has peak to peak cogging torque of 2.46 N·m. while improved motor with slot opening displacement has peak to peak cogging toque of 1.26 N·m. Peak to peak cogging torque is reduced from 2.46 N·m to 1.26 N·m with marginal compromise in average torque.

Table 2

Comparison of the reference and upgraded axial flux motor designs

Sr. no.	Parameters	Initial	Upgraded design with slot opening shift
1	Cogging torque, N·m	2.46	1.26
2	Average torque, N·m	15.85	14.65

The FFT analysis of the profile of cogging torque is shown in Fig. 10. Cogging torque fundamental and even order components are reduced significantly, as indicated.

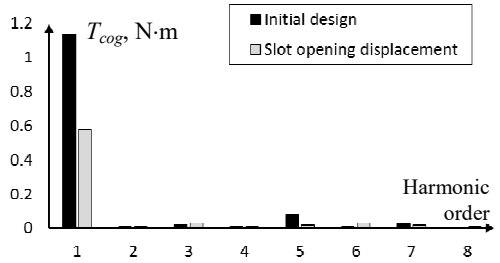

Fig. 10. FFT analysis of cogging torque profile

It's necessary to compare the back EMF waveforms of the reference and upgraded motors [26]. Comparison of back EMF waveforms before and after application of slot displacement technique is depicted in Fig. 11. Back EMF waveform is improved with slot opening displacement technique in comparison to the initially designed reference motor.

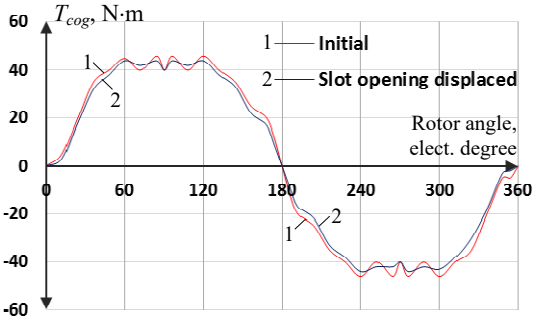

Fig. 11.Back EMF wave forms of reference design and improved design

The FFT analysis of back EMF profile is shown on Fig. 12. It is observed that fundamental component is slightly reduced from 48 V to 45.9 V and total harmonic distortion is reduced form 13.73 % to 12.41 %.

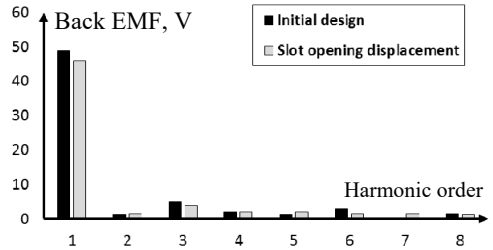

Fig. 12. FFT analysis of back EMF waveforms

Electromagnetic field analysis is performed to evaluate flux densities in various motor sections and to validate reference and improved designs. Maxwell's equations are fundamental equations governing interaction of electric and magnetic fields within an electrical machine.

Finite element method is used to solve this equation for flux density calculation. Assessing the flux density in

different motor parts is very important because it is one of the key design variables. Iron losses and overall performance of motor are influenced by flux density. Flux density is assumed based on expected performance and properties of magnetic material. If actual flux density surpasses maximum permissible flux density of respective material, motor operates in the region of saturation with reduced efficiency. Opposite to that if actual flux density is below the assumed flux density than derating of motor and poor utilization of material is observed.

Figure 13 shows flux density distribution in improved stator with displaced slot openings. It is examined that there is close agreement between actual flux densities and assumed flux densities in various sections. Analytical design of magnetic sections is validated on account of closeness between assumed and real flux densities.

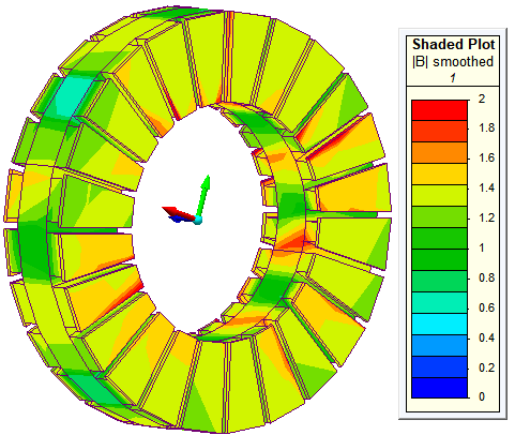

Fig. 13. Flux density plot of improved stator

Conclusion. Reduction of the cogging torque of axial flux brushless DC motors designed for low speed vehicular applications is highly desirable. This paper presents slot opening displacement technique for cogging torque reduction of double rotor sandwiched stator surface permanent magnet axial flux brushless DC motor. The motor that was initially designed is used as a reference motor, and its electromagnetic analysis is done using 3D finite element analysis. Slot opening displacement is performed to 48 slot 16 pole double rotor sandwiched stator axial flux brushless DC motor with an objective of cogging torque reduction. It is analysed that peak to peak cogging torque is reduced by 48.78 % with marginal reduction in average torque. Back electromotive force wave form of improved motor remains symmetrical. Slot opening displacement technique is effective in reduction of cogging torque of double rotor sandwiched stator axial flux brushless DC motor and can be applied to other topologies of permanent magnet motors as well.

Conflict of interest. The author declares no conflict of interest.

REFERENCES

1. Akkouchi K., Rahmani L., Lebied R. New application of artificial neural network-based direct power control for permanent magnet synchronous generator. *Electrical Engineering & Electromechanics*, 2021, no. 6, pp. 18-24. doi: https://doi.org/10.20998/2074-272X.2021.6.03.

2. Panchal T.H., Patel A.N., Patel R.M. Reduction of cogging torque of radial flux permanent magnet brushless DC motor by magnet shifting technique. *Electrical Engineering & Electromechanics*, 2022, no. 3, pp. 15-20. doi: https://doi.org/10.20998/2074-272X.2022.3.03

3. Chan C.C. Axial-Field Electrical Machines - Design and Applications. *IEEE Transactions on Energy Conversion*, 1987, vol. EC-2, no. 2, pp. 294-300. doi: https://doi.org/10.1109/TEC.1987.4765844.

4. Aydin M., Huang S., Lipo T. A. Axial Flux Permanent Magnet Disc Machines: A Review. *Research Report*, 2004, no. 10, pp. 1-11.

5. Rahim N.A., Ping H.W., Tadjuddin M. Design of Axial Flux Permanent Magnet Brushless DC Motor for Direct Drive of Electric Vehicle. *2007 IEEE Power Engineering Society General Meeting*, 2007, pp. 1-6. doi: https://doi.org/10.1109/PES.2007.385615.

6. Aydin M., Zhu Z.Q., Lipo T.A., Howe D. Minimization of Cogging Torque in Axial-Flux Permanent-Magnet Machines: Design Concepts. *IEEE Transactions on Magnetics*, 2007, vol. 43, no. 9, pp. 3614-3622. doi: https://doi.org/10.1109/TMAG.2007.902818.

7. Islam R., Husain I., Fardoun A., McLaughlin K. Permanent Magnet Synchronous Motor Magnet Designs with Skewing for Torque Ripple and Cogging Torque Reduction. *2007 IEEE Industry Applications Annual Meeting*, 2007, pp. 1552-1559. doi: https://doi.org/10.1109/07IAS.2007.240.

8. Chu W.Q., Zhu Z.Q. Investigation of Torque Ripples in Permanent Magnet Synchronous Machines With Skewing. *IEEE Transactions on Magnetics*, 2013, vol. 49, no. 3, pp. 1211-1220. doi: https://doi.org/10.1109/TMAG.2012.2225069.

9. Chabchoub M., Ben Salah I., Krebs G., Neji R., Marchand C. PMSM cogging torque reduction: Comparison between different shapes of magnet. *2012 First International Conference on Renewable Energies and Vehicular Technology*, 2012, pp. 206-211. doi: https://doi.org/10.1109/REVET.2012.6195272.

10. Jong Gun Lee, Yu Ki Lee, Gwan Soo Park. Effects of V-skew on the cogging torque in permanent magnet synchronous motor. *2013 International Conference on Electrical Machines and Systems (ICEMS)*, 2013, pp. 122-124. doi: https://doi.org/10.1109/ICEMS.2013.6754536.

11. Boukais B., Zeroug H. Magnet Segmentation for Commutation Torque Ripple Reduction in a Brushless DC Motor Drive. *IEEE Transactions on Magnetics*, 2010, vol. 46, no. 11, pp. 3909-3919. doi: https://doi.org/10.1109/TMAG.2010.2057439.

12. Wenliang Zhao, Lipo T.A., Byung-Il Kwon. Material-Efficient Permanent-Magnet Shape for Torque Pulsation Minimization in SPM Motors for Automotive Applications. *IEEE Transactions on Industrial Electronics*, 2014, vol. 61, no. 10, pp. 5779-5787. doi: https://doi.org/10.1109/TIE.2014.2301758.

13. Bin Zhang, Xiuhe Wang, Ran Zhang, Xiaolei Mou. Cogging torque reduction by combining teeth notching and rotor magnets skewing in PM BLDC with concentrated windings. *2008 International Conference on Electrical Machines and Systems*, 2008, pp. 3189-3192.

14. Petrov I., Ponomarev P., Alexandrova Y., Pyrhonen J. Unequal Teeth Widths for Torque Ripple Reduction in Permanent Magnet Synchronous Machines With Fractional-Slot Non-Overlapping Windings. *IEEE Transactions on Magnetics*, 2015, vol. 51, no. 2, pp. 1-9. doi: https://doi.org/10.1109/TMAG.2014.2355178.

15. Park G.-J., Kim Y.-J., Jung S.-Y. Design of IPMSM Applying V-Shape Skew Considering Axial Force Distribution and Performance Characteristics According to the Rotating Direction. *IEEE Transactions on Applied Superconductivity*, 2016, vol. 26, no. 4, pp. 1-5. doi: https://doi.org/10.1109/TASC.2016.2543267.

16. Upadhayay P., Rajagopal K.R. Torque ripple reduction using magnet pole shaping in a surface mounted Permanent Magnet BLDC motor. *2013 International Conference on Renewable Energy Research and Applications (ICRERA)*, 2013, pp. 516-521. doi: https://doi.org/10.1109/ICRERA.2013.6749809.

17. Sarac V. Performance optimization of permanent magnet synchronous motor by cogging torque reduction. *Journal of Electrical Engineering*, 2019, vol. 70, no. 3, pp. 218-226. doi: https://doi.org/10.2478/jee-2019-0030.

18. Yu H.-C., Yu B.-S., Yu J., Lin C.-K. A Dual Notched Design of Radial-Flux Permanent Magnet Motors with Low Cogging Torque and Rare Earth Material. *IEEE Transactions on Magnetics*, 2014, vol. 50, no. 11, pp. 1-4. doi: https://doi.org/10.1109/TMAG.2014.2329139.
19. Aydin M., Gulec M. Reduction of Cogging Torque in Double-Rotor Axial-Flux Permanent-Magnet Disk Motors: A Review of Cost-Effective Magnet-Skewing Techniques With Experimental Verification. *IEEE Transactions on Industrial Electronics*, 2014, vol. 61, no. 9, pp. 5025-5034. doi: https://doi.org/10.1109/TIE.2013.2276777.
20. Park G.-J., Kim Y.-J., Jung S.-Y. Design of IPMSM Applying V-Shape Skew Considering Axial Force Distribution and Performance Characteristics According to the Rotating Direction. *IEEE Transactions on Applied Superconductivity*, 2016, vol. 26, no. 4, pp. 1-5. doi: https://doi.org/10.1109/TASC.2016.2543267.
21. Jia L., Lin M., Le W., Li N., Kong Y. Dual-Skew Magnet for Cogging Torque Minimization of Axial Flux PMSM With Segmented Stator. *IEEE Transactions on Magnetics*, 2020, vol. 56, no. 2, pp. 1-6. doi: https://doi.org/10.1109/TMAG.2019.2951704.
22. Wanjiku J., Khan M.A., Barendse P.S., Pillay P. Influence of Slot Openings and Tooth Profile on Cogging Torque in Axial-Flux PM Machines. *IEEE Transactions on Industrial Electronics*, 2015, vol. 62, no. 12, pp. 7578-7589. doi: https://doi.org/10.1109/TIE.2015.2458959.
23. Kumar P., Srivastava R.K. Cost-Effective Stator Modification Techniques for Cogging Torque Reduction in Axial Flux Permanent Magnet Machines. *2018 IEEE Transportation Electrification Conference and Expo, Asia-Pacific (ITEC Asia-Pacific)*, 2018, pp. 1-5. doi: https://doi.org/10.1109/ITEC-AP.2018.8433291.
24. Patel A.N., Suthar B.N. Cogging Torque Reduction of Sandwiched Stator Axial Flux Permanent Magnet Brushless DC Motor using Magnet Notching Technique. *International Journal of Engineering*, 2019, vol. 32, no. 7, pp. 940-946. doi: https://doi.org/10.5829/ije.2019.32.07a.06.
25. Dosiek L., Pillay P. Cogging Torque Reduction in Permanent Magnet Machines. *IEEE Transactions on Industry Applications*, 2007, vol. 43, no. 6, pp. 1565-1571. doi: https://doi.org/10.1109/TIA.2007.908160.
26. Surong Huang, Jian Luo, Leonardi F., Lipo T.A. A general approach to sizing and power density equations for comparison of electrical machines. *IEEE Transactions on Industry Applications*, 1998, vol. 34, no. 1, pp. 92-97. doi: https://doi.org/10.1109/28.658727.

Received 22.08.2022
Accepted 21.12.2022
Published 07.03.2023

A.N. Patel[1]*, PhD, Associate Professor,*
[1] Department of Electrical Engineering,
Institute of Technology, Nirma University, India,
e-mail: amit.patel@nirmauni.ac.in (Corresponding Author)

How to cite this article:
Patel A.N. Slot opening displacement technique for cogging torque reduction of axial flux brushless DC motor for electric two-wheeler application. *Electrical Engineering & Electromechanics*, 2023, no. 2, pp. 7-13. doi: https://doi.org/10.20998/2074-272X.2023.2.02

UDC 621.3.013 https://doi.org/10.20998/2074-272X.2023.2.03

T. Amieur, D. Taibi, S. Kahla, M. Bechouat, M. Sedraoui

Tilt-fractional order proportional integral derivative control for DC motor using particle swarm optimization

Introduction. *Recently, the most desired goal in DC motor control is to achieve a good robustness and tracking dynamic of the set-point reference speed of the feedback control system.* ***Problem.*** *The used model should be as general as possible and consistently represent systems heterogeneous (which may contain electrical, mechanical, thermal, magnetic and so on).* ***Goal.*** *In this paper, the robust tilt-fractional order proportional integral derivative control is proposed. The objective is to optimize the controller parameters from solving the criterion integral time absolute error by particle swarm optimization. The control strategy is applied on DC motor to validate the efficiency of the proposed idea.* ***Methods.*** *The proposed control technique is applied on DC motor where its dynamic behavior is modeled by external disturbances and measurement noises.* ***Novelty****. The proposed control strategy, the synthesized robust tilt-fractional order proportional integral derivative speed controller is applied on the DC motor. Their performance and robustness are compared to those provided by a proportional integral derivative and fractional order proportional integral derivative controllers.* ***Results.*** *This comparison reveals superiority of the proposed robust tilt-fractional order proportional integral derivative speed controller over the remaining controllers in terms of robustness and tracking dynamic of the set-point reference speed with reduced control energy*. References 21, table 1, figures 14.

Key words: **DC motor, speed control, fractional order proportional integral derivative, particle swarm optimization.**

Вступ*. Останнім часом найбільш бажаною метою керування двигуном постійного струму є досягнення гарної надійності та динамічного відстеження заданої опорної швидкості системи керування зі зворотним зв'язком.* ***Проблема****. Використовувана модель має бути якомога загальнішою і несуперечливо представляти різнорідні системи (які можуть містити електричні, механічні, теплові, магнітні тощо).* ***Мета****. У цій статті пропонується робастне управління похідною пропорційного інтеграла дробового порядку нахилу. Мета полягає в тому, щоб оптимізувати параметри контролера шляхом вирішення критерію інтегральної абсолютної тимчасової помилки шляхом оптимізації рою частинок. Стратегія управління застосовується до двигуна постійного струму для перевірки ефективності запропонованої ідеї.* ***Методи****. Пропонований метод управління застосовується до двигуна постійного струму, динамічна поведінка якого моделюється зовнішніми перешкодами та шумами вимірів.* ***Новизна****. Пропонована стратегія управління, синтезований робастний пропорційно-інтегрально-диференціальний регулятор швидкості нахилу дробового порядку застосовується до двигуна постійного струму. Їх продуктивність та надійність порівнюються з показниками, що забезпечуються контролерами пропорційної інтегральної похідної та пропорційної інтегральної похідної дробового порядку.* ***Результати****. Це порівняння показує перевагу запропонованого робастного пропорційно-інтегрально-диференціального регулятора швидкості нахилу дробового порядку над іншими регуляторами з погляду робастності та динамічного відстеження заданої опорної швидкості зі зменшеною енергією управління.* Бібл. 21, табл. 1, рис. 14.

Ключові слова: **двигун постійного струму, регулювання швидкості, пропорційна інтегральна похідна дробового порядку, оптимізація рою частинок.**

Introduction. The growing interest in electric motors is justified by the need for industrial variable speed processes. This solution makes it possible to control a process or a system with minimal expenditure of energy and raw materials.

DC motor, by its very nature, has a high torque vs. speed characteristic, enabling it to deal with high resistive torques and absorb sudden rises in load effortlessly; the motor speed adapts to the load. In addition, DC motors are an ideal way of achieving the miniaturization that is so desirable to designers, since they offer a high efficiency as compared with other technologies.

The most desired goal in DC motor control is to achieve a good robustness and tracking dynamic of the set-point reference speed of the feedback control system. To achieve this goal, the used model should be as general as possible and consistently represent systems heterogeneous (which may contain electrical, mechanical, thermal, magnetic and so on), and all proposed DC motor models unavoidably incorporate uncertainties and external disturbances.

Controllers based on fractional order calculus are gaining more and more interests from the control community. This type of controllers may involve fractional operators and/or fractional systems in their structure or implementation. They have been introduced in the control applications in a continuous effort to enhance the system control quality performances and robustness.

Actually, a success among researchers is the fractional order proportional integral derivative (FOPID) [1]. In fact, since the development of the first control approach using the fractional proportional integral derivative (PID) controller, different design approaches were proposed [2-4]. On the other hand, in recent years it is remarkable the increasing number of studies related to the application of fractional controllers in science and engineering areas [5, 6], more concretely a fractional sliding mode control [7]. In literature, fractional PID controller is frequently used to control a first order plus dead time system [8]. But, only few design methods are considered for second order plus dead time system [9]. The robust control strategies have been proposed to determine the parameters of a robust controller. The majority of them use appropriate optimization tools to solve the weighted mixed sensitivity problem such as: H_∞ control through solution of Riccati equations and linear matrix inequality approach [10, 11]. Among them, proposed a new robust tilt-PID controller based upon an automatic selection of adjustable fractional weights for permanent magnet synchronous motor drive control, the min-max optimization algorithm to solve the weighted-mixed sensitivity problem [12].

Goal. In this paper, DC motor is controlled by a proposed tilt-fractional order proportional integral derivative (T-FOPID) speed control. The parameters of the proposed controller are optimally learned by using particle swarm optimization (PSO), and the optimization performance target is chosen as the integral time absolute error (ITAE). The performance and robustness of the T-FOPID controller are compared in time domain by the FOPID and classical PID controllers. This comparison reveals the superiority of the proposed T-FOPID controller over the remaining controllers in terms of ensuring good tracking accuracy and the ability for rejecting the internal and external influences and minimization of the measurement noise.

The mathematical model of DC motor. Torque of a DC motor is proportional to its armature current and current field. The winding field of a DC motor gets excited from a separate power supply, which is independent of its armature current. To achieve a linear variation of torque, one current (either field or armature) is kept constant while varying the other and it is possible in a DC motor because its current armature and field are independent of each other. Therefore, DC motors can be divided into two types depending up on how its torque is being controlled, namely armature-controlled DC motors and field-controlled DC motors.

As the discussion about the field-controlled DC motor is out of scope of this paper, we shall continue our discussion with armature-controlled DC motors.

In an armature-controlled DC motor which is shown in Fig. 1, the excitation for the winding field is kept constant and the torque is varied by varying the supply voltage connected to the armature. In some cases, a permanent magnet is used instead of winding field to produce the magnetic flux which is again independent of the armature current. Such motors are called permanent magnet DC motors [3].

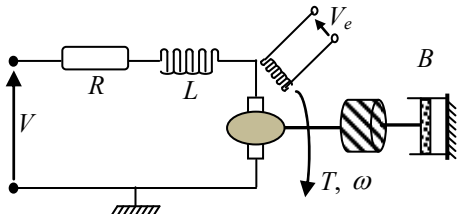

Fig. 1.Schematic diagram of the armature-controlled DC motor

A well-known linear model of DC motor for the speed control system is shown in Fig. 2.

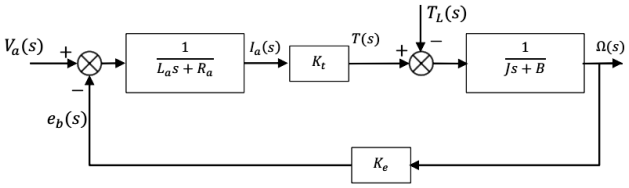

Fig. 2. Block diagram of armature-controlled DC motor

The transfer function relating the armature voltage $V_a(s)$ and angular velocity $\Omega(s)$ with $T_L(s)$ =0:

$$\frac{\Omega(s)}{V_a(s)} = \frac{K_t}{L_a J s^2 + (L_a B + R_a J)s + R_a B + K_t K_e}. \quad (1)$$

The transfer function relating the load torque $T_L(s)$ and angular velocity $\Omega(s)$ with $V_a(s) = 0$:

$$\frac{\Omega(s)}{T_L(s)} = \frac{L_a s + R_a}{L_a J s^2 + (L_a B + R_a J)s + R_a B + K_t K_e}. \quad (2)$$

The nominal values of DC motor are summarized in Table 1 [13].

Table 1

DC motor parameters

Motor parameters	Value
Moment of inertia J, kg·m^2/s^2	0.0988
Viscous friction coefficient B, N·m·s/rad	0.000587
Torque constant K_t, N·m/A	0.67609
Armature resistance R_a, Ω	1.5
Armature inductance L, H	0.2
Voltage constant K_e, V/(rad/s)	0.67609

Tilt-fractional order proportional integral derivative (T-FOPID). The general structure of the proposed T-FOPID controller is shown in Fig. 3.

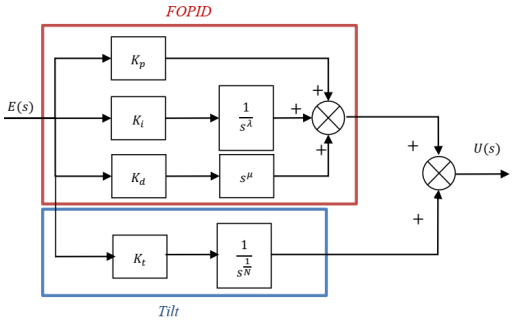

Fig. 3. Block diagram of proposed T-FOPID controller

The transfer function of the proposed T-FOPID controller is given by:

$$K(s, X) = \frac{K_t}{s^{\frac{1}{N}}} + \left(K_p + \frac{K_i}{s^\lambda} + K_d \cdot s^\mu \right). \quad (3)$$

The tilt component has a fractional order transfer function represented by $(s^{-1/N})$, where adjustable parameter N is preferably chosen between 2 and 3. Here, $X = (K_t, N, K_p, K_i, K_d, \lambda, \mu)^T$ is the design vector to be optimized by an adequate optimization algorithm. The search space limiting the optimal components of the proposed T-PID controller is defined by:

$$\begin{cases} K_{t_{\min}} \le K_t \le K_{t_{\max}}; \\ 2 \le N \le 3; \\ K_{p_{\min}} \le K_p \le K_{p_{\max}}; \\ K_{i_{\min}} \le K_i \le K_{i_{\max}}; \\ K_{d_{\min}} \le K_d \le K_{d_{\max}}; \\ 0 < \lambda < 1; \\ 0 < \mu < 1. \end{cases} \quad (4)$$

Tuning of T-FOPID by PSO algorithm. Many intelligence algorithms are proposed for tuning the T-FOPID parameters. Tuning T-FOPID parameters by the optimal algorithms such as the genetic algorithm and PSO algorithm. However, it is slow to search the best solution [14, 15].

The PSO concept consists of changing the velocity (or acceleration) of each particle toward its p_{best} and the g_{best} position at each time step. Each particle tries to modify its current position and velocity according to the distance between its current position and p_{best}, and the distance between its current position and g_{best} as shown in the following. At each step n, by using the individual best position, p_{best}, and global best position, g_{best}, a new velocity for the i^{th} particle is updated by [16]:

$$V_i(n) = wV_i(n-1) + c_1 r_1 \left(p_{best_i} - p_i(n-1) \right) + c_2 r_2 \left(g_{best_i} - p_i(n-1) \right), \quad (5)$$

where w is the constriction factor; p_i is the position vector; r_1 and r_2 are the random numbers between [0; 1]; c_1 and c_2 are the positive constant learning rates, called self-confidence and swarm confidence respectively.

Each of the three terms of the velocity update equation has different roles in the PSO algorithm [17].

The first term $wV_i(n)$ is the inertia component, which is responsible for keeping the particle moving in the same direction as it was originally heading. The value of the inertial coefficient w is typically between 0.8 and 1.2, which can either dampen the particle's inertia or accelerate the

particle in its original direction. Generally, lower values of the inertial coefficient speed up the convergence of the swarm to optima, and higher values of the inertial coefficient encourage exploration of the entire search space [18].

The second term $c_1 r_1(p_{best_i} - p_i(n-1))$, called the cognitive component, which acts as the particle's memory, causing it to tend to return to the regions of the search space in which it has experienced high individual fitness. The cognitive coefficient c_1 is usually close to 2, and affects the size of the step that the particle takes toward its individual best candidate solution p_{best_i}.

The third term $c_2 r_2(g_{best_i} - p_i(n-1))$, called the social component, causes the particle to move to the best region that the swarm has found so far. The social coefficient c_2 is typically close to 2, and represents the size of the step that the particle takes toward the global best candidate solution g_{best_i} the swarm has found up until that point.

The random values r_1 in the cognitive component and r_2 in the social component which causes these components to have a stochastic influence on the velocity update. This stochastic nature causes each particle to move in a semi-random manner heavily influenced in the directions of the individual best solution of the particle and global best solution of the swarm.

In order to keep the particles from moving too far beyond the search space, we use a technique called velocity clamping to limit the maximum velocity of each particle. For a search space bounded by the range $[p_{\min}, p_{\max}]$, velocity clamping limits the velocity to the range $[V_{\min}, V_{\max}]$, where $V_{\max} = k(p_{\max} - p_{\min})/2$. The value represents a user-supplied velocity clamping factor, $0.1 \le k \le 1$.

Based on the updated velocity, each particle changes its position as follows [19]:

$$p_i(n) = p_i(n-1) + V_i(n). \tag{6}$$

The position is confined within the range of $[p_{\min}, p_{\max}]$. If the position violates these limits, it is forced to its proper values. Changing position by this way enables the i^{th} particle to search around its local best position, p_{best}, and global best position, g_{best}

$$p_i = \begin{cases} p_{\min} & \text{if} \quad p_i < p_{\max}; \\ p_i & \text{if} \quad p_{\min} < p_i < p_{\max}; \\ p_{\max} & \text{if} \quad p_i > p_{\max}; \end{cases} \tag{7}$$

The PSO is an algorithm with population. It starts with a random initialization of the swarm in the space of research. With each iteration of the algorithm, each particle is moved according to the equations of motion which are given by (5), (6).

Objective function. As already mentioned, the fitness function to be minimized is the ITAE performance criterion [20, 21]. The integral of the absolute magnitude of error (ITAE) criterion is defined as

$$ITAE = \int_0^T t|e(t)|\mathrm{d}t\,. \tag{8}$$

The ITAE performance criterion index has the advantages of producing smaller overshoots and oscillations than the IAE (integral of the absolute error) or the ISE (integral square error) performance indices. In addition, it is the most sensitive of the three, i.e., it has the best selectivity. The ITSE (integral time-square error) index is somewhat less sensitive and is not comfortable computationally. Since it is not practicable to integrate up to infinity, the convention is to choose a value of T sufficiently large so that $e(t)$ for $t > T$ is negligible.

Tuning parameters of T-FOPID by PSO algorithm. Optimization by PSO consists of designing the optimization goal, i.e., the fitness function and then encoding the parameters to be searched. The PSO algorithm runs until the stop condition is satisfied. The best particle's position gives the optimized parameters.

The parameters of the T-FOPID controller (Fig. 4) to be optimized has seven unknown parameters to be tuned $X = (K_t, N, K_p, K_i, K_d, \lambda, \mu)^T$. Hence the present problem of controller tuning can be solved by an application of the PSO algorithm for optimization on a seven-dimensional solution space, each particle has a seven-dimensional position and velocity vector.

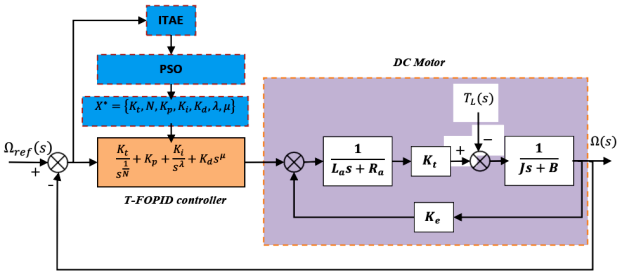

Fig. 4. Feedback T-FOPID control of DC motor

The optimization process based on the PSO is summarized by the flowchart, depicted in Fig. 5.

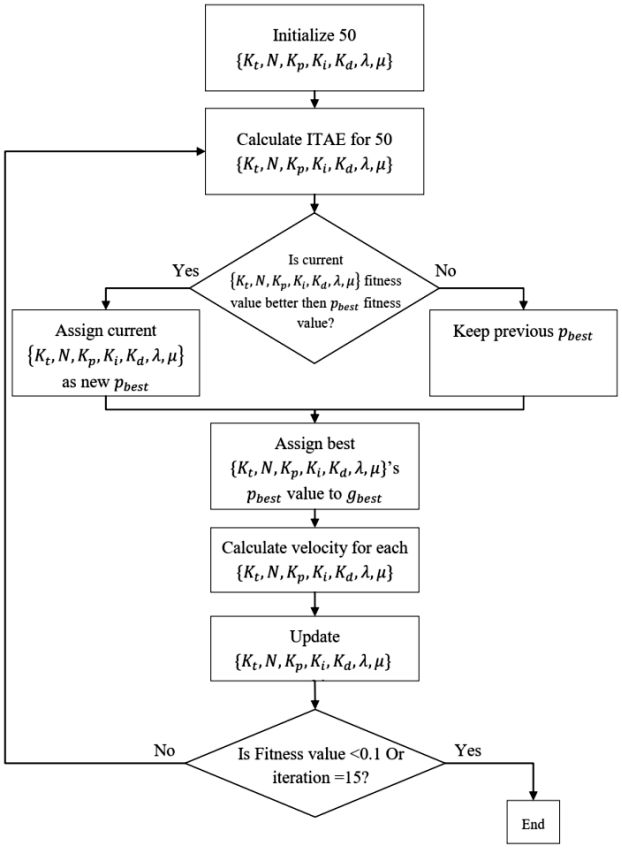

Fig. 5. The flowchart providing the robust T-FOPID speed controller tuning by PSO algorithm

Simulation results and discussion. The nominal values of DC motor are summarized in Table 1, the nominal voltage

$V_a = 120$ V. The transfer function relating the armature voltage $V_a(s)$ and angular velocity $\Omega(s)$ with $T_L(s) = 0$:

$$\frac{\Omega(s)}{V_a(s)} = \frac{0.67609}{0.01976 \cdot s^2 + 0.14832 \cdot s + 0.45798}.$$

The transfer function relating the load torque $T_L(s)$ and angular velocity $\Omega(s)$ with $V_a(s) = 0$:

$$\frac{\Omega(s)}{T_L(s)} = \frac{0.2 \cdot s + 1.5}{0.01976 \cdot s^2 + 0.14832 \cdot s + 0.45798}.$$

The corresponding optimization problem contains seven unknown variables. It is expressed as follows:

$$X^* \subset X = \begin{cases} 0 \le K_t \le 3; \\ 2 \le N \le 3; \\ 0 \le K_p \le 50; \\ 0 \le K_i \le 50; \\ 0 \le K_d \le 5; \\ 0 < \lambda < 1; \\ 0 < \mu < 1. \end{cases}$$

This problem is solved by the PSO, in which the following tuning parameters are used (Fig. 6):

- SwarmSize = 50;
- OFun = @FFtfopidfunction;
- MaxIter = 15;
- MinFit = 0.1.

The provided optimal solution X^* by the PSO allows determining the following T-FOPID, FOPID and PID controllers [15]:

$$K_{T-FOPID}(s) = \frac{0.501}{s^{1/3}} + 16.6384 + \frac{30}{s^{0.8144}} + 2.2729 \cdot s^{0.9049};$$

$$K_{FOPID}(s) = 12.1348 + \frac{50}{s^{0.985}} + 2.4856 \cdot s^{0.979};$$

$$K_{PID}(s) = 15.3326 + \frac{36.8206}{s} + 2.029 \cdot \left(\frac{180.2349}{1 + 180.2349 \cdot \left(\frac{1}{s} \right)} \right).$$

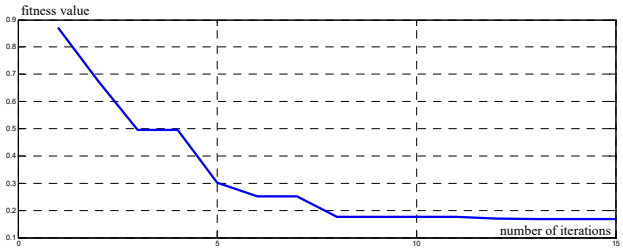

Fig. 6. The best provided minimization using the PSO of the fitness value

The above mentioned three controllers are connected with the linear nominal *DC* model and the obtained feedback control system is then excited by the three exogenous inputs: mechanical speed reference, disturbance and sensor noise signals. The load torque input $T_L = 20$ N·m, applied at the starting time $t = 4$ s. The random signal of zero mean and Gaussian distribution with a variance equal to 10^{-3} with the star-time $t = 7$ s. Therefore, Fig. 7, 11, 12, 14 compare the mechanical speeds provided by the three PID, FOPID and T-FOPID speed controllers. Otherwise, where their control signals are compared in Fig. 14.

Tracking echelon signal reference speed. The nominal reference speed of this motor is 157 rad/s (120 V is the supply voltage).

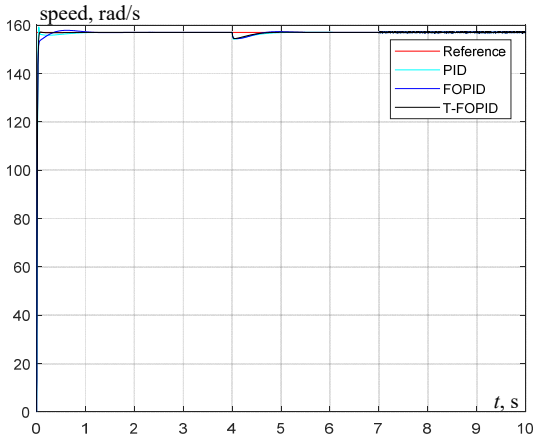

Fig. 7. The given speed with torque load and measurement noise presence

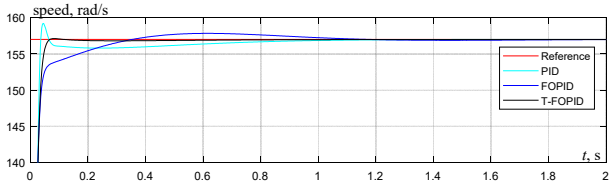

Fig. 8. Zoom of the given speed parts of transient-state

Torque load rejection. The presence of the load torque input T_L = 20 N·m, which is applied at the starting time $t = 4$ s. From the Fig. 7, we conclude that the T-FOPID controller allows tracking the reference speed with high accuracy. Figure 8, the zoom parts given speed of transient-state and Fig. 9, the zoom parts given speed of the presence load torque input T_L = 20 N·m, applied at the starting time $t = 4$ s. In Fig. 10, the zoom parts give speed of the presence measurement noise random signal of zero mean and Gaussian distribution with a variance equal to 10^{-3} with the star-time $t = 7$ s.

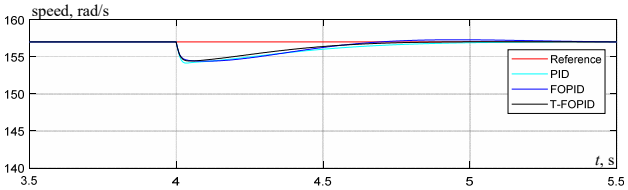

Fig. 9. Zoom of the given speed parts of torque load

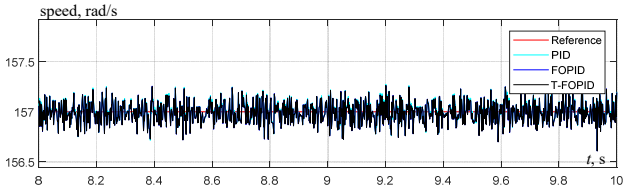

Fig. 10. Zoom of the given speed parts of measurement noise

Tracking rectangular signal reference speed. Used to excite the feedback control system. The input is assumed by:

$$\omega_{ref} = \begin{cases} 157 \text{ rad/s} & 0 \le t \le 2 \text{ s} \quad \text{and} \quad 6 \text{ s} < t \le 10 \text{ s}; \\ -157 \text{ rad/s} & 2 \text{ s} \le t \le 6 \text{ s}. \end{cases}$$

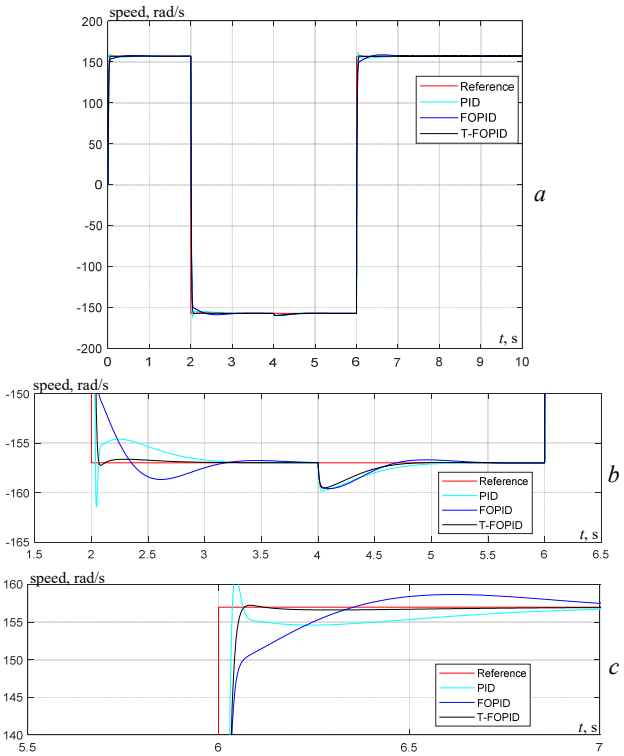

Fig. 11. *a* – the given speed for reference speed rectangular signal by the three controllers *PID, FOPID* and *T-FOPID*; *b*, *c* – the zoom parts

Tracking sinusoidal signal reference speed. The reference speed input is assumed to be a sinusoidal signal based sample type. It is given with the amplitude $A = 157$, where 100 samples per period $T = 3.14$ s.

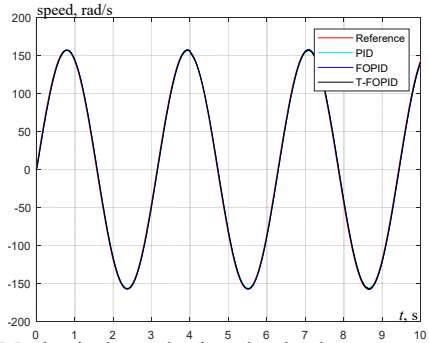

Fig. 12. Mechanical speeds given by the three controllers PID, FOPID and T-FOPID

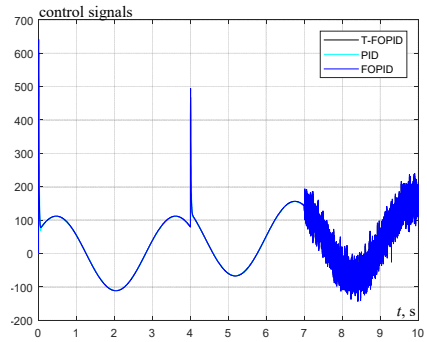

Fig. 13. Control signals by the three PID, FOPID and T-FOPID speed controllers

Therefore, the output signals given with T-FOPID, FOPID and PID controllers are compared in Fig. 12, where in their control signals are compared in Fig. 13 with reference speed input is a sinusoidal signal.

Tracking triangular signal reference speed. The second reference speed input is assumed to be a triangular signal with the amplitude $A = 157$ and the period $T = 2$ s.

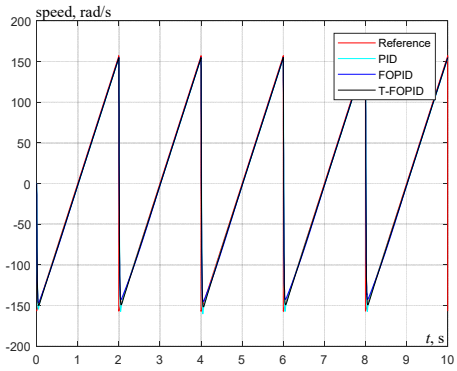

Fig. 14. Mechanical speeds given by the three controllers PID, FOPID and T-FOPID

Despite changing the speed to several forms (rectangular signal Fig. 11, sinusoidal signal Fig. 12 and triangular signal Fig. 14), we note that the T-FOPID controller tracks it with high accuracy.

Conclusions. In this paper we have proposed the new robust tilt-fractional order proportional integral derivative controller, for the optimization of parameters in this controller we used the particle swarm optimization algorithm. It is a very simple and efficient algorithm which gave optimal parameters of proposed controller, based on the integral time absolute error criterion. The speed of a DC motor in a closed loop with tilt-fractional order proportional integral derivative controller. First, we subjected the dc motor to different speeds (constant signal, rectangular signal, sinusoidal signal and triangular signal), we noticed the ability of the proposed controller to change the dc motor speed to follow these speeds with high accuracy in a short time. Secondly, we studied the efficiency of the proposed controller in rejecting the external influences (torque load) and minimization of the measurement noise. Finally, we compared the performance of the proportional integral derivative and fractional order proportional integral derivative controllers to confirm the superiority and efficiency of the tilt-fractional order proportional integral derivative controller in tracking accuracy and the ability to reject the internal and external influences. Based on these results, it can be said that the proposed controller is very effective and reliable in controlling the speed of the *DC* motor.

Conflict of interest. The authors declare that they have no conflicts of interest.

REFERENCES

1. Podlubny I. Fractional-order systems and $PI^{\lambda}D^{\mu}$-controllers. *IEEE Transactions on Automatic Control*, 1999, vol. 44, no. 1, pp. 208-214. doi: https://doi.org/10.1109/9.739144.

2. Monje C.A., Vinagre B.M., Feliu V., Chen Y. Tuning and auto-tuning of fractional order controllers for industry applications. *Control Engineering Practice*, 2008, vol. 16, no. 7, pp. 798-812. doi: https://doi.org/10.1016/j.conengprac.2007.08.006.

3. Amieur T., Sedraoui M., Amieur O. Design of Robust Fractional-Order PID Controller for DC Motor Using the Adjustable Performance Weights in the Weighted-Mixed Sensitivity Problem. *IAES International Journal of Robotics and*

Automation (IJRA), 2018, vol. 7, no. 2, pp. 108-118. doi: https://doi.org/10.11591/ijra.v7i2.pp108-118.
4. Regad M., Helaimi M., Taleb R., Gabbar H., Othman A. Optimal frequency control in microgrid system using fractional order PID controller using krill herd algorithm. *Electrical Engineering & Electromechanics*, 2020, no. 2, pp. 68-74. doi: https://doi.org/10.20998/2074-272X.2020.2.11.
5. Barbosa R.S., Tenreiro Machado J.A., Jesus I.S. Effect of fractional orders in the velocity control of a servo system. *Computers & Mathematics with Applications*, 2010, vol. 59, no. 5, pp. 1679-1686. doi: https://doi.org/10.1016/j.camwa.2009.08.009.
6. Tavakoli-Kakhki M., Haeri M. Fractional order model reduction approach based on retention of the dominant dynamics: Application in IMC based tuning of FOPI and FOPID controllers. *ISA Transactions*, 2011, vol. 50, no. 3, pp. 432-442. doi: https://doi.org/10.1016/j.isatra.2011.02.002.
7. Ardjal A., Mansouri R., Bettayeb M. Fractional sliding mode control of wind turbine for maximum power point tracking. *Transactions of the Institute of Measurement and Control*, 2019, vol. 41, no. 2, pp. 447-457. doi: https://doi.org/10.1177/0142331218764569.
8. Li M., Zhou P., Zhao Z., Zhang J. Two-degree-of-freedom fractional order-PID controllers design for fractional order processes with dead-time. *ISA Transactions*, 2016, vol. 61, pp. 147-154. doi: https://doi.org/10.1016/j.isatra.2015.12.007.
9. Chen K., Tang R., Li C. Phase-constrained fractional order PI^{λ} controller for second-order-plus dead time systems. *Transactions of the Institute of Measurement and Control*, 2017, vol. 39, no. 8, pp. 1225-1235. doi: https://doi.org/10.1177/0142331216634427.
10. Aidoud M., Sedraoui M., Lachouri A., Boualleg A. A robustification of the two degree-of-freedom controller based upon multivariable generalized predictive control law and robust H_{∞} control for a doubly-fed induction generator. *Transactions of the Institute of Measurement and Control*, 2018, vol. 40, no. 3, pp. 1005-1017. doi: https://doi.org/10.1177/0142331216673425.
11. Patra S., Sen S., Ray G. A linear matrix inequality approach to parametric H_{∞} loop shaping control. *Journal of the Franklin Institute*, 2011, vol. 348, no. 8, pp. 1832-1846. doi: https://doi.org/10.1016/j.jfranklin.2011.05.006.
12. Amieur T., Bechouat M., Sedraoui M., Kahla S., Guessoum H. A new robust tilt-PID controller based upon an automatic selection of adjustable fractional weights for permanent magnet synchronous motor drive control. *Electrical Engineering*, 2021, vol. 103, no. 3, pp. 1881-1898. doi: https://doi.org/10.1007/s00202-020-01192-3.
13. Aashoor F.A.O., Robinson F.V.P. Maximum power point tracking of PV water pumping system using artificial neural based control. *3rd Renewable Power Generation Conference (RPG 2014)*, Naples, 2014, pp. 1-6, doi: https://doi.org/10.1049/cp.2014.0923.
14. Aghababa M.P. Optimal design of fractional-order PID controller for five bar linkage robot using a new particle swarm optimization algorithm. *Soft Computing*, 2016, vol. 20, no. 10, pp. 4055-4067. doi: https://doi.org/10.1007/s00500-015-1741-2.
15. Hekimoglu B. Optimal Tuning of Fractional Order PID Controller for DC Motor Speed Control via Chaotic Atom Search Optimization Algorithm. *IEEE Access*, 2019, vol. 7, pp. 38100-38114. doi: https://doi.org/10.1109/ACCESS.2019.2905961.
16. Anwar N., Hanif A., Ali M.U., Zafar A. Chaotic-based particle swarm optimization algorithm for optimal PID tuning in automatic voltage regulator systems. *Electrical Engineering & Electromechanics*, 2021, no. 1, pp. 50-59. doi: https://doi.org/10.20998/2074-272X.2021.1.08.
17. Bouraghda S., Sebaa K., Bechouat M., Sedraoui M. An improved sliding mode control for reduction of harmonic currents in grid system connected with a wind turbine equipped by a doubly-fed induction generator. *Electrical Engineering & Electromechanics*, 2022, no. 2, pp. 47-55. doi: https://doi.org/10.20998/2074-272X.2022.2.08.
18. Marini F., Walczak B. Particle swarm optimization (PSO). A tutorial. *Chemometrics and Intelligent Laboratory Systems*, 2015, vol. 149, pp. 153-165. doi: https://doi.org/10.1016/j.chemolab.2015.08.020.
19. Kao C.-C., Chuang C.-W., Fung R.-F. The self-tuning PID control in a slider–crank mechanism system by applying particle swarm optimization approach. *Mechatronics*, 2006, vol. 16, no. 8, pp. 513-522. doi: https://doi.org/10.1016/j.mechatronics.2006.03.007.
20. Kumar Sahu R., Panda S., Biswal A., Chandra Sekhar G.T. Design and analysis of tilt integral derivative controller with filter for load frequency control of multi-area interconnected power systems. *ISA Transactions*, 2016, vol. 61, pp. 251-264. doi: https://doi.org/10.1016/j.isatra.2015.12.001.
21. Barisal A.K. Comparative performance analysis of teaching learning based optimization for automatic load frequency control of multi-source power systems. *International Journal of Electrical Power & Energy Systems*, 2015, vol. 66, pp. 67-77. doi: https://doi.org/10.1016/j.ijepes.2014.10.019.

Received 13.10.2022
Accepted 08.12.2022
Published 07.03.2023

Toufik Amieur [1,2], *Associate Professor,*
Djamel Taibi [3], *PhD, Assistant Professor,*
Sami Kahla [4], *Associate Professor,*
Mohcene Bechouat [2, 5], *PhD, Associate Professor,*
Moussa Sedraoui [2], *Professor,*
[1] Department of Electrical Engineering,
Echahid Cheikh Larbi Tebessi University-Tebessa, Algeria
[2] The Telecommunications Laboratory (LT),
University 8 May 1945 Guelma, Algeria,
e-mail: amieur.toufik@univ-tebessa.dz (Corresponding Author);
sedraoui.moussa@univ-guelma.dz
[3] Department of Electrical Engineering,
Kasdi Merbah University-Ouargla, Algeria,
e-mail: taibi.djamel@yahoo.fr
[4] A Research Center in Industrial Technologies (CRTI), Algeria,
e-mail: samikahla40@yahoo.com
[5] Automatic and Electromechanic Department,
University of Ghardaia, Algeria,
e-mail: mohcene.oui@gmail.com

How to cite this article:
Amieur T., Taibi D., Kahla S., Bechouat M., Sedraoui M. Tilt-fractional order proportional integral derivative control for DC motor using particle swarm optimization. *Electrical Engineering & Electromechanics*, 2023, no. 2, pp. 14-19. doi: https://doi.org/10.20998/2074-272X.2023.2.03

UDC 621.3.013 https://doi.org/10.20998/2074-272X.2023.2.04

R.S. Kumar, C.S.R. Reddy, B.M. Chandra

Optimal performance assessment of intelligent controllers used in solar-powered electric vehicle

Introduction. *Increasing vehicle numbers, coupled with their increased consumption of fossil fuels, have drawn great concern about their detrimental environmental impacts. Alternative energy sources have been the subject of extensive research and development. Due to its high energy density, zero emissions, and use of sustainable fuels, the battery is widely considered one of the most promising solutions for automobile applications. A major obstacle to its commercialization is the battery's high cost and low power density.* ***Purpose***. *Implementing a control system is the primary objective of this work, which is employed to change the energy sources in hybrid energy storage system about the load applied to the drive.* ***Novelty.*** *To meet the control objective, a speed condition-based controller is designed by considering four separate math functions and is programmed based on different speed ranges. On the other hand, the conventional/intelligent controller is also considered to develop the switching signals related to the DC-DC converter's output and applied the actual value.* ***Methods.*** *According to the proposed control strategy, the adopted speed condition based controller is a combined conventional/intelligent controller to meet the control object.* ***Practical value.*** *In this work, three different hybrid controllers adopted speed condition based controller with artificial neural network controller, adopted speed condition based controller with fuzzy logic controller, and adopted speed condition based controller with proportional-integral derivative controller are designed and applied separately and obtain the results at different load conditions in MATLAB/Simulink environment. Three hybrid controller's execution is assessed based on time-domain specifications.* References 19, table 2, figures 40.
Key words: **solar power, proportional-integral derivative controller, artificial neural network controller, fuzzy logic controller.**

Вступ. *Збільшення кількості транспортних засобів у поєднанні із збільшенням споживання ними викопного палива викликало серйозну заклопотаність з приводу їх згубного впливу на навколишнє середовище. Альтернативні джерела енергії були предметом інтенсивних досліджень та розробок. Завдяки високій щільності енергії, нульовим викидам та використанню екологічно чистих видів палива акумулятор широко вважається одним із найперспективніших рішень для застосувань у автомобілях. Основною перешкодою для його комерціалізації є висока вартість батареї та низька питома потужність.* ***Мета***. *Впровадження системи управління, яка використовується для зміни джерел енергії в системі гібридної накопичення енергії в залежності від навантаження, прикладеного до приводу, є основною метою цієї роботи.* ***Новизна***. *Для досягнення мети управління контролер на основі умов швидкості розроблено з урахуванням чотирьох окремих математичних функцій та запрограмовано на основі різних діапазонів швидкостей. З іншого боку, вважається, що звичайний/інтелектуальний контролер виробляє сигнали перемикання, пов'язані з вихідним сигналом перетворювача постійного струму, та застосовує фактичне значення.* ***Методи***. *Відповідно до запропонованої стратегії управління прийнятий контролер на основі умов швидкості є комбінованим традиційним/інтелектуальним контролером для задоволення об'єкта управління.* ***Практична цінність***. *У цій роботі три різних гібридних контролери, що використовують контролер на основі умов швидкості з контролером штучної нейронної мережі, контролер на основі адаптованих умов швидкості з контролером з нечіткою логікою та контролер на основі прийнятих умов швидкості з пропорційно-інтегрально-диференціальним контролером, розроблені та застосовуються окремо та отримують результати за різних умов навантаження у середовищі MATLAB/Simulink. Робота трьох гібридних контролерів оцінюється з урахуванням специфікацій у часовій області.* Бібл. 19, табл. 2, рис. 40.
Ключові слова: **сонячна енергія, пропорційно-інтегральний похідний контролер, контролер штучної нейронної мережі, контролер нечіткої логіки.**

Introduction. Most of the greenhouse content is produced from a conventional transportation system, which is harmful to the entire universe. To save the atmosphere from destructive gases released by the Internal Combustion (IC) engine-based vehicles, battery-based vehicles are introduced. Thereafter solar power-based vehicles are also designed to increase the environmentally friendly probability. Single energy source powered electric vehicles have taken some draws back like driving range and peak power production during transient state conditions. Multiple sources powered electric vehicles are again designed to drawbacks present in single-power electric vehicles. The main problem associated with multiple power source vehicles is the switching of energy sources related to the dynamics of the vehicle. In this, a different control scheme is intended to achieve the accurate transition of energy sources.

A system is designed especially for solar power-based electric vehicles. With the designed system, separate space is created for vehicles for charging the main sources [1]. The separate power system is constructed only with solar power, which is used to share the power from the conventional grid because the designed conventional power system is supplying power to general purposes like lighting, industries, and utilities. To meet the electric vehicles, load by dismissing, the burden on conventional power systems a solar power system is constructed which is exclusively for electric vehicle charging [2, 3]. A predictive controller is designed based on various nonlinearities, which are present in vehicles. Moreover, the designed controller is used for changing the energy source of solar power electric vehicles that may battery to supercapacitor vice versa [4]. The control strategy is designed with two separate controllers for an easy-shifting of energy sources of Hybrid Energy Storage System (HESS), battery, and Ultra Capacitor (UC). The designed control strategy is useful during changing energy sources precisely [5, 6]. An adaptive supervisory management control strategy is proposed for multiple energy sources powered by electric vehicles and the proposed strategy is useful to share the power between different sources present in HESS [7, 8]. Various power electronic devices are proposed to charge the battery present in plug-in electric or hybrid vehicles, in that some of the devices will take more time and some will take less time for continuous ON and OFF conditions used to control the voltage levels of converters [9, 10]. Separate fuel cell, electric and hybrid electric vehicle architectures are presented and compared to the drawbacks and advantages of those systems. Moreover, it is used to select the type of vehicle for a particular application [11].

Research focuses on the development of an echelon battery. It is possible to use echelon-use batteries in battery energy storage systems (BESS) in the power grid, but the

energy management strategy should differ from that of a traditional battery [12]. The main purpose of this system is to provide sufficient energy to different loads and minimize the energy deficit and the loss of power supply probability (LPSP) [13]. For energy storage to provide multiple grid services effectively and safely, Energy Management Systems (EMSs) and optimization methods are essential [14]. With five parameters, the fractional-order controller is more flexible and robust for microgrid perturbations than the classical Proportional-Integral derivative (PID) controller. A new optimization technique called Krill Herd is used to optimize the parameters of the fractional order PID controller. Compared with other optimization methods like Particle Swarm Optimization (PSO), this is a suitable optimization method [15, 16]. For reducing the effects of PV power intermittency on the stability of the electric grid, a novel algorithm for EMS is proposed, which is combined with a storage system. EMS controls power flow from the PV generator to the grid based on the predetermined PV power level in the simulation model. The PV system and energy storage system are connected to the same DC bus [17].

Description of Photovoltaic Array (PVA). Figure 1 illustrates [18] the PVA model which is obtained from several PVA modules. The PVA includes series R_{se}, shunt R_{sh} and load R_L resistance. In the same way, the photon I_{ph}, the diode I_0, and load I_{pv} currents are represented by their flowing direction.

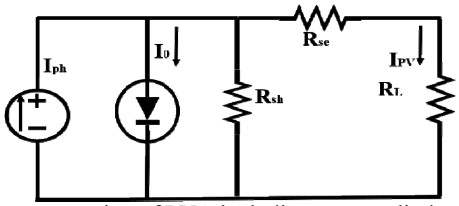

Fig. 1. Representation of PVA including source, diode, and load

The current from the input of the circuit is characterized by I_{ph}

$$I_{ph} = \left[I_{scr} + I_K \cdot (T - 298)\right] \cdot \lambda / 1000 , \quad (1)$$

where I_K is the short-circuit current of cell at 25 °C and 1000 W/m^2; T is the junction temperature, K; λ is the solar irradiation, W/m^2.

The reverse saturation current of the module is given by

$$I_{rs} = I_{scr} / \left[\exp(q \cdot V_{oc} / N_S \cdot k \cdot A \cdot T) - 1\right]. \quad (2)$$

Module saturation current is represented with I_0 and is given as

$$I_0 = I_{rs}\left[\frac{T}{T_r}\right]^3 \exp\left[\frac{q \cdot E_{g0}}{B \cdot k}\left\{\frac{1}{T_r} - \frac{1}{T}\right\}\right]. \quad (3)$$

The total current of the PVA module is given as

$$I_{pv} = N_P \cdot I_0\left[\exp\left\{\frac{q \cdot \left(V_{pv} + I_{pv} R_s\right)}{N_s \cdot A \cdot k \cdot T}\right\} - 1\right], \quad (4)$$

where I_{rs}, I_{scr}, V_{oc}, V_{pv}, I_{pv}, R_s are the reverse saturation current, short circuit current, open circuit voltage, cell voltage, cell current, and resistance of the circuit; k is the Boltzmann's constant; q is the electron charge; T_r is the nominal temperature (298.15 K); E_{g0} is the band gap energy of the semiconductor; N_s, N_p are the number of cells connected in series and in parallel, respectively; A, B are the ideality factors.

System model with proposed control configuration. The main block diagram with different sources and the solar panel is represented in Fig. 2 [5]. The major source battery is rechargeable and gets charged from the solar panel during the daytime. Here battery can discharge the energy to the load during sunlight is unavailable time. The two controller's output signal is compared at the circuit breaker block, to produce controlled switching pulses. The electric drive is connected across the DC bus, which is a combination of two DC-DC converters' outputs. The control switches shown in the block diagram are used to control the flow from the PVA to the battery and unidirectional converter (UDC). Here bidirectional converter (BDC) is used to do the two-directional operations.

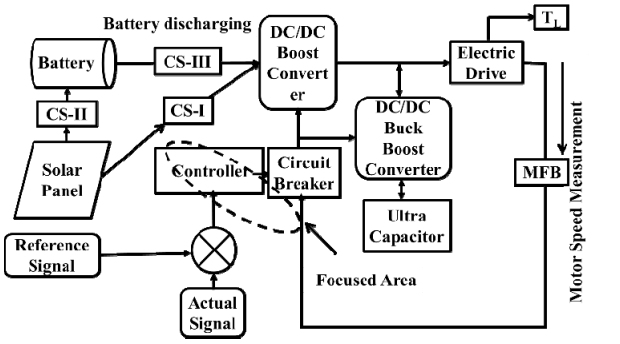

Fig. 2. Representation of the proposed scheme with a block diagram

Figure 3 [6] is representing the proposed model with DC-DC converters with three switches S_1, S_2, and S_3. Here switches S_1 and S_3 are used for boost operation whereas switch S_2 is used to perform the buck operation. The ON and OFF condition of the converts is always decided by the vehicle load condition which is again related to motor speed. The UC is associated with the BDC side, in the same way, the battery is linked at the UDC end. The main source always sends energy to load except for starting and heavy load. On the other hand, UC can send power to load during transient state conditions and gets charged from the battery during no-load periods.

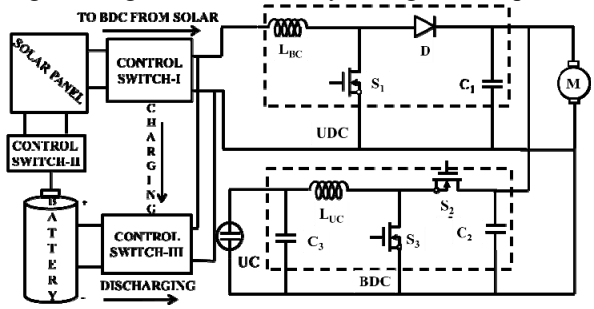

Fig. 3. Circuit representation with converters and source

About controllers used in recommended method. In this work total, four controllers were used based on the proposed control strategy. Those are Speed condition-based (SCB), Artificial Neural Network (ANN), Fuzzy Logic Controller (FLC), and PID controllers. In this section description of all controllers is given.

SCB controller is the main controller utilized in the projected control approach. This controller design is always related to the motor's speed. This will develop 4-outputs U_1, U_2, U_3, and U_4 by taking input value as speed. Depending upon the speed ranges, the particular output of SCB is in the active state, which again will decide the regulated signals to the switch existing in the BDC and UDC.

ANN controller. The general architecture of the ANN controller for obtaining the output signal is represented in Fig. 4 [19]. Here the required output of the controller always depends upon the delayed output and delayed inputs of the ANN controller. Here back propagation method is adopted to

obtain the desired output from the applied converters. The z-inverse model is utilized here to send the signals from the output to the input of the network.

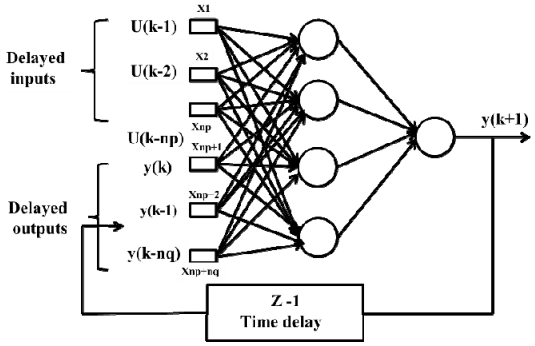

Fig. 4. The ANN controller diagrammatic representation

PID controller. The mathematical equation related to the PID controller (Fig. 5) has been represented with the below equation

$$y(t) \propto \left(e(t) + \int e(t)\mathrm{d}t + \frac{\mathrm{d}e(t)}{\mathrm{d}t} \right); \quad (5)$$

$$y(t) = k_p \cdot e(t) + k_i \int e(t)\mathrm{d}t + k_d \frac{\mathrm{d}e(t)}{\mathrm{d}t}; \quad (6)$$

where k_p, k_i, k_d, $e(t)$ represent the proportional, integral, derivative gains and error value.

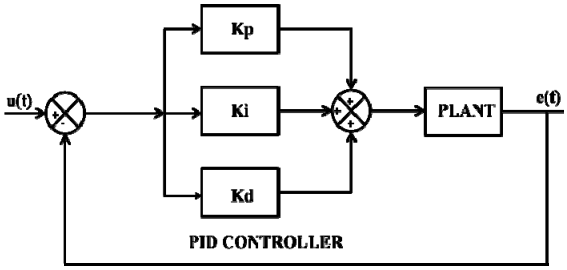

Fig. 5. PID block diagram model with three gain values

Fuzzy Logic Controller (FLC). Figure 6 [9] illustrates how FLCs are typically structured. For the output of the fuzzy logic controller to be rectified, separate mathematical modeling need not be performed. The type of membership function selected depends on the requirements of the system. Most commonly, triangular, or trapezoidal shapes are used. Afterward, the inference was performed using a rule base. Here, the output variables were managed using a rule base. The fuzzy logic controller considered each rule base to determine the result. This FLC system measures error (E) and change in error (CE) as inputs, which means FLC output is the result of error and change in error.

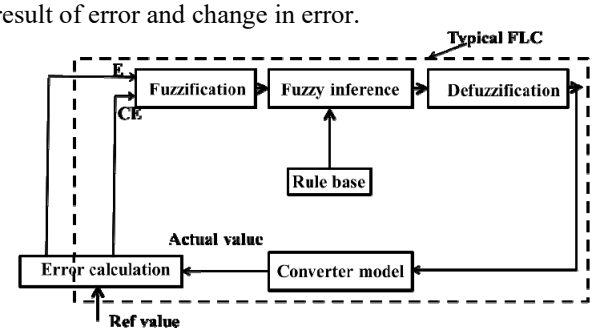

Fig. 6. General model representation of an FLC network

Main circuit with proposed technique. The main circuit operation is divided into four modes based on a load applied. In mode one, the total power demanded by the motor is supplied from the UC due to a heavy load, in mode two of operation battery, and UC combined to meet the load requirement. During mode three, the battery only supplies the load requirement, in the fourth mode of operation battery can supply power to UC as well as load. Figures 7-10 are corresponding to different modes of operation of electric motor [15].

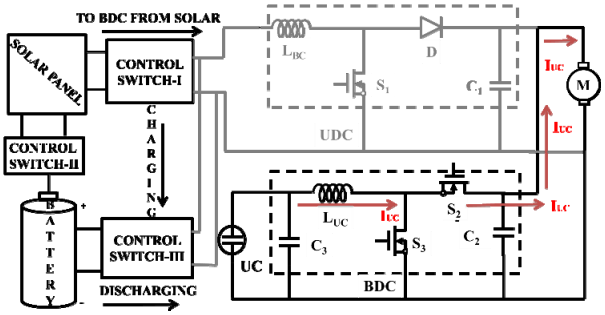

Fig. 7. Mode ONE related circuit model with BDC and UDC

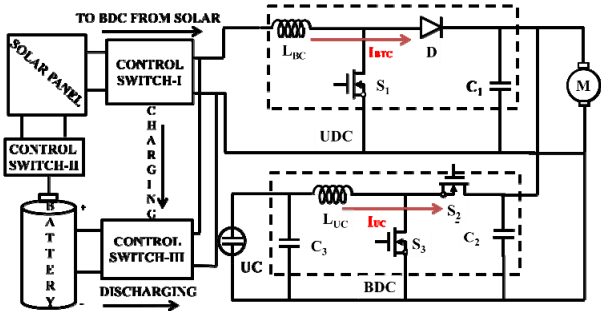

Fig. 8. Mode TWO related circuit model with BDC and UDC

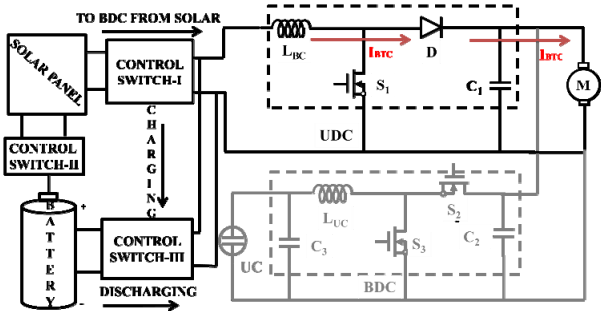

Fig. 9. Mode THREE related circuit model with BDC and UDC

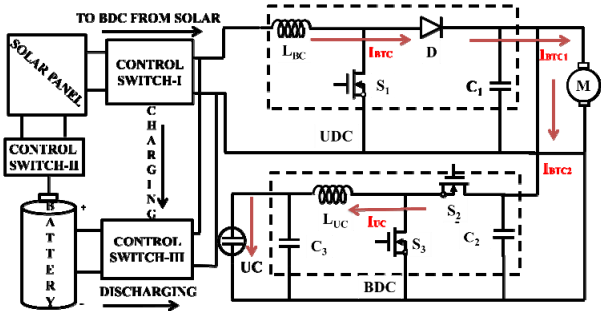

Fig. 10. Mode FOUR related circuit model with BDC and UDC

Presentation of proposed control strategy technique. Figure 11 is representing how the measured signals are generated related to the motor's speed in four modes of operation.

The SCB generates the four different output pulses as per the speed range of an electric motor as follows

1. If the $N \leq 4800$ rpm then math function U_1 only is in an active state and remaining all math functions are disabled.

2. The speed range is $4600 \le N \le 4800$ rpm then math functions U_1, and U_2 are in the active state and the remaining two-math function disabled state.

3. If speed is $4801 \le N \le 4930$ rpm then math function U_3 is in the active state and remains all are disabled.

4. The $N \ge 4931$ rpm the math function U_4 is in the active state and remain math functions are disabled.

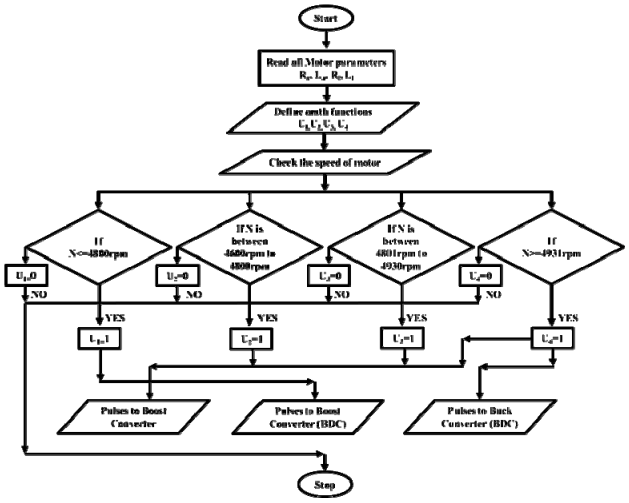

Fig. 11. Three converter pulse signal production of flow chart model

Figures 12-14 demonstrate the development of the regulated pulses to the switches S_1, S_2, and S_3 and which are obtained as per the outputs of the SCB as follows. If the output sign of the SCB is whichever U_2, or U_3, or U_4 then the regulated pulse is produced to the switch S_1. When the output of the SCB is only U_4, the regulated pulses are developed to S_2. If the output of the SCB is whichever U_1 or U_2 then the regulated pulses are offered to S_3.

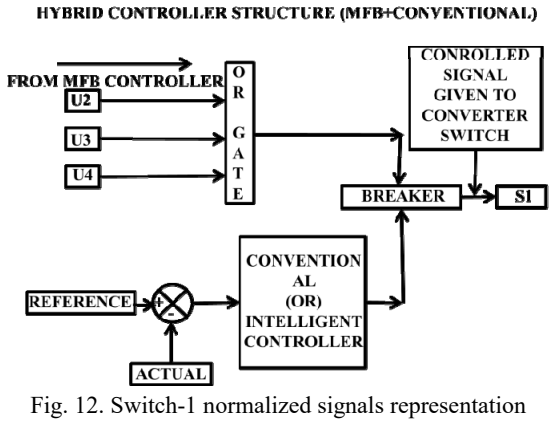

Fig. 12. Switch-1 normalized signals representation

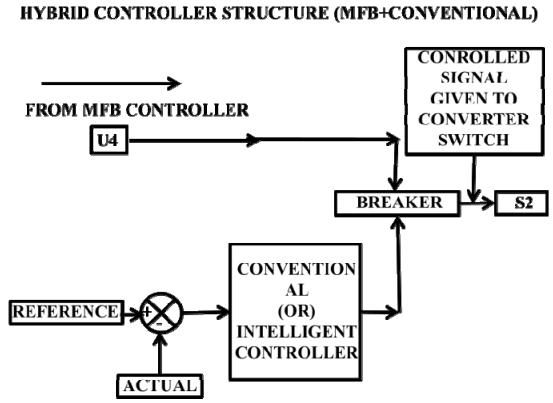

Fig. 13. Switch-2 normalized signals representation

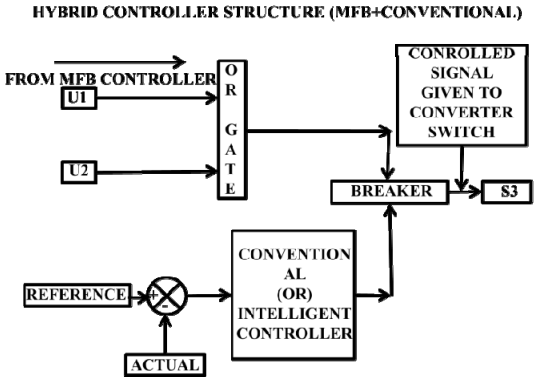

Fig. 14. Switch-3 normalized signals representation

Simulation outcomes and considerations. The outcomes after successful simulation are presented in this section. The SCB with ANN controller's speed, current, and switching signals generation plots are shown in Figures continuously 15, 21, 27, 33 and 18, 24, 30, 36. Similarly, SCB with PID output responses of a motor is represented in Figures 16, 22, 28, 34 on the other hand, Figures 19, 25, 31, 37 are indicating the switching signal delivered to a particular switch existing in BDC and UDC. Finally, SCB with fuzzy logic controller's output responses is shown in Figures 17, 23, 29 and 35 similarly. Figures 20, 26, 32, and 38 are the switching signals formed to BDC and UDC.

Mode-I results.

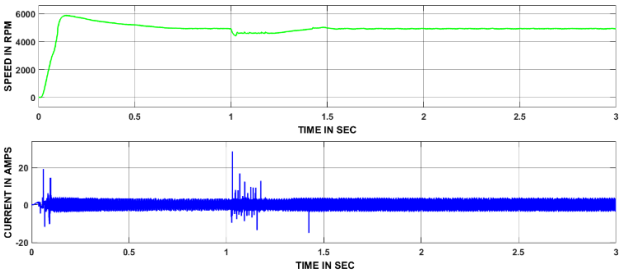

Fig. 15. Output responses of the electric drive related to Mode-I (SCB+ANN)

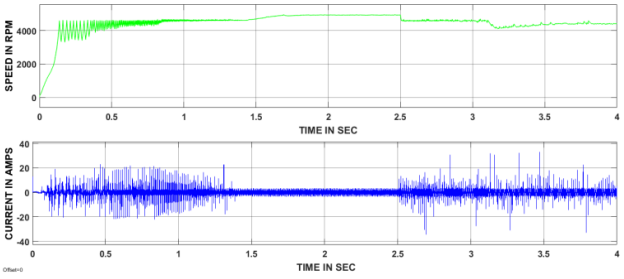

Fig. 16. Output responses of the electric drive related to Mode-I (SCB+PID)

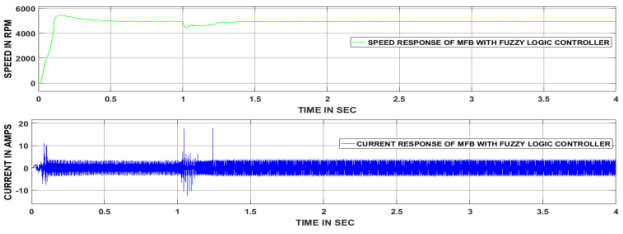

Fig. 17. Output responses of the electric drive related to Mode-I (SCB+FLC)

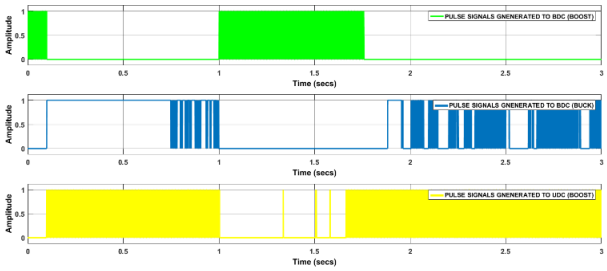

Fig. 18. Pulses of converters by SCB+ANN, Mode-I

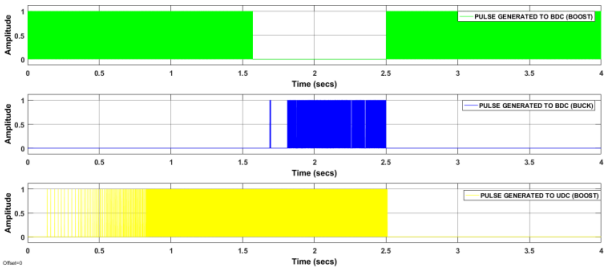

Fig. 19. Pulses of converters by SCB+PID, Mode-I

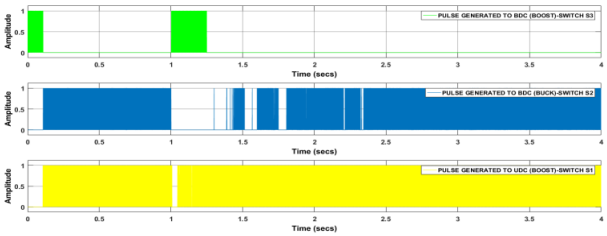

Fig. 20. Pulses of converters by SCB+FLC, Mode-I

Mode-II results.

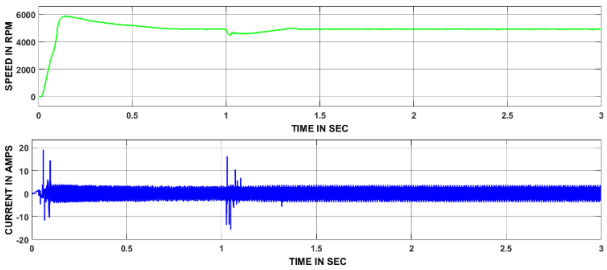

Fig. 21. Output responses of the electric drive related to Mode-II (SCB+ANN)

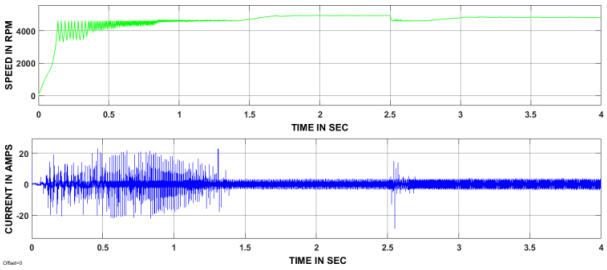

Fig. 22. Output responses of the electric drive related to Mode-II (SCB+PID)

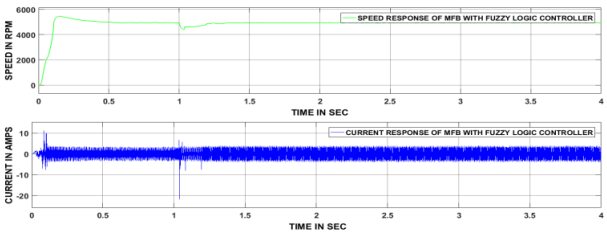

Fig. 23. Output responses of the electric drive related to Mode-II (SCB+FLC)

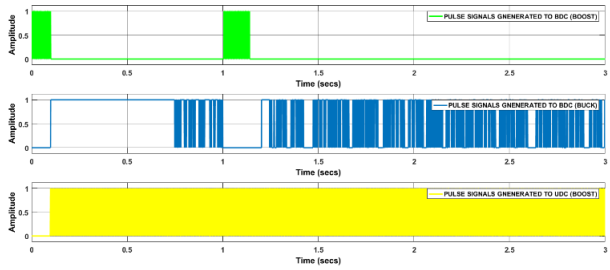

Fig. 24. Pulses of converters by SCB+ANN, Mode-II

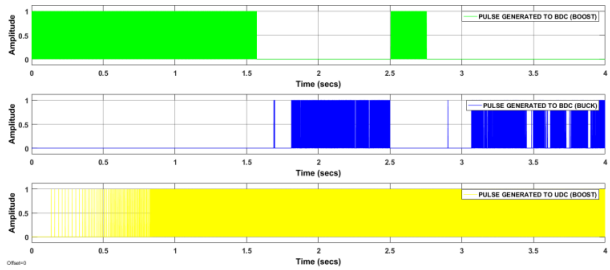

Fig. 25. Pulses of converters by SCB+PID, Mode-II

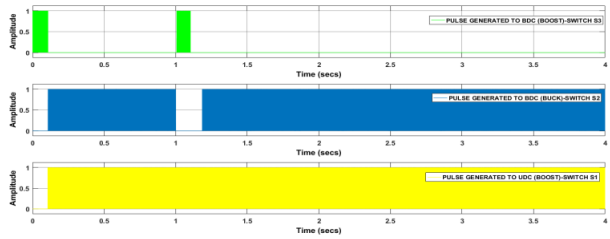

Fig. 26. Pulses of converters by SCB+FLC, Mode-II

Mode-III results.

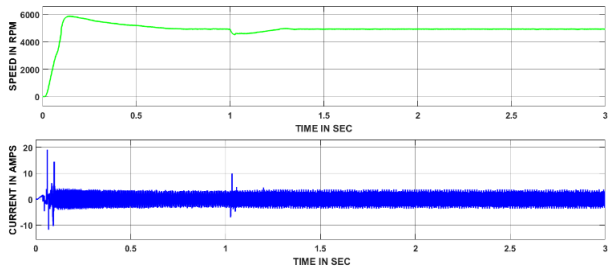

Fig. 27. Output responses of the electric drive related to Mode-III (SCB+ANN)

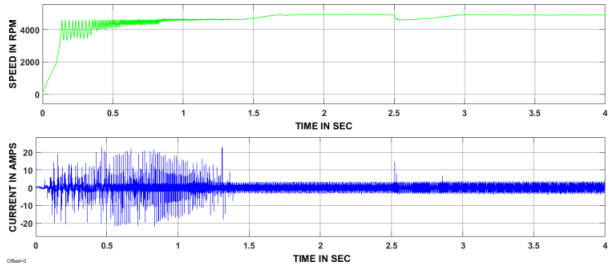

Fig. 28. Output responses of the electric drive related to Mode-I (SCB+PID)

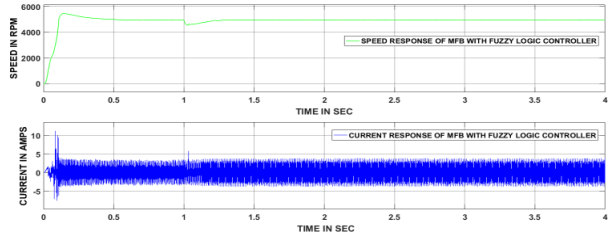

Fig. 29. Output responses of the electric drive related to Mode-I (SCB+FLC)

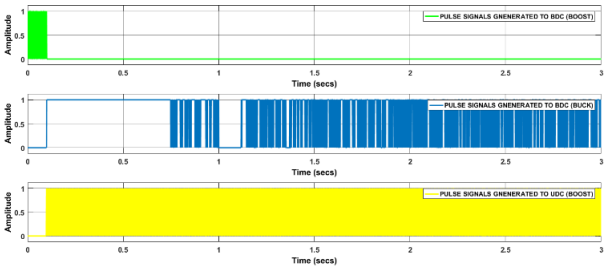

Fig. 30. Pulses of converters by SCB+ANN, Mode-III

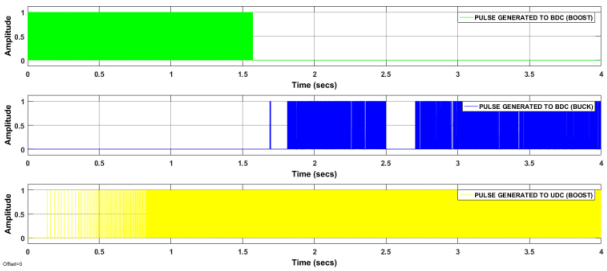

Fig. 31. Pulses of converters by SCB+PID, Mode-III

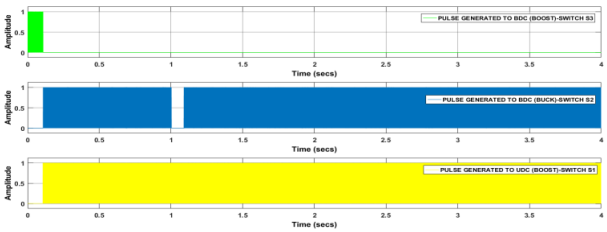

Fig. 32. Pulses of converters by SCB+FLC, Mode-III

Mode-IV results.

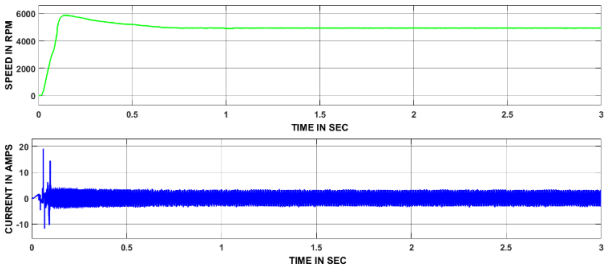

Fig. 33. Output responses of the electric drive related to Mode-IV (SCB+ANN)

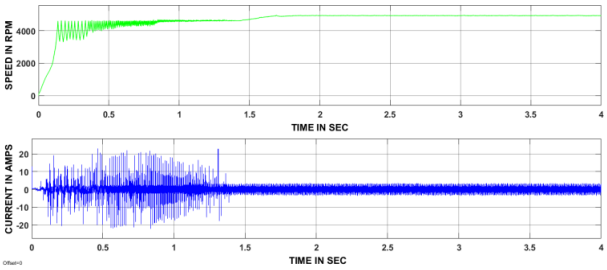

Fig. 34. Output responses of the Electric drive related to Mode-I (SCB+PID)

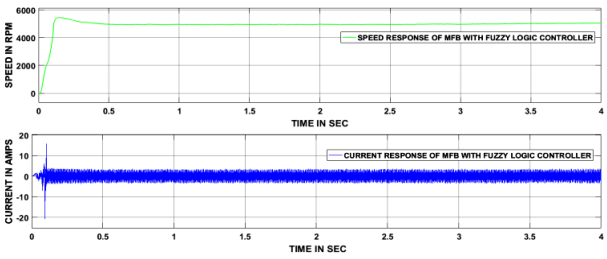

Fig. 35. Output responses of the electric drive related to Mode-I (SCB+FLC)

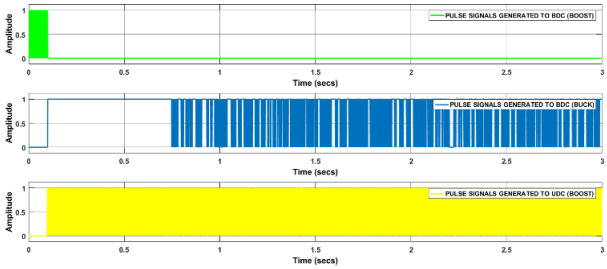

Fig. 36. Pulses of converters by SCB+ANN, Mode-IV

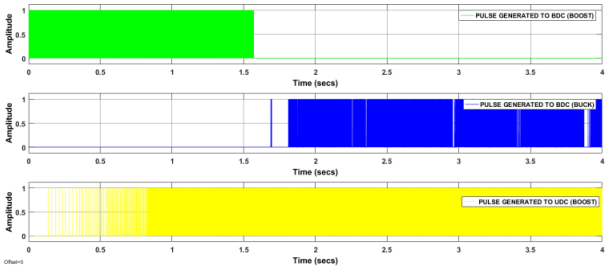

Fig. 37. Pulses of converters by SCB+PID, Mode-IV

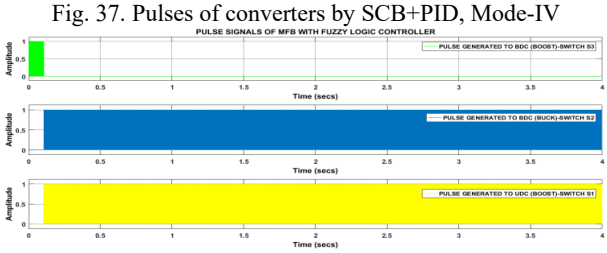

Fig. 38. Pulses of converters by SCB+FLC, Mode-IV

Battery parameters. Figure 39 represents the battery parameters which include state of charge (SOC), voltage, and current corresponding to charge and discharge. Here the positive sign of the current shows the battery charge period and a negative sign is corresponding to the discharge.

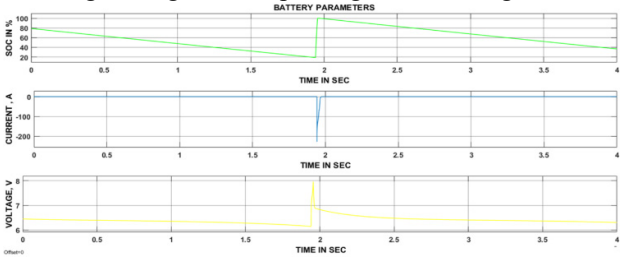

Fig. 39. Different parameters of the battery

About PVA parameters. Different inputs are provided to the solar panel to generate power at different voltage levels. Here the main input parameter of the solar panel is temperature and irradiance, based on the maximum power tracking algorithm a duty cycle is generated to the DC-DC converter of the solar panel. The provided duty cycle of the solar panel converter is always decided on the constant output voltage level corresponding to different input variations of a solar panel.

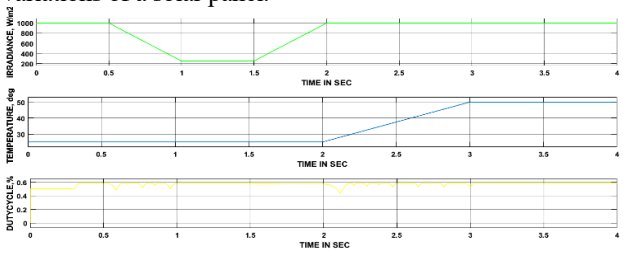

Fig. 40. Various parameters of the PVA module

Table 1 reveals the steady-state reaching for different controllers during four modes of operation. Among all the

controllers SCB with ANN, FLC, and PID, responses are not reached the steady state under any load conditions.

Table 1

The controllers' performance representation based on steady-state time

Controller	Time taken by the individual controller based on the load applied, s			
	Mode-I	Mode-II	Mode-III	Mode-IV
SCB+ANN	0.75	0.25	0.10	Load free
SCB+FLC	0.25	0.15	0.11	Load free
SCB+PID	–	0.40	0.20	Load free

Table 2 shows the 3 controller's performance analyses. Among all the controllers SCB+ANN provides better results in all the aspects except maximum peak overshoot.

Table 2

Representation of three controller's performance related to time-domain specification

Controller	Delay time, s	Rise time, s	Peak time, s	Settling time, s	Maximum peak overshoot, %
MFB+ANN	0,05	0,08	0,1	0,6	12
MFB+FLC	0,09	0,15	0,18	0,55	8
MFB+PID	0,15	1,55	1,6	1,65	7

Conclusions. Three different hybrid controllers are designed according to the proposed control approach. The considered speed condition based controller regulated switching signals generated by the artificial neural network/fuzzy logic/proportional integral derivative controllers, which is used to control the output voltage level of bidirectional converter and unidirectional converter related to the motor's speed. Among all the controllers used in this paper, speed condition based controller played a vital role and salted it as a common controller. Three hybrid controllers, speed condition based controller with artificial neural network, speed condition based controller with fuzzy logic, and speed condition based controller with proportional integral derivative are implemented individually to the main circuit in 4-different modes corresponding to the load applied and attain satisfactory results. Performance and comparative analysis are done among the three-hybrid controller by considering distinct time-domain measurements.

Conflict of interest. The authors declare that they have no conflicts of interest.

REFERENCES

1. Chandra Mouli G.R., Bauer P., Zeman M. System design for a solar powered electric vehicle charging station for workplaces. *Applied Energy*, 2016, vol. 168, pp. 434-443. doi: https://doi.org/10.1016/j.apenergy.2016.01.110.

2. Kydd P.H., Anstrom J.R., Heitmann P.D., Komara K.J., Crouse M.E. Vehicle-Solar-Grid Integration: Concept and Construction. *IEEE Power and Energy Technology Systems Journal*, 2016, vol. 3, no. 3, pp. 81-88. doi: https://doi.org/10.1109/JPETS.2016.2558471.

3. Kim N., Biglarbegian M., Parkhideh B. Flexible high efficiency battery-ready PV inverter for rooftop systems. *2018 IEEE Applied Power Electronics Conference and Exposition (APEC)*, 2018, pp. 3244-3249. doi: https://doi.org/10.1109/APEC.2018.8341567.

4. Amin Bambang R.T., Rohman A.S., Dronkers C.J., Ortega R., Sasongko A. Energy Management of Fuel Cell/Battery/Supercapacitor Hybrid Power Sources Using Model Predictive Control. *IEEE Transactions on Industrial Informatics*, 2014, vol. 10, no. 4, pp. 1992-2002. doi: https://doi.org/10.1109/TII.2014.2333873.

5. Katuri R., Gorantla S. Realization of prototype hardware model with a novel control technique used in electric vehicle application. *Electrical Engineering*, 2020, vol. 102, no. 4, pp. 2539-2551. doi: https://doi.org/10.1007/s00202-020-01052-0.

6. Katuri R., Gorantla S. Design and Comparative Analysis of Controllers Implemented to Hybrid Energy Storage System Based Solar-powered Electric Vehicle. *IETE Journal of Research*, 2021, pp. 1-23. doi: https://doi.org/10.1080/03772063.2021.1941328.

7. Akar F., Tavlasoglu Y., Vural B. An Energy Management Strategy for a Concept Battery/Ultracapacitor Electric Vehicle With Improved Battery Life. *IEEE Transactions on Transportation Electrification*, 2017, vol. 3, no. 1, pp. 191-200. doi: https://doi.org/10.1109/TTE.2016.2638640.

8. Kollimalla S.K., Ukil A., Beng G.H., Manandhar U., Tummuru N.R. Optimization of charge/discharge rates of a battery using a two stage rate-limit control. *2017 IEEE Power & Energy Society General Meeting*, 2017, pp. 1-1. doi: https://doi.org/10.1109/PESGM.2017.8273807.

9. Katuri R., Gorantla S. Optimal Performance of Lithium-Ion Battery and Ultra-Capacitor with A Novel Control Technique Used In E-Vehicles. *Journal of New Materials for Electrochemical Systems*, 2020, vol. 23, no. 2, pp. 139-150. doi: https://doi.org/10.14447/jnmes.v23i2.a11.

10. Katuri R., Rao G.S. Modelling and simulation of Math function based controller combined with PID for smooth switching between the battery and ultracapacitor. *Australian Journal of Electrical and Electronics Engineering*, 2019, vol. 16, no. 3, pp. 163-175. doi: https://doi.org/10.1080/1448837X.2019.1640009.

11. Meradji M., Cecati C., Wang G., Xu D. Dynamic modeling and optimal control for hybrid electric vehicle drivetrain. *2016 IEEE International Conference on Industrial Technology (ICIT)*, 2016, pp. 1424-1429. doi: https://doi.org/10.1109/ICIT.2016.7474967.

12. Li X., Ma R., Wang L., Wang S., Hui D. Energy Management Strategy for Hybrid Energy Storage Systems with Echelon-use Power Battery. *2020 IEEE International Conference on Applied Superconductivity and Electromagnetic Devices (ASEMD)*, 2020, pp. 1-2. doi: https://doi.org/10.1109/ASEMD49065.2020.9276135.

13. Zhou H., Zhou Y., Hu J., Yang G., Xie D., Xue Y., Nordstrom L. LSTM-based Energy Management for Electric Vehicle Charging in Commercial-building Prosumers. *Journal of Modern Power Systems and Clean Energy*, 2021, vol. 9, no. 5, pp. 1205-1216. doi: https://doi.org/10.35833/MPCE.2020.000501.

14. Byrne R.H., Nguyen T.A., Copp D.A., Chalamala B.R., Gyuk I. Energy Management and Optimization Methods for Grid Energy Storage Systems. *IEEE Access*, 2018, vol. 6, pp. 13231-13260. doi: https://doi.org/10.1109/ACCESS.2017.2741578.

15. Li X., Wang S. Energy management and operational control methods for grid battery energy storage systems. *CSEE Journal of Power and Energy Systems*, 2021, no. 5, pp. 1026-1040. doi: https://doi.org/10.17775/CSEEJPES.2019.00160.

16. Regad M., Helaimi M., Taleb R., Gabbar H., Othman A. Optimal frequency control in microgrid system using fractional order PID controller using krill herd algorithm. *Electrical Engineering & Electromechanics*, 2020, no. 2, pp. 68-74. doi: https://doi.org/10.20998/2074-272X.2020.2.11.

17. Slama F., Radjeai H., Mouassa S., Chouder A. New algorithm for energy dispatch scheduling of grid-connected solar photovoltaic system with battery storage system. *Electrical Engineering & Electromechanics*, 2021, no. 1, pp. 27-34. doi: https://doi.org/10.20998/2074-272X.2021.1.05.

18. Pakkiraiah B., Sukumar G.D. A new modified MPPT controller for improved performance of an asynchronous motor drive under variable irradiance and variable temperature. *International Journal of Computers and Applications*, 2016, vol. 38, no. 2-3, pp. 61-74. doi: https://doi.org/10.1080/1206212X.2016.1188586.

19. Pakkiraiah B., Durga Sukumar G. Enhanced Performance of an Asynchronous Motor Drive with a New Modified Adaptive Neuro-Fuzzy Inference System-Based MPPT Controller in Interfacing with dSPACE DS-1104. *International Journal of Fuzzy Systems*, 2017, vol. 19, no. 6, pp. 1950-1965. doi: https://doi.org/10.1007/s40815-016-0287-5.

Received 17.09.2022
Accepted 09.12.2022
Published 07.03.2023

R.S. Kumar[1], *Assistant Professor,*
C.S.R. Reddy[2], *Professor,*
B.M. Chandra[3], *Professor,*
[1] Department of Electrical and Electronics Engineering,
Keshav Memorial Institute of Technology, India,
e-mail: rajasathishkumar38@gmail.com (Corresponding Author)
[2] Department of Electrical and Electronics Engineering,
B V Raju Institute of Technology, India,
e-mail: csubbaramireddy2020@gmail.com
[3] Department of Electrical and Electronics Engineering,
QIS College of Engineering and Technology, India,
e-mail: bmoulichandra@gmail.com

How to cite this article:
Kumar R.S., Reddy C.S.R., Chandra B.M. Optimal performance assessment of intelligent controllers used in solar-powered electric vehicle. *Electrical Engineering & Electromechanics*, 2023, no. 2, pp. 20-26. doi: https://doi.org/10.20998/2074-272X.2023.2.04

UDC 621.3.013 https://doi.org/10.20998/2074-272X.2023.2.05

B.I. Kuznetsov, T.B. Nikitina, I.V. Bovdui, O.V. Voloshko, V.V. Kolomiets, B.B. Kobylianskyi

The method of multi-objective parametric design of magnetic field active canceling robust system for residential multy-story buildings closed to double-circuit overhead power lines

Aim. *Development the method of multi-objective parametric design for robust system of active canceling of magnetic field based on binary preference relations of local objective for multi-objective minimax optimization problem.* ***Methodology***. *Spatial location coordinates of the compensating winding and the current in the shielding winding were determined during the preference-based multi-objective parametric design of systems of active canceling based on solution of the vector minimax optimization, in whith the vector objective function calculated based on Biot-Savart's law. The solution of this vector minimax optimization problem calculated based on nonlinear Archimedes algorithm. Components of Jacobi matrix and Hesse matrix calculated based on multi-swarm multi-agent optimization.* ***Results.*** *Theoretically and experimentally confirmed the effectiveness of reducing the level of the magnetic field in residential multy-storey old building of a double-circuit overhead power transmission lines with a barrel-type arrangement of wires by means of active shielding with two compensation winding.* ***Originality.*** *The method of multi-objective parametric design for robust system of active canceling of magnetic field based on binary preference relations of local objective for multi-objective minimax optimization problem is developed.* ***Practical value***. *It is shown the possibility to reduce the level of magnetic field in residential multy-storey old building closed to double-circuit overhead power transmission lines with a barrel-type arrangement of wires by means of system of active canceling with two canceling winding to a level safe for the population with an induction of 0.5 μT.* References 52, figures 8.

Key words: **double-circuit overhead power transmission line, barrel-type arrangement of wires, magnetic field, system of active canceling, multi-objective parametric design, computer simulation, experimental research**.

Мета. *Розробка методу багатокритеріального параметричного проектування системи активного екранування на основі бінарних відносин переваги локальних критеріїв векторної мінімаксної оптимізації.* ***Методологія***. *Просторові координати розташування компенсаційних обмоток та струми в цих обмотках визначали під час багатокритеріального параметричного проектування системи активного екранування на основі бінарних відносин переваги векторної мінімаксної оптимізації, в якій векторна цільова функція розрахована на основі закона Біо-Савара. Рішення цієї задачи векторної мінімаксної оптимізації розраховано на основі нелінійного алгоритму Архімеда. Елементи матриць Якобі та Гессе розраховано на основі багаторойної багатоагентної оптимізації.* ***Результати***. *Теоретично та експериментально підтверджена ефективність зниження рівня магнітного поля в житлових багатоповерхових приміщеннях старої забудови дволанцюгових повітряних ліній електропередачі з бочкоподібним розташуванням проводів за допомогою активного екранування з двома компенсаційними обмотками.* ***Оригінальність***. *Розроблено метод багатокритеріального параметричного проектування системи активного екранування на основі бінарних відносин переваги локальних критеріїв векторної мінімаксної оптимізації.* ***Практична цінність***. *Показана можливість зниження рівня магнітного поля в житлових багатоповерхових приміщеннях старої забудови дволанцюгових повітряних ліній електропередачі з бочкоподібним розташуванням проводів за допомогою активного екранування з двома компенсаційними обмотками до до безпечного для населення рівня з індуцією 0,5 μT.* Бібл. 52, рис. 8.

Ключові слова: **дволанцюгова повітряна лінія електропередачі, бочкоподібне розташування проводів, магнітне поле, система активного екранування, багатокритеріальне параметричне проектування, комп'ютерне моделювання, експериментальні дослідження.**

Introduction. According to the experts of the World Health Organization [1] and European Parliament [2], electromagnetic pollution of the environment at the end of the 20th century reached a level typical of pollution by harmful chemical substances. Therefore, the reduction of the techno genic electromagnetic field in the residential and natural environment has now become one of the primary global environmental problems that determine the quality and life expectancy of people, the preservation and reproduction of biotic and landscape diversity.

High-voltage power lines are one of the most dangerous sources of electromagnetic fields for people. They create in the surrounding space an intense magnetic field of power frequency, which covers large populated areas. Experts of the World Health Organization [1], European Parliament [2] and Global Cancer Statistics: GLOBOCAN [3] discovered the carcinogenic properties of the magnetic field of power lines with its weak but long-term effect on people, which poses a threat to the health of hundreds of thousands of people living near power lines.

Therefore, over the past 15 years, sanitary standards constantly strengthened around the world from the maximum permissible level of magnetic field (MF) induction of power frequency and intensive research is being conducted to develop methods for normalizing the magnetic field [4–23].

In Ukraine, near one-story residential old buildings a single-circuit power lines with a triangular arrangement of wires most often pass, and near multi-storey residential old buildings double-circuit power lines with an arrangement of barrel-type wires most often pass [4–7]. As an example, such a line is shown in Fig. 1.

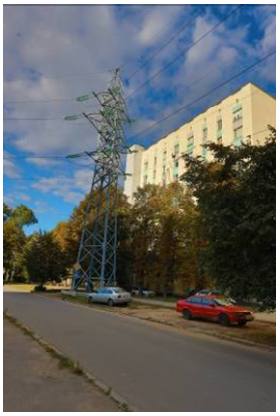

Fig. 1. Multi-storey residential old building closed to double-circuit power lines with an arrangement of barrel-type wires

System of active canceling (SAC) is an automatic control system that includes a control object – plant, amplifiers, measuring devices and the automatic control

device itself. The system of active canceling is designed to cancelate for the induction of the initial magnetic field, i.e. the system of active canceling is designed to maintain the level of induction of the resulting magnetic field at a zero level. Consequently, according to the International Federation Automatic Control (IFAC) terminology [24, 25], according to the algorithm of the functioning of the system of active canceling, it is a stabilization system, and the initial magnetic field is a disturbing influence.

According to the IFAC terminology [24, 25], the control algorithm is a system with two degrees of freedom [26–29]. To implement the open-loop control algorithm, the SAC uses magnetic field sensors located outside the canceling zone. With the help of these sensors, the induction of the initial magnetic field is actually cut off and the open-loop control algorithm for the disturbing effect is implemented in the SAC.

To form currents in canceling windings according to the closed-loop control algorithm, the SAC uses magnetic field sensors located at points in the canceling space. Moreover, during the design of the SAC, it is necessary to determine not only the structures and parameters of the regulator of such a system with two degrees of freedom, but also to determine the number, as well as the spatial arrangement and spatial orientation of these magnetic field sensors.

Unlike the design of classical automatic control system, when the actuators are given [30–33], the main task of the SAC design is also to determine the number, as well as the spatial location and spatial orientation of canceling windings, with the help of which a canceling magnetic field is generated. These windings are essentially magnetic actuators of the SAC. At the same time, during the design of the SAC, it is also necessary to determine the number of ampere-turns in the canceling windings, which, along with the geometric opening of these windings, will make it possible to determine the parameters of the SAC power amplifiers [17–23].

A feature of the design of the SAC, in contrast to the design of classical automatic control system, is the need to implement a given algorithm of operation in stabilizing the resulting magnetic field at a zero level of induction not at one point in the canceling space, but at a plurality of points in the canceling space. Therefore, even with one cancelate winding, the output of such a single-circuit system of active canceling is the magnetic field induction vector at the considered points of the canceling space. In general, this vector is infinite–dimensional, since the canceling space under consideration contains an infinite number of points.

Therefore, the problem of system design is a multi-criteria optimization problem.The parameters of the initial magnetic field model are known inaccurately and change in time, and, therefore, the designed system must be robust. Therefore, the problem of designing such a robust system is a multi-criteria minimax optimization problem. In addition when designing sush system it is presence of conflict situations. Minimization of the level of induction at one point in space leads to an increase the level of induction at another point in space due to undercanceling or overcanceling of the initial magnetic field.

The purpose of this work is development the method of multi-objective parametric design for robust system of active canceling of magnetic field based on binary preference relations of local objective for multi-objective minimax optimization problem.

Statement of the problem of multi-objective parametric design of system of active canceling. Consider the design of robust SAC of magnetic field. Let us first consider the mathematical model of the induction of the initial magnetic field. Note that the effectiveness of the compensation of the initial magnetic field is determined by the ratio of the effective values of the inductions of the initial and resulting magnetic field. However, the SAC as a classical automatic control system is a dynamic system and operates in real time [18]. Therefore, for the synthesis of the SAC, a mathematical model of the instantaneous value of the induction vector of the initial magnetic field is required.

Let's set the instantaneous values of the currents $I(t)$ in the wires of the power transmission line. Then, the instantaneous value of the elementary induction vector $\mathrm{d}B(P_i, t)$ of the initial MF at the considered point of the space point P_i at the time t calculated based on Biot–Savart law [4, 5]

$$\mathrm{d}B(P_i,t) = \frac{\mu_0 I(t)}{4\pi}\frac{\mathrm{dL}_i \times R_i}{\left|R_i\right|^3}, \qquad (1)$$

where R_i is the vector from the differential current element generic field in point P_i, $\mathrm{d}L_i$ is the elementary length vector of the current element, μ_0 is the vacuum magnetic permeability. Based on (1) one can calculate instantaneous value of the initial magnetic field induction vector $B_P(P_i, t)$ at time t at points P_i generated by all wires of all transmission lines.

Let us introduce the vector X of the desired parameters of the SAC, the components of which are number and geometrical parameters and coordinates of compensating windings, the number of ampere-turns and the phase shift of the open-loop control current of each compensating winding, gain coefficients of closed current regulators of each compensating winding, number and location coordinates and spatial orientation angles of magnetic field sensors.

Let us introduce the vector δ of the parameters of the uncertainty of the control object of the SAC, the components of which are the parameters of the uncertainty of the mathematical model of the initial magnetic field and canceling windings [34–38].

Then for the specified values of the vectors X of the desired parameters of the SAC and the vector δ of the parameters of the uncertainty of the control object of the SAC, the instantaneous value of the induction vector $B_W(X, \delta, P_i, t)$ magnetic field can be calculated, generated by all canceling windings at the considered point P_i in space at the time t by integrating the instantaneous value of the differential of the elementary induction vector of the magnetic field generated by the elementary sections of all compensating windings.

Then the vector $B_R(X, \delta, P_i, t)$ of the instantaneous value of the induction of the resulting magnetic field can be calculated as the sum of the vector $B_P(P_i, t)$ of the instantaneous value of the induction of the initial agnetic field generated by the transmission line and the vector

$B_W(X, \delta, P_i, t)$ of the instantaneous value of the magnetic field induction generated by the all compensation windings

$$B_R(X,\delta,P_i,t) = B_P\left(P_i,t\right) + B_W(X,\delta,P_i,t). \qquad (2)$$

Based on the vector $B_R(X, \delta, P_i, t)$ of the instantaneous value of the induction of the resulting magnetic field, integrating over time over the interval of the period of change in the induction of the magnetic field, the effective value of the induction $B_R(X, \delta, P_i)$ of the resulting magnetic field at the considered point P_i in the screening space can be calculated. Then the design problem of system of active canceling can be formulated as the following minimax optimization problem

$$B_R(X^*,\delta^*) = \min_X \max_\delta \max_{P_i} B_R(X,\delta,P_I). \qquad (3)$$

As a result of solving this minimax optimization problem, it is necessary to find the minimum over the vector X, the maximum over the vector δ from the maximum value of the induction vector over the entire set of considered points P_i in the screening space. Note that in this minimax optimization problem, the desired vectors X and δ are the vectors of real values, the points P_i of the screening space under consideration are integer variables.

Although this minimax problem is a scalar optimization problem, the difficulties in solving this problem are primarily due to the fact that among the optimized variables there are both integer and real variables. To simplify the solution of this original scalar optimization problem, we reduce it to the solution of the vector optimization problem

$$B_R(X^*,\delta^*) = \min_X \max_\delta B_R(X,\delta). \qquad (4)$$

In this problem, a vector objective function is introduced

$$B_R(X,\delta) = \langle B_R(X,\delta,P_1)\rangle. \qquad (5).$$

The components $B_R(X, \delta, P_i)$ of which are the effective values of the induction of the resulting magnetic field at all considered points of the screening space. Despite the fact that the original minimax scalar optimization problem of (3) is reduced to solving the minimax vector optimization problem (4), the solution of this vector optimization problem is simpler, since its variables are real numbers.

In this minimax optimization problem it is necessary to find the minimum of the vector objective function by the vector X, but the maximum of the same vector objective function by the vector δ.

The method for solving a minimax vector optimization problem based on binary preference relations. If only one vector objective function is given, then the solution of the problem is the set of unimprovable solutions – the Pareto set of optimal solutions [39, 40]. From the point of view of practical application, such a statement of the optimization problem is an ill-posed problem, since the solution in the form of a Pareto optimal set of unimprovable solutions is devoid of engineering sense [41–43].

A feature of solving the design problem of the system of active canceling is the presence of conflict situations. An attempt to minimize the level of disease in one space while indicating the level of disease in other points in space using a canceling windings system.

The simplest approach to solving a vector optimization problem is to reduce a vector optimization problem to a scalar optimization problem by folding the vector criterion into a scalar criterion using the accepted trade-off scheme.

To comply with sanitary standards, it is necessary that the level of induction at all points of the considered shielding space does not exceed the maximum allowable level specified by sanitary standards, which makes it possible to normalize individual criteria of the vector criterion [42, 43]. Therefore, we normalize the real values $B_R(X, \delta, P_i)$ of the induction of the resulting magnetic field at a point P_i relative to the maximum allowable level $B_{\max}$ of induction, specified in sanitary standards as follows

$$B_{RN}\left(X,\delta,P_i\right) = B(X,\delta,P_I)/B_{\max}.$$

In this case, the normalized particular criteria $B_{RN}(X, \delta, P_i)$ are in the range $0 \le B_{RN}(X, \delta, P_i) \le 1$. Approximation of the normalized value i a particular criterion for one corresponds to a tense situation. If the value of the normalized value of the particular criterion approaches zero, then this corresponds to a calm situation.

To solve this minimax multicriteria optimization problem, the simplest nonlinear trade-off scheme is used, in which the original multicriteria problem was reduced to two one-criterion problems

$$\begin{aligned} X^* &= \arg\min_{\bar{X}} \sum_{i=1}^{J} \alpha_i \left[1 - B_{RN}(X,\delta,P_I)\right]^{-1}; \\ \delta^* &= \arg\max_{\delta} \sum_{i=1}^{J} \alpha_i \left[1 - B_{RN}(X,\delta,P_I)\right]^{-1}, \end{aligned} \qquad (6)$$

where α_i is the weighting coefficients characterizing the importance of particular criteria and determining the preference for certain criteria by the decision-maker. Naturally, such a formalization of the solution of the multicriteria optimization problem by reducing it to a single-criterion problem allows one to reasonably choose one single point from the area of compromises – the Pareto area. However, this «single» point can be further tested in order to further improve the trade-off scheme from the point of view of the decision-maker.

Note that such a nonlinear trade-off scheme (6) actually corresponds to the method of penalty functions with an interior point, since when approaching i criterion $B_{RN}(X, \delta, P_i)$ to one, i.e. in a tense situation, scalar optimization is actually performed only according to this tense particular criterion, and the remaining criteria with a calm situation are practically not taken into account during optimization. However, at the beginning of optimization, it is necessary to make sure that all particular criteria are in the admissible regions, i.e., that the conditions $0 \le B_{RN}(X, \delta, P_i) \le 1$ for all normalized partial criteria. Otherwise, particular criteria for which these conditions are not met are translated into direct restrictions.

This non-linear trade-off scheme allows criteria to be selected according to the intensity of the situation. If any criterion is close to its limiting value, then its normalized value approaches unity. Then this nonlinear compromise scheme, in fact, using a scalar criterion, reduces the

problem of minimizing the sum of criteria to minimizing this criterion alone, according to which there is a tense situation. If, according to other criteria, the situation is calm and their relative values are far from unity, then such a nonlinear trade-off scheme acts similarly to a simple linear trade-off scheme. Thus, with the help of this nonlinear compromise scheme, in fact, the tension of the situation according to individual criteria is a priori introduced into the scalar criterion. It can be shown that this nonlinear trade-off scheme satisfies the Pareto optimality condition, i.e. using this scheme, it is possible to determine a point from the region of unimprovable solutions.

The considered nonlinear trade-off scheme corresponds to the method of penalty functions with an interior point. This assumes that the starting point is valid. When synthesizing dynamical systems, there is usually a situation where the starting point is invalid. Moreover, as a result of multicriteria synthesis, some local criteria may not be met at all.

However, in fact, such an approach replaces one problem of an infinite set of Pareto optimal solutions with another, as a rule, even more difficult problem of an infinite set of optimal solutions for an infinite set of trade-off schemes of pleasant folding of a vector criterion into a scalar one. At the same time, both the original vector optimization problem is ill-posed, and the problem of determining the compromise scheme is also all-posed.

To correctly determine one single solution from the set of Pareto nonimprovable optimal solutions, it is necessary to supplement the initial formulation of the vector optimization problem in the form of a vector objective function with some additional conditions.

When calculating the both solutions (6) constraints on the geometric dimensions and coordinates of the spatial arrangement of the compensating windings , constraints on currents in the windings X, as well as constraints on the vector δ of the uncertainty parameters of the models and magnetic field active cancelling system in the form of vector constraints

$$G_B(X,\delta) \le G_{B_{\max}} . \qquad (7)$$

Taking into account restrictions on the required variables and values of the components of the vector objective function usually leads to some narrowing of the initial set of Pareto optimal solutions, however, as a rule, the set is the solution to such a problem.

However, in order to narrow this set to one point, in addition to the original vector objective function and restrictions, additional conditions for preferring individual solutions from the set of non-improvable Pareto optimal solutions are required. One of the correct approaches to solving the problem of vector optimization is the use of binary preference relations, which allow choosing the most preferable one from two unimprovable solutions.

To select one single solution from the Pareto optimal solutions, use binary preference relations.

A feature of the considered problem of the design of the system of active canceling is the possibility of setting such binary preference relations.

Of the two solutions presented for comparison of their Pareto optimal solutions, the more preferable solution is the one for which the maximum value of induction, chosen from the set of all considered points in the screening space, has the smallest value. The use of such a binary preference relation makes it possible to correctly choose from the entire Pareto set of unimprovable solutions such a solution that provides the minimum value of the maximum value of the induction on the entire set of considered points in the screening space.

To narrow these sets, we use binary preference relations in the form

$$\max_{i=1,m}\max_{\delta} B_R\left(P_i, X_j^*, \delta_j^*\right) < \max_{i=1,m}\max_{\delta} B\left(P_i, \dots X_k^*, \delta_k^*\right). \quad (8)$$

Based on these relationships and (8), the X_j^* and δ_j^* solutions are more preferable than the X_k^* and δ_k^* solutions.

Consistent application of binary preference relations in solving a vector optimization problem allows one to correctly choose from the entire set of non-Pareto-improvable optimal solutions one – the only solution that is the most preferable from the entire set from the point of view of binary preference relations.

The Archimedes optimization algorithm for solving a minimax vector optimization problem. The feature of the considered problem of minimax vector optimization problem (5) is that calculation of the values of vector objective function, even for one value of the desired parameters, requires significant computational resources. First, to calculate the instantaneous values of the induction vectors of the resulting magnetic field at the considered points of the shielding space, it is necessary to integrate the expressions of the Biot–Savart law over the lengths of all wires of the power transmission line and compensating windings. Then, to calculate the effective values of the induction vectors at the considered points of the screening space, it is necessary to integrate the calculated instantaneous values of the induction vectors of the resulting magnetic in time over the interval of the magnetic field oscillation period.

Another feature of the considered problem of minimax vector optimization problem (5) is the presence of several local minima, due to the formation of the induction of the resulting magnetic field with the help of several wires of power transmission lines – three, six, nine, twelve, etc.; and several wires of compensation windings – one, two, three, six, twelve, twenty-four, etc. Moreover, these local extrema have very steep surfaces, which causes zigzag motions of getting stuck when searching for an extremum using first-order methods. Therefore, to find a globally optimal solution from a set of local criteria, it is necessary to apply special algorithms. Therefore, in order to find the optimal solution to this problem, it is necessary to carefully choose an algorithm that allows minimizing the number of calculations of the vector objective function.

Currently, the most widely used are multi-agent stochastic optimization methods that use only the speed of particles. To find the solution of minimax vector optimization problem (5) from Pareto-optimal decisions [39, 40] taking into account the preference relations, we used special nonlinear algorithms of stochastic multi-agent optimization [44, 45]. To calculate the components $X_{ij}(t)$ optimal values of the vector X of the desired parameters using the following steps

$$
\begin{aligned}
&X_{ij}(t+1) = X_{ij}(t) + V_{ij}(t+1),\\
&V_{ij}(t+1) = W_{1j}V_{ij}(t) + C_{1j}R_{1j}(t)*\ldots\\
&\ldots * H(P_{1ij}(t) - E_{1ij}(t))\left[Y_{ij}(t) - \ldots\right.\\
&\left.\ldots - X_{ij}(t)\right] + C_{2j}R_{2j}(t)H(P_{1ij}(t) - \ldots\\
&\ldots - E_{2ij}(t))\left[Y_j^*(t) - X_{ij}(t)\right],
\end{aligned}
\tag{9}
$$

where $X_{ij}(t)$ and $V_{ij}(t)$ are the position and velocity of i particle of j swarm; $Y_{ij}(t)$ and Y_j^* – the best–local and global positions of the i particle, found respectively by only one i particle and all the particles of j swarm; random numbers $R_{ij}(t)$, $E_{ij}(t)$ and constants C_{ij}, P_{ij}, W_j are tuning parameters; H is the Heaviside function.

To calculate the optimal values of the vector δ using the similarly steps.

In fact, these algorithms are a first-order random search algorithm, since only the particle velocity is used in the search – the first-order derivative of the scalar objective function or the gradient of the vector objective function. When finding derivatives in deterministic search methods, this algorithm is usually referred to as gradient descent and the matrix of first derivatives is called as Jacobian.

In random search, the motion of the particle is carried out in the direction of the maximum growth of the component of the objective function, found in the process of random search. In general, this direction serves as an estimate of the direction of the gradient in a random search. Naturally, such an increment of the objective function serves as an analogue of the first derivative – the rate of change of the objective function.

First-order methods have good convergence in the region far from the local optimum, when the first derivative has significant values. The main disadvantage of first-order search methods, which use only the first derivative – the speed of particles, is their low efficiency of the search and the possibility of getting stuck in the search near the local minimum, where the value of the rate of change of the objective function tends to zero. At the same time, in the region of the local optimum, the second derivative, the acceleration of the movement of particles, on the contrary, has a large value and its use allows, theoretically, in one step, to get to the point of the local optimum without the occurrence of zigzag jamming movements when using the first-order search [39, 40].

Note that with deterministic search methods, along with first-order algorithms, second-order algorithms are also widely used. These are the algorithms in particular, the algorithms of Newton, Newton–Gaus, Newton–Raphson.

The update rule $X(t+1)$ in the Newton–Raphson algorithm is as follows

$$
\begin{aligned}
X(t+1) &= X(t) - \left(\frac{\partial^2 B_R(X,\delta)}{\partial X^2}(t)\right)^{-1} \times \ldots\\
&\ldots \times \frac{\partial B_R(X,\delta)}{\partial X}(t);\\
\delta(t+1) &= \delta(t) + \left(\frac{\partial^2 B_R(X,\delta)}{\partial \delta^2}(t)\right)^{-1} \times \ldots\\
&\ldots \times \frac{\partial B_R(X,\delta)}{\partial \delta}(t),
\end{aligned}
\tag{10}
$$

where the Hessians elements are denoted as

$$
\left(\frac{\partial^2 B_R(X,\delta)}{\partial X^2}(t)\right), \quad \left(\frac{\partial^2 B_R(X,\delta)}{\partial \delta^2}(t)\right)
$$

and the Jacobians are denoted as

$$
\frac{\partial B_R(X,\delta)}{\partial X}(t), \quad \frac{\partial B_R(X,\delta)}{\partial \delta}(t)
$$

of vector objective function $B(X, \delta)$, respectively, for the desired vectors X and δ.

The solution of equation (10) requires an explicit inversion of the Hesse matrix. This process can be computationally intensive.

To date, the most widely used algorithms are Levenberg–Maquard [40]. The idea of these methods is to replace the Hesse matrix with some matrix, which is iteratively calculated.

The Jacobian components are the first derivatives of the vector objective function – gradient vectors, the components of which are the velocity of the corresponding components of the vector objective function with respect to the corresponding variables. The Hessian components are the second derivatives of the vector objective function, the components of which are the accelerations of the corresponding components of the vector objective function with respect to the corresponding variables.

The Hessian components $A_{ij}(t)$ – accelerations of i particle of j swarm calculated similarly (9) using the following expressions

$$
\begin{aligned}
&A_{ij}(t+1) = W_{2j}A_{ij}(t) + C_{3j}R_{3j}(t) \times \ldots\\
&\ldots \times H(P_{3ij}(t) - E_{3ij}(t))\left[Z_{ij}(t) - \ldots\right.\\
&\left.\ldots - V_{ij}(t)\right] + C_{4j}R_{4j}(t)H(P_{4ij}(t) - \ldots\\
&\ldots - E_{4ij}(t))\left[Z_j^*(t) - V_{ij}(t)\right],
\end{aligned}
\tag{11}
$$

where $A_{ij}(t)$ the accelerations of i particle of j swarm; $Z_{ij}(t)$ and Z_j^* are the best–local and global velocity of the i particle, found respectively by only one i particle and all the particles of j swarm. Similarly (9) random numbers $R_{ij}(t)$, $E_{ij}(t)$ and constants $C_{ij}(t)$, $P_{ij}(t)$, W_j are tuning parameters, H is the Heaviside function.

To calculate the optimal values of the vector δ using the similarly steps (11).

The advantage of second-order algorithms is the ability to determine not only the direction of movement, but also the size of the movement step to the optimum, so that with a quadratic approximation of the objective function, the optimum is found in one iteration. When solving real non-linear programming problems, the use of second-order methods can significantly reduce the number of iterations to find the optimum. In particular, this is how the sequential quadratic programming or successive quadratic programming method works.

The price for this is more complex calculations that must be performed first to calculate the matrix of second derivatives – the Hessian matrix, and then to determine the direction of movement and the size of the step towards the optimum. Therefore, despite the decrease in the number of iterations, the total time to find the optimum using second-order algorithms may differ slightly from first-order methods.

To take these constraints (7) into account when searching for solutions, we used special particle swarm

optimization method for constrained optimization problems [44–49]. To take these binary preference relations (8) into account when searching for solutions, we used special evolutionary algorithms for multiobjective optimizations [50–52].

The use of the Archimedes algorithm for calculating minimax vector optimization problem (5) solutions with vector constraints (7) and binary preference relations (8) it possible to significantly reduce the calculating time [39, 40].

Multi-objective parametric design of system of active canceling. Based on the developed method the parametric design of two-loops systems of active canceling of the magnetic field generated by 110 kV two-circuits overhead power lines with a «Barrel» type arrangement of wires in mujty-storey old building has been performed. As result of parametric design, the coordinates of the location of two canceling windings was calculated, as well as the currents and phases in two canceling windings.

In Fig. 2 are shown two-circuit power transmission line with the arrangement of wires of the «Barrel» type, two canceling windings and mujty-storey old building.

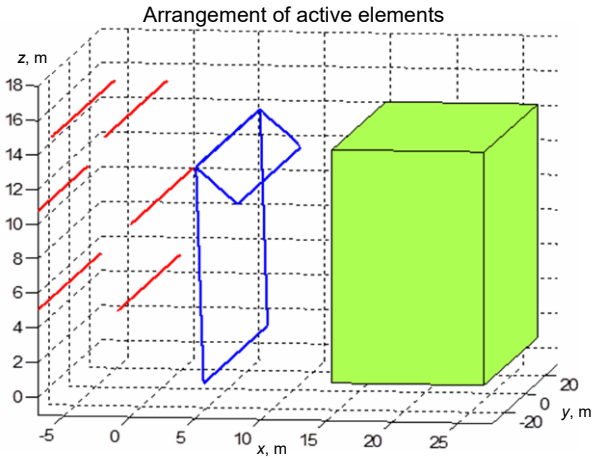

Fig. 2. Two-circuit power transmission line with the arrangement of wires of the «Barrel» type and two canceling windings

The system of active canceling contains two canceling windings. On Fig. 3 are shown the dependences of the calculated induction of the initial and resulting magnetic field.

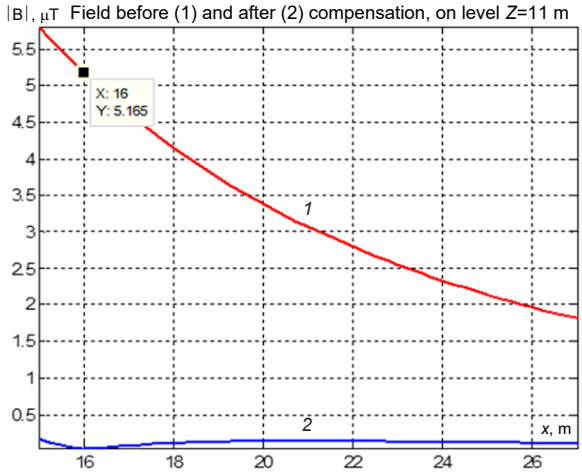

Fig. 3. Dependencies of the calculated induction of the initial and resulting magnetic field

The initial magnetic field induction is in the range from 5.75 μT to 1.8 μT. The resulting magnetic field induction does not exceed 0.2 μT in the entire range under consideration. The canceling factor more than 20 units.

The design of model of system of active canceling. To conduct experimental studies, a model of a two-circuit power transmission line with the arrangement of wires of the «Barrel» type in scale 7.5 was developed. On Fig. 4 is shown a photo of this model.

Fig. 4. Model of a two-circuit power transmission line with the arrangement of wires of the «Barrel» type

For this model, the system of active canceling was design. On Fig. 5 are shown a photo of the both canceling windings of the model of system of active canceling.

Fig. 5. Model of both canceling windings

Consider now spatiotemporal characteristic system of active canceling. In Fig. 6,*a* shows the spatiotemporal characteristic of the initial magnetic field, the resulting magnetic field and the spatiotemporal characteristic of the magnetic field generated only by both canceling windings.

As can be seen from Fig. 6,*a*, the spatiotemporal characteristic of the initial magnetic field and the magnetic field generated by two canceling windings practically coincide, and the spatiotemporal characteristic of the resulting magnetic field occupies a rather small area compared to the area of the spatiotemporal characteristic of the initial magnetic field, which causes a rather high value of the canceling factor – about ten units.

Let us now consider spatiotemporal characteristic of magnetic field when only single first canceling winding is in operation.

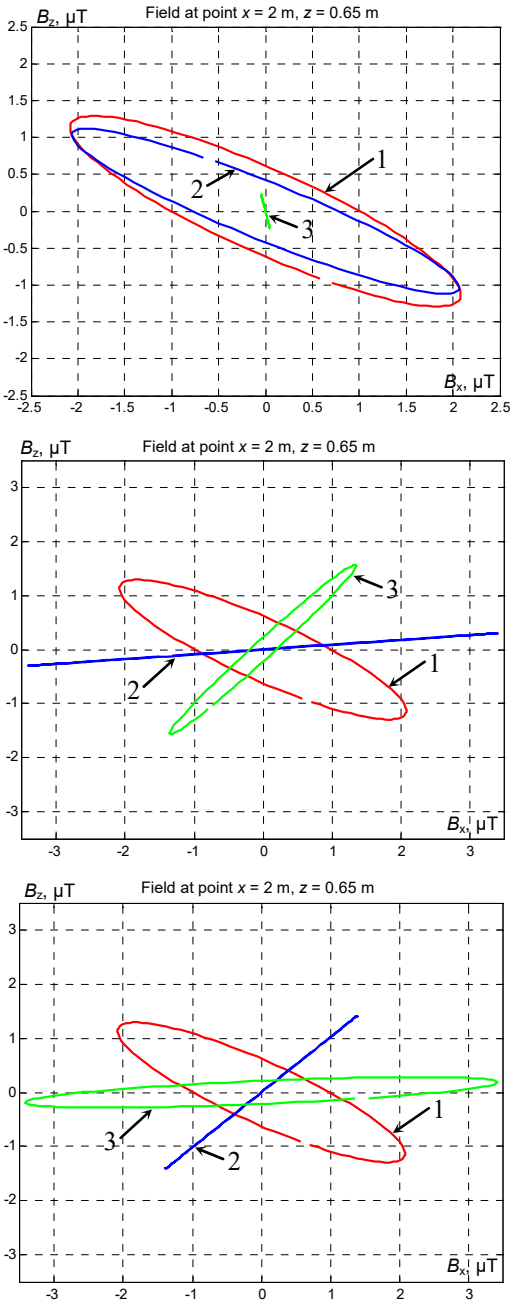

Fig. 6. The spatiotemporal characteristics of the initial magnetic field (1), the magnetic field generated only by compensation windings (2) and the resulting magnetic field (3)

Figures 6,*b* and Fig. 6,*c* show the spatiotemporal characteristic during the operation of only one first and only single second canceling windings. Note that when only one first or only one second canceling windings is working, there is a clear overcompensation of the initial magnetic field. At the same time, the efficiency of canceling of the initial magnetic field when only one first winding is operating is only 1.1 units, and when only one second winding is operating, the induction of the resulting magnetic field generally exceeds the induction of the original magnetic field by 1.5 times, so that the canceling factor ramen is less than unity and is 0.66 units.

The adjustment of model of system of active canceling. In the course of adjustment of model of system of active canceling it is necessary to experimentally determine the values of two phase shifts and two amplitudes of currents of open regulators and two gain factors of closed current regulators of both canceling windings.

First we consider spatiotemporal characteristic the resulting magnetic field generated by the power transmission line and only the first canceling winding. First, the magnitude of the phase shift and the amplitude of the current of the open-loop controller of the first winding were experimentally adjusting so that the spatiotemporal characteristic of the resulting magnetic field was parallel to the spatiotemporal characteristic generated only by the second winding, which is shown in Fig. 6,*c*. Such adjustment is necessary so that when the second winding is connected, it is possible to effectively compensate for the resulting magnetic field during the operation of the power transmission line and only the first winding.

On Fig. 7,*a* is shown the spatiotemporal characteristic of the resulting magnetic field during the operation of the power transmission line and only the first winding as a result of adjusting the open current regulators of the first winding.

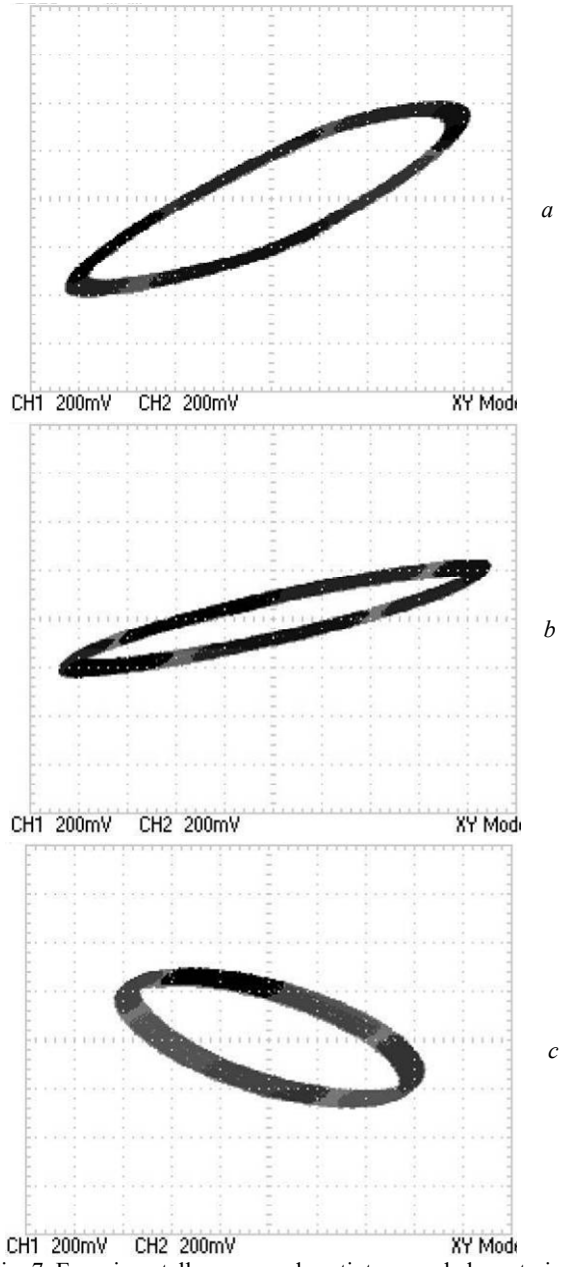

Fig. 7. Experimentally measured spatiotemporal characteristic of the model of the system of active canceling

Then, for the attachment of an open current regulator of the second winding, we turn off the first winding. Now, the phase shift value and the amplitude of the current of the open-loop controller of the second winding are experimentally adjusted in such a way that the spatiotemporal characteristic of the resulting magnetic field is parallel to the spatiotemporal characteristic generated only by the first winding, which is shown in Fig. 7,*b*. Such adjustment is necessary so that when the first winding is connected, it is possible to effectively compensate for the resulting magnetic field during the operation of the power transmission line and only the second winding. On Fig. 7,*b* is shown the spatiotemporal characteristic of the resulting magnetic field during the operation of the power transmission line and only the second winding as a result of adjusting the open current regulators of the second winding.

Now, with the power transmission line turned on, we simultaneously turn on both windings and additionally adjust the open current regulators of the first and second windings so that the spatiotemporal characteristic of the resulting magnetic field has a minimum area. On Fig. 7,*c* is shown spatiotemporal characteristic of magnetic field generated by simultaneously operating the first and second windings. This spatiotemporal characteristic practically coincides with the spatiotemporal characteristic of the initial magnetic field generated only by the model of power transmission line and is shown in Fig. 7,*c*.

Results of experimental studies. Consider the effectiveness of canceling of initial magnetic field by model of the system of active canceling with the parameters of the controllers tuned when the model was adjustment. In Fig. 8 are shown experimentally measured *a*) induction of the initial and resulting magnetic field and *b*) canceling factor, which experimentally measured on the model of SAC.

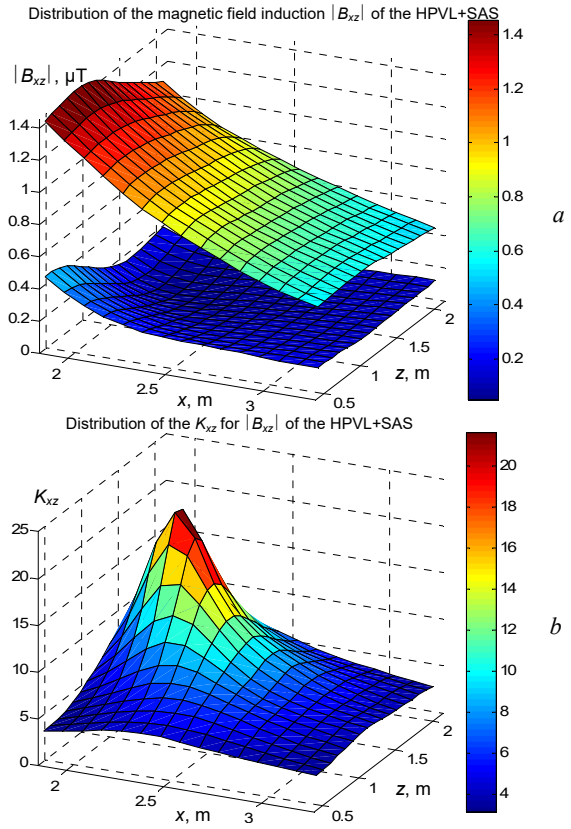

Fig. 8. Experimentally measured *a*) induction of the initial and resulting magnetic field and *b*) canceling factor of the model of SAC

As can be seen from this Fig. 8,*b*, the experimentally measured on the model of SAC canceling factor in a small area of space is 25 units.

Conclusions.

1. The method of multi-objective parametric design for robust system of active canceling of magnetic field based on binary preference relations of local objective for multi-objective minimax optimization problem was development.

2. The parametric design of robust system of active canceling according to the developed method reduced to computing the solution of vector minimax optimization problem based on binary preference relations. This solution calculated based on stochastic nonlinear Archimedes algorithms. Components of Jacobi matrix and Hesse matrix calculated based on multi-swarm multi-agent optimization. The vector of objective function of minimax optimization problem and constraints calculation based on Bio–Savart's law.

3. Using the developed method the parametric design of two-loops systems of active canceling of the magnetic field generated by 110 kV two-circuits overhead power lines with a «Barrel» type arrangement of wires in mujty-storey old building has been performed. As result of parametric design, the coordinates of the location of two canceling windings was calculated, as well as the currents and phases in two canceling windings.

4. Based on theoretical and experimental research on physical scale model of a double-circuit power transmission line it is shown the possibility to reduce the level of magnetic field in multy-storey old building from power transmission line with a «Barrel» type arrangement of wires by means of active canceling with two canceling winding with initial induction of 5.7 μT to a safe level for the population with an induction of 0.5 μT.

Acknowledgment. The authors express their gratitude to the engineers A.V. Sokol and A.P. Shevchenko of the department of magnetism of technical object of A. Pidhornyi Institute of Mechanical Engineering Problems of the National Academy of Sciences of Ukraine for the creative approach and courage shown during the creation under fire, under martial law, of an experimental installation and successful testing of a laboratory model of the system of active canceling.

Conflict of interest. The authors declare that they have no conflicts of interest.

REFERENCES

1. *The International EMF Project. Radiation & Environmental Health Protection of the Human Environment World Health Organization*. Geneva, Switzerland, 1996. 2 p. Available at: https://www.who.int/initiatives/the-international-emf-project (Accessed 25.07.2022).

2. *Directive 2013/35/EU of the European Parliament and of the Council of 26 June 2013 on the minimum health and safety requirements regarding the exposure of workers to the risks arising from physical agents (electromagnetic fields)*. Available at: http://data.europa.eu/eli/dir/2013/35/oj (Accessed 25.07.2022).

3. Sung H., Ferlay J., Siegel R.L., Laversanne M., Soerjomataram I., Jemal A., Bray, F. Global Cancer Statistics 2020: GLOBOCAN Estimates of Incidence and Mortality Worldwide for 36 Cancers in 185 Countries. *CA: A Cancer Journal for Clinicians*, 2021, vol. 71, no. 3, pp. 209-249. doi: https://doi.org/10.3322/caac.21660.

4. Rozov V.Yu., Grinchenko V.S., Yerisov A.V., Dobrodeyev P.N. Efficient shielding of three-phase cable line magnetic field by

passive loop under limited thermal effect on power cables. *Electrical Engineering & Electromechanics*, 2019, no. 6, pp. 50-54. doi: https://doi.org/10.20998/2074-272x.2019.6.07.
5. Rozov V.Y., Pelevin D.Y., Pielievina K.D. External magnetic field of urban transformer substations and methods of its normalization. *Electrical Engineering & Electromechanics*, 2017, no. 5, pp. 60-66. doi: https://doi.org/10.20998/2074-272X.2017.5.10.
6. Rozov V.Yu., Reutskyi S.Yu., Pelevin D.Ye., Kundius K.D. Approximate method for calculating the magnetic field of 330-750 kV high-voltage power line in maintenance area under voltage. *Electrical Engineering & Electromechanics*, 2022, no. 5, pp. 71-77. doi: https://doi.org/10.20998/2074-272X.2022.5.12.
7. Rozov V.Yu., Kundius K.D., Pelevin D.Ye. Active shielding of external magnetic field of built-in transformer substations. *Electrical Engineering & Electromechanics*, 2020, no. 3, pp. 24-30. doi: https://doi.org/10.20998/2074-272x.2020.3.04.
8. Salceanu A., Paulet M., Alistar B.D., Asiminicesei O. Upon the contribution of image currents on the magnetic fields generated by overhead power lines. *2019 International Conference on Electromechanical and Energy Systems (SIELMEN)*. 2019. doi: https://doi.org/10.1109/sielmen.2019.8905880.
9. Del Pino Lopez J.C., Romero P.C. Influence of different types of magnetic shields on the thermal behavior and ampacity of underground power cables. *IEEE Transactions on Power Delivery*, Oct. 2011, vol. 26, no. 4, pp. 2659-2667. doi: https://doi.org/10.1109/tpwrd.2011.2158593.
10. Hasan G.T., Mutlaq A.H., Ali K.J. The Influence of the Mixed Electric Line Poles on the Distribution of Magnetic Field. *Indonesian Journal of Electrical Engineering and Informatics (IJEEI)*, 2022, vol. 10, no. 2, pp. 292-301. doi: https://doi.org/10.52549/ijeei.v10i2.3572.
11. Victoria Mary S., Pugazhendhi Sugumaran C. Investigation on magneto-thermal-structural coupled field effect of nano coated 230 kV busbar. *Physica Scripta*, 2020, vol. 95, no. 4, art. no. 045703. doi: https://doi.org/10.1088/1402-4896/ab6524.
12. Ippolito L., Siano P. Using multi-objective optimal power flow for reducing magnetic fields from power lines. *Electric Power Systems Research*, 2004, vol. 68, no. 2, pp. 93-101. doi: https://doi.org/10.1016/S0378-7796(03)00151-2.
13. Barsali S., Giglioli R., Poli D. Active shielding of overhead line magnetic field: Design and applications. *Electric Power Systems Research*, May 2014, vol. 110, pp. 55-63. doi: https://doi.org/10.1016/j.epsr.2014.01.005.
14. Bavastro D., Canova A., Freschi F., Giaccone L., Manca M. Magnetic field mitigation at power frequency: design principles and case studies. *IEEE Transactions on Industry Applications*, May 2015, vol. 51, no. 3, pp. 2009-2016. doi: https://doi.org/10.1109/tia.2014.2369813.
15. Beltran H., Fuster V., García M. Magnetic field reduction screening system for a magnetic field source used in industrial applications. *9 Congreso Hispano Luso de Ingeniería Eléctrica (9 CHLIE)*, Marbella (Málaga, Spain), 2005, pp. 84-99. Available at: https://www.researchgate.net/publication/229020921_Magnetic_field_reduction_screening_system_for_a_magnetic_field_source_used_in_industrial_applications (Accessed 22.06.2021).
16. Bravo-Rodríguez J., Del-Pino-López J., Cruz-Romero P. A Survey on Optimization Techniques Applied to Magnetic Field Mitigation in Power Systems. *Energies*, 2019, vol. 12, no. 7, p. 1332. doi: https://doi.org/10.3390/en12071332.
17. Canova A., del-Pino-López J.C., Giaccone L., Manca M. Active Shielding System for ELF Magnetic Fields. *IEEE Transactions on Magnetics*, March 2015, vol. 51, no. 3, pp. 1-4. doi: https://doi.org/10.1109/tmag.2014.2354515.
18. Canova A., Giaccone L. Real-time optimization of active loops for the magnetic field minimization. *International Journal of Applied Electromagnetics and Mechanics*, Feb. 2018, vol. 56, pp. 97-106. doi: https://doi.org/10.3233/jae-172286.
19. Canova A., Giaccone L., Cirimele V. Active and passive shield for aerial power lines. *Proc. of the 25th International Conference on Electricity Distribution (CIRED 2019)*, 3-6 June 2019, Madrid, Spain. Paper no. 1096. Available at: https://www.cired-repository.org/handle/20.500.12455/290 (Accessed 28 May 2021).
20. Canova A., Giaccone L. High-performance magnetic shielding solution for extremely low frequency (ELF) sources. *CIRED - Open Access Proceedings Journal*, Oct. 2017, vol. 2017, no. 1, pp. 686-690. doi: https://doi.org/10.1049/oap-cired.2017.1029.
21. Celozzi S. Active compensation and partial shields for the power-frequency magnetic field reduction. *2002 IEEE International Symposium on Electromagnetic Compatibility*, Minneapolis, MN, USA, 2002, vol. 1, pp. 222-226. doi: https://doi.org/10.1109/isemc.2002.1032478.
22. Celozzi S., Garzia F. Active shielding for power-frequency magnetic field reduction using genetic algorithms optimization. *IEE Proceedings - Science, Measurement and Technology*, 2004, vol. 151, no. 1, pp. 2-7. doi: https://doi.org/10.1049/ip-smt:20040002.
23. Celozzi S., Garzia F. Magnetic field reduction by means of active shielding techniques. *WIT Transactions on Biomedicine and Health*, 2003, vol. 7, pp. 79-89. doi: https://doi.org/10.2495/ehr030091.
24. Martynenko G. Practical application of the analytical method of electromagnetic circuit analysis for determining magnetic forces in active magnetic bearings. *2020 IEEE Problems of Automated Electrodrive. Theory and Practice (PAEP)*, 2020, pp. 1-4, doi: https://doi.org/10.1109/paep49887.2020.9240774.
25. Martynenko G., Martynenko V. Modeling of the dynamics of rotors of an energy gas turbine installation using an analytical method for analyzing active magnetic bearing circuits. *2020 IEEE KhPI Week on Advanced Technology (KhPIWeek)*, 2020, pp. 92-97. doi: https://doi.org/10.1109/KhPIWeek51551.2020.9250156.
26. Buriakovskyi S.G., Maslii A.S., Pasko O.V., Smirnov V.V. Mathematical modelling of transients in the electric drive of the switch – the main executive element of railway automation. *Electrical Engineering & Electromechanics*, 2020, no. 4, pp. 17-23. doi: https://doi.org/10.20998/2074-272X.2020.4.03.
27. Ostroverkhov M., Chumack V., Monakhov E., Ponomarev A. Hybrid Excited Synchronous Generator for Microhydropower Unit. *2019 IEEE 6th International Conference on Energy Smart Systems (ESS)*, Kyiv, Ukraine, 2019, pp. 219-222. doi: https://doi.org/10.1109/ess.2019.8764202.
28. Ostroverkhov M., Chumack V., Monakhov E. Ouput Voltage Stabilization Process Simulation in Generator with Hybrid Excitation at Variable Drive Speed. *2019 IEEE 2nd Ukraine Conference on Electrical and Computer Engineering (UKRCON)*, Lviv, Ukraine, 2019, pp. 310-313. doi: https://doi.org/10.1109/ukrcon.2019.8879781.
29. Tytiuk V., Chornyi O., Baranovskaya M., Serhiienko S., Zachepa I., Tsvirkun L., Kuznetsov V., Tryputen N. Synthesis of a fractional-order $PI^{\lambda}D^{\mu}$-controller for a closed system of switched reluctance motor control. *Eastern-European Journal of Enterprise Technologies*, 2019, no. 2 (98), pp. 35-42. doi: https://doi.org/10.15587/1729-4061.2019.160946.
30. Zagirnyak M., Chornyi O., Zachepa I. The autonomous sources of energy supply for the liquidation of technogenic accidents. *Przeglad Elektrotechniczny*, 2019, no. 5, pp. 47-50. doi: https://doi.org/10.15199/48.2019.05.12.
31. Chornyi O., Serhiienko S. A virtual complex with the parametric adjustment to electromechanical system parameters. *Technical Electrodynamics*, 2019, pp. 38-41. doi: https://doi.org/10.15407/techned2019.01.038.
32. Shchur I., Kasha L., Bukavyn M. Efficiency Evaluation of Single and Modular Cascade Machines Operation in Electric Vehicle. *2020 IEEE 15th International Conference on Advanced Trends in Radioelectronics, Telecommunications and Computer Engineering (TCSET)*, Lviv-Slavske, Ukraine, 2020, pp. 156-161. doi: https://doi.org/10.1109/tcset49122.2020.235413.
33. Shchur I., Turkovskyi V. Comparative Study of Brushless DC Motor Drives with Different Configurations of Modular Multilevel Cascaded Converters. *2020 IEEE 15th International Conference on Advanced Trends in Radioelectronics, Telecommunications and Computer Engineering (TCSET)*,

Lviv-Slavske, Ukraine, 2020, pp. 447-451. doi: https://doi.org/10.1109/tcset49122.2020.235473.
34. Ostroumov I., Kuzmenko N., Sushchenko O., Pavlikov V., Zhyla S., Solomentsev O., Zaliskyi M., Averyanova Y., Tserne E., Popov A., Volosyuk V., Ruzhentsev N., Dergachov K., Havrylenko O., Kuznetsov B., Nikitina T., Shmatko O. Modelling and simulation of DME navigation global service volume. *Advances in Space Research*, 2021, vol. 68, no. 8, pp. 3495-3507. doi: https://doi.org/10.1016/j.asr.2021.06.027.
35. Averyanova Y., Sushchenko O., Ostroumov I., Kuzmenko N., Zaliskyi M., Solomentsev O., Kuznetsov B., Nikitina T., Havrylenko O., Popov A., Volosyuk V., Shmatko O., Ruzhentsev N., Zhyla S., Pavlikov V., Dergachov K., Tserne E. UAS cyber security hazards analysis and approach to qualitative assessment. In: Shukla S., Unal A., Varghese Kureethara J., Mishra D.K., Han D.S. (eds) *Data Science and Security. Lecture Notes in Networks and Systems*, 2021, vol. 290, pp. 258-265. Springer, Singapore. doi: https://doi.org/10.1007/978-981-16-4486-3_28.
36. Zaliskyi M., Solomentsev O., Shcherbyna O., Ostroumov I., Sushchenko O., Averyanova Y., Kuzmenko N., Shmatko O., Ruzhentsev N., Popov A., Zhyla S., Volosyuk V., Havrylenko O., Pavlikov V., Dergachov K., Tserne E., Nikitina T., Kuznetsov B. Heteroskedasticity analysis during operational data processing of radio electronic systems. In: Shukla S., Unal A., Varghese Kureethara J., Mishra D.K., Han D.S. (eds) *Data Science and Security. Lecture Notes in Networks and Systems*, 2021, vol. 290, pp. 168-175. Springer, Singapore. doi: https://doi.org/10.1007/978-981-16-4486-3_18.
37. Shmatko O., Volosyuk V., Zhyla S., Pavlikov V., Ruzhentsev N., Tserne E., Popov A., Ostroumov I., Kuzmenko N., Dergachov K., Sushchenko O., Averyanova Y., Zaliskyi M., Solomentsev O., Havrylenko O., Kuznetsov B., Nikitina T. Synthesis of the optimal algorithm and structure of contactless optical device for estimating the parameters of statistically uneven surfaces. *Radioelectronic and Computer Systems*, 2021, no. 4, pp. 199-213. doi: https://doi.org/10.32620/reks.2021.4.16.
38. Volosyuk V., Zhyla S., Pavlikov V., Ruzhentsev N., Tserne E., Popov A., Shmatko O., Dergachov K., Havrylenko O., Ostroumov I., Kuzmenko N., Sushchenko O., Averyanova Yu., Zaliskyi M., Solomentsev O., Kuznetsov B., Nikitina T. Optimal Method for Polarization Selection of Stationary Objects Against the Background of the Earth's Surface. *International Journal of Electronics and Telecommunications*, 2022, vol. 68, no. 1, pp. 83-89. doi: https://doi.org/10.24425/ijet.2022.139852.
39. Gal'chenko V.Y., Vorob'ev M.A. Structural synthesis of attachable eddy-current probes with a given distribution of the probing field in the test zone. *Russian Journal of Nondestructive Testing*, Jan. 2005, vol. 41, no. 1, pp. 29-33. doi: https://doi.org/10.1007/s11181-005-0124-7.
40. Halchenko V.Y., Ostapushchenko D.L., Vorobyov M.A. Mathematical simulation of magnetization processes of arbitrarily shaped ferromagnetic test objects in fields of given spatial configurations. *Russian Journal of Nondestructive Testing*, Sep. 2008, vol. 44, no. 9, pp. 589-600. doi: https://doi.org/10.1134/S1061830908090015.
41. Ostroumov I., Kuzmenko N., Sushchenko O., Zaliskyi M., Solomentsev O., Averyanova Y., Zhyla S., Pavlikov V., Tserne E., Volosyuk V., Dergachov K., Havrylenko O., Shmatko O., Popov A., Ruzhentsev N., Kuznetsov B., Nikitina T. A probability estimation of aircraft departures and arrivals delays. In: Gervasi O. et al. (eds) *Computational Science and Its Applications – ICCSA 2021. ICCSA 2021. Lecture Notes in Computer Science*, vol. 12950, pp. 363-377. Springer, Cham. doi: https://doi.org/10.1007/978-3-030-86960-1_26.
42. Chystiakov P., Chornyi O., Zhautikov B., Sivyakova G. Remote control of electromechanical systems based on computer simulators. *2017 International Conference on Modern Electrical and Energy Systems (MEES)*, Kremenchuk, Ukraine, 2017, pp. 364-367. doi: https://doi.org/10.1109/mees.2017.8248934.
43. Zagirnyak M., Bisikalo O., Chorna O., Chornyi O. A Model of the Assessment of an Induction Motor Condition and Operation Life, Based on the Measurement of the External Magnetic Field. *2018 IEEE 3rd International Conference on Intelligent Energy and Power Systems (IEPS)*, Kharkiv, 2018, pp. 316-321. doi: https://doi.org/10.1109/ieps.2018.8559564.
44. Ummels M. *Stochastic Multiplayer Games Theory and Algorithms*. Amsterdam University Press, 2010. 174 p.
45. Shoham Y., Leyton-Brown K. *Multiagent Systems: Algorithmic, Game-Theoretic, and Logical Foundations.* Cambridge University Press, 2009. 504 p.
46. Ray T., Liew K.M. A Swarm Metaphor for Multiobjective Design Optimization. *Engineering Optimization*, 2002, vol. 34, no. 2, pp. 141-153. doi: https://doi.org/10.1080/03052150210915.
47. Zilzter Eckart. *Evolutionary algorithms for multiobjective optimizations: methods and applications*. PhD Thesis Swiss Federal Institute of Technology, Zurich, 1999. 114 p.
48. Xiaohui Hu, Eberhart R.C., Yuhui Shi. Particle swarm with extended memory for multiobjective optimization. *Proceedings of the 2003 IEEE Swarm Intelligence Symposium*. SIS'03 (Cat. No.03EX706), Indianapolis, IN, USA, 2003, pp. 193-197. doi: https://doi.org/10.1109/sis.2003.1202267.
49. Pulido G.T., Coello C.A.C. A constraint-handling mechanism for particle swarm optimization. *Proceedings of the 2004 Congress on Evolutionary Computation* (IEEE Cat. No.04TH8753), Portland, OR, USA, 2004, vol. 2, pp. 1396-1403. doi: https://doi.org/10.1109/cec.2004.1331060.
50. Michalewicz Z., Schoenauer M. Evolutionary Algorithms for Constrained Parameter Optimization Problems. *Evolutionary Computation*, 1996, vol. 4, no. 1, pp. 1-32. doi: https://doi.org/10.1162/evco.1996.4.1.1.
51. Zhyla S., Volosyuk V., Pavlikov V., Ruzhentsev N., Tserne E., Popov A., Shmatko O., Havrylenko O., Kuzmenko N., Dergachov K., Averyanova Y., Sushchenko O., Zaliskyi M., Solomentsev O., Ostroumov I., Kuznetsov B., Nikitina T. Statistical synthesis of aerospace radars structure with optimal spatio-temporal signal processing, extended observation area and high spatial resolution. *Radioelectronic and Computer Systems*, 2022, no. 1, pp. 178-194. doi: https://doi.org/10.32620/reks.2022.1.14.
52. Xin-She Yang, Zhihua Cui, Renbin Xiao, Amir Hossein Gandomi, Mehmet Karamanoglu. *Swarm Intelligence and Bio-Inspired Computation: Theory and Applications*, Elsevier Inc., 2013. 450 p.

Received 01.09.2022
Accepted 21.10.2022
Published 07.03.2023

B.I. Kuznetsov[1], *Doctor of Technical Science, Professor,*
T.B. Nikitina[2], *Doctor of Technical Science, Professor,*
I.V. Bovdui[1], *PhD, Senior Research Scientist,*
O.V. Voloshko[1], *PhD, Junior Research Scientist,*
V.V. Kolomiets[2], *PhD, Assistant Professor,*
B.B. Kobylianskyi[2], *PhD, Associate Professor,*
[1] A. Pidhornyi Institute of Mechanical Engineering Problems of the National Academy of Sciences of Ukraine,
2/10, Pozharskogo Str., Kharkiv, 61046, Ukraine,
e-mail: kuznetsov.boris.i@gmail.com (Corresponding Author)
[2] Educational scientific professional pedagogical Institute of Ukrainian Engineering Pedagogical Academy,
9a, Nosakov Str., Bakhmut, Donetsk Region, 84511, Ukraine,
e-mail: tatjana55555@gmail.com; nnppiuipa@ukr.net

How to cite this article:
Kuznetsov B.I., Nikitina T.B., Bovdui I.V., Voloshko O.V., Kolomiets V.V., Kobylianskyi B.B. The method of multi-objective parametric design of magnetic field active canceling robust system for residential multy-story buildings closed to double-circuit overhead power lines. *Electrical Engineering & Electromechanics*, 2023, no. 2, pp. 27-36. doi: https://doi.org/10.20998/2074-272X.2023.2.05

UDC 621.3.013 https://doi.org/10.20998/2074-272X.2023.2.06

R. Saifi

Implementation of a new flux rotor based on model reference adaptive system for sensorless direct torque control modified for induction motor

Introduction. *In order to realize an efficient speed control of induction motor, speed sensors, such as encoder, resolver or tachometer may be utilized. However, some problems appear such as, need of shaft extension, which decreases the mechanical robustness of the drive, reduce the reliability, and increase in cost.* ***Purpose.*** *In order to eliminate of speed sensors without losing. Several solutions to solve this problem have been suggested. Based on the motor fundamental excitation model, high frequency signal injection methods. The necessity of external hardware for signal injection and the adverse influence of injecting signal on the motor performance do not constitute an advantage for this technique. Fundamental model-based strategies method using instantaneous values of stator voltages and currents to estimate the rotor speed has been investigate. Several other methods have been proposed, such as model reference adaptive system, sliding mode observers, Luenberger observer and Kalman filter. The* ***novelty*** *of the proposed work consists in presenting a model reference adaptive system based speed estimator for sensorless direct torque control modified for induction motor drive. The model reference adaptive system is formed with flux rotor and the estimated stator current vector.* ***Methods.*** *The reference model utilizes measured current vector. On the other hand, the adjustable model uses the estimated stator current vector. The current is estimated through the solution of machine state equations.* ***Practical value****. The merits of the proposed estimator are demonstrated experimentally through a test-rig realized via the dSPACE DS1104 card in various operating conditions. The experimental results show the efficiency of the proposed speed estimation technique. Experimental results show the effectiveness of the proposed speed estimation method at nominal speed regions and speed reversal, and good results with respect to measurement speed estimation errors obtained.* References 20, table 1, figures 9.

Key words: **induction motor, model reference adaptive system, sensorless speed, direct torque control.**

Вступ*. Щоб реалізувати ефективне керування швидкістю асинхронного двигуна, можна використовувати датчики швидкості, такі як енкодер, резольвер або тахометр. Однак виникають деякі проблеми, такі як необхідність подовження валу, що знижує механічну міцність приводу, знижує надійність та збільшує вартість.* ***Мета****. Для усунення датчиків швидкості без втрати. Було запропоновано кілька рішень на вирішення цієї проблеми. На основі моделі основного порушення двигуна використовуються методи подачі високочастотного сигналу. Необхідність зовнішнього обладнання для подачі сигналу та несприятливий вплив подачі сигналу на роботу двигуна не є перевагою цього методу. Досліджено метод стратегій на основі фундаментальних моделей з використанням миттєвих значень напруг та струмів статора для оцінки швидкості обертання ротора. Було запропоновано кілька інших методів, таких як еталонна адаптивна система моделі, спостерігачі режиму ковзання, спостерігач Люенбергера і фільтр Калмана.* ***Новизна*** *запропонованої роботи полягає у поданні модельної еталонної адаптивної системи оцінки швидкості прямого бездатчикового управління моментом, модифікованої для асинхронного електроприводу. Еталонна адаптивна система моделі формується з магнітним потоком ротора та оціненим вектором струму статора.* ***Методи.*** *Еталонна модель використовує вимірюваний вектор струму. З іншого боку, модель, що регулюється, використовує передбачуваний вектор струму статора. Струм оцінюється шляхом вирішення рівнянь стану машини.* ***Практична цінність****. Переваги запропонованого оцінювача продемонстровані експериментально на тестовій установці, реалізованій на платі dSPACE DS1104 у різних умовах експлуатації. Експериментальні результати свідчать про ефективність запропонованої методики оцінки швидкості. Експериментальні результати показують ефективність запропонованого методу оцінки швидкості в областях номінальних швидкостей та реверсивних швидкостей, а також хороші результати щодо отриманих похибок оцінки швидкості вимірювання.* Бібл. 20, табл. 1, рис. 9.

Ключові слова: **асинхронний двигун, еталонна адаптивна система, бездатчикова швидкість, пряме управління крутним моментом.**

Introduction. Speed information is mandatory for the operation of a modified direct torque control (DTC) for induction motor (IM) based on amplitude and angle control of stator flux.

The rotor speed can be measured through a sensor or may be estimated using voltage, current signals and the information of machine parameters. Use of speed sensor is associated with problems, such as, reduction of mechanical robustness of the drive, need of shaft extension, reduced reliability in hazardous environment, and increased cost. Therefore, a speed sensorless drive has a clear edge over the traditional vector controlled drive [1].

The motor speed for sensorless control can be estimated by different methods [2-5]. The simplest technique is based on the rotor flux vector coordinates obtained using the induction motor model, based on the slip calculation and angular velocity of rotor flux vector. This technique is very popular and quite simple to implement, but the obtained precision is very bad due to a great sensitiveness to motor parameter uncertainties. The other techniques are based on the extended Kalman filters or extended Luenberger observers [3, 5], which are very robust to the induction motor parameter variations or identification errors, but are very more complex and difficult in technical realization. The other solution for speed estimation is based on the model reference adaptive system (MRAS) principle, in which an error vector is created from the outputs of two models, both dependent on different motor parameters. The error is driven to zero through adjustment of a parameter that affects one of models.

The MRAS approach has the characteristic in the simplicity and easy of used models, which are simulators of chosen electromagnetic state variables of the induction machine, in comparison with extended state observers or Kalman filters or nonlinear. Thus they are easy in and simple implementation and have direct physical interpretation.

The basic structure of the MRAS is shown in Fig. 1. The error signal may be formulated with flux [6-10], back-EMF, reactive power and active power [11-16]. The flux-based MRAS (F-MRAS) is first introduced in [6].

The goal of the work is to develop a model reference adaptive system with flux rotor for speed estimation of sensorless control of induction motor drive. The reference model utilizes measured current vector. On the other

hand, the adjustable model uses the estimated stator current vector. The current is estimated through the solution of machine state equations. Current, being a vector quantity, is configured in terms of flux rotor.

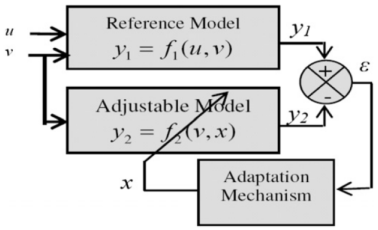

Fig. 1. Basic structure of MRAS

Proposed speed estimator. The structure of the proposed MRAS (F-MRAS) is shown in Fig. 2, which utilizes (1) in the reference model and (2) in the adjustable model. Note that both the models are in stationary reference frame. Measured current is used in the reference model, whereas estimated current is considered for the adjustable model.

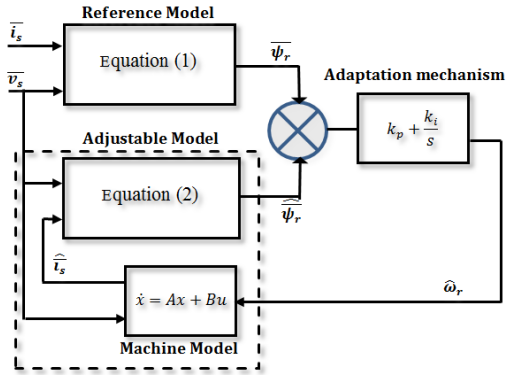

Fig. 2. Structure of the proposed MRAS

The current is estimated through the solution of machine state equations. The state space representation of induction motor in stationary reference frame is expressed in (3) and (4). The complete sensorless DTC for induction motor drives based on amplitude and angle control of stator flux is shown in Fig. 3.

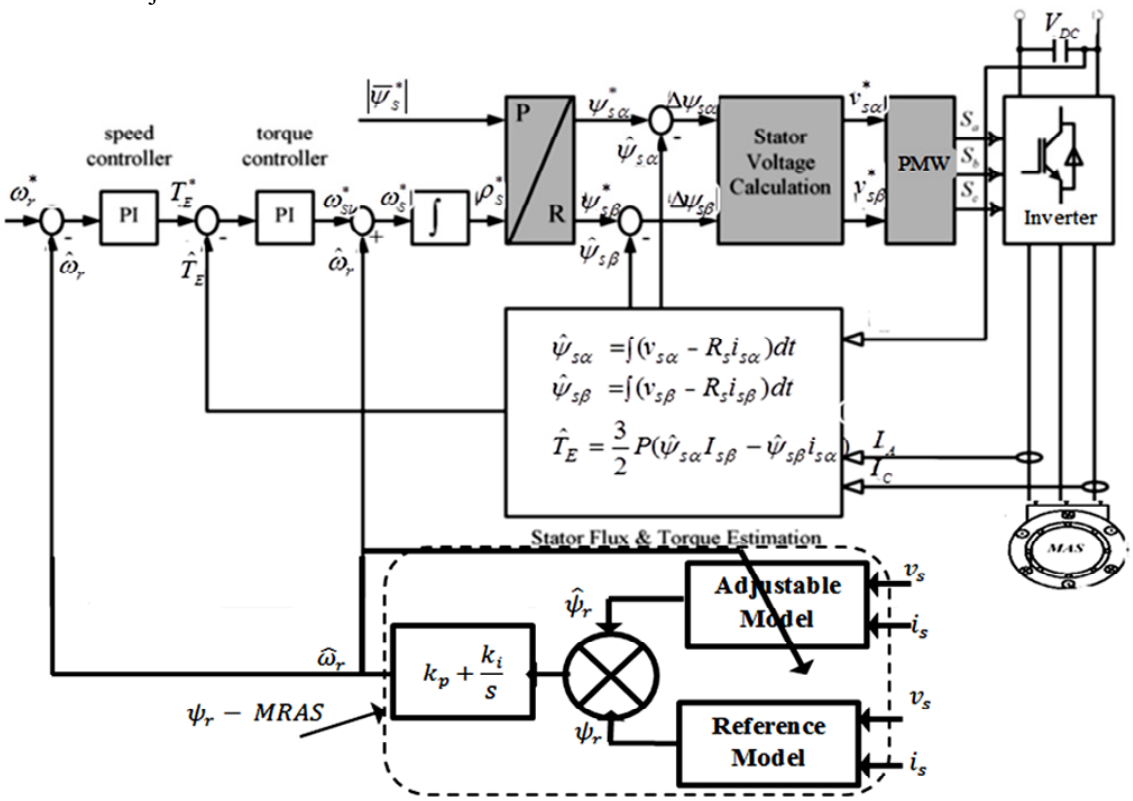

Fig. 3. Sensorless Direct Torque Control based on Amplitude and Angle control of Stator flux (DTC-AAS) with proposed speed estimator

$$\dot{\bar{\Psi}}_r = \frac{L_r}{L_m}\left(\bar{v}_s - R_s\bar{i}_s - \sigma L_s\dot{\bar{i}}_s\right); \quad (1)$$

$$\dot{\hat{\bar{\Psi}}}_r = \frac{L_r}{L_m}\left(\bar{v}_s - R_s\hat{\bar{i}}_s - \sigma L_s\dot{\hat{\bar{i}}}_s\right); \quad (2)$$

$$\frac{d}{dt}\begin{bmatrix} i_{s\alpha} \\ i_{s\beta} \\ \psi_{r\alpha} \\ \psi_{r\beta} \end{bmatrix} = \begin{bmatrix} -a_1 & 0 & a_2 & a_3\omega_r \\ 0 & -a_1 & -a_3\omega_r & a_2 \\ a_4 & 0 & -a_5 & -\omega_r \\ 0 & a_4 & \omega_r & -a_5 \end{bmatrix}\begin{bmatrix} i_{s\alpha} \\ i_{s\beta} \\ \psi_{r\alpha} \\ \psi_{r\beta} \end{bmatrix} + \frac{1}{\sigma L_s}\begin{bmatrix} 1 & 0 \\ 0 & 1 \\ 0 & 0 \\ 0 & 0 \end{bmatrix}\begin{bmatrix} v_{s\alpha} \\ v_{s\beta} \end{bmatrix}; \quad (3)$$

$$\begin{bmatrix} i_{s\alpha} \\ i_{s\beta} \end{bmatrix} = \begin{bmatrix} 1 & 0 & 0 & 0 \\ 0 & 1 & 0 & 0 \end{bmatrix}\begin{bmatrix} i_{s\alpha} \\ i_{s\beta} \\ \psi_{r\alpha} \\ \psi_{r\beta} \end{bmatrix}, \quad (4)$$

where

$$a_1 = \frac{1}{\sigma L_s}\left(R_s + \frac{L_m^2}{L_r T_r}\right), a_2 = \frac{1}{\sigma L_s}\left(\frac{L_m}{L_r T_r}\right),$$

$$a_3 = \frac{1}{\sigma L_s}\left(\frac{L_m}{L_r}\right), a_4 = \frac{L_m}{T_r}, a_5 = \frac{1}{T_r}$$

R_s, L_s, R_r, L_r are the resistances and cyclic inductances of stator and rotor respectively; $\bar{v}_s$, $\bar{i}_s$, $\bar{\psi}_r$ are the voltage, current vectors of stator and flux vector of rotor; L_m, ω_r are the mutual inductance and electric motor speed (or rotor frequency); $\sigma = 1 - L_m^2/L_s L_r$ is the motor dispersion coefficient.

PI design of MRAS-based speed estimator. It is important to design the adaptation mechanism of the MRAS according to the hyper-stability concept. This will

result in a stable and quick response system where the convergence of the estimated value to the actual value can be assured with suitable dynamic characteristics. The induction machine model in the synchronously rotating (ω_{mr}) reference frame can be expressed as:

$$\frac{d}{dt}\begin{bmatrix} i_{sd} \\ i_{sq} \\ \psi_{rd} \\ \psi_{rq} \end{bmatrix} = \begin{bmatrix} -a_1 & \omega_{mr} & a_2 & a_3\omega_r \\ -\omega_{mr} & -a_1 & -a_3\omega_r & a_2 \\ a_4 & 0 & -a_5 & \omega_{sl} \\ 0 & a_4 & -\omega_{sl} & -a_5 \end{bmatrix}\begin{bmatrix} i_{sd} \\ i_{sq} \\ \psi_{rd} \\ \psi_{rq} \end{bmatrix} + \\ + \frac{1}{\sigma L_s}\begin{bmatrix} 1 & 0 \\ 0 & 1 \\ 0 & 0 \\ 0 & 0 \end{bmatrix}\begin{bmatrix} v_{sd} \\ v_{sq} \end{bmatrix}; \tag{5}$$

$$\begin{bmatrix} i_{sd} \\ i_{sq} \end{bmatrix} = \begin{bmatrix} 1 & 0 & 0 & 0 \\ 0 & 1 & 0 & 0 \end{bmatrix}\begin{bmatrix} i_{sd} \\ i_{sq} \\ \psi_{rd} \\ \psi_{rq} \end{bmatrix}. \tag{6}$$

Let us assume that

$x = \begin{bmatrix} i_{sd} & i_{sq} & \Psi_{rd} & \Psi_{rq} \end{bmatrix}^T$; $u = \begin{bmatrix} v_{sd} & v_{sq} \end{bmatrix}^T$, $y = \begin{bmatrix} i_{sd} & i_{sq} \end{bmatrix}^T$,

where v_{sd}, v_{sq}, i_{sd}, i_{sq} are the *d-q* components of stator voltage and currents respectively; Ψ_{rd}, Ψ_{rq} are the *d-q* components of rotor flux.

Therefore, in the state space form, (5) and (6) become,

$$\dot{x} = Ax + Bu\ ; \tag{7}$$

$$y = Cx + Du\ . \tag{8}$$

The small signal representation of the above state space equations, described by (7) and (8) are:

$$\Delta\dot{x} = A\Delta x + \Delta A x_0\ ; \tag{9}$$

$$\Delta y = C\Delta x\ , \tag{10}$$

or

$$\Delta y = C(SI - A)^{-1}\Delta A x_0\ , \tag{11}$$

where $x_0 = \begin{bmatrix} i_{sd0} & i_{sq0} & \Psi_{rd0} & \Psi_{rq0} \end{bmatrix}^T$ represents the operating point. The expression of ΔA is:

$$\Delta A = \begin{bmatrix} 0 & 0 & 0 & a_3 \\ 0 & 0 & -a_3 & 0 \\ a_4 & 0 & 0 & -1 \\ 0 & a_4 & 1 & 0 \end{bmatrix}\Delta\omega_r \tag{12}$$

and

$$C = \begin{bmatrix} 1 & 0 & 0 & 0 \\ 0 & 1 & 0 & 0 \end{bmatrix}. \tag{13}$$

From (11), using (12) and (13), the expression of Δy becomes:

$$\Delta y = \begin{bmatrix} \Delta i_{sd} \\ \Delta i_{sq} \end{bmatrix} = \begin{bmatrix} 1 & 0 & 0 & 0 \\ 0 & 1 & 0 & 0 \end{bmatrix}(SI - A)^{-1} \times \\ \times \begin{bmatrix} 0 & 0 & 0 & a_3 \\ 0 & 0 & -a_3 & 0 \\ a_4 & 0 & 0 & -1 \\ 0 & a_4 & 1 & 0 \end{bmatrix}\begin{bmatrix} i_{sd0} \\ i_{sq0} \\ \psi_{rd0} \\ \psi_{rq0} \end{bmatrix}\Delta\omega_r. \tag{14}$$

Using (14), the transfer functions of $\Delta i_{sd}/\Delta\omega_r$ and $\Delta i_{sq}/\Delta\omega_r$ can be expressed as:

$$\frac{\Delta i_{sd}}{\Delta\omega_r} = \frac{(C_{14} - a_3C_{12})\psi_{rd0}}{|SI - A|}\ ; \tag{15}$$

$$\frac{\Delta i_{sq}}{\Delta\omega_r} = \frac{(C_{24} - a_3C_{22})\psi_{rd0}}{|SI - A|}\ , \tag{16}$$

where

$$adj(SI - A) = \begin{bmatrix} C_{11} & C_{12} & C_{13} & C_{14} \\ C_{21} & C_{22} & C_{23} & C_{24} \\ C_{31} & C_{32} & C_{33} & C_{34} \\ C_{41} & C_{42} & C_{43} & C_{44} \end{bmatrix}. \tag{17}$$

Now, the error equation is:

$$\varepsilon = \overline{\psi}_r \otimes \hat{\overline{\psi}}_r = \psi_{rq}\hat{\psi}_{rd} - \hat{\psi}_{rq}\psi_{rd}\ , \tag{18}$$

where:

$$\psi_{rd} = \frac{L_r}{sL_m}(v_{sd} - (R_s + s\sigma L_s)i_{sd})\ ; \tag{19}$$

$$\psi_{rq} = \frac{L_r}{sL_m}(v_{sq} - (R_s + s\sigma L_s)i_{sq})\ ; \tag{20}$$

$$\hat{\psi}_{rd} = \frac{L_r}{sL_m}(v_{sd} - (R_s + s\sigma L_s)\hat{i}_{sd})\ ; \tag{21}$$

$$\hat{\psi}_{rq} = \frac{L_r}{sL_m}(v_{sq} - (R_s + s\sigma L_s)\hat{i}_{sq})\ . \tag{22}$$

From (18), using (19) – (22), the error equation becomes:

$$\varepsilon = \frac{L_r(R_s + s\sigma L_s)}{sL_m}\left[v_{sq0}\left(i_{sd} - \hat{i}_{sd}\right) - v_{sd0}\left(i_{sq} - \hat{i}_{sq}\right) + \right. \\ \left. + \left(\hat{i}_{sd}i_{sq} - \hat{i}_{sq}i_{sd}\right)\right] \tag{23}$$

or

$$\varepsilon = \frac{L_r(R_s + s\sigma L_s)}{sL_m}\left[\left(v_{sq0}\Delta i_{sd} - v_{sd0}\Delta i_{sq}\right) + \right. \\ \left. + \left(\hat{i}_{sd}i_{sq} - \hat{i}_{sq}i_{sd}\right)\right] \tag{24}$$

For simplify the calculation, with the assumption of negligible the second term on the right-hand side of equation (24). With this assumption, the equation can be approximated as:

$$\varepsilon = \frac{L_r(R_s + s\sigma L_s)}{sL_m}\left(v_{sq0}\Delta i_{sd} - v_{sd0}\Delta i_{sq}\right). \tag{25}$$

The rotor flux error due to the small perturbation of rotor speed $\Delta\omega_r$ in the adjustable model can be expressed as:

$$\frac{\varepsilon}{\Delta\omega_r} = \frac{L_r(R_s + s\sigma L_s)}{sL_m}\left(v_{sq0}\frac{\Delta i_{sd}}{\Delta\omega_r} - v_{sd0}\frac{\Delta i_{sq}}{\Delta\omega_r}\right). \tag{26}$$

Putting the expressions of $\Delta i_{sd}/\Delta\omega_r$ and $\Delta i_{sq}/\Delta\omega_r$ (which are obtained from (15) and (16) respectively) into (26), the error transfer function becomes:

$$\frac{\varepsilon}{\Delta\omega_r} = \frac{\psi_{rd0}L_r(R_s + s\sigma L_s)}{sL_m}\left[\frac{v_{sq0}(C_{14} - a_3C_{12})}{|SI - A|} - \right. \\ \left. - \frac{v_{sd0}(C_{24} - a_3C_{22})}{|SI - A|}\right] = G_1(s). \tag{27}$$

Using the error transfer function (27), the closed loop block diagram of the MRAS is shown in Fig. 4. The closed loop transfer function between ω_r and $\hat{\omega}_r$ can be expressed as:

$$\frac{\omega_r}{\hat{\omega}_r} = \frac{G_1(s)\left(K_{Pmras} + \dfrac{K_{\mathrm{Im}ras}}{s}\right)}{1 + G_1(s)\left(K_{Pmras} + \dfrac{K_{\mathrm{Im}ras}}{s}\right)}. \quad (28)$$

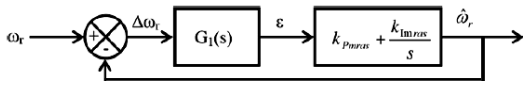

Fig. 4. Closed loop representation of the ψ_t^i MRAS based speed estimator

Improved rotor flux estimator. The drawbacks of the estimation of the rotor flux based on voltage model using open-loop integration as shown in (1) and (2) are DC drift and saturation problems. In this paper, improved rotor flux estimator by integrating algorithm with an amplitude limiter in polar coordinates is used to overcome the problems associated with the pure integrator [17-20]. The rotor flux estimator is shown in Fig. 5 is the limitation in Cartesian coordinates is performed as follows:

$$Z_L = \begin{cases} \sqrt{\lambda_\alpha^2 + \lambda_\beta^2} & \text{if} \quad \sqrt{\lambda_\alpha^2 + \lambda_\beta^2} < L; \\ L & \text{if} \quad \sqrt{\lambda_\alpha^2 + \lambda_\beta^2} > L, \end{cases} \quad (29)$$

where Z_L is the output of the limiter; L is the limit value. L should be equal approximately to the to the stator flux reference. The limited components of the stator flux are then simply scaled with the ratio of the limited amplitude and unlimited amplitude:

$$Z_{\alpha L} = \frac{\sqrt{\lambda_\alpha^2 + \lambda_\beta^2}}{Z_L}\lambda_\alpha; \quad Z_{\beta L} = \frac{\sqrt{\lambda_\alpha^2 + \lambda_\beta^2}}{Z_L}\lambda_\beta, \quad (30)$$

where $Z_{\alpha L}$ and $Z_{\beta L}$ are the output limited values.

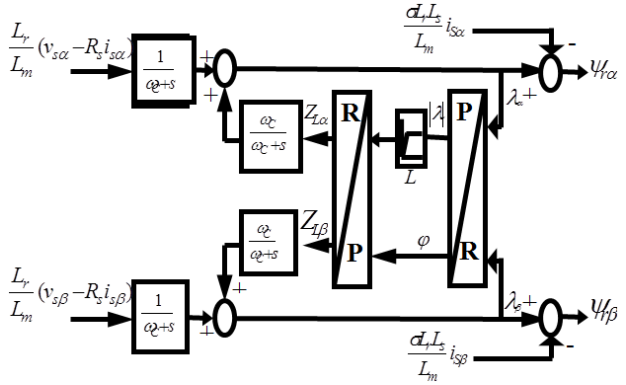

Fig. 5. Block diagram of the improved integrator algorithm with limited amplitude

Experimental setup. The experimental setup of the proposed control system is represented by the structure of the experimental setup shown in Fig. 6. It consists of a dSPACE DS1103 controller board with TMS320F240 slave processor, ADC interface board CP1103, a 4-pole induction motor with parameters listed in Table 1. A three-phase PMW inverter is connected to supply 500 V DC bus voltage, with the switching frequency and the dead time of 2 kHz and 70 μs, respectively.

The DS1103 board is installed in Pentium III 1.0 GHz PC for software development and results visualization. The control program is written in MATLAB/Simulink real time interface with sampling time of 100μs. A photograph of the experimental setup is shown in Fig. 7.

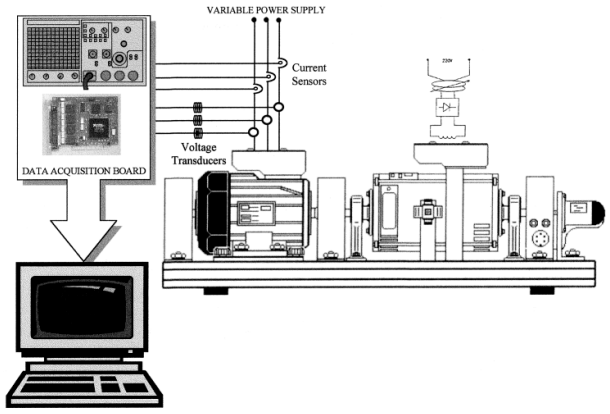

Fig. 6. Structure of the experimental setup

Table 1

Induction motor parameters

Parameter	Value
IM mechanical power P_n, kW	0.9
Nominal voltage V_n, V	220
Nominal current I_n, A	1.82
Nominal speed N, rpm	1400
Stator resistance R_s, Ω	12.75
Rotor resistance R_r, Ω	5.1498
Stator self-inductance L_s, H	0.4991
Rotor self-inductance L_r, H	0.4331
Mutual inductance L_m, H	0.4331
Moment of inertia J, kg·m^2	0.0035
Supply frequency f, Hz	50
Pole pairs number p	2

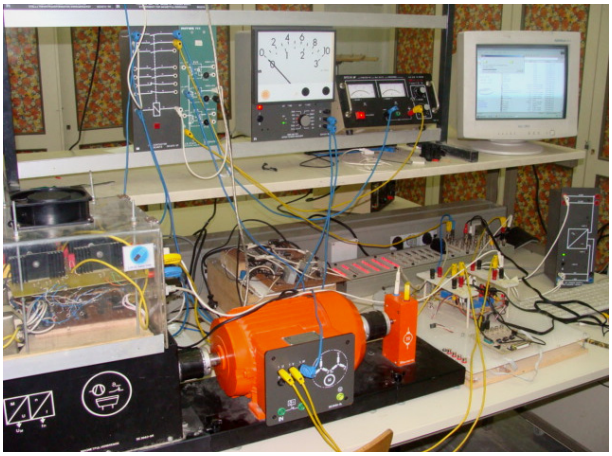

Fig. 7. View of the experimental setup

Experimental results. In the following tests, the estimated speed is used for speed control, where the drive is working as a sensorless DTC-AAS. The encoder speed is used for comparison purposes only. Selected experimental results for the tests are shown in the following section.

Test 1. Load torque rejection at 157 rad/s. This test examines the load torque disturbance rejection capability of the sensorless drive. Figure 8 shows in the (0 s ≤ t < 35 s) test between zero speed and 157 rad/s under a load torque from 11,5 s to 22 s. It can be observed that the rotor speed is not affected by the load torque change and the rotor speed error is small is available in Fig. 8,*a* and Fig. 8,*b*. It is found that the change in torque electromagnetic is shown in Fig. 8,*c*. The stator current is shown in Fig. 8,*d*, which follow the envelope of the load-torque. Some small stator flux oscillations can be observed but is maintained constant throughout the operation is available in Fig. 8,*e*.

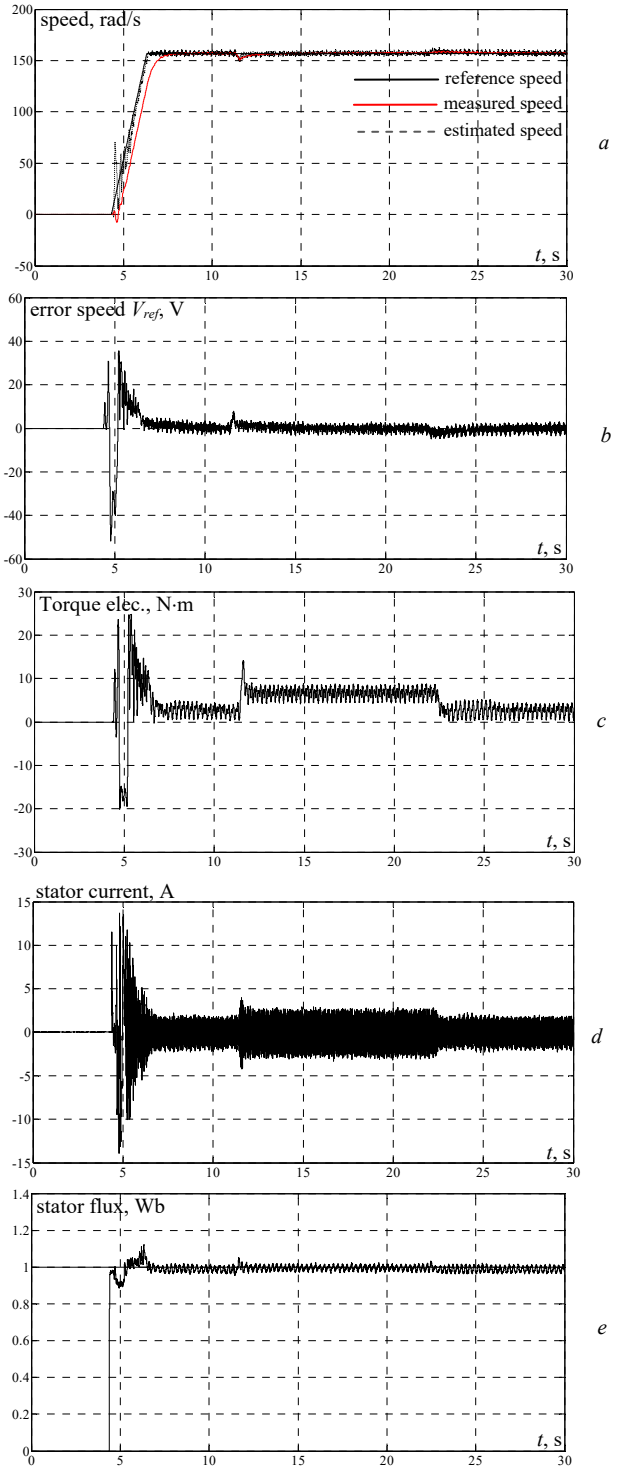

Fig. 8. Transient response for changing of load torque

Test 2. The speed reversal. The tracking performance of the sensorless drive is observed in Fig. 9 for a ramp speed command. Rotor reference speed is gradually increased from 0 to 157 rad/s during 2 s. Thereafter, the command speed is maintained constant at 50 rad/s up to 18.5 s. The speed reversal is taken place during 18.5-22.5 s. The rotor command speed is fixed to 157 rad/s after 22.5 s. The actual motor speed for such speed command is shown in Fig. 9,*a*. The speed estimation error is available in Fig. 9,*b*. It is noticed that the estimation error is small during steady state. The stator current increase during reversal operation is available in Fig. 9,*d*. Some small stator flux oscillations can be observed is shown in Fig. 9,*e*. The experimental results confirm that the proposed speed sensorless DTC for IM based on amplitude and angle control of stator flux method can satisfactorily estimate rotor speed and that it is possible to control the speed of an induction motor with the proposed method.

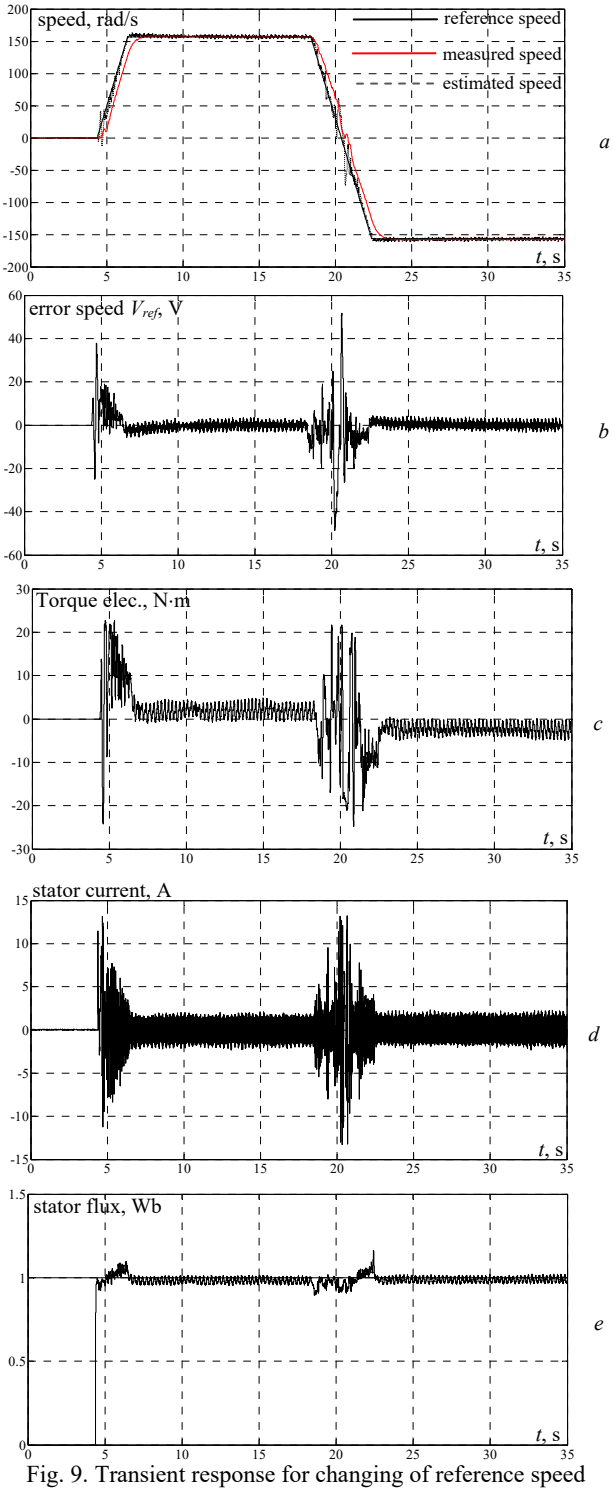

Fig. 9. Transient response for changing of reference speed

Conclusion. New speed estimation method for sensorless induction motor drive using model reference adaptive system has been presented in this paper. The model reference adaptive system is formulated with rotor flux. The algorithm needs the on-line solution of machine state equations. The realized estimator has used to perform the direct torque control for induction motor

drives based on amplitude and angle. Experimental results for different speed profiles had shown. Although a small error and a small fluctuation are observed for the speed estimation, that the proposed new model reference adaptive system observer was able to estimate the actual speed. Thus the effectiveness of the proposed method of speed estimation is verified.

Conflict of interest. The author declares no conflict of interest.

REFERENCES

1. Maiti S., Chakraborty C. A new instantaneous reactive power based MRAS for sensorless induction motor drive. *Simulation Modelling Practice and Theory*, 2010, vol. 18, no. 9, pp. 1314-1326. doi: https://doi.org/10.1016/j.simpat.2010.05.005.

2. Chaabane H., Khodja D.E., Chakroune S., Hadji D. Model reference adaptive backstepping control of double star induction machine with extended Kalman sensorless control. *Electrical Engineering & Electromechanics*, 2022, no. 4, pp. 3-11. doi: https://doi.org/10.20998/2074-272X.2022.4.01.

3. Farhan A., Saleh A., Abdelrahem M., Kennel R., Shaltout A. High-Precision Sensorless Predictive Control of Salient-Pole Permanent Magnet Synchronous Motor based-on Extended Kalman Filter. *2019 21st International Middle East Power Systems Conference (MEPCON)*, 2019, pp. 226-231. doi: https://doi.org/10.1109/MEPCON47431.2019.9008188.

4. Ammar A., Kheldoun A., Metidji B., Ameid T., Azzoug Y. Feedback linearization based sensorless direct torque control using stator flux MRAS-sliding mode observer for induction motor drive. *ISA Transactions*, 2020, vol. 98, pp. 382-392. doi: https://doi.org/10.1016/j.isatra.2019.08.061.

5. Khamari D., Benlaloui I., Ouchen S., Makouf A., Drid S., Alaoui L.C., Ouriagli M. LPV Induction Motor Control with MRAS Speed Estimation. *2019 8th International Conference on Systems and Control (ICSC)*, 2019, pp. 460-464. doi: https://doi.org/10.1109/ICSC47195.2019.8950563.

6. Kumar R., Das S., Bhaumik A. Speed sensorless model predictive current control of doubly-fed induction machine drive using model reference adaptive system. *ISA Transactions*, 2019, vol. 86, pp. 215-226. doi: https://doi.org/10.1016/j.isatra.2018.10.025.

7. Xie H., Wang F., Zhang W., Garcia C., Rodriguez J., Kennel R. Predictive Field Oriented Control based on MRAS Current Estimator for IM Drives. *2020 IEEE 9th International Power Electronics and Motion Control Conference (IPEMC2020-ECCE Asia)*, 2020, pp. 1029-1032. doi: https://doi.org/10.1109/IPEMC-ECCEAsia48364.2020.9367976.

8. Guo X., Yin Z., Zhang Y., Bai C. Position sensorless control of PMLSM based on adaptive complex coefficient sliding mode observer. *Energy Reports*, 2022, vol. 8, pp. 687-695. doi: https://doi.org/10.1016/j.egyr.2022.02.271.

9. Babes B., Hamouda N., Kahla S., Amar H., Ghoneim S.S.M. Fuzzy model based multivariable predictive control design for rapid and efficient speed-sensorless maximum power extraction of renewable wind generators. *Electrical Engineering & Electromechanics*, 2022, no. 3, pp. 51-62. doi: https://doi.org/10.20998/2074-272X.2022.3.08.

10. Ankarao M., Kumar M.V., Dmesh P. Dynamic Performance Analysis of Reactive Power and Improved Rotor Flux Based MRAS for Induction Motor Drives Employing PI and Fuzzy Controller. *2018 2nd IEEE International Conference on Power Electronics, Intelligent Control and Energy Systems (ICPEICES)*, 2018, pp. 892-896. doi: https://doi.org/10.1109/ICPEICES.2018.8897401.

11. Boukhechem I., Boukadoum A., Boukelkoul L., Lebied R. Sensorless direct power control for three-phase grid side converter integrated into wind turbine system under disturbed grid voltages. *Electrical Engineering & Electromechanics*, 2020, no. 3, pp. 48-57. doi: https://doi.org/10.20998/2074-272X.2020.3.08.

12. Agha Kashkooli M.R., Jovanovic M.G. Sensorless adaptive control of brushless doubly-fed reluctance generators for wind power applications. *Renewable Energy*, 2021, vol. 177, pp. 932-941. doi: https://doi.org/10.1016/j.renene.2021.05.154.

13. El Daoudi S., Lazrak L., El Ouanjli N., Ait Lafkih M. Sensorless fuzzy direct torque control of induction motor with sliding mode speed controller. *Computers & Electrical Engineering*, 2021, vol. 96, art. no. 107490. doi: https://doi.org/10.1016/j.compeleceng.2021.107490.

14. Zhang M., Cheng M., Zhang B. Sensorless Control of Linear Flux-Switching Permanent Magnet Motor Based on Improved MRAS. *2018 IEEE 9th International Symposium on Sensorless Control for Electrical Drives (SLED)*, 2018, pp. 84-89. doi: https://doi.org/10.1109/SLED.2018.8486093.

15. Fereka D., Zerikat M., Belaidi A. MRAS Sensorless Speed Control of an Induction Motor Drive based on Fuzzy Sliding Mode Control. *2018 7th International Conference on Systems and Control (ICSC)*, 2018, pp. 230-236. doi: https://doi.org/10.1109/ICoSC.2018.8587844.

16. Wang G., Zhang H. A new speed adaptive estimation method based on an improved flux sliding-mode observer for the sensorless control of PMSM drives. *ISA Transactions*, 2022, vol. 128, pp. 675-685. doi: https://doi.org/10.1016/j.isatra.2021.09.003.

17. Haider Khan M.S., Kumar Mallik S. Mechanical sensorless control of a rotor-tied DFIG wind energy conversion system using a high gain observer. *Journal of King Saud University - Engineering Sciences*. 2022, no. 04, pp. 1-9. doi: https://doi.org/10.1016/j.jksues.2022.05.005.

18. Khan Y.A., Verma V. Implementation of a new speed estimation technique for vector controlled switched reluctance machines. *Measurement*, 2022, vol. 198, art. no. 111315. https://doi.org/10.1016/j.measurement.2022.111315.

19. El Merrassi W., Abounada A., Ramzi M. Advanced speed sensorless control strategy for induction machine based on neuro-MRAS observer. *Materials Today: Proceedings*, 2021, vol. 45, pp. 7615-7621. doi: https://doi.org/10.1016/j.matpr.2021.03.081.

20. Laggoun Z.E.Z., Benalla H., Nebti K. A power quality enhanced for the wind turbine with sensorless direct power control under different input voltage conditions. *Electrical Engineering & Electromechanics*, 2021, no. 6, pp. 64-71. doi: https://doi.org/10.20998/2074-272X.2021.6.09.

Received 13.10.2022
Accepted 08.12.2022
Published 07.03.2023

R. Saifi [1]*, Doctor of Electrical Engineering,*
[1] Department of Electrical Engineering, Faculty of Technology, Ferhat Abbas University Setif 1, Algeria,
e-mail: saifi_rabie@univ-setif.dz (Corresponding Author)

How to cite this article:
Saifi R. Implementation of a new flux rotor based on model reference adaptive system for sensorless direct torque control modified for induction motor. *Electrical Engineering & Electromechanics*, 2023, no. 2, pp. 37-42. doi: https://doi.org/10.20998/2074-272X.2023.2.06

UDC 621.314 https://doi.org/10.20998/2074-272X.2023.2.07

G. Priyanka, J. Surya Kumari, D. Lenine, P. Srinivasa Varma, S. Sneha Madhuri, V. Chandu

MATLAB-Simulink environment based power quality improvement in photovoltaic system using multilevel inverter

Introduction. *In this world of technical advancement, conventional resources are at the stage of destruction. To avoid such problems, we are going to use an alternative energy source namely solar by photovoltaic effect. The demand for multilevel inverters increased as they are used for different dynamic (high) voltage and dynamic (high) power appliances as they are capable of producing the output wave shape with low total harmonic distortion.* ***Novelty.*** *A new multilevel inverter is used in adding a (bidirectional) two way switch in between the capacitor and a traditional H-bridge module. This produces a better sine wave. By series connection of these two H-bridge modules, nine levels output voltage including zero is possible. The* ***purpose*** *of the proposed topology is reduction in the number of switches and it gives the good result with comparatively less power loss when it is compared with the other normal basic traditional inverters of the same output quality.* ***Methods.*** *In this paper, sinusoidal pulse width modulation technique is used for the working of the switches in the multilevel inverter. The* ***results*** *are verified by using simulation and also experimental setup is done. From the results it is observed that the proposed topology with reduced number of switches gives lower electromagnetic interference, lower harmonic distortion.* ***Practical value****. The total harmonic distortion value in the simulation is 14.4 % and practically it is 13.8 %.* References 25, table 4, figures 15.

Key words: **multilevel inverter, pulse width modulation, cascaded multilevel inverter, standard test conditions, cascaded H-bridge multilevel, space vector modulation.**

Вступ*. У світі технічного прогресу звичайні ресурси перебувають у стадії руйнації. Щоб уникнути таких проблем, ми збираємося використати альтернативне джерело енергії, а саме сонячну енергію з фотоелектричним ефектом. Попит на багаторівневі інвертори збільшився, оскільки вони використовуються для різних динамічних (високих) напруг та динамічних (високих) потужностей, оскільки вони здатні формувати вихідну форму хвилі з низьким гармонічним загальним спотворенням.* ***Новизна****. Новий багаторівневий інвертор використовується для додавання двостороннього перемикача між конденсатором і традиційним модулем Н-моста. Це дає найкращу синусоїду. При послідовному з'єднанні двох модулів Н-моста можливо дев'ять рівнів вихідної напруги, включаючи нуль.* ***Метою*** *запропонованої топології є зменшення кількості перемикачів, що дає хороший результат при порівняно менших втратах потужності порівняно з іншими традиційними звичайними інверторами з такою ж вихідною якістю.* ***Методи****. У цій статті для роботи перемикачів у багаторівневому інверторі використовується метод широтно-імпульсної синусоїдальної модуляції.* ***Результати*** *перевіряються за допомогою моделювання, а також виконується експеримент. З результатів видно, що пропонована топологія зі зменшеною кількістю перемикачів дає менші електромагнітні перешкоди, менші гармонійні спотворення.* ***Практична цінність****. Сумарне значення гармонійних спотворень при моделюванні складає 14,4 %, а практично – 13,8 %.* Бібл. 25, табл. 4, рис. 15.

Ключові слова: **багаторівневий інвертор, широтно-імпульсна модуляція, каскадний багаторівневий інвертор, стандартні умови випробувань, каскадний багаторівневий Н-міст, просторово-векторна модуляція.**

Introduction. The command for non-conventional resources has increased drastically due to scarcity of fossil fuels and greenhouse effect. Among these, wind and solar energy are admired because of the improvement in power electronics technology. Solar energy has many applications because of its advantages of having low maintenance and pollution free. Over the last 20 years, the necessity for non-renewable solar energy has expanded by the range of 20-25 % per year. This is mainly because of its decrease in the prices of solar panels. This resulted in the subsequent modifications: 1) the η of solar cells has raised; 2) industrialized machinery developments; 3) economies value of the scale. The relevant harmonics can be decreased by enhancing the output of the inverter. In current years, researchers and manufacturers are concentrating on multilevel inverters [1] because of their various benefits over the conventional pulse width modulation (PWM) inverters because as they have improved smaller filter size, lesser total harmonic distortion (THD), output waveforms, lower electromagnetic interference (EMI) and others [2].

One of the most desirable converters is the multilevel inverters (MLIs). MLIs are nothing but the converters which have the higher quantity of the output voltage levels when compared with the conventional inverters [3]. The main benefit of these MLIs is the higher output voltage levels [4] i.e. like a staircase wave shape, which is closer as that of the sinusoidal waveform. Hence these MLIs will have a lower THD. The various types of MLIs are cascaded H-bridge (CHB), flying capacitor (capacitor clamped), and diode clamped (neutral clamped). The most common type of MLIs is the CHB because of its modular structure [5].

Among these three, cascaded MLI (CMLI) has a modular structure and it has advantages of having less number of components when compared with the other two topologies, and moreover, it has many applications in the electrical engineering field [6]. There are several modulation and control strategies being, including the following: [7] multilevel selective harmonic elimination, multilevel sinusoidal, and space vector modulation (SVM). The main disadvantage of the SVM is that the mathematical modeling and the selection of switching states are complicated [2, 8, 9]. To overcome these drawbacks, multicarrier PWM is used as the control strategy.

PV array. The Earth has an abundant supply of solar energy. The sun has the capability of providing enough energy to the world per annum. In fact, the proportion of solar radiation reaching the earth surface for three-day duration is equal to the energy stored in all the non-renewable energy sources.

The smallest building block of a solar module comprises a *P-N* junction which is useful for converting the light energy into electrical energy and it is called the solar cell. The equivalent circuit of the solar cell is shown

in Fig. 1. It is a form of a tool for which the electrical parameters, such as current, voltage, or resistance, varies when exposed to sunlight [10]. The solar panels can be used as a light sensitive cell (photo detector), which is helpful for detecting the solar light (infrared detectors), near the visible range [11]. The basic principle of operation of a photovoltaic (PV) cell has 3 basic requirements:

- either electron-hole pair generating or exacting by the absorption of light;
- the detachment of charge carriers of opposing types;
- the distinct extraction of these carriers to another exterior circuit.

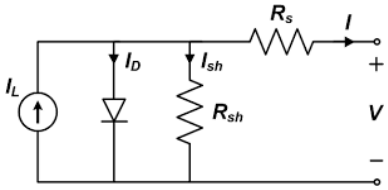

Fig. 1. Equivalent circuit of solar cell

On Fig. 1: I_L is the light developed current; I_D is the diode current; R_{sh} is the shunt resistance that gives us the information about the leakage current; R_s is the series resistance which tells us about the migration of charge carriers. A group of PV cells forms the solar arrays and solar modules. It consists of the following formula:

$$I = n_p \cdot I_g - n_p \cdot I_{rs}\left[\exp\left(\frac{q}{k \cdot T \cdot A \cdot n_s}\right) - 1\right], \qquad (1)$$

where n_p is the count of cells that are coupled in parallel; I_g is the insulation current; I_{rs} is the reverse saturation current; n_s is the series connected solar cells; T is the temperature, K; A is the ideality factor; q is the charge; k is the Boltzmann constant [12].

***I-V* and *P-V* characteristics.** Figure 2 shows the *I-V* and *P-V* characteristics of the solar cell. A curve drawn between current and voltage is nothing but *I-V* curve. This shows an inverse relation. The area of this curve gives us the information about the maximum power that a panel could produce at the maximum current and the maximum voltage conditions. The region of this curve declines while increasing the solar cell voltage due to its incline in temperature. Because of the variations in habitat conditions, the maximum power point will also change which indicates the change in temperature and irradiance levels [13].

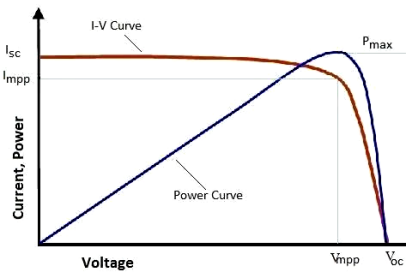

Fig. 2. *I-V* and *P-V* characteristics of solar cell

The final PV solar model is evaluated in standard test conditions (STC). These conditions are kept same in all over the world and performed in irradiance of 1000 W/m^2 under a temperature of 25 °C. Simulation of the solar PV model executes the *I-V* and *P-V* characteristics curves. Generally a good agreement was observed between various performance parameters results of reference model and simulated PV model at STC.

Proposed topology. The main disadvantage of conventional CMLI is more number of DC sources and as the level increases, the number of devices also inclines [14-16]. So as to achieve this, an improved topology has been introduced. The merits of this novel topology are the number of switches and the numbers of sources that are required are reduced [17]. The proposed topology is shown in Fig. 3.

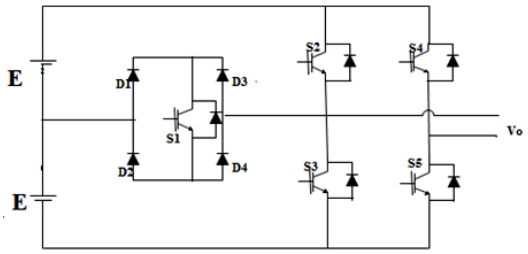

Fig. 3. Five levels CMLI

Based on the operating principle, Fig. 3 generates five levels of output voltage i.e. 2*E*, *E*, 0, –*E*, –2*E*. The switch combination has been shown in Table 1.

Table 1

Five level CMLI output voltage

Switching sequence*					Output voltage (V_o)
S1	S2	S3	S4	S5	
0	1	0	0	1	2E
1	0	0	0	1	E
0	0 or 1	1 or 0	0 or 1	1 or 0	0
1	0	0	1	0	–*E*
0	0	1	1	0	–2*E*

*(switch ON = 1, switch OFF = 0)

To obtain the output voltage 2*E*, S2 and S5 switches have to be turned ON, and for obtaining the level *E*, S1 and S5 has to be in ON position. Similarly for 0 either S3 and S5 or S2 and S4 has to be in turn ON position, for –E switches S1 and S4 need to be turned on; for –2*E* devices S3 and S4 are to be turned ON.

Nine-level inverter. The circuit topology of a nine-level inverter is shown in Fig. 4 and in Table 2.

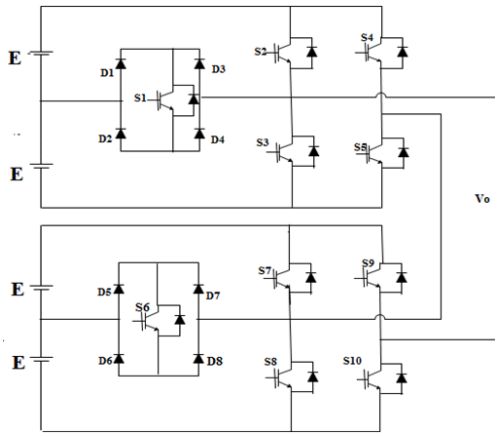

Fig. 4. Nine level CMLI

In five-level each module in the inverter produces 2*E*, *E*, 0, –*E*, –2*E*. Hence the proposed nine-level multilevel inverter can be formed by cascading operation of two five-level inverters. This produces the nine output voltages as 4*E*, 3*E*, 2*E*, *E*, 0, –*E*, –2*E*, –3*E*, –4*E*. Since each of the terminal in the output of the inverter is

connected in series; the output voltage will be obtained by adding the terminal voltages of every inverter [18-20].

Table 2

Nine level CMLI output voltage

Switching sequence*										Output voltage (V_o)
S1	S2	S3	S4	S5	S6	S7	S8	S9	S10	
0	1	0	0	1	0	1	0	0	1	$4E$
1	0	0	0	1	0	1	0	0	1	$3E$
0	0	0	0	0	0	1	0	0	1	$2E$
0	0	0	0	0	1	0	0	0	1	E
0	0	0	0	0	0	0	0	0	0	0
0	0	0	0	0	1	0	0	1	0	$-E$
0	0	0	0	0	0	0	1	1	0	$-2E$
1	0	0	1	0	0	0	1	1	0	$-3E$
0	0	1	1	0	0	0	1	1	0	$-4E$

*(switch ON = 1, switch OFF = 0)

Modulation technique. The classification of the modulation techniques are shown in Fig. 5. MLI control strategy uses two types of PWM methods. One of them is the high switching frequency and the other is fundamental switching frequency [21].

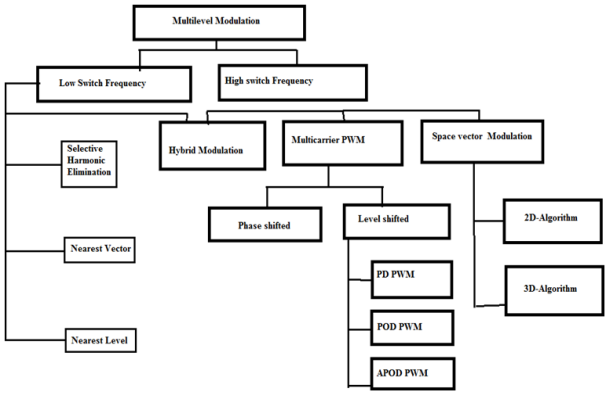

Fig. 5. Classification of multilevel modulation

The categorization of high switching frequency is as follows: space vector PWM, selective harmonics elimination PWM and SPWM [22]. Among these techniques, the popular method is SPWM that is used for most of the multilevel inverters, because of its simplicity and ease of implementation [23].

In this paper multicarrier PWM technique is used. This can be used for three or more than three levels. These are classified into two types namely level shift, and phase shift.

Level shifting PWM. Level shift is again subdivided into phase opposition disposition PWM (POD PWM), alternate phase opposition disposition PWM (APODPWM) and phase disposition PWM (PD PWM) [24, 25].

In this process, all carriers will be in phase with each other and also have the identical magnitude along with the identical frequency. This is done by comparing the reference sinusoidal wave with the vertically shifted carrier wave as shown in Fig. 6. This uses N–1 carrier signs to produce the output voltage of the inverter with N-level.

Some of the advantages of PWM based switching power converter over the other techniques and the conventional PWM is the most widely used technique all over the world because of its advantages or because of that its disadvantages do not have that big concern in most of the applications compared with its advantages. Some can be in its easy to implement and control and in its compatibility with almost all the modern digital applications. However it has also some disadvantages that might reduce its volubility in some applications, such as its attenuation of the fundamental frequency amplitude, its THD is reduced by increasing the switching frequency but that will lead to the increase of switching losses; which means greater stresses on the associated switching devices and creation of high frequency components with high amplitudes.

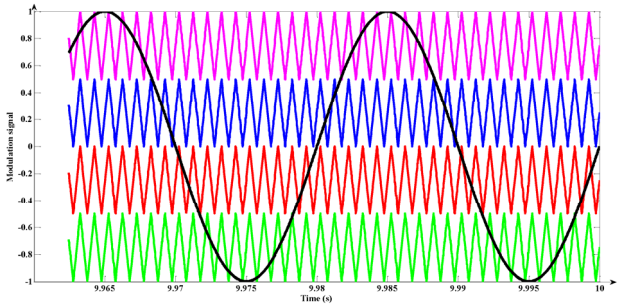

Fig. 6. Multicarrier PWM technique

Simulation results. All this proposed work is verified in MATLAB. The technique of multicarrier modulation is used for pulse generation. The solar panel is connected to the cascaded H-bridge MLI and the results are observed in Simulink. Figures 7, 8 show the PV and V-I characteristics of the solar collector. The output of this solar collector is taken at the temperature of 25 °C and at the radiance of 1000 W/m^2.

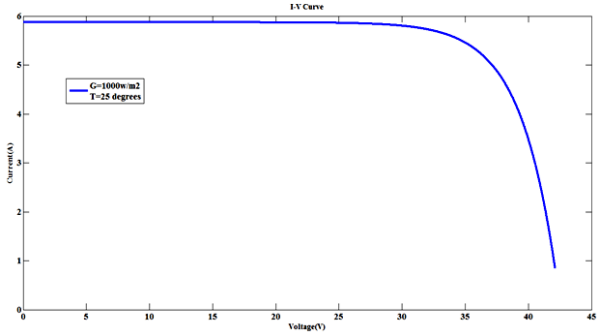

Fig. 7. I-V characteristics of solar panel

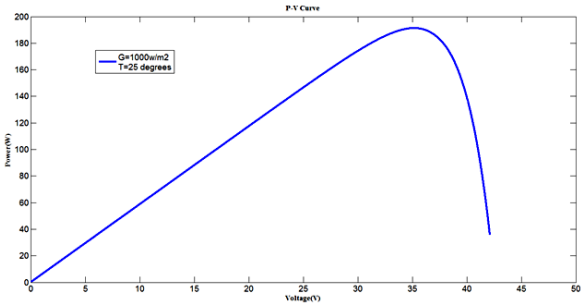

Fig. 8. P-V characteristics of solar panel

Figures 9-12 show the different levels of the output terminal voltage waveform. This concludes that as the modulation index declines the count of levels also declines and the magnitude of the voltage also gets declined as shown in the Table 3. It is also observed that the THD goes on increasing as the count of output voltage levels declines. Hence it is recommended to use a modulation index nearer to unity by which the count of the output levels gets increased.

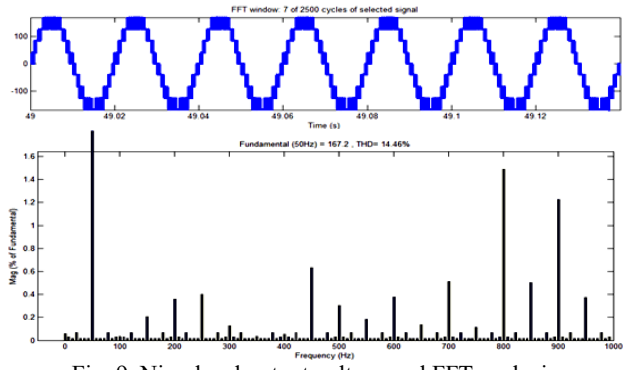

Fig. 9. Nine-level output voltage and FFT analysis of cascaded H-bridge MLI

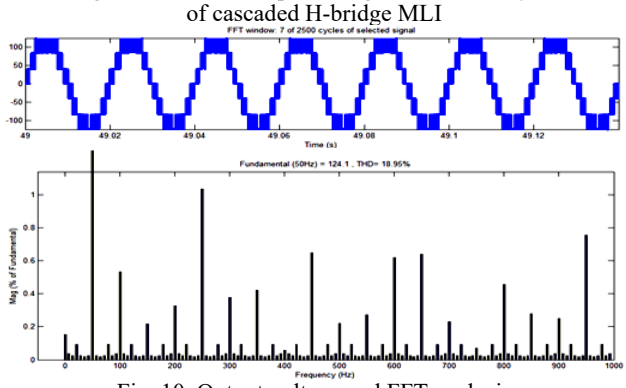

Fig. 10. Output voltage and FFT analysis of cascaded H-bridge MLI at M=0.75

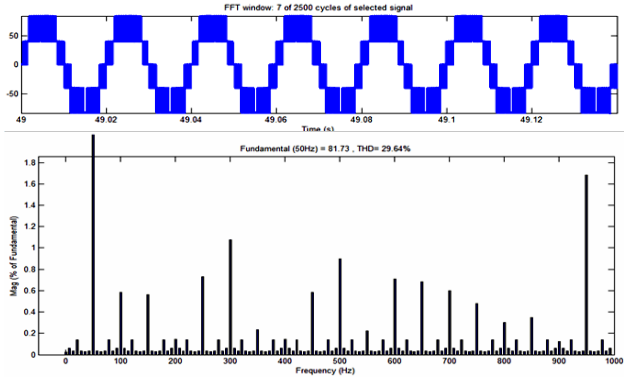

Fig. 11. Output voltage and FFT analysis of cascaded H-bridge MLI at $M = 0.5$

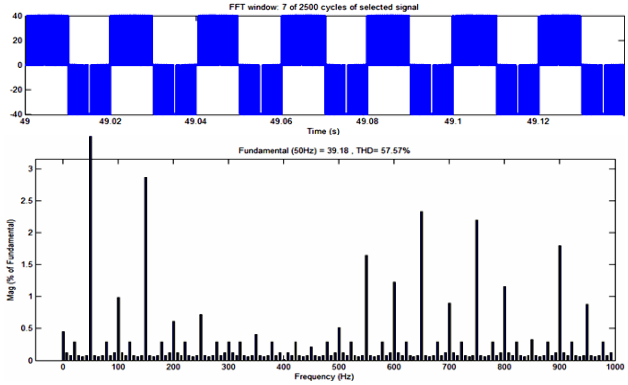

Fig. 12. Output voltage and FFT analysis of cascaded H-bridge MLI at $M = 0.25$

Table 3

Variations of THD with various modulation index

Modulation index	Output voltage (V_o)	No. of levels	THD
1	167.2	9	14.46 %
0.75	124.91	7	18.95 %
0.5	81.73	5	29.64 %
0.25	39.18	3	57.57 %

Experimental results. A prototype single phase 9-level CHBM has been built using 12.3 V for each bridge, 1A MOSFET as switching device, firing pulses to the switching devices are given through a delay circuit. The experimental results are represented in Fig. 13-15.

Components which were used:

- Switching device IRF840 MOSFET – 10 pcs;
- Diodes FR107 – 8 pcs;
- DC link capacitors 2200 μF/35 V – 4 pcs;
- Driver circuit IC for H-bridge IR2110 – 4 pcs;
- Driver circuit IC for bidirectional switch TLP250 – 2 pcs;
- OPTO isolator used for all PWM inputs 6N137 – 10 pcs;
- Buffer circuit used for impedance matching purpose cd4050ic – 3 pcs;
- Isolated +15 V power supply for driver circuits – 4 pcs;
- Power circuit input supply 12/1A DC – 2 pcs.

FPGA SPARTAN6 will be used to generate the gate signals for all switching devices miscellaneous items etc.

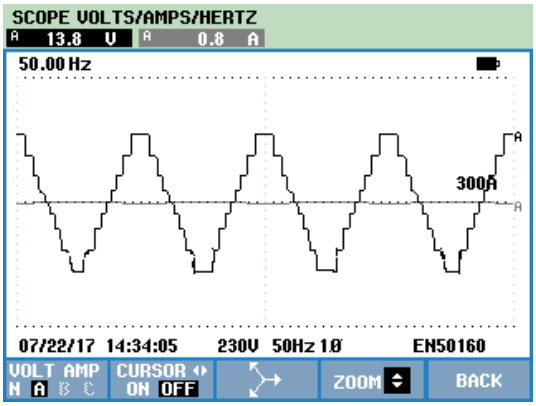

Fig. 13. 9-level output voltages

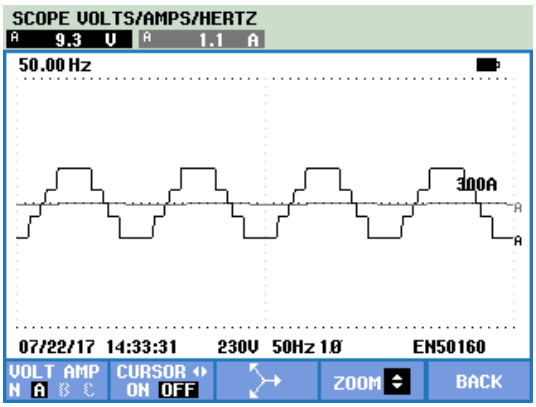

Fig. 14. Output of first H-bridge

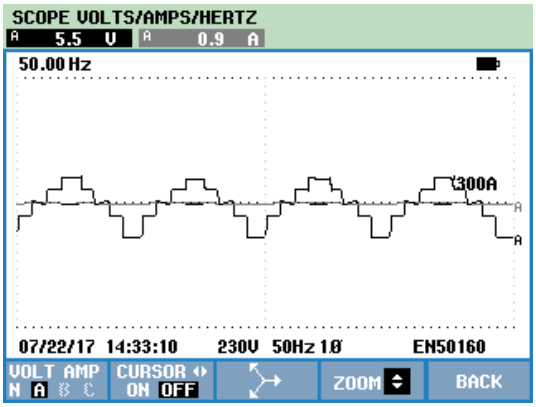

Fig. 15. Output of second H-bridge

In the Table 4 the practical values along with the simulated values are compared and the THD values are shown.

Table 4

Comparison of THD, %

H-bridge	THD (practical)	THD (simulated)
Nine-level	13.8 %	14.4 %

Other MLIs are not capable of producing higher level of output voltage due to increase in switch, number of DC sources and cost; however CMLI is capable of producing higher level voltage with qualitative waveform by using less number of switches. THD content in experimental and in simulation is 13.8 % and 14.4 %, which indicate that the output waveform is nearly sinusoidal. Thus the proposed topology for MLI shows some encouraging attributes when compared to traditional topologies. The keen observation between the experimental and simulation is that the THD is less in the experiment point of view when compared to the simulation.

Conclusions. This undertaking deal with the outline and execution implementation of single-phase nine-level cascaded H-bridge multilevel inverter for *R* load with multicarrier level-shifted pulse width modulation method fed with solar panel. The proposed work has benefits like less count of the switches, less electromagnetic interference, lower harmonic distortion and the total harmonic distortion obtained in this work is 14.4 %. The forthcoming work of this topography can be enlarged by connecting it to the grid. The equivalent multilevel inverter topography can be used for the hybrid grid which uses the integration of DC and AC sources like solar, wind, batteries, AC loads. It can also be used for hybrid microgrid i.e., in the case of interlinking converters which is bidirectional.

Conflict of interest. The authors declare that they have no conflicts of interest.

REFERENCES

1. Sung-Jun Park, Feel-Soon Kang, Man Hyung Lee, Cheul-U Kim. A new single-phase five-level PWM inverter employing a deadbeat control scheme. *IEEE Transactions on Power Electronics*, 2003, vol. 18, no. 3, pp. 831-843. doi: https://doi.org/10.1109/TPEL.2003.810837.

2. Keliang Zhou, Danwei Wang. Relationship between space-vector modulation and three-phase carrier-based PWM: a comprehensive analysis [three-phase inverters]. *IEEE Transactions on Industrial Electronics*, 2002, vol. 49, no. 1, pp. 186-196. doi: https://doi.org/10.1109/41.982262.

3. Rodriguez J., Jih-Sheng Lai, Fang Zheng Peng. Multilevel inverters: a survey of topologies, controls, and applications. *IEEE Transactions on Industrial Electronics*, 2002, vol. 49, no. 4, pp. 724-738. doi: https://doi.org/10.1109/TIE.2002.801052.

4. Malinowski M., Gopakumar K., Rodriguez J., Perez M.A. A Survey on Cascaded Multilevel Inverters. *IEEE Transactions on Industrial Electronics*, 2010, vol. 57, no. 7, pp. 2197-2206. doi: https://doi.org/10.1109/TIE.2009.2030767.

5. Poh Chiang Loh, Holmes D.G., Lipo T.A. Implementation and control of distributed PWM cascaded multilevel inverters with minimal harmonic distortion and common-mode voltage. *IEEE Transactions on Power Electronics*, 2005, vol. 20, no. 1, pp. 90-99. doi: https://doi.org/10.1109/TPEL.2004.839830.

6. Thakre K., Mohanty K.B., Ahmed H., Nayak A.K. Modified Cascaded Multilevel Inverter with Reduced Component Count. *2017 14th IEEE India Council International Conference (INDICON)*, 2017, pp. 1-5. doi: https://doi.org/10.1109/INDICON.2017.8488031.

7. Poh Chiang Loh, Holmes D.G., Fukuta Y., Lipo T.A. Reduced common-mode modulation strategies for cascaded multilevel inverters. *IEEE Transactions on Industry Applications*, 2003, vol. 39, no. 5, pp. 1386-1395. doi: https://doi.org/10.1109/TIA.2003.816547.

8. Rodriguez J., Jih-Sheng Lai, Fang Zheng Peng. Multilevel inverters: a survey of topologies, controls, and applications. *IEEE Transactions on Industrial Electronics*, 2002, vol. 49, no. 4, pp. 724-738. doi: https://doi.org/10.1109/TIE.2002.801052.

9. Sirisha B., Kumar P.S. A simplified space vector PWM for cascaded H-Bridge inverter including over modulation operation. *2016 IEEE Annual India Conference (INDICON)*, 2016, pp. 1-6. doi: https://doi.org/10.1109/INDICON.2016.7839038.

10. Gonzalez D.A., McCall J.C. Design of Filters to Reduce Harmonic Distortion in Industrial Power Systems. *IEEE Transactions on Industry Applications*, 1987, vol. IA-23, no. 3, pp. 504-511. doi: https://doi.org/10.1109/TIA.1987.4504938.

11. Selvaraj J., Rahim N.A. Multilevel Inverter For Grid-Connected PV System Employing Digital PI Controller. *IEEE Transactions on Industrial Electronics*, 2009, vol. 56, no. 1, pp. 149-158. doi: https://doi.org/10.1109/TIE.2008.928116.

12. Naderi R., Rahmati A. Phase-Shifted Carrier PWM Technique for General Cascaded Inverters. *IEEE Transactions on Power Electronics*, 2008, vol. 23, no. 3, pp. 1257-1269. doi: https://doi.org/10.1109/TPEL.2008.921186.

13. Rahim N.A., Chaniago K., Selvaraj J. Single-Phase Seven-Level Grid-Connected Inverter for Photovoltaic System. *IEEE Transactions on Industrial Electronics*, 2011, vol. 58, no. 6, pp. 2435-2443. doi: https://doi.org/10.1109/TIE.2010.2064278.

14. Sujitha N., Ramani K. A new Hybrid Cascaded H-Bridge Multilevel inverter - Performance analysis. *IEEE-International Conference On Advances In Engineering, Science And Management (ICAESM-2012)*, Nagapattinam, India, 2012, pp. 46-50.

15. Babaei E., Alilu S., Laali S. A New General Topology for Cascaded Multilevel Inverters With Reduced Number of Components Based on Developed H-Bridge. *IEEE Transactions on Industrial Electronics*, 2014, vol. 61, no. 8, pp. 3932-3939. doi: https://doi.org/10.1109/TIE.2013.2286561.

16. Babaei E., Laali S., Bayat Z. A Single-Phase Cascaded Multilevel Inverter Based on a New Basic Unit With Reduced Number of Power Switches. *IEEE Transactions on Industrial Electronics*, 2015, vol. 62. no. 2, pp. 922-929. doi: https://doi.org/10.1109/TIE.2014.2336601.

17. Rahim N.A., Selvaraj J. Multistring Five-Level Inverter With Novel PWM Control Scheme for PV Application. *IEEE Transactions on Industrial Electronics*, 2010, vol. 57, no. 6, pp. 2111-2123. doi: https://doi.org/10.1109/TIE.2009.2034683.

18. Naik B.S., Suresh Y., Venkataramanaiah J., Panda A.K. A Hybrid Nine-Level Inverter Topology With Boosting Capability and Reduced Component Count. *IEEE Transactions on Circuits and Systems II: Express Briefs*, 2021, vol. 68, no. 1, pp. 316-320. doi: https://doi.org/10.1109/TCSII.2020.2998496.

19. Arbune P.A., Gaikwad A. Comparative Study of Three level and five level Inverter. *International Journal of Advanced Research in Electrical, Electronics and Instrumentation Engineering*, 2016, vol. 5, no. 2, pp. 681-686. doi: https://doi.org/10.15662/IJAREEIE.2016.0502005.

20. Babaei E., Laali S., Bayat Z. A Single-Phase Cascaded Multilevel Inverter Based on a New Basic Unit With Reduced Number of Power Switches. *IEEE Transactions on Industrial Electronics*, 2015, vol. 62, no. 2, pp. 922-929. doi: https://doi.org/10.1109/TIE.2014.2336601.

21. Abdulhamed Z.E., Esuri A.H., Abodhir N.A. New Topology Of Asymmetrical Nine-Level Cascaded Hybrid Bridge Multilevel Inverter. *2021 IEEE 1st International Maghreb Meeting of the Conference on Sciences and Techniques of Automatic Control and Computer Engineering MI-STA*, 2021, pp. 430-434. doi: https://doi.org/10.1109/MI-STA52233.2021.9464511.

22. Bekhouche R., Khoucha F., Benrabah A., Benmansour K., Benbouzid M.E.H. Comparison of PWM Techniques for Modular Multilevel Converter: A Comparison Based on Different Voltage Level Waveforms. *020 1st International*

Conference on Communications, Control Systems and Signal Processing (CCSSP), 2020, pp. 460-465. doi: https://doi.org/10.1109/CCSSP49278.2020.9151588.

23. Bicak A., Gelen A. Comparisons of Different PWM Methods with Level-Shifted Carrier Techniques for Three-Phase Three-Level T-Type Inverter. *2020 7th International Conference on Electrical and Electronics Engineering (ICEEE)*, 2020, pp. 28-32. doi: https://doi.org/10.1109/ICEEE49618.2020.9102489.

24. Louarem S., Kebbab F.Z., Salhi H., Nouri H. A comparative study of maximum power point tracking techniques for a photovoltaic grid-connected system. *Electrical Engineering & Electromechanics*, 2022, no. 4, pp. 27-33. doi: https://doi.org/10.20998/2074-272X.2022.4.04.

25. Sahraoui H., Mellah H., Drid S., Chrifi-Alaoui L. Adaptive maximum power point tracking using neural networks for a photovoltaic systems according grid. *Electrical Engineering & Electromechanics*, 2021, no. 5, pp. 57-66. doi: https://doi.org/10.20998/2074-272X.2021.5.08.

Received 26.08.2022
Accepted 15.12.2022
Published 07.03.2023

G. Priyanka[1], *Assistant Professor,*
J. Surya Kumari [1], *Associate Professor,*
D. Lenine[1], *Professor,*
P. Srinivasa Varma[2], *Professor,*
S. Sneha Madhuri [3], *Assistant Professor,*
V. Chandu[4], *Research Scholar,*
[1] Department of Electrical & Electronics Engineering, RGM College of Engineering and Technology, India, e-mail: priyankagana004@gmail.com; jdsk.23@gmail.com (Corresponding Author); lenine.eee@gmail.com
[2] Department of Electrical & Electronics Engineering, Koneru Lakshmaiah Education Foundation, India, e-mail: pinnivarma@kluniversity.in
[3] Department of Electrical & Electronics Engineering, SVR Engineering College, India, e-mail: snehamadhurisettem@gmail.com
[4] Department of Electrical & Electronics Engineering, SRM Institute of Science and Technology, India, e-mail: chanduv43@gmail.com

How to cite this article:
Priyanka G., Surya Kumari J., Lenine D., Srinivasa Varma P., Sneha Madhuri S., Chandu V. MATLAB-Simulink environment based power quality improvement in photovoltaic system using multilevel inverter. *Electrical Engineering & Electromechanics*, 2023, no. 2, pp. 43-48. doi: https://doi.org/10.20998/2074-272X.2023.2.07

UDC 621.314 https://doi.org/10.20998/2074-272X.2023.2.08

D. Sakri, H. Laib, S.E. Farhi, N. Golea

Sliding mode approach for control and observation of a three phase AC-DC pulse-width modulation rectifier

Introduction. *For AC-DC conversion systems, the electrical systems typically use thyristor or diode bridge rectifiers, which have relatively poor performance. Nowadays, three-phase pulse-width modulation rectifiers are widely applied in various applications for their well-known intrinsic benefits, such as adjustable DC link voltage, unity power factor, bidirectional power flow and very low total harmonic distortion.* ***Purpose****. The objective of this work is to achieve better stability and dynamic performance using sliding mode strategy for control and observation.* ***Methods****. For that purpose, first a sliding mode controller is introduced on the DC-link side to ensure a fast and accurate response of the output load voltage. Then, the sliding mode approach is employed to control the quadrature and direct components of power to maintain the input power factor at unity. Finally, this approach is used to design two observers for grid voltage estimation and online variation of load resistance. To overcome the problem associated with the use of the classical low-pass filter, an adaptive compensation algorithm is used to compensate the attenuation of the amplitude and phase delay of the observed grid voltages. This algorithm is based on the use of the two low-pass filters in cascade and ensures the minimization of chattering.* ***Results****. Comparative studies have been carried out between sliding mode control method for controlling the three-phase AC-DC pulse-width modulation rectifier and other conventional techniques. The validation by simulation and the tests carried out gave very satisfactory results and proved the effectiveness and feasibility of the sliding mode for both control and observation of three phase pulse-width modulation rectifier.* References 25, table 2, figures 19.

Key words: **direct power control, three phase pulse-width modulation rectifier, sliding mode control, double-low pass filter, unity power factor.**

Вступ*. Для AC-DC систем перетворення електричні системи зазвичай використовують тиристорні або діодні мостові випрямлячі, які мають відносно погані характеристики. В даний час трифазні випрямлячі з широтно-імпульсною модуляцією широко застосовуються з різними цілями завдяки їх добре відомим внутрішнім перевагам, таким як регульована напруга у ланці постійного струму, одиничний коефіцієнт потужності, двонаправлений потік потужності та дуже низькі загальні гармонічні спотворення.* ***Метою*** *даної роботи є досягнення кращої стабільності та динамічних характеристик з використанням стратегії ковзного режиму для контролю та спостереження.* ***Методи****. З цією метою спочатку на стороні ланки постійного струму вводиться регулятор режиму ковзання, щоб забезпечити швидку і точну реакцію на вихідну напругу навантаження. Потім використовується метод ковзного режиму для управління квадратурною та прямою складовими потужності, щоб підтримувати вхідний коефіцієнт потужності рівним одиниці. Нарешті цей підхід використовується для розробки двох спостерігачів для оцінки напруги мережі та зміни опору навантаження в режимі онлайн. Для подолання проблеми, пов'язаної з використанням класичного низькочастотного фільтру, використовується алгоритм адаптивної компенсації, що компенсує загасання амплітуди і фазової затримки напруг мережі, що спостерігаються. Цей алгоритм заснований на використанні двох низькочастотних фільтрів у каскаді та забезпечує мінімізацію брязкоту.* ***Результати****. Були проведені порівняльні дослідження між методом керування ковзним режимом для керування трифазним випрямлячем AC-DC з широтно-імпульсною модуляцією та іншими традиційними методами. Перевірка за допомогою моделювання та проведені випробування дали дуже задовільні результати та довели ефективність та здійсненність ковзного режиму як для управління, так і для спостереження за трифазним випрямлячем з широтно-імпульсною модуляцією.* Бібл. 25, табл. 2, рис. 19.

Ключові слова: **пряме керування потужністю, трифазний випрямляч з широтно-імпульсною модуляцією, ковзне керування, подвійний низькочастотний фільтр, одиничний коефіцієнт потужності.**

Introduction. In recent years, advances in the field of power electronics have contributed to the development of new static converter structures that allow the modulation of electrical energy according to industrial use. These converters are widely used in industrial or domestic fields, such as non-controlled diodes and controlled thyristor rectifiers. These converters behave like non-linear loads, absorbing harmonic currents that have a very negative impact on the electrical grid. Indeed, it can cause a number of disturbances, ranging from equipment dysfunction to complete destruction.

Harmonic pollution is a phenomenon that leads to the degradation of power quality, especially the distortion of the voltage wave, which increases the rate of harmonic distortion of the current that can exceed a value of 30 % [1]. Unfortunately, this value does not conform to the international standards imposed by the specialized organisms: IEC 61000, EN 50160 and IEEE Standard 519 which impose total harmonic distortion (THD) limits of 3 % for voltages and 5 % for currents [1]. In this situation, and to overcome this kind of problem, several solutions have been developed: curative solutions such as active filters and preventive solutions such as pulse width modulation rectifiers. Low harmonic pollution, controllable reactive power, adjustable DC-link voltage, unit power factor and bi-directional power flow are some advantages of this converter topology [2-7].

Because of its higher performances than the traditional thyristor or diode rectifier bridge, the three-phase pulse-width modulation (PWM) rectifier is now widely utilized in industry, including power supplies for microelectronics, wind power production, telecommunications equipment, etc [8]. The design of these non-polluting converters, combined with a judicious choice of control, provides a significant improvement current waveform of the electrical grid and guarantees operation with a unity power factor.

In this context, many techniques have been applied to three-phase PWM rectifiers to improve power quality. Voltage-oriented control, which derives from field-oriented control applied to AC machines, is one of the efficient techniques that permit decoupled control. It consists of eliminating the voltage quadrature component in order to ensure an indirect and decoupled control of the power. The voltage references for the direct and quadrature components are generated from the current controllers in the rotating frame. Since position data is necessary for all d-q transformations in voltage-oriented

control, position information can be obtained via estimation of the virtual flux or from measurement or observation of grid voltages. As for the reference of the direct current component, it is obtained from the regulation of DC-link voltage, while the reference of the quadrature component is set to zero in order to have a unitary power factor operation.

By analogy to the direct torque control of AC machines in the stationary α-β frame, another control technique for PWM rectifiers proposed by Ohnishi in 1991 so-called direct power control (DPC) and later developed by Takahachi and Noguchi in 1998 [9, 10].

In DPC, it is possible to control directly the active and reactive power by selecting the appropriate inverter state from a predefined switching table. For each sampling time, the appropriate inverter voltage vectors are selected according to the errors between the active and reactive powers and their references and the position of the voltage vector. The active power reference is provided by a PI controller for DC-link voltage while the reactive power reference is maintained at zero to ensure unity power factor. Two DPC configurations can be used: DPC based on measured or estimated voltage vectors (V-DPC) [1, 9, 11-12]: the position is determined by voltage vectors, and the instantaneous powers are calculated from voltage and current vectors. DPC based on virtual flux [1, 13-16]: where the estimated fluxes define the position and the instantaneous powers are calculated from the current and fluxes vectors. However, the classical direct power control has many disadvantages, such as: a variable switching frequency due to the hysteresis comparators, a high filter inductance value to obtain a smooth current, a low sampling period is required for accurate power estimation, and its implementation requires a fast microprocessor and an ADC due to its high sampling frequency requirement [17].

In order to improve the classical DPC, this strategy is combined with the sliding mode control (SMC) approach, which is distinguished by its robustness to parametric variations and external perturbations [18, 19]. In addition, the SMC is used to design simple, efficient and more economical observers which eliminates the need for physical sensors and reduces cost.

In this perspective, this paper aims to improve the dynamic and static performances of direct power control using the sliding mode approach. This improvement can be illustrated by comparison with other techniques in terms of THD and power factor. To achieve these objectives, enhancements have been introduced by:

- substituting the PI controller of the DC-link voltage with SMC;
- ensuring direct and decoupled control for both active and reactive power;
- replacing grid voltage sensors with a sliding mode observer combined with a double-low-pass filter to minimize the chattering phenomenon and to compensate amplitude attenuation and phase errors;
- on-line estimating variation in load resistance.

Three phase PWM rectifier model. A three-phase PWM rectifier's topology is given by Fig. 1, where i_a, i_b, i_c and e_a, e_b, e_c are the three-phase grid currents and voltages, V_a, V_b, V_c are the input voltages of three-phase PWM rectifier, L and R are the inductance and resistance of interconnecting filters and R_L is the load resistor of the DC side.

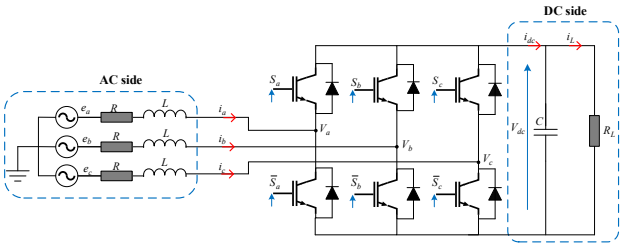

Fig. 1. Electrical circuit of a three phase PWM rectifier

According to the per phase equivalent circuit in Fig. 2, the AC side equations can be given as:

$$\begin{cases} L\dfrac{di_a}{dt} = e_a - Ri_a - V_a; \\ L\dfrac{di_b}{dt} = e_b - Ri_b - V_b; \\ L\dfrac{di_c}{dt} = e_c - Ri_c - V_c. \end{cases} \quad (1)$$

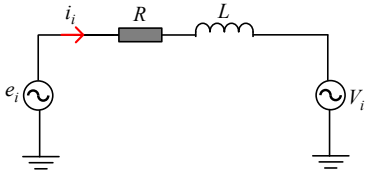

Fig. 2. Per phase model of three phase PWM rectifier

For the DC side, the equation is written as:

$$C\frac{\mathrm{d}V_{dc}}{\mathrm{d}t} = (S_a i_a + S_b i_b + S_c i_c) - \frac{V_{dc}}{R_L}. \quad (2)$$

In the (α, β) frame, the three-phase boost rectifier model can be written as:

$$\begin{cases} L\dfrac{\mathrm{d}i_\alpha}{\mathrm{d}t} = e_\alpha - Ri_\alpha - V_\alpha; \\ L\dfrac{\mathrm{d}i_\beta}{\mathrm{d}t} = e_\beta - Ri_\beta - V_\beta; \\ C\dfrac{\mathrm{d}V_{dc}}{\mathrm{d}t} = (S_\alpha i_\alpha + S_\beta i_\beta) - \dfrac{V_{dc}}{R_L}. \end{cases} \quad (3)$$

SMC-based DPC of three phase PWM rectifier. The block scheme of SMC-based DPC is given in Fig. 3. Sliding mode controllers are utilized to regulate the DC-link voltage, active power, and reactive power.

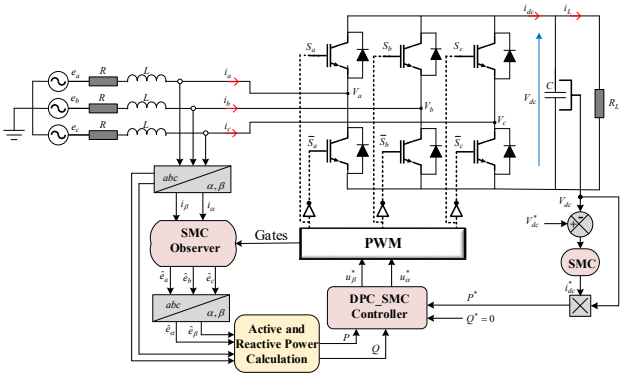

Fig. 3. DPC-SMC of three phase PWM rectifier

DC-link voltage sliding mode control. To determine the sliding surface, the general form is given as [10]:

$$S(t) = \left(\lambda + \frac{\mathrm{d}}{\mathrm{d}t}\right)^{n-1} e(t) + K\int_0^t e(t)\mathrm{d}t, \quad (4)$$

where $e(t)$ is the error between the reference and controlled values; λ, K are the strictly positive constants; n is the relative degree, which corresponds to the number of differentiations required for the output, until the control appears. In our case, n is set to 1, which gives the following sliding mode surface of DC-link voltage:

$$S_{dc}(t)=e_{dc}(t)+K_1\int e_{dc}(t)\mathrm{d}t\,, \tag{5}$$

where K_1 is the positive gain and:

$$e_{dc}(t)=V_{dc}^{*}(t)-V_{dc}(t), \tag{6}$$

by taking the first derivative of the sliding surface, we have:

$$\dot{S}_{dc}=\dot{e}_{dc}+K_1e_{dc}=\dot{V}_{dc}^{*}+\frac{V_{dc}}{R_LC}+K_1\left(V_{dc}^{*}-V_{dc}\right)-\frac{1}{C}i_{dc}\,. \tag{7}$$

In steady state, $\dot{S}_{dc}=S_{dc}=0$ which gives:

$$i_{dc}^{*}=C\dot{V}_{dc}^{*}+\frac{V_{dc}}{R_L}+K_1C\left(V_{dc}^{*}-V_{dc}\right)+K_{dc}\mathrm{sign}\left(S_{dc}\right), \tag{8}$$

where K_{dc} is the positive constant and the function sign(S_{dc}) is substituted by a smooth function (saturation), to minimize the chattering effect. It is given as:

$$\mathrm{sat}\left(S_{dc}\right)=\begin{cases}+1 & \text{if } S_{dc}>\gamma;\\ -1 & \text{if } S_{dc}<\gamma;\\ \dfrac{S_{dc}}{\gamma} & \text{if } \left|S_{dc}\right|\le\gamma,\end{cases} \tag{9}$$

where γ is the smooth factor.

Stability analysis. Let us take the Lyapunov's function as follows:

$$V_c=\frac{1}{2}S_{dc}^2\,. \tag{10}$$

The time derivative of this function is:

$$\dot{V}_c=S_{dc}\dot{S}_{dc}\,. \tag{11}$$

Substituting the derivative of the surface with its expression, we get:

$$\dot{V}_c=S_{dc}\begin{pmatrix}\dot{V}_{dc}^{*}-\left(\dot{V}_{dc}^{*}+\dfrac{V_{dc}}{R_LC}+K_1\left(V_{dc}^{*}-V_{dc}\right)\right)\\ -\dfrac{K_{dc}}{C}\mathrm{sign}\left(S_{dc}\right)+\dfrac{V_{dc}}{CR_L}+K_1\left(V_{dc}^{*}-V_{dc}\right)\end{pmatrix}, \tag{12}$$

$$\dot{V}_c=-S_{dc}\frac{K_{dc}}{C}\mathrm{sign}\left(S_{dc}\right)=-\frac{K_{dc}}{C}\left|S_{dc}\right|\,. \tag{13}$$

For $\dot{V}_c<0$, K_{dc} must be a positive constant. Finally the reference of active and reactive powers can be written as:

$$\begin{cases}P^{*}=V_{dc}i_{dc};\\ Q^{*}=0.\end{cases} \tag{14}$$

where i_{dc} is the DC-link current.

Active and reactive powers control. In this part, sliding mode controllers are introduced to ensure that the powers track their imposed desired values. The sliding surfaces of active and reactive powers are given as:

$$\begin{cases}S_P=e_P+K_2\int e_P\mathrm{d}t;\\ S_Q=e_Q+K_3\int e_Q\mathrm{d}t,\end{cases} \tag{15}$$

where:

$$\begin{cases}e_p=P-P^{*};\\ e_Q=Q-Q^{*},\end{cases} \tag{16}$$

where K_2 and K_3 are the positive gains. The surface derivatives are given as:

$$\begin{cases}\dot{S}_P=\dot{e}_P+K_2e_P;\\ \dot{S}_Q=\dot{e}_Q+K_3e_Q,\end{cases} \tag{17}$$

where:

$$\begin{cases}P=e_\alpha i_\alpha+e_\beta i_\beta;\\ Q=e_\beta i_\alpha-e_\alpha i_\beta.\end{cases} \tag{18}$$

Substituting active and reactive powers by their expressions and calculating the derivative of surface functions in matrix format, we can obtain:

$$\dot{S}_{PQ}=F+DU\,, \tag{19}$$

where:

$$D=\begin{bmatrix}-\dfrac{e_\alpha}{L} & -\dfrac{e_\beta}{L}\\ -\dfrac{e_\alpha}{L} & \dfrac{e_\beta}{L}\end{bmatrix},\quad U=\begin{bmatrix}V_\alpha\\ V_\beta\end{bmatrix}\text{ and}$$

$$F=\begin{bmatrix}\dot{V}_\alpha i_\alpha+\dot{V}_\beta i_\beta+\left(K_2-\dfrac{R}{L}\right)P+\dfrac{1}{L}\left(V_\alpha^2+V_\beta^2\right)-\dot{P}^{*}-K_2P^{*}\\ \dot{V}_\beta i_\alpha-\dot{V}_\alpha i_\beta+\left(K_3-\dfrac{R}{L}\right)Q-\dot{Q}^{*}-K_3Q^{*}\end{bmatrix},$$

where U is the vector control and F is theindependent term. In a steady state, to obtain the equivalent control term:

$$\dot{S}_{PQ}=0\,. \tag{20}$$

So:

$$U_{eq}=-D^{-1}F\,. \tag{21}$$

Finally, the control vector is given as:

$$U=U_{eq}+U_{NL}=-D^{-1}\left[F+K_{PQ}\mathrm{sign}\left(S_{PQ}\right)\right]. \tag{22}$$

The Lyapunov's function derivative is given by:

$$\begin{aligned}V_{PQ}&=S_{PQ}\dot{S}_{PQ}=\\ &=S_{PQ}\left(F+DU\right)=\\ &=S_{PQ}\left(F+D\left[-D^{-1}\left[F+K_{PQ}sign\left(S_{PQ}\right)\right]\right]\right)\end{aligned} \tag{23}$$

Simplification gives:

$$\dot{V}_{PQ}=-K_{PQ}\left|S_{PQ}\right|, \tag{24}$$

so $\dot{V}_{PQ}<0$ only if K_{PQ} is the positive constant.

SMC-based grid voltages observer. From the dynamical model of three phase boost rectifier in (α, β) frame , the current model can be given as:

$$\frac{\mathrm{d}i_g}{\mathrm{d}t}=\frac{1}{L}\left(e_g-Ri_g-V_g\right), \tag{25}$$

where $i_g=\left[i_\alpha\ i_\beta\right]^T$, $e_g=\left[e_\alpha\ e_\beta\right]^T$ and $V_g=\left[V_\alpha\ V_\beta\right]^T$.

The sliding mode observer model is expressed as:

$$\frac{\mathrm{d}\hat{i}_g}{\mathrm{d}t}=\frac{1}{L}\left(G\mathrm{sign}\left(S_g\right)-R\hat{i}_g-V_g\right), \tag{26}$$

where $S_g=i_g-\hat{i}_g$ is the observer's sliding surface of the

current, $\hat{i}_g = \begin{bmatrix}\hat{i}_\alpha & \hat{i}_\beta\end{bmatrix}^T$ is the estimated current vector, $G = \begin{bmatrix}G_1 & G_2\end{bmatrix}^T$ and G_1, G_2 are the positive gains.

From the previous equations (25), (26), we get:

$$\frac{\mathrm{d}S_g}{\mathrm{d}t} = \frac{1}{L}\left(e_g - RS_g - G\,\mathrm{sign}\left(S_g\right)\right), \tag{27}$$

when sliding mode is reached $\dot{S}_g = 0$, estimated grid voltages can be expressed as:

$$e_g = G\,\mathrm{sign}\left(S_g\right). \tag{28}$$

A low-pass filter (LPF) that also reduces the impact of the chattering phenomenon can be used to produce the grid voltages.

$$e_{gf} = LPF\left(G\,\mathrm{sign}\left(S_g\right)\right), \tag{29}$$

where $e_{gf} = \begin{bmatrix}e_{\alpha f} & e_{\beta f}\end{bmatrix}^T$ is the observer's filtered output in (α, β) frame.

The use of the LPF to minimize the chattering of a sliding mode observer has the disadvantage of attenuating the amplitude of the observed signal and creating a phase delay between the estimated and the signal to be estimated. To remedy this problem in [20] authors have proposed an adaptive algorithm to compensate the attenuation caused on the amplitude and the phase delay. This algorithm also has the advantage of being insensitive to the variation of the frequency of the grid voltage, which improves the precision of the observation illustrated in Fig. 4.

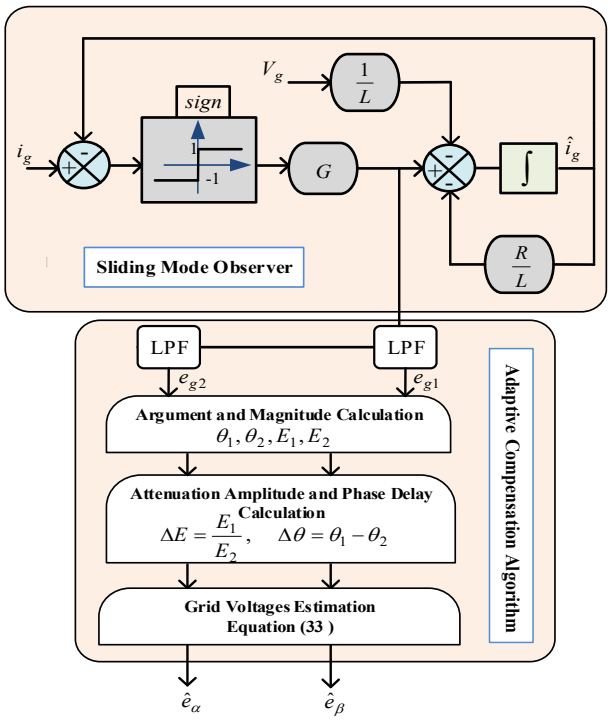

Fig. 4. Sliding mode-based grid voltages observer

The strategy of this algorithm is based on the use of two identical filters of low-pass type in a cascade (with same cut-off frequency ω_c).

$$\begin{cases} e_{g1} = \dfrac{\omega_c}{s+\omega_c} e_{gf}; \\ e_{g2} = \dfrac{\omega_c}{s+\omega_c} e_{g1}. \end{cases} \tag{30}$$

Amplitudes and arguments of outputs of previous filters can be calculated as follows:

$$\begin{cases} E_1 = \left\|e_{g1}\right\|; & \theta_1 = \arg\left(e_{g1}\right); \\ E_2 = \left\|e_{g2}\right\|; & \theta_2 = \arg\left(e_{g2}\right). \end{cases} \tag{31}$$

The errors in amplitudes and phases can be deduced as:

$$\begin{cases} \Delta E = \dfrac{E_1}{E_2}; \\ \Delta\theta = \theta_1 - \theta_2. \end{cases} \tag{32}$$

Finally, we can get the expressions of the estimated grid voltages by taking into account the compensation of the amplitude attenuation and the phase deviation, as:

$$\begin{cases} \hat{e}_\alpha = E_2 \Delta E^2 \cos\left(\theta_2 + 2\Delta\theta\right); \\ \hat{e}_\beta = E_2 \Delta E^2 \sin\left(\theta_2 + 2\Delta\theta\right). \end{cases} \tag{33}$$

Load resistance observer [21]. From the DC side voltage equation, the following two equations can be written as:

$$\begin{cases} \dfrac{\mathrm{d}V_{dc}}{\mathrm{d}t} = \dfrac{1}{C}\left(S_\alpha i_\alpha + S_\beta i_\beta\right) - \dfrac{V_{dc}}{CR_L}; \\ \dfrac{\mathrm{d}\hat{V}_{dc}}{\mathrm{d}t} = \dfrac{1}{C}\left(S_\alpha i_\alpha + S_\beta i_\beta\right) - \dfrac{\hat{V}_{dc}}{CR_{L0}} + \lambda\,\mathrm{sign}\left(e_V\right), \end{cases} \tag{34}$$

where $\hat{V}_{dc}$ is the observed DC-link voltage and R_{L0} is the nominal value of load resistance, the error observation is given as:

$$e_V = V_{dc} - \hat{V}_{dc}. \tag{35}$$

In addition, the error dynamic equation:

$$\begin{aligned} \frac{\mathrm{d}e_V}{\mathrm{d}t} &= \frac{\mathrm{d}V_{dc}}{\mathrm{d}t} - \frac{\mathrm{d}\hat{V}_{dc}}{\mathrm{d}t} = \\ &= -\left(\frac{V_{dc}}{CR_L} - \frac{\hat{V}_{dc}}{CR_{L0}}\right) - \lambda\,\mathrm{sign}\left(e_V\right), \end{aligned} \tag{36}$$

where λ is the positive constant that satisfies:

$$\lambda > \left| -\left(\frac{V_{dc}}{CR_L} - \frac{\hat{V}_{dc}}{CR_{L0}}\right)\right|, \tag{37}$$

when sliding mode is reached in finite time, equivalent control:

$$V_{dc} = \hat{V}_{dc} \Rightarrow \left(\frac{\hat{V}_{dc}}{CR_L} - \frac{V_{dc}}{CR_{L0}}\right) = V_{R,eq}, \tag{38}$$

where $V_{R,eq}$ is the equivalent control [22, 23] of the observer. Its estimate $\hat{V}_{R,eq}$ can be generated by the LPF:

$$\hat{V}_{R,eq} = LPF\left(\lambda\,\mathrm{sign}\left(e_V\right)\right). \tag{39}$$

Finally, the estimated load resistance can be deduced from its nominal value and the observer's output:

$$\hat{R}_L = -\frac{C\hat{V}_{R,eq}}{\hat{V}_{dc}} + R_{L0}. \tag{40}$$

Simulation results and discussions. To illustrate the effectiveness and the feasibility of the enhanced DPC based on sliding mode approach for control and observation, simulation studies were carried out with MATLAB/Simulink under several operations conditions. For this purpose, all three-phase PWM rectifier parameters are summarized in Table 1.

Table 1

Three phase PWM rectifier parameters

Parameters	Values
Grid frequency f, Hz	50
Grid voltage V, V	120
Reference of DC-link voltage V_{dc}^{*}, V	300
Grid side inductance L, mH	16
Grid side resistance R, Ω	0.1
DC-link capacitor C, μF	1100
Load resistance R_L, Ω	40→80
PWM frequency f_P, kHz	15

Several tests were carried out using MATLAB/Simulink to test the performance of DPC control based on SMC. In the first test, and for a variable load profile depicted by Fig. 5 the DPC-SMC block diagram is simulated for two operating conditions: with grid voltage measurement from 0 to 1.5 s and then without grid voltage sensor using a sliding mode observer from 1.5 s to 3 s.

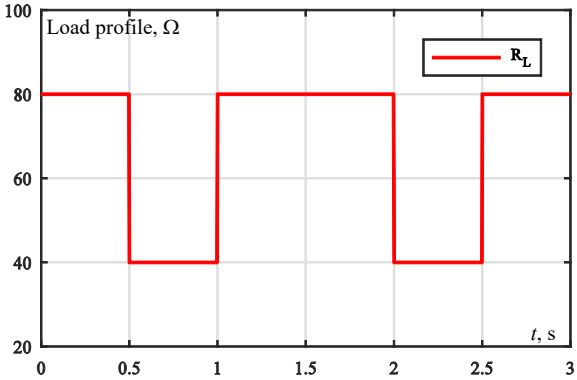

Fig. 5. Load profile

The curves obtained are illustrated by Fig. 6–11 and the following comments can be carried out.

In the presence of disturbance and according to Fig. 6, the DC-link voltage tracks perfectly its imposed reference (300 V) with a disturbance rejection considered good at the moments of load variation.

Figure 7 shows the evolution of active and reactive power. It is very clear that the active power has behavior identical to that of the reference generated reflecting the applied load. It is equal to 1195 W for R = 80 Ω and then increases to 2300 W when the load passes to R = 40 Ω. On the same Fig. 7, it can be seen that reactive power has a zero average value, which guarantees a unitary power factor, and therefore the grid current and voltage are always in phase (Fig. 9).

Under a variable load profile, Fig. 10 shows the waveforms of the three voltages measured and estimated using a sliding mode-based observer. Whatever the operating conditions, the introduction of the voltage observer at time 1.5 s gives good results and the estimated grid voltages show no amplitude attenuation or phase delay compared to the actual signal. This is justified by the introduction of a compensation algorithm.

As for the power quality, for both with and without grid voltage observer operating conditions, the THD is less than 5 %, which is in accordance with IEEE 519 International Standards Fig. 11 for various operating conditions.

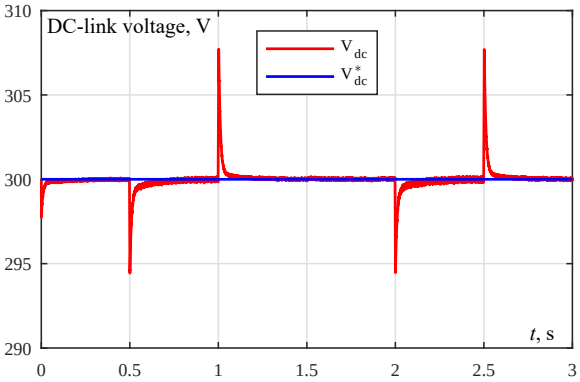

Fig. 6. DC-link voltage regulation

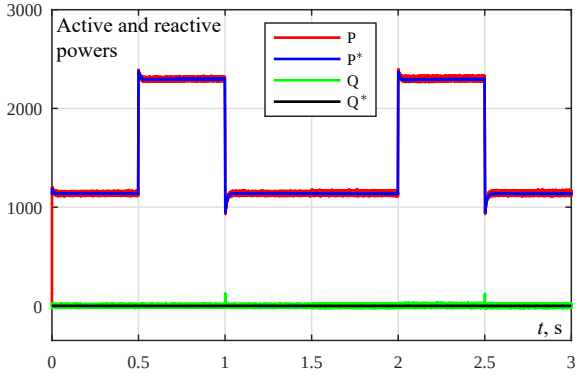

Fig. 7. Active and reactive powers

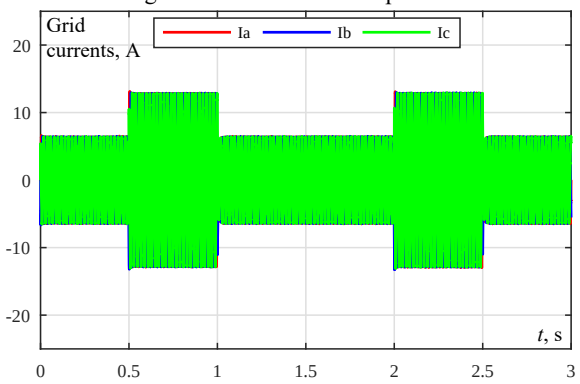

Fig. 8. Three-phase grid currents

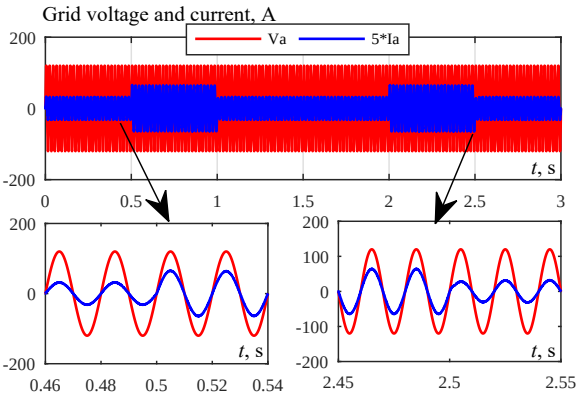

Fig. 9. Grid voltage and current

Another test is done in open loop to illustrate the advantages of the observer associated with double LPFs and a compensation algorithm. Examination of Fig. 12, 13 shows that the errors in amplitude and phase are very noticeable when the observer uses a single LPF. At time t = 0.5 s, the system based on double LPFs and a compensation algorithm is introduced. It is easy to notice that the amplitude attenuation and the phase delay can be compensated.

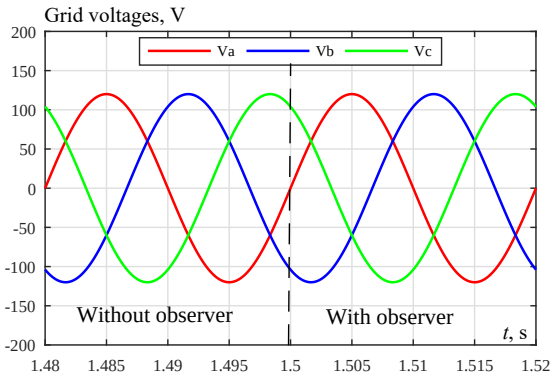

Fig. 10. Grid voltage with and without observer

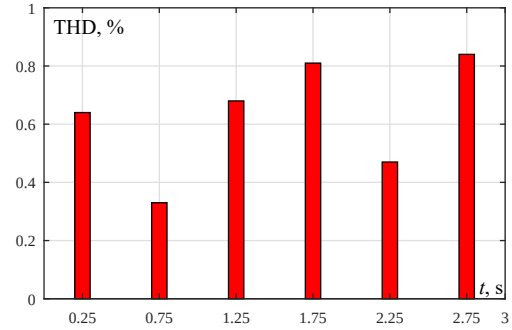

Fig. 11. THD of grid current

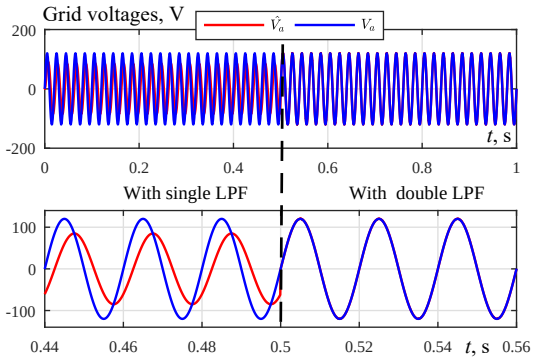

Fig. 12. Observed grid line voltage with compensation algorithm

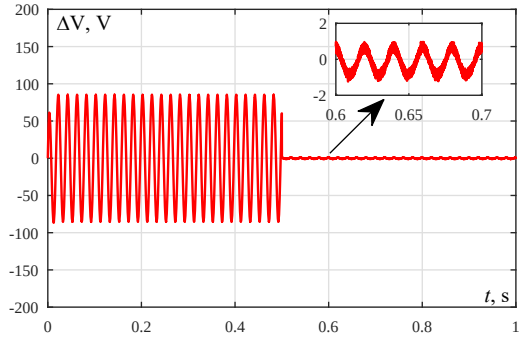

Fig. 13. Grid voltage observation error

The second test evaluates the DPC-SMC without a grid voltage sensor and with online estimation of the load variation using a sliding mode observer and under a load variable profile.

The results show that the performance of the sensorless DPC-SMC control is always better. Figure 14 shows that the observer accurately estimates the load variation which is reflected by the low estimation errors shown in Fig. 15.

In Fig. 16, the measured the DC-link voltage tracks perfectly its reference, which confirms the good design of the voltage controller.

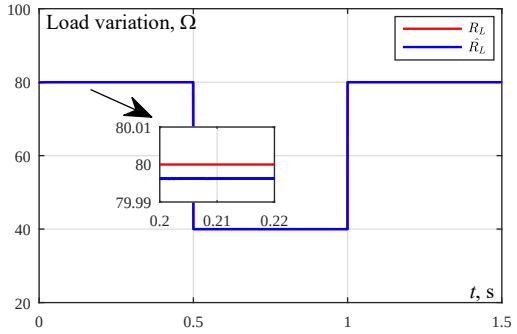

Fig. 14. Load observation

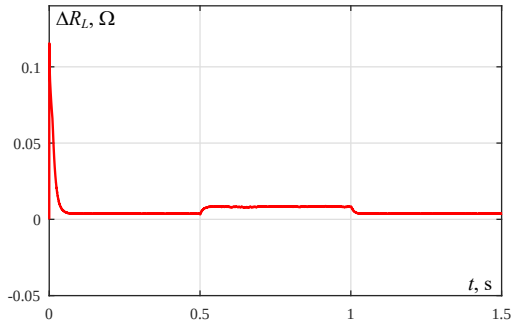

Fig. 15. Error in load estimation

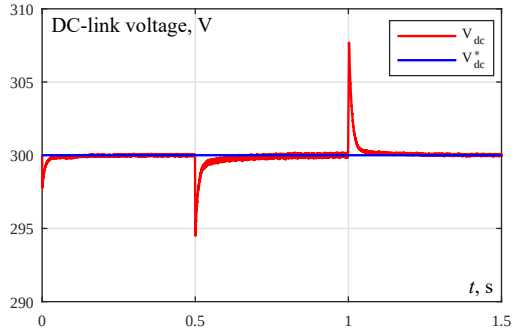

Fig. 16. Behavior of DC-link voltage

For Fig. 17 depicting the evolution of the instantaneous active and reactive powers, it is very clear that they present a fast dynamic and track their references without overshoot.

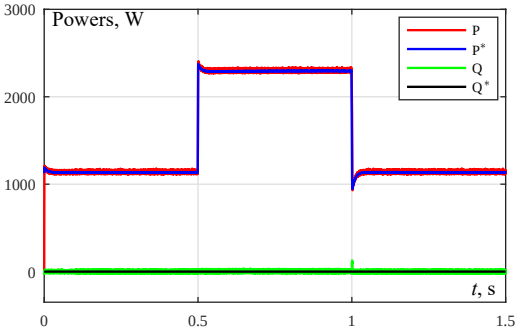

Fig. 17. Instantaneous active and reactive power

The high quality of the grid line current (sinusoidal waveform) is confirmed by a good unit power factor, as shown in Fig. 19, and by the low THD values indicated by the bars in Fig. 18 for various operating conditions.

Table 2 presents a comparison between DPC-SMC and other control techniques based on several terms.

Table 2

Comparison between conventional control strategies and DPC-SMC

	DPC-SMC	DPC [24]	Other techniques [25]
THD, %	1.13	3.17	3.35→12.2
Power factor	1	1	0.98→0.99

From this comparative table, the DPC-SMC control shows its superiority over the other techniques.

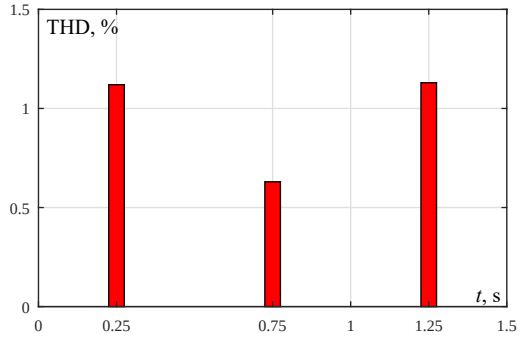

Fig. 18. THD of grid current

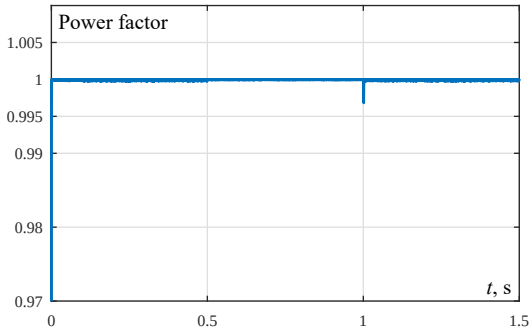

Fig. 19. Power factor

Conclusions.

In this paper, the classical direct power control has been combined with a sliding mode control to control active and reactive power and to ensure an accurate regulation of DC-link voltage. To eliminate the need for voltage sensors and to get the online variation of load resistance, sliding mode based observers have been designed for this purpose. Through a series of tests, especially in the presence of disturbances, it has been shown that:

1. The sliding mode offers a clear improvement to the DC-link voltage regulation regardless of the load profile.

2. The combination of the sliding mode approach with direct power control has eliminated the need for a switching table, thus reducing the control complexity.

3. High performance instantaneously decoupled power control achieved using a sliding mode control which provides a unity power factor.

4. The sliding mode-based grid voltage observer combined with the compensation algorithm provided accurate results with minimum chattering compared to the single low-pass filter case.

5. A good power quality is justified by a lower total harmonic distortion value.

6. The direct power control – sliding mode control gives better performance than conventional techniques with a total harmonic distortion value less than 5 % and a power factor close to unity.

Conflict of interest. The authors declare that they have no conflicts of interest.

REFERENCES

1. Bouafia A. *Techniques de commande prédictive et floue pour les systèmes électroniques de puissance : application aux redresseurs MLI*. Doctoral Thesis, University of Setif, Algeria, 2010. (Fra).

2. Bechouche A., Seddiki H., Abdeslam D.O., Rahoui A., Triki Y., Wira P. Predictive direct power control with virtual-flux estimation of three-phase PWM rectifiers under nonideal grid voltages. *2018 IEEE International Conference on Industrial Technology (ICIT)*, 2018, pp. 806-811. doi: https://doi.org/10.1109/ICIT.2018.8352281.

3. Bechouche A., Seddiki H., Abdeslam D.O., Mesbah K. Adaptive AC filter parameters identification for voltage-oriented control of three-phase voltage-source rectifiers. *International Journal of Modelling, Identification and Control*, 2015, vol. 24, no. 4, pp. 319-331. doi: https://doi.org/10.1504/IJMIC.2015.072985.

4. Bouafia A., Gaubert J.-P., Krim F. Predictive Direct Power Control of Three-Phase Pulsewidth Modulation (PWM) Rectifier Using Space-Vector Modulation (SVM). *IEEE Transactions on Power Electronics*, 2010, vol. 25, no. 1, pp. 228-236. doi: https://doi.org/10.1109/TPEL.2009.2028731.

5. Norniella J.G., Cano J.M., Orcajo G.A., Rojas C.H., Pedrayes J.F., Cabanas M.F., Melero M.G. Improving the Dynamics of Virtual-Flux-Based Control of Three-Phase Active Rectifiers. *IEEE Transactions on Industrial Electronics*, 2014, vol. 61, no. 1, pp. 177-187. doi: https://doi.org/10.1109/TIE.2013.2245614.

6. Rahoui A., Bechouche A., Seddiki H., Abdeslam D.O. Grid Voltages Estimation for Three-Phase PWM Rectifiers Control Without AC Voltage Sensors. *IEEE Transactions on Power Electronics*, 2018, vol. 33, no. 1, pp. 859-875. doi: https://doi.org/10.1109/TPEL.2017.2669146.

7. Friedli T., Hartmann M., Kolar J.W. The Essence of Three-Phase PFC Rectifier Systems – Part II. *IEEE Transactions on Power Electronics*, 2014, vol. 29, no. 2, pp. 543-560. doi: https://doi.org/10.1109/TPEL.2013.2258472.

8. Zhang Z., Xie Y., Le J., Chen L. Decoupled State-Feedback and Sliding-Mode Control for Three-Phase PWM Rectifier. *2009 Asia-Pacific Power and Energy Engineering Conference*, 2009, pp. 1-5. doi: https://doi.org/10.1109/APPEEC.2009.4918252.

9. Noguchi T., Tomiki H., Kondo S., Takahashi I. Direct power control of PWM converter without power-source voltage sensors. *IEEE Transactions on Industry Applications*, 1998, vol. 34, no. 3, pp. 473-479. doi: https://doi.org/10.1109/28.673716.

10. Barkat S., Tlemcani A., Nouri H. Direct power control of the PWM rectifier using sliding mode control. *International Journal of Power and Energy Conversion*, 2011, vol. 2, no. 4, pp. 289-306. doi: https://doi.org/10.1504/IJPEC.2011.041883.

11. Escobar G., Stankovic A.M., Carrasco J.M., Galvan E., Ortega R. Analysis and design of direct power control (DPC) for a three phase synchronous rectifier via output regulation subspaces. *IEEE Transactions on Power Electronics*, 2003, vol. 18, no. 3, pp. 823-830. doi: https://doi.org/10.1109/TPEL.2003.810862.

12. Vazquez S., Sanchez J.A., Carrasco J.M., Leon J.I., Galvan E. A Model-Based Direct Power Control for Three-Phase Power Converters. *IEEE Transactions on Industrial Electronics*, 2008, vol. 55, no. 4, pp. 1647-1657. doi: https://doi.org/10.1109/TIE.2008.917113.

13. Malinowski M., Kazmierkowski M.P., Hansen S., Blaabjerg F., Marques G.D. Virtual-flux-based direct power control of three-phase PWM rectifiers. *IEEE Transactions on Industry Applications*, 2001, vol. 37, no. 4, pp. 1019-1027. doi: https://doi.org/10.1109/28.936392.

14. Malinowski M., Jasinski M., Kazmierkowski M.P. Simple Direct Power Control of Three-Phase PWM Rectifier Using Space-Vector Modulation (DPC-SVM). *IEEE Transactions on Industrial Electronics*, 2004, vol. 51, no. 2, pp. 447-454. doi: https://doi.org/10.1109/TIE.2004.825278.

15. Cichowlas M., Malinowski M., Kazmierkowski M.P., Sobczuk D.L., Rodriguez P., Pou J. Active Filtering Function of Three-Phase PWM Boost Rectifier Under Different Line Voltage Conditions. *IEEE Transactions on Industrial Electronics*, 2005, vol. 52, no. 2, pp. 410-419. doi: https://doi.org/10.1109/TIE.2005.843915.

16. Antoniewicz P., Kazmierkowski M.P. Virtual-Flux-Based Predictive Direct Power Control of AC/DC Converters With Online Inductance Estimation. *IEEE Transactions on Industrial*

Electronics, 2008, vol. 55, no. 12, pp. 4381-4390. doi: https://doi.org/10.1109/TIE.2008.2007519.
17. Francis M. *Performance of Direct Power Controlled Grid-connected Voltage Source Converters*. Doctoral Thesis, University of Newcastle, England, 2017.
18. Bouraghda S., Sebaa K., Bechouat M., Sedraoui M. An improved sliding mode control for reduction of harmonic currents in grid system connected with a wind turbine equipped by a doubly-fed induction generator. *Electrical Engineering & Electromechanics*, 2022, no. 2, pp. 47-55. doi: https://doi.org/10.20998/2074-272X.2022.2.08.
19. Guezi A., Bendaikha A., Dendouga A. Direct torque control based on second order sliding mode controller for three-level inverter-fed permanent magnet synchronous motor: comparative study. *Electrical Engineering & Electromechanics*, 2022, no. 5, pp. 10-13. doi: https://doi.org/10.20998/2074-272X.2022.5.02.
20. Guo L., Li Y., Jin N., Dou Z., Wu J. Sliding mode observer-based AC voltage sensorless model predictive control for grid-connected inverters. *IET Power Electronics*, 2020, vol. 13, no. 10, pp. 2077-2085. doi: https://doi.org/10.1049/iet-pel.2019.1075.
21. Shtessel Y., Baev S., Biglari H. Unity Power Factor Control in Three-Phase AC/DC Boost Converter Using Sliding Modes. *IEEE Transactions on Industrial Electronics*, 2008, vol. 55, no. 11, pp. 3874-3882. doi: https://doi.org/10.1109/TIE.2008.2003203.
22. Edwards C., Spurgeon S. *Sliding Mode Control*. CRC Press, 1998. doi: https://doi.org/10.1201/9781498701822.
23. Utkin V., Gulder J., Shijun M. *Sliding Mode Control in Electromechanical Systems. 2nd ed.* New York, Taylor & Francis, 1999.
24. Lamterkati J., Khafallah M., Ouboubker L. A New DPC for Three-phase PWM rectifier with unity power factor operation. *International Journal of Advanced Research in Electrical, Electronics and Instrumentation Engineering*, 2014, vol. 3, no. 4, pp. 8273-8285.
25. Darshanam M.D., Hariharan D.R. Research on Three phase Voltage Source PWM Rectifier Based on Direct Current Control. *International Journal of Engineering and Advanced Technology*, 2019, vol. 9, no. 1, pp. 6864-6867. doi: https://doi.org/10.35940/ijeat.A2989.109119.

Received 11.09.2022
Accepted 21.12.2022
Published 07.03.2023

Djamel Sakri [1], *Doctor of Electrotechnical, Professor,*
Hichem Laib [1], *Doctor of Electrotechnical, Professor,*
Salah Eddine Farhi [1], *Doctor of Electrotechnical,*
Noureddine Golea [1], *Doctor of Electrotechnical, Professor,*
[1] Laboratory of Electrical Engineering and Automatic (LGEA), Larbi Ben M'hidi University Oum El Bouaghi, 04000, Algeria, e-mail: sk_djamel@yahoo.fr (Corresponding author), hichem_elt@yahoo.fr, salahfarhi04@gmail.com, nour_golea@yahoo.fr

How to cite this article:
Sakri D., Laib H., Farhi S.E., Golea N. Sliding mode approach for control and observation of a three phase AC-DC pulse-width modulation rectifier. *Electrical Engineering & Electromechanics*, 2023, no. 2, pp. 49-56. doi: https://doi.org/10.20998/2074-272X.2023.2.08

UDC 621.314 https://doi.org/10.20998/2074-272X.2023.2.09

R. Sindhuja, S. Padma

Bipolar DC output fed grounded DC-AC converter for photovoltaic application

Introduction. *In recent years the usage of electricity has increased tremendously as the electrical needs and loads got increased. Hence the researchers focused on the electricity generation from renewable sources in order to promote sustainable green environment. Owing to the lesser cost and more reliable high efficiency system with reduced use of equipments became prominent for the grid connected photovoltaic single phase systems. The* ***novelty*** *of this proposed converters are to reduce total power loss and to analyze the performance of the converter under various modulation index and to have lesser harmonics using sinusoidal pulse width modulation technique for both T-type and F-type inverter. Interest of the work is to merge two DC-DC converters which have same output voltage in order to have transformer less utilization of power. This has given pathway to develop a new DC-DC converter network by merging the common input nodes of CUK and SEPIC converter.* ***Purpose.*** *This similar structure of both converters made it easy to combine the input stages of and to get bipolar output.* ***Methods.*** *Here we can get bipolar output without the utilization of transformer which minimizes the overall size of the proposed system. In this paper, a combined CUK-SEPIC based grid connected transformerless inverter for photovoltaic application is suggested.* ***Results.*** *The suggested converter is simulated using MATLAB and the results were discussed. Further the circuit is extended with a 1 kW F-type inverter to demonstrate grid connection of the converter.* ***Practical value.*** *This converter can be implemented for photovoltaic applications for obtaining the bipolar DC output from the DC source.* References 16, table 4, figures 12.

Key words: **combined CUK-SEPIC converter, bipolar inverter, T-type inverter, F-type inverter, maximum power point tracking, transformerless inverter, single phase photovoltaic systems.**

Вступ. *В останні роки використання електроенергії значно зросло, оскільки потреби в електроенергії та навантаження збільшились. Тому дослідники зосередилися на виробництві електроенергії з відновлюваних джерел, щоб сприяти стійкому зеленому середовищу. Через меншу вартість та більш надійну високоефективну систему зі зменшеним використанням обладнання набули популярності фотоелектричні однофазні системи, підключені до мережі.* ***Новизна*** *пропонованих перетворювачів полягає у зниженні загальних втрат потужності та аналізі характеристик перетворювача при різних індексах модуляції, а також у зменшенні гармонік з використанням методу широтно-імпульсної модуляції синусоїдального типу для інверторів як Т-типу, так і F-типу. Інтерес роботи полягає в об'єднанні двох перетворювачів постійного струму з однаковою вихідною напругою, щоб мати менше використання потужності трансформатора. Це дозволило розробити нову мережу перетворювачів постійного струму шляхом об'єднання загальних вхідних вузлів перетворювача CUK та SEPIC.* ***Мета***. *Подібна структура обох перетворювачів дозволила легко поєднати вхідні каскади та отримати біполярний вихідний сигнал.* ***Методи***. *Тут ми можемо отримати біполярний вихід без використання трансформатора, що мінімізує загальний розмір пропонованої системи. У цій статті пропонується комбінований безтрансформаторний інвертор на основі CUK-SEPIC, підключений до мережі, для фотоелектричних застосувань.* ***Результати***. *Пропонований перетворювач моделюється за допомогою MATLAB, результати обговорюються. Далі схема розширена інвертором F-типу потужністю 1 кВт, щоб продемонструвати підключення перетворювача до мережі.* ***Практична цінність***. *Цей перетворювач може бути реалізований для фотоелектричних застосувань для отримання біполярного виходу постійного струму джерела постійного струму.* Бібл. 16, табл. 4, рис. 12.

Ключові слова: **комбінований перетворювач CUK-SEPIC, біполярний інвертор, інвертор Т-типу, інвертор F-типу, відстеження точки максимальної потужності, безтрансформаторний інвертор, однофазні фотоелектричні системи.**

Introduction.

A. DC-DC converters for photovoltaic application. Solar photovoltaic (PV) systems started ruling the recent era of power generation as its renewable and widely available resource. Hence the research started on that topic to increase the utilization of solar energy in an efficient way, which has given rise to wide varieties of DC-DC converter. Since the output whence the solar PV cell is DC we need to integrate the photovoltaic system with an efficient DC-DC converter topology. The non-isolated topology of DC-DC converter is of copious types [1]. The differentiation of copious DC-DC converter is presented in Table 1, which explains the count of devices used and expression for output voltage along with nature of output whether unipolar or bipolar.

Table 1

Commonly used DC-DC converter

Converter	Voltage output	Input current	Voltage gain	No. of switches	No. of diodes	No. of inductors	No. of capacitors
Buck	Unipolar	Intermittent	D	1	1	1	1
Boost	Unipolar	Uninterrupted	$1/(1–D)$	1	1	1	1
Buck-Boost converter	Unipolar	Intermittent	$D/(1–D)$	1	1	1	1
CUK	Unipolar	Uninterrupted	$–D/(1–D)$	1	1	2	2
SEPIC	Unipolar	Uninterrupted	$D/(1–D)$	1	1	2	2
Combined Charging System	Bipolar	Uninterrupted	$2D/(1–D)$	1	2	3	4

The major building block of PV application is the DC-DC converter hence the proper choice of DC-DC converter is much needed for efficient utilization of resource. In PV applications, boost converters are widely employed for DC-DC conversion, but only with stepping-up voltages ratios [2-4]. Both the increased and decreased voltage conversion are feasible with the buck-boost converter but the main drawback is the discontinuous input current which stops the converter from optimal tracking of maximum power point tracking (MPPT) without decoupling capacitor [5]. The output voltage expression of CUK and SEPIC converter both are same but the only difference between them is the reversal of

current. The input current in both these converter is continuous and have wide range of operating voltage in it. The main losses associated with DC-DC converters are losses associated with switches, inductor winding loss, diode conduction loss and inductor core loss. The minimization of the leakage current has been the main drawback in transformerless topology [6-9]. The proposed converter also has same number of switches like other DC-DC converter and in addition we can achieve a bipolar output from it with reduced current ripple [9]. The nature of high input current ripple limits the performance of MPPT. In order to enhance the PV system efficiency the input current ripple has to be minimized by using suitable modulation technique [10, 11]. The proposed converter reduces peak inductor current by minimizing input current ripple. This keeps the PV system to operate near MPP thereby improving the total power extracted.

B. Configuration of PV system. Generally PV systems are used for configuring with the single phase AC grids with earth connection. Apart from the voltage boost or buck capability offered by the various DC-DC converters the main factor to be considered is the impact of the leakage current. There are various inverters out of which the H-bridge inverter which has been used widely introduces leakage current to pass through the PV panel parasitic capacitance [10, 11] as shown in Fig 1,*a*.

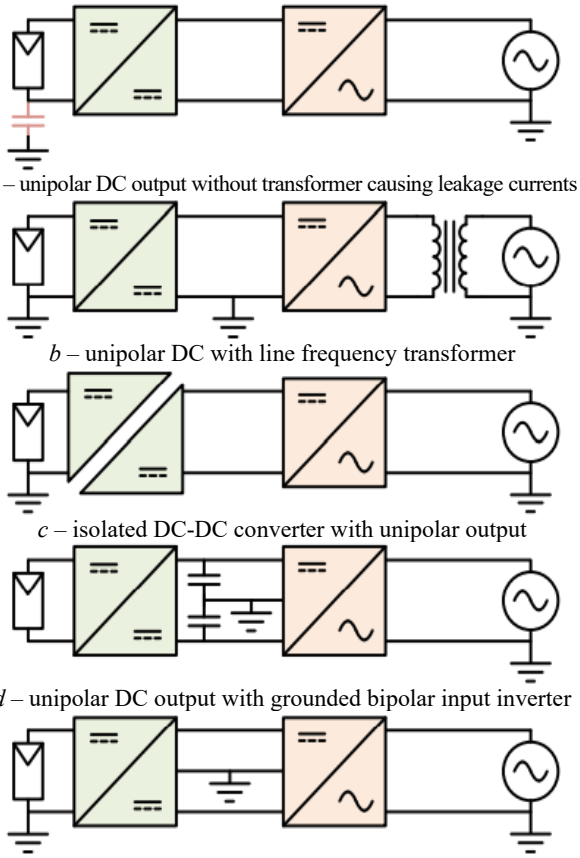

a – unipolar DC output without transformer causing leakage currents

b – unipolar DC with line frequency transformer

c – isolated DC-DC converter with unipolar output

d – unipolar DC output with grounded bipolar input inverter

e – bipolar DC output with grounded bipolar input inverter

Fig. 1. Variety of grounding choices for PV systems

This leakage current problem can be mitigated easily using a transformer operating at line frequency between the PV system and grid in order to provide ground connection as shown in Fig. 1,*b*, but the main drawback with this method is that the system becomes bulky, costly and heavy [12]. Hence this problem is met by utilizing the concept of isolated DC-DC converter topology as shown in Fig. 1,*c* but the drawback over here is it provides the unipolar output. This condition can be met by introducing a grounded bipolar input inverter as shown in Fig. 1,*d*. It makes no difference whether a low- or high-frequency transformer is used, topologies without owing transformer are having more efficiency, lighter in weight, and less expensive than isolated inverters. However, by making use of non-isolated PV inverters, ground leakage currents because of parasitic capacitance are a major concern [13]. The decoupling method will tend to boost the efficiency of systems by chopping the complexity and losses of the system. In view to eliminate the decoupling issues and to eliminate the usage of transformer the alternate solution is the use of an inverter with the grounded bipolar DC output. The configuration as shown in Fig. 1,*e* eliminates all the problems discussed above and mitigate the leakage current issues without the use of transformer. Hence the system becomes less complex and more reliable. This DC output has to be fed with DC-AC converter for which many inverters are available. To have lesser harmonics cascaded multilevel inverters can be utilized [14]. But main drawback is the need of bipolar inverter [15].

C. Proposed CUK-SEPIC converter. The suggested converter used the benefits of both CUK and SEPIC converter in order to produce a bipolar output. The proposed CUK-SEPIC converter has been in investigation recently and it's found to be the best solution for a reliable and efficient PV systems. Since, both the CUK and the SEPIC converter's input stages are same it made an idea to combine both the converters input stage. Thus by having the common input switching stages both the converters is connected. Since the voltage expression for the output is same in case of CUK and SEPIC it paved a way of generating DC bus. Since the polarity of output is reversed in CUK and SEPIC the SEPIC produce a positive voltage bus and CUK produces a negative voltage bus and both are of same magnitude. As a result, the output generates a bipolar DC bus. The configuration of this proposed combination of CUK-SEPIC converter is shown in Fig. 2,*a*. The suggested structure has the one single common switching node.

When the switch is turned on in the manner depicted in Fig. 2,*b* the inductors present in the circuit L_{in}, L_s and L_c will be in charging state whereas the capacitors C_s and C_c discharges and the direction of the current will be as shown in the Fig. 2,*b*. During the turn off of the switch the vice versa will happen. The inductors present in the circuit L_{in}, L_s and L_c will be in discharging state whereas the capacitors C_s and C_c starts charging and the direction of the current will be as shown in the Fig. 2,*c*.

The proposed converter is having ability of providing both enlarged and reduced voltage ratios since the gain when it comes to voltage is $2D/(1–D)$. This implies that if the duty ratio (D) which is the proportion of switch turn on time to complete time period is less than 0.5 the suggested converter operates in step down or buck mode and if the duty ratio (D) is greater than 0.5 then the suggested converter will operate in the step-up or buck mode of operation. Thereby achieving an output voltage in wide range is possible to get achieved using this proposed combination of CUK and SEPIC converter. As we take into account the output voltage gain

across both converter together, the voltage gain will be $2D/(1–D)$ which regulates wide variation in input voltages. In reality, the capacitor of enough capacitance should be connected before coupling with inverter in order to decouple the PV array from the 100 Hz ripple, allowing for continuous power output and keeping the PV panel operating at its MPP.

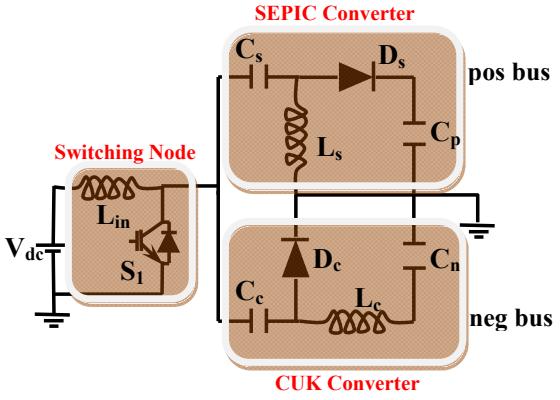

a – proposed CUK-SEPIC converter topology

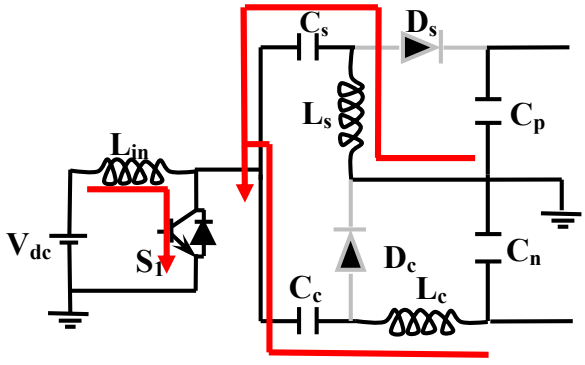

b – proposed CUK-SEPIC converter during ON state

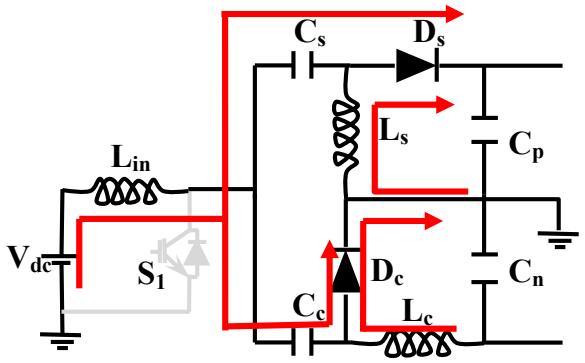

c – proposed CUK-SEPIC converter topology during OFF state

Fig. 2.

Bipolar inverter grid integrated with PV solar.

A. MPPT. The prerequisite of the input current of the converter, which controls the output current of the PV system and hence power, is explained by the *P-V* and *I-V* curves [1]. In order to make the maximum power and for the purpose to handle system efficiently and effectively we need to steer the PV panel at its optimum operating point. There are several algorithms which helps us to operate the panel at its MPP which makes system efficient one. The Perturb and Observe (P&O) algorithm is used here. The flowchart of the P&O algorithm is as shown in the Fig. 3. The MPPT controller sends an updated reference value to a PI current controller, which receives it. In most cases, the MPPT's reference would vary smoothly [1].

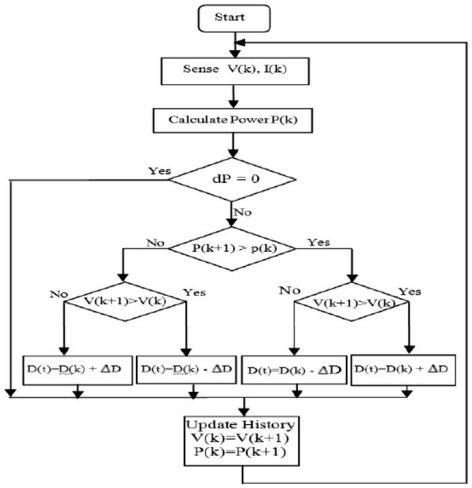

Fig. 3. Flowchart of P&O algorithm

B. Bipolar T-type inverter. As we need to export this DC into the grid we need to integrate our system with an inverter configuration for converting DC power from the solar panel into AC power. Inverters can be of unipolar DC input type or bipolar DC input type. The main disadvantage of the unipolar type is that it cannot provide the leakage current elimination. Hence we need to opt for the bipolar DC input structure type inverter. The bipolar inverter likes half bridge inverter, T-type inverter, flying capacitor/capacitor-clamped inverter [1]. In this paper we have simulated for T-type inverter. The pattern in which switches need to be triggered is shown in Table 2.

Table 2

T-type inverter switching states

State	V_{out}	S_1	S_2	S_3	S_4
P	$+V_{DC}/2$	1	1	0	0
0	0	0	1	1	0
N	$-V_{DC}/2$	0	0	1	1

The overall converter composition is as shown in the Fig. 3. The converter is designed as per the specification given in Table 3. The main drawback in T-type inverter is increased voltage stress across the switches.

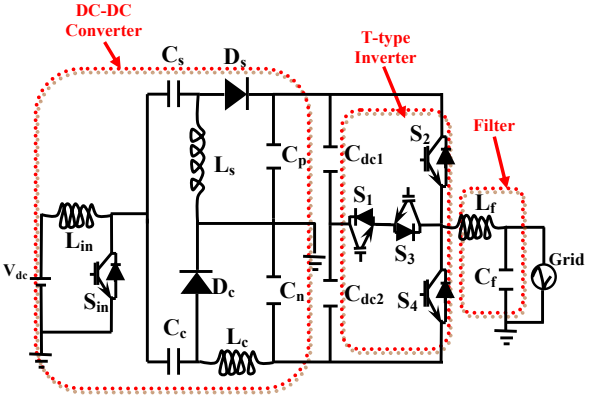

Fig. 4. Overall proposed system with T-type inverter

Table 3

Converter specification

Component	Values	Component	Values	Component	Values
L_{in}	545 μH	C_p	5 μF	L_c	891 μH
C_s	1.5 μF	C_n	0.33 μF	L_f	330 μH
C_c	0.47 μF	L_s	891 μH	C_f	1 μF

C. Bipolar F-type inverter. Figure 5 depicts the F-type inverter's phase-leg power circuit. It is a topologically

modified T-type inverter circuit in which the bidirectional switch's common-emitter node is explored in order to reduce voltage stress in the forming power switches. It operates in the same way as its neutral point clamped. As a result, it can generate three output voltages with reference to the neutral-point n: $0.5 \cdot V_{dc}$, $0 \cdot V_{dc}$, and $-0.5 \cdot V_{dc}$ [16]. Table 4 shows the switching states of the power switches as well as the generated inverter output voltages. The letters P, O, and N in this table reflect the inverter's positive, zero, and negative voltage states, respectively. The logic states 1 and 0 indicate the ON and OFF switching states of the power switches, respectively.

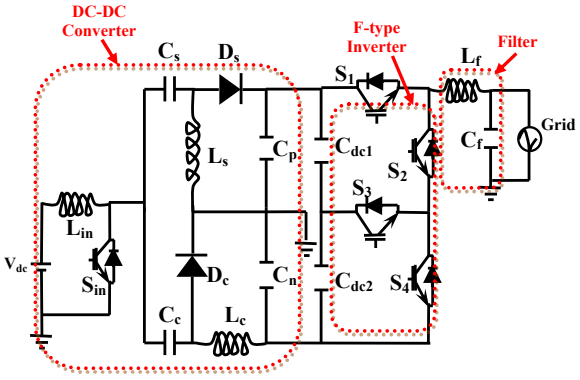

Fig. 5. Overall proposed system with F-type inverter

Table 4

The F-type inverter switching states

State	V_{out}	S_1	S_2	S_3	S_4
P	$+V_{DC}/2$	1	0	1	0
0	0	0	1	1	0
N	$-V_{DC}/2$	0	1	0	1

D. Sinusoidal pulse width modulation (SPWM) technique. SPWM is a phase modulation technology that uses an inverter phase-leg based operational basis to generate gating signals. The phase angle shift is the only control parameter that differs. Its expansion to a multiphase multilevel system provides minimal computational problems when compared to space vector modulation. When pure sinusoidal references are used in the modulation process, the SPWM approach has the drawback of underutilizing the dc-link voltage in power converters. One strategy for extending the modulation index range in the linear modulation area beyond unity with SPWM is to add the zero-sequence component in accordance with the min–max function principle.

E. Estimation of power loss. Because it has a direct impact on the converter's efficiency, the converter's loss calculation is an important factor for assessing its performance. Conduction and switching losses are the two most typical types of losses in a converter. The conduction current, $i(t)$, and the turn-on resistance, R_S and R_D, where S and D stand for switch and diode, respectively, are linked to conduction losses. Because a switch consists of both a transistor and an anti-parallel diode, both are considered for computing losses. Both of these are calculated as follows:

$$P_{con(S)}(t) = [V_s + R_s I \wedge \beta(t)] \cdot I(t); \quad (1)$$

$$P_{con(D)}(t) = [V_D + R_D I \wedge \beta(t)] \cdot I(t), \quad (2)$$

where specification can be found in the Datasheet.

The sum of (1) and (2) is the overall conduction losses of a switch. The number of transistors (N_S) and diodes (N_D) that conduct instantly determine the average conduction loss of a converter.

The quantity of energy dissipated during each phase determines the switching losses, which are classified into two categories: turn-off losses and turn-on losses. The following formula (3) and (4) is used to calculate these losses:

$$E_{off(S)} = \int_0^{t_{off}} v(t) \cdot i(t) \mathrm{d}t; \quad (3)$$

$$E_{on(S)} = \int_0^{t_{on}} v(t) \cdot i(t) \mathrm{d}t. \quad (3)$$

During the turn-on and turn-off times, energy is lost across each switch. Energy lost across s^{th} switch are $E_{off,\,s}$ and $E_{on,s}$, respectively. And t_{off} and t_{on} represent the time it takes for the switch to turn on and off, respectively, while t represents the period. The power loss is calculated for various modulation indexes and shown in Fig. 6. It is clear from Fig. 7 that the losses in F-type converter are less compared to T-type inverter.

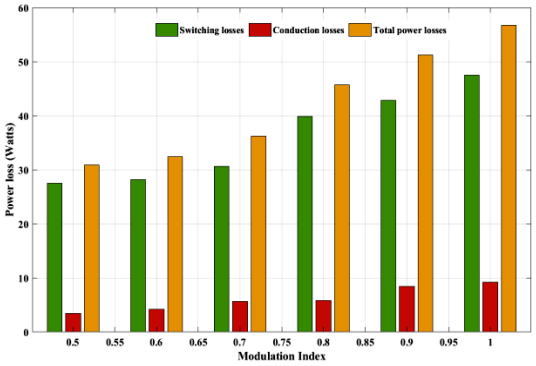

Fig. 6. Power loss for varying modulation index

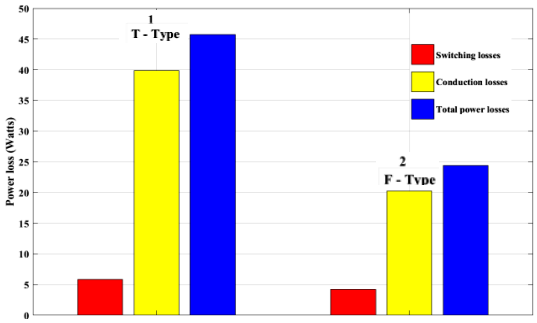

Fig. 7. Total power loss for T-type and F-type configuration

F. Simulation results. The proposed CUK-SEPIC converter is combined with the bipolar F-type inverter in place to analyze the waveform and its operation. The converter's DC input is supplied by a solar PV panel, which is then monitored by an MPPT controller. The P&O algorithm is used in the MPPT controller and simulated. The LC filter is been chosen for this purpose. The converter utilizes a decoupling capacitor of 100 µF in order to remove the 100 Hz ripple in the system. A 1 kW F-type inverter has been designed to serve this proposed DC-DC converter [1]. The switching frequency is around 100 kHz, and the rated input voltage is 360 V DC. The suggested converter can achieve a wide variation in the output voltages gain of the converter. It can dispense both expanded and shrunken voltage ranges. The complete setup of the network is shown in Fig. 8.

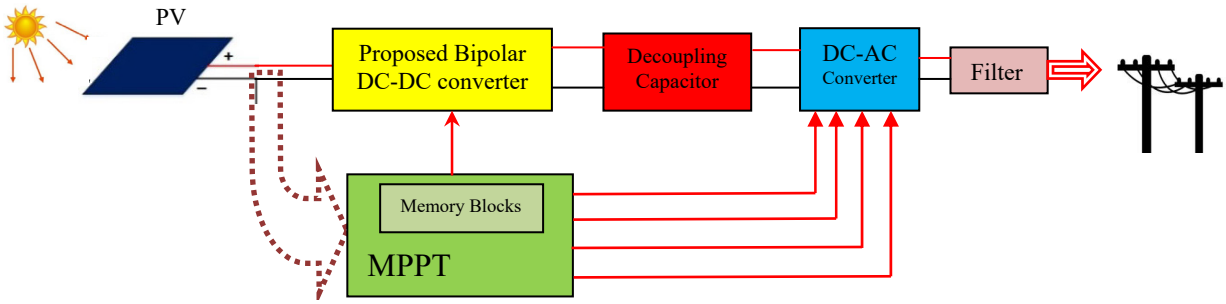

Fig. 8. Overall system of proposed network

The common switching node at the input side provides the possibility of bipolar output at the DC-DC converter side. Figure 9,*a* shows the switching current waveform in the common input node. The CUK converter provides the negative output and the SEPIC converter provides the positive output this necessitates the possibility of occurrence of bipolar DC bus. Figures 9,*b*,*c* depict the current through L_C and L_S. Figures 9,*d*,*e* show the current obtained through the positive and negative bus.

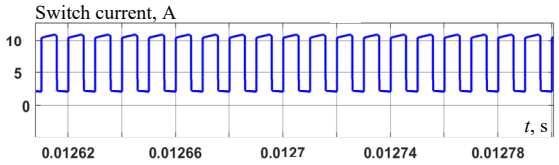

a – common node switching current

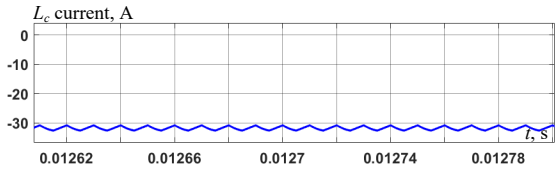

b – current through CUK side inductor

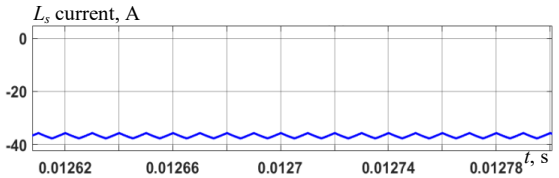

c – current through SEPIC side inductor

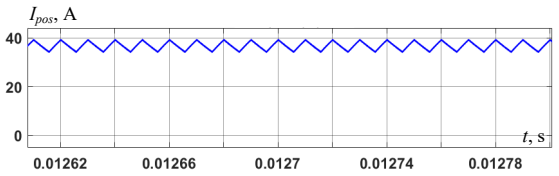

d – current through positive bus

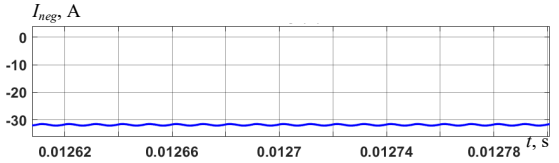

e – current through negative bus

Fig. 9

Figure 10 represents the bipolar DC voltage obtained at the result of the above said converter.

The overall system topology of integrated proposed CUK-SEPIC converter with MPPT controller connected with the bipolar F-type inverter is illustrated in Fig. 5. The following circuit was built, simulated and the results were obtained using MATLAB. Figure 11 depicts the output voltage and current waveforms obtained across the inverter output. In order to visualize the output waveform *R* load is considered as 100 Ω.

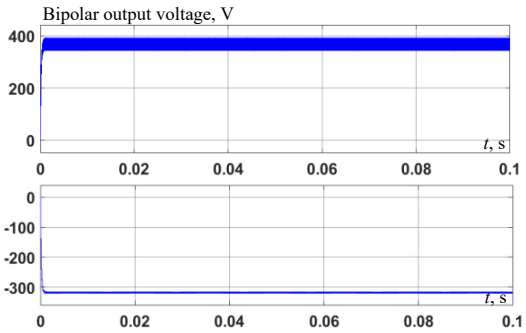

Fig. 10. Bipolar DC bus voltage

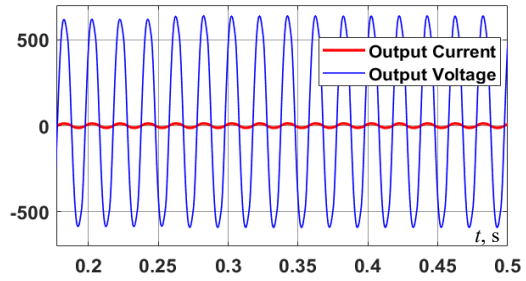

Fig. 11. AC grid output voltage and current

The overall system topology of hardware setup with PV integrated proposed CUK-SEPIC converter with MPPT controller connected with the bipolar F-type inverter is illustrated in Fig. 8 and the developed module in MATLAB/Simulink environment is depicted in Fig. 12 which has CUK-SEPIC converter fed DC-AC inverter.

Conclusions. The similarity in the structure of the CUK and SEPIC converters' input stages made the development of this proposed converter with the single common switching node and as the CUK converter imparts the negative voltage and the SEPIC converter imparts the positive voltage and both the voltage is of same magnitude which added advantage of obtaining the bipolar DC voltage at the terminal of the DC-DC converter. The transformerless utilization of this converter paves the way of lesser cost and complexity. Because of the bipolar inverter utilised in the circuit, the converter's input current ripple is reduced and leakage current is removed. When compared to T-type converter the F-type converter, F-type converter reduces the total conduction losses by 47.8 %. Thus F-type inverter produces lesser switching and conduction losses paying the way for the better efficient inverter topology.

Conflict of interest. The authors declare that they have no conflicts of interest.

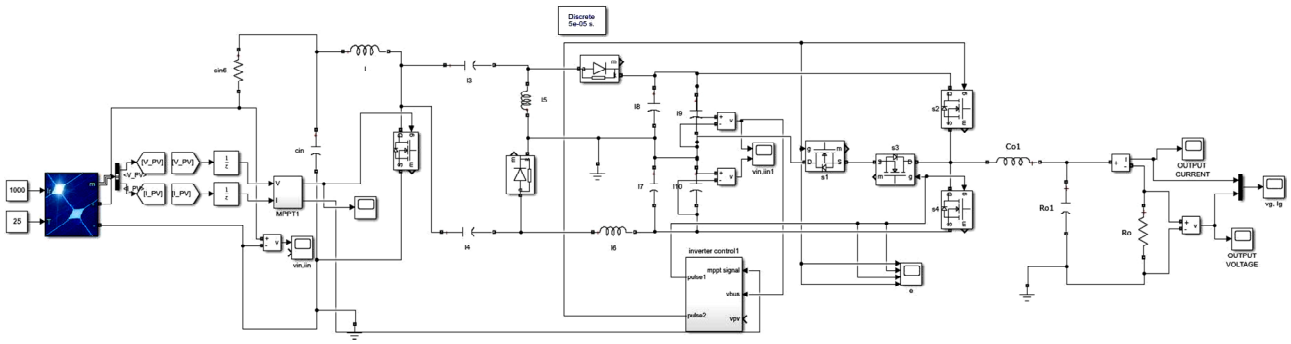

Fig. 12. Overall system of proposed network

REFERENCES

1. Parimalasundar E., Senthil Kumar R., Chandrika V.S., Suresh K. Fault diagnosis in a five-level multilevel inverter using an artificial neural network approach. *Electrical Engineering & Electromechanics*, 2023, no. 1, pp. 31-39. doi: https://doi.org/10.20998/2074-272X.2023.1.05

2. Meneses D., Blaabjerg F., Garcia O., Cobos J.A. Review and Comparison of Step-Up Transformerless Topologies for Photovoltaic AC-Module Application. *IEEE Transactions on Power Electronics*, 2013, vol. 28, no. 6, pp. 2649-2663. doi: https://doi.org/10.1109/TPEL.2012.2227820.

3. Parimalasundar E., Kumar N.M.G., Geetha P., Suresh K. Performance investigation of modular multilevel inverter topologies for photovoltaic applications with minimal switches. *Electrical Engineering & Electromechanics*, 2022, no. 6, pp. 28-34. doi: https://doi.org/10.20998/2074-272X.2022.6.05.

4. Maalandish M., Hosseini S.H., Jalilzadeh T. High step-up dc/dc converter using switch-capacitor techniques and lower losses for renewable energy applications. *IET Power Electronics*, 2018, vol. 11, no. 10, pp. 1718-1729. doi: https://doi.org/10.1049/iet-pel.2017.0752.

5. Banaei M.R., Bonab H.A.F. A Novel Structure for Single-Switch Nonisolated Transformerless Buck–Boost DC–DC Converter. *IEEE Transactions on Industrial Electronics*, 2017, vol. 64, no. 1, pp. 198-205. doi: https://doi.org/10.1109/TIE.2016.2608321.

6. Suresh K., Parimalasundar E. Design and Implementation of Universal Converter. *IEEE Canadian Journal of Electrical and Computer Engineering*, 2022, vol. 45, no. 3, pp. 272-278. doi: https://doi.org/10.1109/ICJECE.2022.3166240.

7. Calais M., Agelidis V.G. Multilevel converters for single-phase grid connected photovoltaic systems-an overview. *IEEE International Symposium on Industrial Electronics. Proceedings. ISIE'98 (Cat. No.98TH8357)*, 1998, vol. 1, pp. 224-229. doi: https://doi.org/10.1109/ISIE.1998.707781.

8. Suresh K., Parimalasundar E. A novel dual-leg DC-DC converter for wide range DC-AC conversion. *Automatika*, 2022, vol. 63, no. 3, pp. 572-579. doi: https://doi.org/10.1080/00051144.2022.2056809.

9. Sonti V., Jain S., Bhattacharya S. Analysis of the Modulation Strategy for the Minimization of the Leakage Current in the PV Grid-Connected Cascaded Multilevel Inverter. *IEEE Transactions on Power Electronics*, 2017, vol. 32, no. 2, pp. 1156-1169. doi: https://doi.org/10.1109/TPEL.2016.2550206.

10. Ferrera M.B., Litran S.P., Duran E., Andujar J.M. A SEPIC-Cuk converter combination for bipolar DC microgrid applications. *2015 IEEE International Conference on Industrial Technology (ICIT)*, 2015, pp. 884-889. doi: https://doi.org/10.1109/ICIT.2015.7125209.

11. Anurag A., Deshmukh N., Maguluri A., Anand S. Integrated DC–DC Converter Based Grid-Connected Transformerless Photovoltaic Inverter With Extended Input Voltage Range. *IEEE Transactions on Power Electronics*, 2018, vol. 33, no. 10, pp. 8322-8330. doi: https://doi.org/10.1109/TPEL.2017.2779144.

12. Siwakoti Y.P., Blaabjerg F. Common-Ground-Type Transformerless Inverters for Single-Phase Solar Photovoltaic Systems. *IEEE Transactions on Industrial Electronics*, 2018, vol. 65, no. 3, pp. 2100-2111. doi: https://doi.org/10.1109/TIE.2017.2740821.

13. Sabry A., Mohammed Z. M., Nordin F.H., Nik Ali N.H., Al-Ogaili A.S. Single-Phase Grid-Tied Transformerless Inverter of Zero Leakage Current for PV System. *IEEE Access*, 2020, vol. 8, pp. 4361-4371. doi: https://doi.org/10.1109/ACCESS.2019.2963284.

14. Siddique M.D., Mekhilef S., Shah N.M., Memon M.A. Optimal Design of a New Cascaded Multilevel Inverter Topology With Reduced Switch Count. *IEEE Access*, 2019, vol. 7, pp. 24498-24510. doi: https://doi.org/10.1109/ACCESS.2019.2890872.

15. Kumar K.V., Kumar R.S. Analysis of Logic Gates for Generation of Switching Sequence in Symmetric and Asymmetric Reduced Switch Multilevel Inverter. *IEEE Access*, 2019, vol. 7, pp. 97719-97731. doi: https://doi.org/10.1109/ACCESS.2019.2929836.

16. Odeh C., Lewicki A., Morawiec M., Kondratenko D. Three-Level F-Type Inverter. *IEEE Transactions on Power Electronics*, 2021, vol. 36, no. 10, pp. 11265-11275. doi: https://doi.org/10.1109/TPEL.2021.3071359.

Received 12.09.2022
Accepted 20.12.2022
Published 07.03.2023

R. Sindhuja[1], *Research Scholar*,
S. Padma[1], *Associate Professor*,
[1] Department of Electrical Engineering,
Faculty of Engineering and Technology,
Annamalai University,
Chidambaram, Tamil Nadu, 608002, India,
e-mail: sindhuja.gct@gmail.com (Corresponding Author);
spadmapnr@gmail.com

How to cite this article:
Sindhuja R., Padma S. Bipolar DC output fed grounded DC-AC converter for photovoltaic application. *Electrical Engineering & Electromechanics*, 2023, no. 2, pp. 57-62. doi: https://doi.org/10.20998/2074-272X.2023.2.09

UDC 621.3 https://doi.org/10.20998/2074-272X.2023.2.10

A. Jani, V.H. Makwana

Modified discrete Fourier transform algorithm for protection of shunt compensated distribution line

Introduction. *The response time of the relay plays vital role when fault occurs on the line. Various algorithms are adopted to increase the sampling rate of the relay which, in turn, improves the response time.* ***Methods****. Discrete Fourier transform and modified discrete Fourier transform are the two algorithms used to calculate the fundamental frequency phasor of the signal required by the relay to initiate trip command. It is known that discrete Fourier transform takes four to five cycles to produce the fundamental frequency phasor but it fails to deal with the decaying DC component. On the other hand, modified discrete Fourier transform improves the response time by removing the decaying DC component along with the other harmonics in just one cycle and a few samples. The* ***aim*** *of this paper is to cover discrete Fourier transform and modified discrete Fourier transform algorithms to analyze the performance of the three overcurrent and one earth fault relaying scheme for different types of faults occurring in the distribution system.* ***Methodology****. The concept of three overcurrent and one earth fault scheme is also explained in this paper for protection of shunt-compensated distribution system. The scheme is designed for variable power factor. MATLAB/Simulink is used as the software tool to validate the results obtained for various types of faults occurring in the system. The* ***results*** *are represented graphically to illustrate the time of response of the protection scheme when shunt compensators are connected at the receiving end of distribution network.* References 16, tables 2, figures 8.

Key words: **modified discrete Fourier transform, three overcurrent and one earth fault protection scheme, shunt compensation, distribution system, response time of relay.**

Вступ*. Час спрацювання реле відіграє життєво важливу роль при виникненні несправності на лінії. Для збільшення частоти дискретизації реле застосовуються різні алгоритми, що, своєю чергою, покращує час спрацювання.* ***Методи****. Дискретне перетворення Фур'є та модифіковане дискретне перетворення Фур'є – це два алгоритми, які використовуються для розрахунку вектора основної частоти сигналу, необхідного для реле подачі команди на відключення. Відомо, що для отримання вектора основної частоти дискретного перетворення Фур'є потрібно від чотирьох до п'яти циклів, але воно не справляється з постійною складовою струму, що згасає. З іншого боку, модифіковане дискретне перетворення Фур'є покращує час спрацювання, видаляючи постійну складову струму, що згасає, разом з іншими гармоніками всього за один цикл і кілька вибірок.* ***Мета*** *цієї статті полягає в тому, щоб охопити алгоритми дискретного перетворення Фур'є та модифікованого дискретного перетворення Фур'є для аналізу характеристик трьох схем реле максимального струму та однієї схеми захисту від замикань на землю для різних типів несправностей, що виникають у розподільчій системі.* ***Методологія****. У статті пояснюється також концепція трьох схем перевантаження по струму і однієї схеми замикання на землю для захисту розподільчої системи з паралельною компенсацією. Схема розрахована на змінний коефіцієнт потужності. MATLAB/Simulink використовується як програмний інструмент для перевірки результатів, отриманих для різних типів відмов, що виникають у системі.* ***Результати*** *представлені графічно, щоб проілюструвати час спрацьовування схеми захисту, коли шунтуючі компенсатори підключені на приймальному кінці розподільної мережі.* Бібл. 16, табл. 2, рис. 8.

Ключові слова: **модифіковане дискретне перетворення Фур'є, три схеми максимального струмового захисту та одна схема захисту від замикань на землю, паралельна компенсація, розподільна система, час спрацювання реле.**

Introduction. Protection of distribution system is the most vulnerable part of the power system protection because it often encounters severe dynamic changes due to change in line loading and uncertainty in power factor [1, 2]. Further, the severity intensifies under abnormal conditions like faults occurring in the network. Such changes are generally dealt with the use of reactive power compensators in the line, which possess controllers and power electronic components [3]. The presence of compensators introduces error in the measurement of fault and system parameters [4, 5]. Hence, the protection scheme needs to be fast and sensitive enough to operate efficiently under all these conditions.

Variation in line loading in distribution network is a major challenge for a relay present at receiving end of the line [5]. Generally, the distribution network is protected by overcurrent and earth-fault relays in the first zone of protection. The most common type of protection scheme used for distribution lines is three overcurrent and one earth-fault (3 O/C & 1 E/F) protection scheme [6]. The protection devices have to be selected carefully and must comply with consonant standards as far as industrial and commercial loads are considered. The presence of distributed generation, for example, may lead to additional challenges to be faced by the relay, where the power flows in both the ways. Such situations demand dynamic settings of the relay, as illustrated in [2].

The time of response of the protection algorithm decides the sensitivity of the relay, which needs to be as high as possible [7]. Earlier the researchers used to apply mimic filters and other such digital filtering techniques in order to damp out the decaying DC component from the current signal required by the relay [7, 8]. Though, due to the disadvantages of these filters, the researchers developed Discrete Fourier Transform (DFT) algorithm to obtain the fundamental component of line current to be fed to the relay [9]. The DFT algorithm usually takes a few cycles to serve the required purpose which makes the protection algorithm slow and erroneous. Thus, Modified Discrete Fourier Transform (MDFT) was proposed in [7, 8] which is capable to produce the fundamental component of current in one cycle and a few samples, thereby, decreasing the response time of the relay.

A number of researchers have proposed optimal techniques of relay coordination using various types of overcurrent relays [1, 3, 10]. Since this paper is designed for education purpose, it covers the basic concepts of shunt compensation and overcurrent protection. The focus of this paper is to illustrate the performance of 3 O/C & 1 E/F protection scheme under different fault conditions, considering the shunt compensators such as Fixed Capacitor Thyristor Controlled Reactor (FCTCR) and Distributed Static Synchronous Compensator (DSTATCOM). The results are obtained using both, DFT and MDFT, algorithms and the comparison between the two algorithms is also explained in the sections below.

Protection of distribution line using overcurrent relay. Overcurrent is defined as very high current flowing

through the line during any fault or abnormal conditions. An overcurrent relay is set to operate when the line current exceeds the threshold limit of the current, called plug setting of the relay. The family of overcurrent relays includes instantaneous, time-delayed, definite time and inverse time overcurrent relays. Inverse-time relays are further classified as normal-inverse, very-inverse, and extremely-inverse.

Instantaneous relays operate within 1-2 cycles when fault occurs in the network. It is generally set to provide protection against short circuit, and hence, it is set for very high values of rated current (may be five times of rated current). Time-delayed relays are used to achieve the features of back-up protection and selectivity in relays.

Definite time relay is set to operate after a definite set time when the current exceeds the pick-up value. The pick-up setting of this relay is generally between 50 to 200 % of rated relay current and these relays are used to protect the radial feeders. In inverse-time overcurrent relays, the operating time of the relay is inversely proportional to the relay current. They are broadly categorized as phase-fault relays and earth-fault relays. For phase relays, the relay setting range is 50-200 % of rated relay current. Earth-fault relays are installed in order to sense the sensitive ground faults, having setting range 5-20 %, 10-40 % or 20-80 % of current transformer (CT) secondary rating, depending upon the sensitivity of the relay required. The generalized relation to define a standard overcurrent relay, given in (1), is written as:

$$t = \frac{\beta}{(PSM)^{\alpha} - 1} \cdot TMS, \qquad (1)$$

where t is the time of operation of relay; PSM is the plug setting multiplier of relay; TMS is the time multiplier setting of the relay. The constants α and β are selected according to the Table 1 for various characteristics [6].

Table 1

Value of α and β for different inverse-time relays

Relay	α	β
Normal inverse	0.02	0.14
Very inverse	1	13.5
Extremely inverse	2	80

Figure 1 shows the operating characteristics of different overcurrent relays discussed in this section.

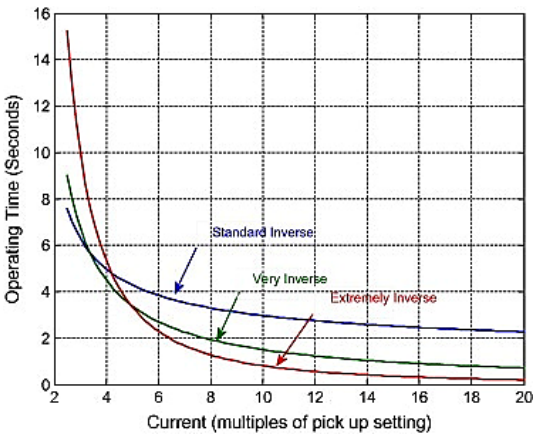

Fig. 1. Characteristics of different types of overcurrent relays

Three overcurrent and one earth-fault relaying scheme. Figure 2 illustrates the schematic diagram of the protection scheme used in this paper to demonstrate the protection of shunt compensated distribution line [6].

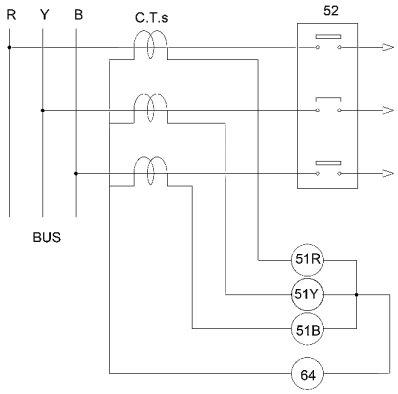

Fig. 2. Schematic diagram of 3 O/C & 1 E/F relaying scheme

In this figure, 51, 52 and 64 denote the international codes used for drawing the protection circuits. 51R, 51Y, 51B stands for overcurrent relays connected in R, Y and B phases of the line, respectively. Further, 52 stands for circuit breaker and 64 stands for earth-fault relay.

The relays used in this paper are set according to the above discussion. When phase faults occur in the line (R-Y, Y-B, R-B, R-Y-B), at least one of the three overcurrent relays shall sense the fault and operate according to the relay settings, following the set characteristics. In the case of phase-to-ground fault (R-g, Y-g, B-g), the residual current follows the path of earth-fault relay, which operates as per the relay settings. However, for double line-to-ground faults (R-Y-g, Y-B-g, R-B-g), both the phase overcurrent relays and the earth-fault relay will sense the fault and operate simultaneously.

Figure 3 describes the flowchart of the relay operation.

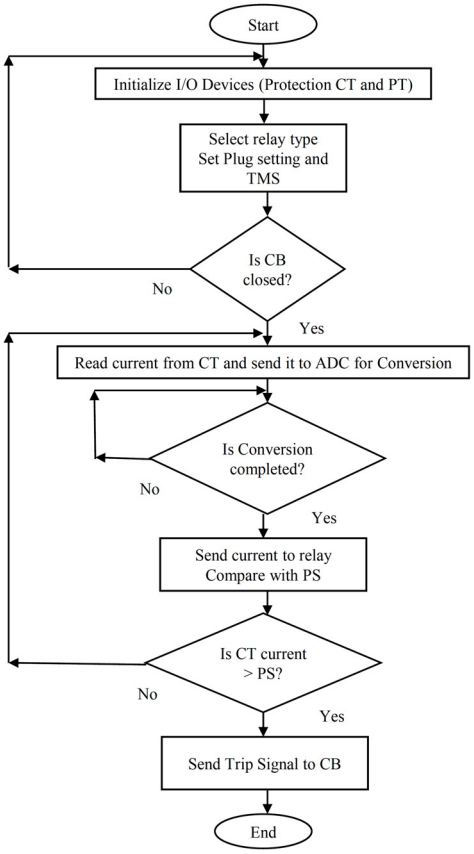

Fig. 3. Flowchart of relay operation

The line parameters are measured at regular intervals using protective current and potential transformers (CTs and PTs). These parameters are then given to the relay as input, where the input signal is first compared with the plug setting of the relay. If the measured current exceeds the set current, then trip signal is generated using mathematical and logical units; otherwise, uninterrupted supply is continued to be supplied to the line.

Protection of shunt compensated distribution line. Figure 4 shows the block diagram of the distribution network protected by 3 O/C & 1 E/F relaying scheme. For MATLAB simulation, 11 kV, 50 Hz radial distribution network, feeding a three-phase load, is considered in this paper. The parameter measurement block measures line current and sends it to the relay logic block. The relay logic block having 3 O/C & 1 E/F relaying logic (as shown in Fig. 3), sends trip signal to the circuit breaker under fault or other abnormal conditions.

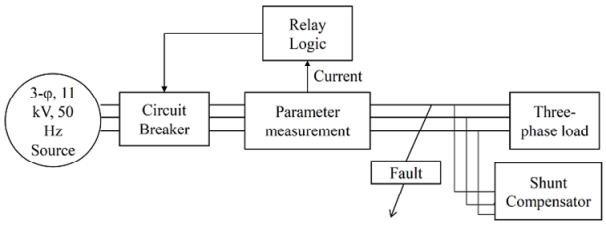

Fig. 4. Block diagram of the circuit used for analysis

Shunt compensators installed in the distribution network. The presence of shunt compensators introduces power disturbances in the measurement of line parameters [11-13], which affects the reach of the relay [14, 15]. Hence, the relay settings need to be adjusted when reactive power compensators are installed to the line to be protected, to avoid mal-operation of main and back-up protection scheme.

Compensation can be either active or passive. Fixed inductors and capacitors providing a fixed percentage of reactive power compensation constitute passive compensators. However, the Static Var Compensators (SVC) and DSTATCOM, which are designed to compensate for variable reactive power demands, constitute active compensators. SVCs comprise of Thyristor Controlled Reactor (TCR), Thyristor Switched Capacitor (TSC), Fixed Capacitor TCR (FCTCR), TSC-TCR etc. This paper covers the analysis of FCTCR and DSTATCOM.

Removal of decaying DC component from input signal. Under normal conditions, the voltage and current signals contain only fundamental and integer harmonic components. The DFT filtering algorithm produces the fundamental component within one cycle for such cases. But when fault occurs, the decaying DC component is also present along with the fundamental and harmonic components. The convergence speed of DFT algorithm reduces to more than 4 cycles due to the presence of decaying DC component. Thus, a MDFT technique is proposed by researchers [8, 9], which takes one cycle and a few samples to produce the fundamental signal during fault condition. It reduces the response time of the relay.

Results and discussions. The algorithm of 3 O/C & 1 E/F relaying scheme is simulated in MATLAB using 11 kV, 50 Hz distribution substation feeding a 3 MW, 0.8 power factor three-phase load. A shunt compensator is installed at the receiving end to improve the power factor from 0.8 to 0.9. Here, results for FCTCR and DSTATCOM are shown in this paper. The relay operation is verified against various phase and ground faults, like L-g, L-L, L-L-g, L-L-L and L-L-L-g. The distribution line length is considered as 20 km.

Power factor correction using FCTCR and DSTATCOM. Both the FCTCR and DSTATCOM are designed to improve the power factor from 0.8 to 0.9. The design is verified in Simulink and provides adequate results, as shown in Fig. 5. Figure 5,*a* shows the voltage, current and power factor of the load for uncompensated line. It can be noticed that the power factor is maintained at 0.8. Figure 5,*b* depicts that the power factor for FCTCR-compensated line has increased to 0.9. Similar is the case in Fig. 5,*c*, where the power factor of DSTATCOM-compensated line is improved to approximately 0.9.

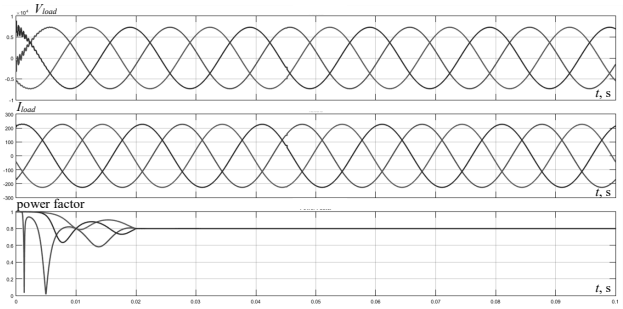

a – without compensation

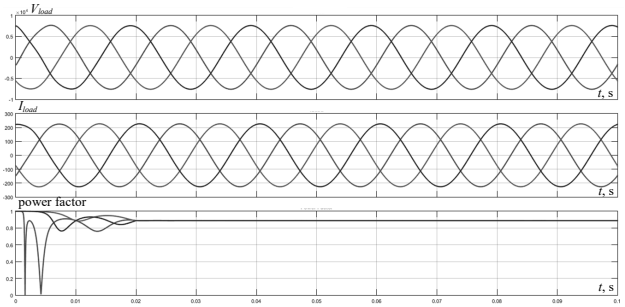

b – FCTCR compensated line

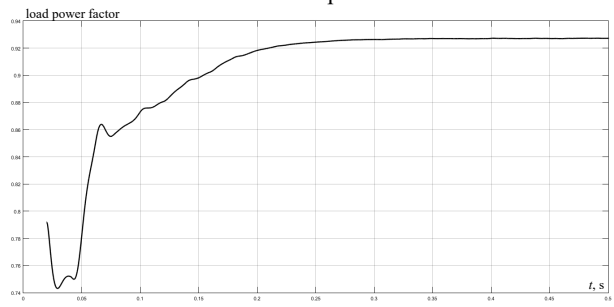

c – DSTATCOM compensated line

Fig. 5. Power factor improvement using FACTS devices

Fault occurring on the shunt compensated distribution network. Figure 6 shows the relay tripping action for L-g, L-L, L-L-g, L-L-L and L-L-L-g faults occurring in a FCTCR-compensated distribution network. Figure 6 consists of six graphs and each graph comprises of three curves of current flowing through R, Y and B phases of the line. It is observed from the simulation results that the E/F relay operates along with the O/C relays only for ground faults. For all other faults, only O/C relay operates.

The high value of current in the faulted phase of the line implies that the fault has occurred in that particular phase. Accordingly, the overcurrent relay corresponding

to the faulted phase will trip the supply to all the three phases. This setting is done because if the breaker is set to trip the faulted phase in the simulation, then some residual fault current flows to the healthy phases of the line, giving erroneous results. The reason for this error is the internal grounding of the elements used in the simulation, which provides a path to the fault current [16].

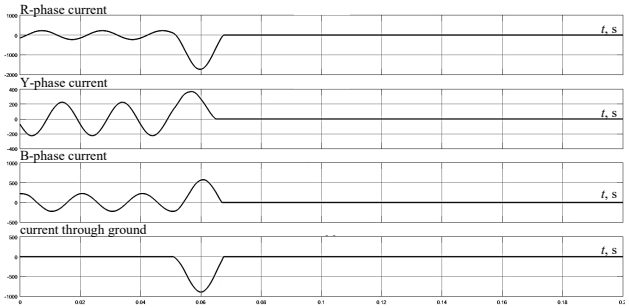

a – instantaneous relay operation for L-g fault

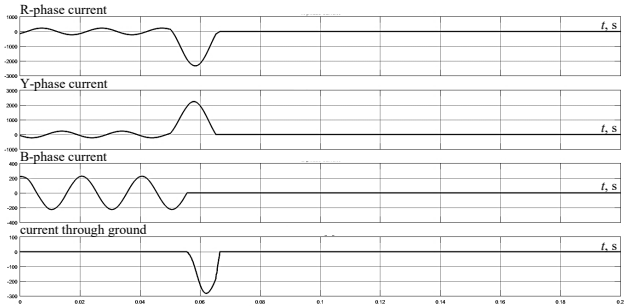

b – instantaneous relay operation for L-L fault

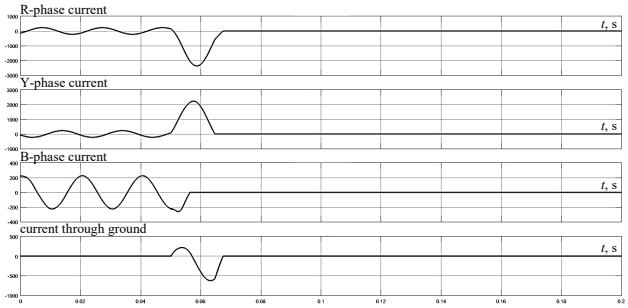

c – instantaneous relay operation for L-L-g fault

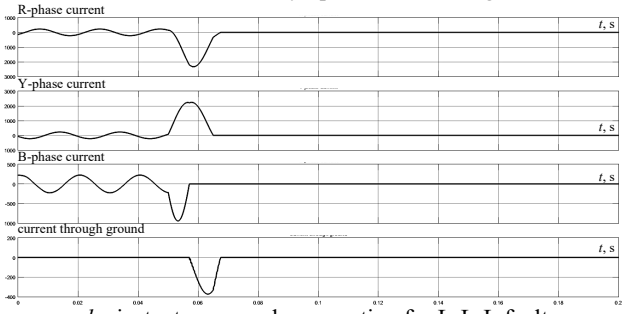

d – instantaneous relay operation for L-L-L fault

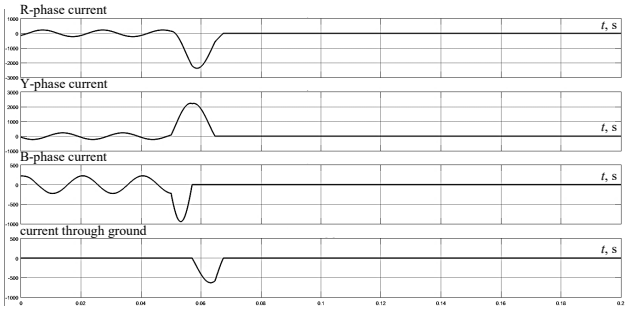

e – instantaneous relay operation for L-L-L-g fault

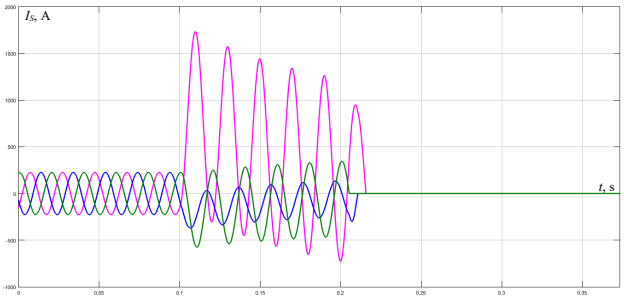

f – definite time relay operation for L-g fault

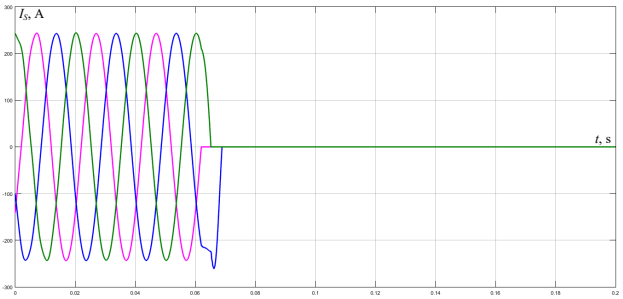

g – IDMT relay operation for L-g fault

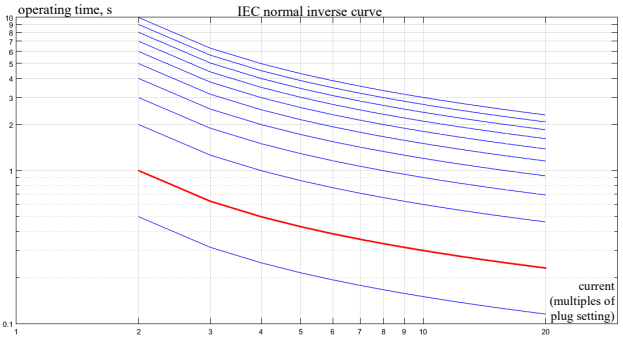

h – normal inverse characteristics of IDMT relay for (*e*)

Fig. 6. Different types of overcurrent relay characteristics for FCTCR-compensated line

Similar results are obtained for DSTATCOM as well, as shown in Fig. 7. Since L-g fault is the most common fault, the results in this section include only L-g fault for definite time overcurrent relay and Inverse Definite Minimum Time (IDMT) relay. The relay is verified to operate accurately for other faults as well, though it is not included in this paper. It is observed that the definite time overcurrent relay sends the trip command after a set delay (0.1 s). In this case, the IDMT relay operates according to (1), when fault occurs on the line. The results are shown for normal-inverse characteristics. Other characteristics given in Table 1, such as very-inverse and extremely inverse, are also tested in MATLAB for FCTCR and DSTATCOM-compensated distribution network considered for simulation.

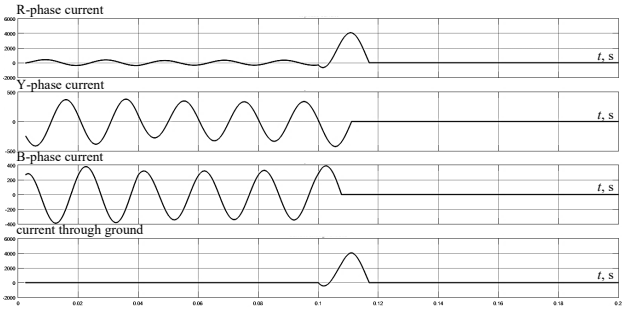

a – instantaneous relay operation for L-g fault

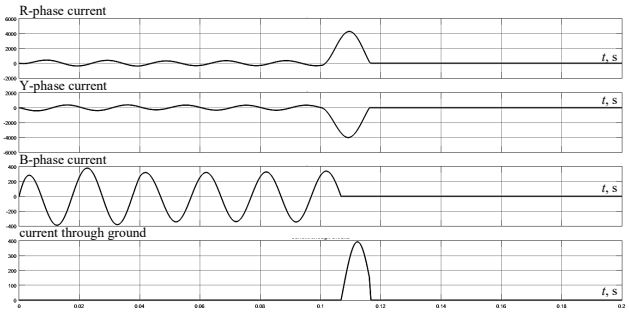

b – instantaneous relay operation for L-L fault

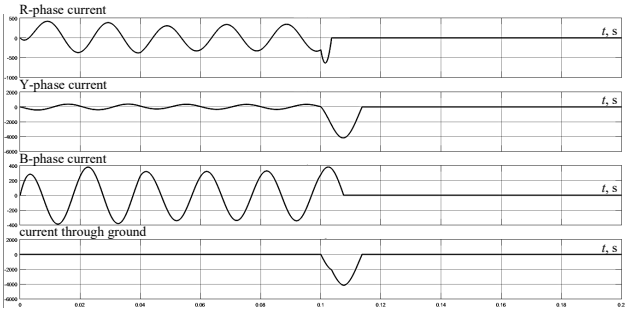

c – instantaneous relay operation for L-L-g fault

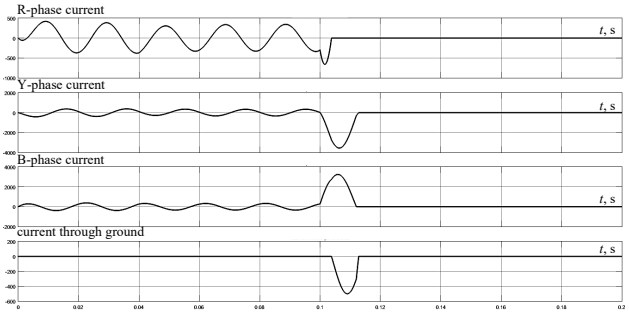

d – instantaneous relay operation for L-L-L fault

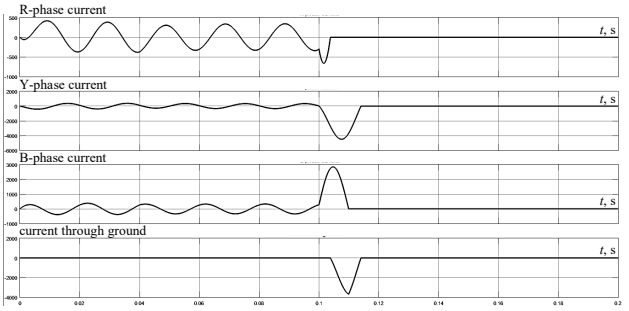

e – instantaneous relay operation for L-L-L-g fault

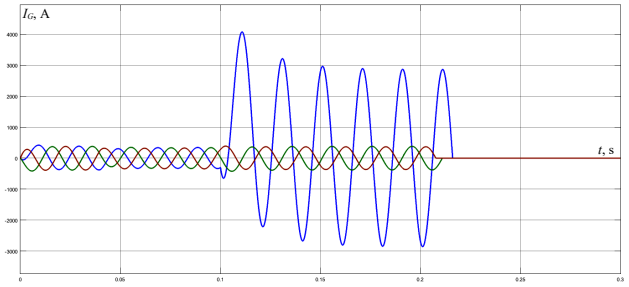

f – definite time relay operation for L-g fault

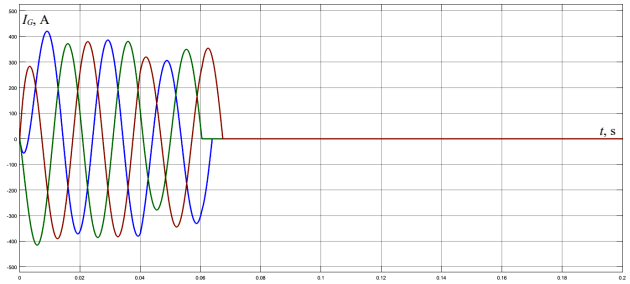

g – IDMT relay operation for L-g fault

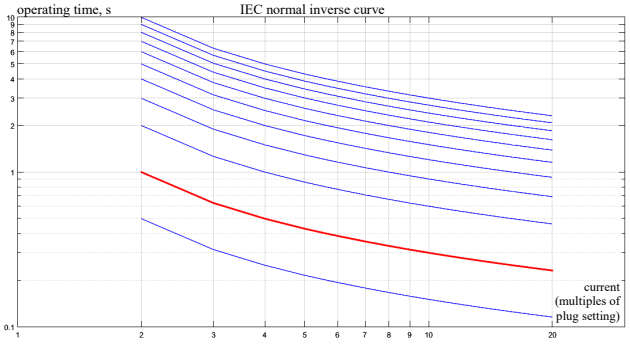

h – normal inverse characteristics of IDMT relay for (*e*)

Fig. 7. Different types of overcurrent relay characteristics for DSTATCOM-compensated line

Based on the simulation results obtained, the operation of the 3 O/C & 1 E/F relaying scheme can be understood using Table 2, which depicts the combination of relays which operates depending upon the type of fault.

Table 2

Relay operation based on the type of fault

Fault	O/C Relay: Phase R	O/C Relay: Phase Y	O/C Relay: Phase B	E/F Relay
R-g	Yes	No	No	Yes
Y-g	No	Yes	No	Yes
B-g	No	No	Yes	Yes
R-Y	Yes	Yes	No	No
Y-B	No	Yes	Yes	No
R-B	Yes	No	Yes	No
R-Y-g	Yes	Yes	No	Yes
Y-B-g	No	Yes	Yes	Yes
R-B-g	Yes	No	Yes	Yes
R-Y-B	Yes	Yes	Yes	No
R-Y-B-g	Yes	Yes	Yes	Yes

Testing of MDFT algorithm for fast response of the relay. The results shown above are obtained by *V-I* measurement block in MATLAB/Simulink, which is based on Fast Fourier Transform (FFT) algorithm. It is mathematically proven that the output of DFT and FFT is same. FFT can do everything a DFT does, but more efficiently and much faster than a DFT. It's an efficient way of computing the DFT. Hence, the output of *V-I* measurement block can be considered as the DFT output.

Figure 8,*a*,*b* shows the output of DFT and MDFT algorithm, respectively, when L-g fault occurs in the simulation circuit considered above for the analysis. It is observed from the output that the magnitude of current is obtained after more than 2 cycles when fault occurs on the line (Fig. 8,*a*). However, MDFT (Fig. 8,*b*) produces the desired output in 1 cycle and a few samples, thereby, improving the time of response of the relaying algorithm.

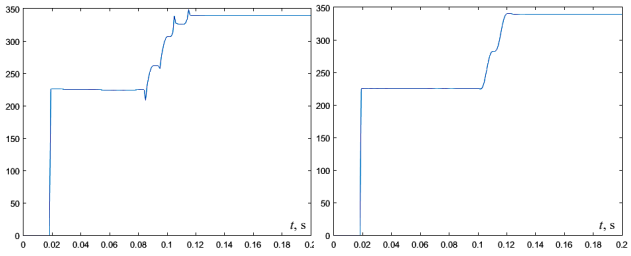

a *b*

Fig. 8. Output response of DFT and MDFT for L-g fault at $t = 80$ ms

Conclusion. This paper discusses the basics and performance of the family of overcurrent relays, such as instantaneous, definite time and inverse definite minimum time relays, for a shunt compensated distribution network. The three overcurrent and one earth-fault protection scheme installed to protect the distribution network and the simulation results verify that the operation of the healthy phase is not affected by the asymmetric faults due to this scheme. Hence, it is concluded that this scheme is more reliable and accurate to protect the network. Also, the presence of static VAR compensators like fixed capacitor thyristor controlled reactor and distribution static synchronous compensator is taken in account and the protection scheme performs precisely against the faults on shunt compensated distribution line as well. Finally, the response time of the relaying algorithm is improved by modified discrete Fourier transform algorithm and the results are compared with conventional discrete Fourier transform which concludes that modified discrete Fourier transform produces the desired output within 1 cycle and a few samples whereas discrete Fourier transform takes more than 2 cycles for the same.

Conflict of interest. The authors declare that they have no conflicts of interest.

REFERENCES

1. Chandraratne C., Woo W.L., Logenthiran T., Naayagi R. T. Adaptive Overcurrent Protection for Power Systems with Distributed Generators. *2018 8th International Conference on Power and Energy Systems (ICPES)*, 2018, pp. 98-103. doi: https://doi.org/10.1109/ICPESYS.2018.8626908.

2. Mahindara V.R., Rodriguez D.F.C., Pujiantara M., Priyadi A., Purnomo M.H., Muljadi E. Practical Challenges of Inverse and Definite-Time Overcurrent Protection Coordination in Modern Industrial and Commercial Power Distribution System. *IEEE Transactions on Industry Applications*, 2021, vol. 57, no. 1, pp. 187-197. doi: https://doi.org/10.1109/TIA.2020.3030564.

3. Filomena A.D., Salim R.H., Resener M., Bretas A.S. Ground Distance Relaying With Fault-Resistance Compensation for Unbalanced Systems. *IEEE Transactions on Power Delivery*, 2008, vol. 23, no. 3, pp. 1319-1326. doi: https://doi.org/10.1109/TPWRD.2007.909210.

4. Albasri F., Sidhu T.S., Varma R. Impact of Shunt-FACTS on Distance Protection of Transmission Lines. *2006 Power Systems Conference: Advanced Metering, Protection, Control, Communication, and Distributed Resources*, 2006, pp. 249-256. doi: https://doi.org/10.1109/PSAMP.2006.285397.

5. Albasri F.A., Sidhu T.S., Varma R.K. Performance Comparison of Distance Protection Schemes for Shunt-FACTS Compensated Transmission Lines. *IEEE Transactions on Power Delivery*, 2007, vol. 22, no. 4, pp. 2116-2125. doi: https://doi.org/10.1109/TPWRD.2007.900283.

6. Oza Bhuvanesh A., Nirmalkumar C. Nair, Rashesh P. Mehta, Vijay H. Makwana. *Power system protection and switchgear. In Chapter 1: Introduction and Philosophy of a Protective Relaying System*. Tata McGraw Hill Education Private Limited, 2010.

7. Jyh-Cherng Gu, Sun-Li Yu. Removal of DC offset in current and voltage signals using a novel Fourier filter algorithm. *IEEE Transactions on Power Delivery*, 2000, vol. 15, no. 1, pp. 73-79. doi: https://doi.org/10.1109/61.847231.

8. Sun-Li Yu, Jyh-Cherng Gu. Removal of decaying DC in current and voltage signals using a modified Fourier filter algorithm. *IEEE Transactions on Power Delivery*, 2001, vol. 16, no. 3, pp. 372-379. doi: https://doi.org/10.1109/61.924813.

9. Chi-Shan Yu, Wen-Hui Chen. Removing decaying DC component in fault currents via a new modify discrete Fourier algorithm. *IEEE Power Engineering Society General Meeting*, 2005, pp. 1041-1046. doi: https://doi.org/10.1109/PES.2005.1489295.

10. Ghotbi-Maleki M., Chabanloo R.M., Zeineldin H.H., Hosseini Miangafsheh S.M. Design of Setting Group-Based Overcurrent Protection Scheme for Active Distribution Networks Using MILP. *IEEE Transactions on Smart Grid*, 2021, vol. 12, no. 2, pp. 1185-1193. doi: https://doi.org/10.1109/TSG.2020.3027371.

11. Hingoranl N.G., Gyugyi L., El-Hawary M.E. *Understanding FACTS: Concepts and Technology of Flexible AC Transmission Systems*. Wiley-IEEE Press, 1999. 432 p. doi: https://doi.org/10.1109/9780470546802.

12. Hingorani N.G. FACTS-flexible AC transmission system. *International Conference on AC and DC Power Transmission*, London, UK, 1991, pp. 1-7.

13. Hingorani N.G. *Flexible AC transmission system (FACTS). Electricity Transmission Pricing and Technology*. Springer, Dordrecht, 1996.

14. Singh A.R., Ahmed A., Dambhare S. Robust distance protection of mid-point shunt compensated transmission line. *2012 IEEE Fifth Power India Conference*, 2012, pp. 1-5. doi: https://doi.org/10.1109/PowerI.2012.6479485.

15. Chemidi A., Benhabib M.C., Bourouis M.A. Performance improvement of shunt active power filter based on indirect control with a new robust phase-locked loop. *Electrical Engineering & Electromechanics*, 2022, no. 4, pp. 51-56. doi: https://doi.org/10.20998/2074-272X.2022.4.07.

16. Sekhane H., Labed D., Labed M.A. Modelling and performance testing of a digital over-current relay enhanced designed model. *Electrical Engineering & Electromechanics*, 2022, no. 3, pp. 71-78. doi: https://doi.org/10.20998/2074-272X.2022.3.10.

Received 31.08.2022
Accepted 19.12.2022
Published 07.03.2023

A. Jani[1], *PhD*, *Research Scholar*,
V.H. Makwana[2], *PhD*, *Professor*,
[1] Gujarat Technological University, India,
e-mail: Asg.8491@gmail.com (Corresponding Author)
[2] GH Patel College of Engineering and Technology, India,
e-mail: Vijay911979@gmail.com

How to cite this article:
Jani A., Makwana V.H. Modified discrete Fourier transform algorithm for protection of shunt compensated distribution line. *Electrical Engineering & Electromechanics*, 2023, no. 2, pp. 63-68. doi: https://doi.org/10.20998/2074-272X.2023.2.10

UDC 621.3 https://doi.org/10.20998/2074-272X.2023.2.11

A. Laifa, B. Ayachi

Application of whale algorithm optimizer for unified power flow controller optimization with consideration of renewable energy sources uncertainty

Purpose. *In this paper an allocation methodology of Flexible Alternating Current Transmission Systems (FACTS) controllers, more specifically, the Unified Power Flow Controller (UPFC) is proposed. As the penetration of Renewable Energy Sources (RESs) into the conventional electric grid increases, its effect on this location must be investigated. Research studies have shown that the uncertainty of RESs in power generation influences the reactive power of a power system network and consequently its overall transmission losses. The* ***novelty*** *of the proposed work consists in the improvement of voltage profile and the minimization of active power loss by considering renewable energy sources intermittency in the network via optimal location of UPFC device. The allocation strategy associates the steady-state analysis of the electrical network, with the location and adjustment of controller parameters using the Whale Optimization Algorithm (WOA) technique.* ***Methodology.*** *In order to determine the location of UPFC, approaches are proposed based on identification of a line which is the most sensitive and effective with respect to voltage security enhancement, congestion alleviation as well as direct optimization approach. The optimum location of UPFC in the power system is discussed in this paper using line loading index, line stability index and optimization method. The objective function is solved using the WOA algorithm and its performance is evaluated by comparison with Particle Swarm Optimization (PSO) algorithm.* ***Results****. The effectiveness of the proposed allocation methodology is verified through the analysis of simulations performed on standard IEEE 30 bus test system considering different load conditions. The obtained results demonstrate that feasible and effective solutions are obtained using the proposed approach and can be used to overcome the optimum location issue. Additionally, the results show that when UPFC device is strategically positioned in the electrical network and uncertainty of RES is considered, there is a significant influence on the overall transmission loss and voltage profile enhancements of the network.* References 31, tables 4, figures 14.
Key words: **unified power flow controller, optimal location, whale optimization algorithm, renewable energy sources, intermittency.**

Мета*. У статті пропонується методологія розподілу контролерів гнучких систем передачі змінного струму (FACTS), зокрема уніфікованого контролера потоку потужності (UPFC). Оскільки проникнення відновлюваних джерел енергії (ВДЕ) у звичайну електричну мережу збільшується, необхідно досліджувати їхній вплив на це. Наукові дослідження показали, що невизначеність ВДЕ у виробленні електроенергії впливає на реактивну потужність мережі енергосистеми і, отже, на її загальні втрати під час передачі.* ***Новизна*** *запропонованої роботи полягає в покращенні профілю напруги та мінімізації втрат активної потужності за рахунок обліку перемежування відновлюваних джерел енергії в мережі за рахунок оптимального розташування пристрою UPFC. Стратегія розподілу пов'язує стаціонарний аналіз електричної мережі з розміщенням та налаштуванням параметрів контролера з використанням методу алгоритму оптимізації кита (WOA).* ***Методологія****. Для визначення розташування UPFC пропонуються підходи, засновані на виявленні лінії, яка є найбільш чутливою та ефективною з точки зору підвищення безпеки за напругою, зменшення навантажень, а також прямий підхід до оптимізації. Оптимальне розташування UPFC в енергосистемі обговорюється в цій статті з використанням індексу завантаження лінії, індексу стійкості лінії та методу оптимізації. Цільова функція вирішується з використанням алгоритму WOA, а її продуктивність оцінюється шляхом порівняння з алгоритмом оптимізації рою частинок (PSO).* ***Результати****. Ефективність запропонованої методології розподілу перевірена за допомогою аналізу моделювання, виконаного на тестовій системі стандартної шини IEEE 30 з урахуванням різних умов навантаження. Отримані результати демонструють, що за допомогою запропонованого підходу виходять здійсненні та ефективні рішення, які можна використовувати для подолання проблеми оптимального розташування. Крім того, результати показують, що коли пристрій UPFC стратегічно розташований в електричній мережі і враховується невизначеність ВДЕ, це значно впливає на загальні втрати при передачі і поліпшення профілю напруги в мережі.* Бібл. 31, табл. 4, рис. 14.
Ключові слова: **уніфікований регулятор потоку потужності, оптимальне розташування, алгоритм оптимізації кита, відновлювані джерела енергії, переривчастість.**

Introduction. Nowadays, the global demand for electricity is increasing which increase the power system stress. The constraints on expanding power generation plants' construction and transmission lines have resulted in a significant gap between power generation and demand [1]. The reliable and secure operation of power systems is then an important task for operators to avoid improper performance such as excessive power losses, congested lines, voltage instabilities and stability problems [2]. In this context, a possible solution to improve the exploitation of the system was the use of Flexible Alternating Current Transmission Systems (FACTS) technologies. The FACTS devices should provide the highest advantage to power networks for maintaining stability and security constraints [3]. Moreover, FACTS can significantly improve the performance of the power system, i.e., improving the voltage profile, reducing power system losses, increasing the permissible power transfer capability, and enhancing the stability and reliability of the system [4]. Many FACTS controllers have been proposed and implemented to control the power system under normal states, as well as under contingency conditions [5]. Among these controllers, the Unified Power Flow Controller (UPFC) is a device which has the capacity to regulate the active power, reactive power, and the voltage of connecting buses.

Like any FACTS controller, UPFC can be deployed anywhere in the power system and its performance will be varied on different transmission lines. Therefore, we will face the problem of where we should install UPFC. For this reason, some performance indices must be defined and satisfied. The factors that can be considered in the selection of the optimal installation and parameter setting of UPFC may be the stability margin improvement, the power transmission capacity increase, and the voltage profile enhancement, etc [6].

However, the placement of UPFCs is a very complex problem, even under the consideration of steady-state

conditions only. An optimal UPFC placement must incorporate not only each possible system topology but must also consider the entire range of possible control settings which may themselves be dependent on system topology [7]. The techniques for optimal location of FACTS devices are broadly classified into three categories, namely the classical optimization methods, sensitivity based methods and meta-heuristic methods [1, 8, 9]. Hybridization can be also used [4, 10].

The meta-heuristic approaches are the well-established method to achieve the best results in the FACTS device placement and location in the power system [11, 12]. Meta-heuristic based methods are inspired by human, natural biological systems intelligence and laws of nature and physics. Examples include but not limited to Genetic Algorithm [13], Particle Swarm Optimization [14], Cuckoo Search Algorithm [15], Grey Wolf Optimization [16], Harmony Search [17], Artificial Bee Colony Algorithm [18], Firefly Algorithm [9], Flower Pollination Algorithm [19], Brainstorm Optimization [20], and Biogeography based optimization [21].

On the other hand, with the continuing increase in demand and unexpanded transmission system due to limitations, the integration of renewable energy sources (RES) into the electrical grid is experiencing a rapid increase across the world. This is facing the current trends in decreasing fossil fuels, increasing pollution levels, and uncontrolled increase in population. Among various types of RES [22], wind and solar photovoltaic based energy sources are the most adopting technologies even at end-user level. As compared to conventional energy sources (CES), the RES have various advantages like reduced active power losses, improved voltage profile and increased overall energy efficiency, etc., however the intermittency nature of RES need to be addressed by the researchers.

The **goal** of this paper is to locate UPFC device in the best possible location to reduce power loss and voltage deviation considering RES integration and intermittency. Stability index and congestion index values are used. A detailed description of the power flow problem incorporating UPFC model is provided. Moreover, the proposed methodology and the Whale Optimization Algorithm (WOA) method are presented. In the proposed methodology, IEEE 30 bus system is considered to validate the system performance.

Modeling of UPFC in the power flow. FACTS devices are equipment that, by means of high power electronics, allows acting on the electrical system in order to make it more reliable, efficient and flexible. The UPFC is a FACTS device able to control simultaneously active power flows, reactive power flows, and voltage magnitude at the UPFC terminals**.** The UPFC consists of two switching converters operated from a common DC link (Fig. 1). These converters are connected to the power system via coupling transformers. One converter is connected in shunt to the sending end node *i* while the second converter is connected in series between the sending and receiving end nodes *i* and *j*. The series converter performs the main function of the UPFC by injecting an AC voltage with controllable magnitude and phase angle in series with the transmission line. The UPFC cannot generate or absorb active power and as such the active power in the two converters must balance when active power loss is neglected. This is achieved via the DC link. The converters, however, may generate or absorb reactive power. The shunt converter can generate or absorb controllable reactive power and provide independent shunt reactive compensation for the line. UPFC can then regulate active and reactive power simultaneously. In principle, a UPFC can perform voltage support, power flow control and dynamic stability improvement in one and the same device.

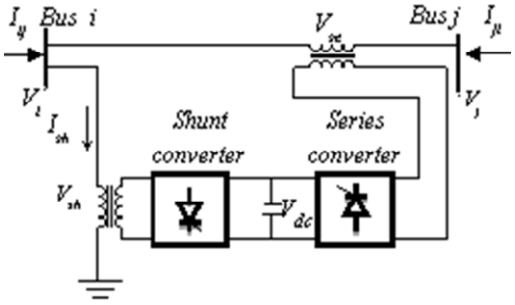

Fig. 1. Operating principle of UPFC

The power flow calculation method used is the traditional Newton-Raphson (NR) method. The following describes the adaptations made in it to incorporate the control representation of the UPFC in the solution process. The NR method is based on the solution of successive linear problems described by (1), where the sub-matrices *H*, *M*, *N* and *L* constitute the Jacobian matrix of the problem and represent the partial derivatives of the nodal power injections (*P* and *Q*) with respect to the state variables (phase angle δ and voltage magnitude *V*)

$$\begin{bmatrix} \Delta P \\ \Delta Q \end{bmatrix} = \begin{bmatrix} H & N \\ M & L \end{bmatrix} \begin{bmatrix} \Delta \delta \\ \Delta V \end{bmatrix}, \tag{1}$$

The UPFC equivalent circuit (Fig. 2) is used to derive the steady-state model. The UPFC model can be incorporated to the power flow equations by adding the UPFC injection powers at buses *i* and *j*. The equivalent circuit allows us to model it in terms of power injection (Fig. 3).

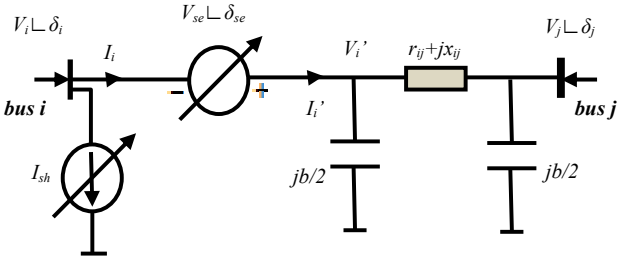

Fig. 2. The equivalent circuit of UPFC

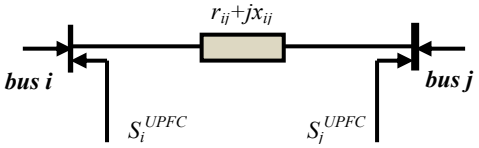

Fig. 3. Power injection model of UPFC

Based on the principle of UPFC and the vector diagram, the following equations can be written:

$$\overline{V_i'} = \overline{V_i} + \overline{V_{se}}, \tag{2}$$

$$Arg(\overline{I_q}) = Arg(\overline{V_i}) \pm \frac{\pi}{2}, \tag{3}$$

$$Arg(\overline{I_p}) = Arg(\overline{V_i}), \quad (4)$$

$$\overline{I_p} = \frac{\Re e\left(\overline{V_{se}} \cdot \overline{I_i'}^*\right)}{\overline{V_i}}, \quad (5)$$

where: $\overline{V_i}$ is the voltage at bus *i*; $\overline{V_{se}}$ is the voltage injected in series with the transmission line through the series transformer; V_{se} is the magnitude and δ_{se} the phase angle of this voltage; I_q is the shunt reactive current of UPFC flowing in the shunt transformer to improve the voltage of the shunt connected bus of UPFC; the current I_p represents the active power demanded by the series converter at the common DC link and supplied or absorbed by the shunt converter.

Then the shunt current of UPFC is

$$\overline{I_{sh}} = I_p + jI_q. \quad (6)$$

Then, the power flow equations from bus *i* to bus *j* and from bus *j* to bus *i* can be written as:

$$\overline{S_{ij}} = P_{ij} + jQ_{ij} = \overline{V_i} \cdot \overline{I_{ij}}^* = \overline{V_i}\left(j\overline{V_i'}\frac{b}{2} + I_p + jI_q + \overline{I_i'}\right)^*; \quad (7)$$

$$\overline{S_{ji}} = P_{ji} + jQ_{ji} = \overline{V_j} \cdot \overline{I_{ji}}^* = \overline{V_j}\left(j\overline{V_j}\frac{b}{2} - \overline{I_i'}\right)^*. \quad (8)$$

The active and reactive power flow in the line having UPFC can be written:

$$\begin{aligned} P_{ij} = {} & \left(V_i^2 + V_{se}^2\right)g_{ij} + 2V_iV_{se}g_{ij}\cos\left(\delta_{se} - \delta_i\right) - \\ & - V_jV_{se}\left[g_{ij}\cos\left(\delta_{se} - \delta_j\right) + b_{ij}\sin\left(\delta_{se} - \delta_j\right)\right] - \\ & - V_iV_j\left[g_{ij}\cos\left(\delta_i - \delta_j\right) + b_{ij}\sin\left(\delta_i - \delta_j\right)\right]; \end{aligned} \quad (9)$$

$$\begin{aligned} P_{ji} = {} & V_j^2 g_{ij} - V_jV_{se}\left[g_{ij}\cos\left(\delta_{se} - \delta_j\right) - b_{ij}\sin\left(\delta_{se} - \delta_j\right)\right] - \\ & - V_iV_j\left[g_{ij}\cos\left(\delta_i - \delta_j\right) - b_{ij}\sin\left(\delta_i - \delta_j\right)\right]; \end{aligned} \quad (10)$$

$$\begin{aligned} Q_{ij} = {} & -V_iI_q - V_i^2\left(b_{ij} + \frac{b}{2}\right) - \\ & - V_iV_{se}\left[g_{ij}\sin\left(\delta_{se} - \delta_j\right) + \left(b_{ij} + \frac{b}{2}\right)\cos\left(\delta_{se} - \delta_j\right)\right] - \\ & - V_iV_j\left[g_{ij}\sin\left(\delta_i - \delta_j\right) - b_{ij}\cos\left(\delta_i - \delta_j\right)\right]; \end{aligned} \quad (11)$$

$$\begin{aligned} Q_{ji} = {} & -V_j^2\left(b_{ij} + \frac{b}{2}\right) - \\ & - V_jV_{se}\left[g_{ij}\sin\left(\delta_{se} - \delta_j\right) + b_{ij}\cos\left(\delta_{se} - \delta_j\right)\right] + \\ & + V_iV_j\left[g_{ij}\sin\left(\delta_i - \delta_j\right) + b_{ij}\cos\left(\delta_i - \delta_j\right)\right], \end{aligned} \quad (12)$$

where

$$g_{ij} + jb_{ij} = \frac{1}{r_{ij} + jx_{ij}}, \quad (13)$$

r_{ij} and x_{ij} are the resistance and reactance of line *i-j*.

The real and reactive power flows for the line *i-j* without UPFC are:

$$P_{ij} = V_i^2 g_{ij} - V_iV_j\left[g_{ij}\cos\left(\delta_i - \delta_j\right) + b_{ij}\sin\left(\delta_i - \delta_j\right)\right]; \quad (14)$$

$$P_{ji} = V_j^2 g_{ij} - V_iV_j\left[g_{ij}\cos\left(\delta_i - \delta_j\right) - b_{ij}\sin\left(\delta_i - \delta_j\right)\right]; \quad (15)$$

$$\begin{aligned} Q_{ij} = {} & -V_i^2\left(b_{ij} + \frac{b}{2}\right) - \\ & - V_iV_j\left[g_{ij}\sin\left(\delta_i - \delta_j\right) - b_{ij}\cos\left(\delta_i - \delta_j\right)\right]; \end{aligned} \quad (16)$$

$$\begin{aligned} Q_{ji} = {} & -V_j^2\left(b_{ij} + \frac{b}{2}\right) + \\ & + V_iV_j\left[g_{ij}\sin\left(\delta_i - \delta_j\right) + b_{ij}\cos\left(\delta_i - \delta_j\right)\right] \end{aligned} \quad (17)$$

We can so derive the active and reactive power injections associated to the UPFC:

$$\begin{aligned} P_i^{UPFC} = {} & -V_{se}^2 g_{ij} - 2V_iV_{se}g_{ij}\cos\left(\delta_i - \delta_{se}\right) + \\ & + V_jV_{se}\left[g_{ij}\cos\left(\delta_j - \delta_{se}\right) - b_{ij}\sin\left(\delta_j - \delta_{se}\right)\right]; \end{aligned} \quad (18)$$

$$P_j^{UPFC} = V_jV_{se}\left[g_{ij}\cos\left(\delta_j - \delta_{se}\right) + b_{ij}\sin\left(\delta_j - \delta_{se}\right)\right]; \quad (19)$$

$$\begin{aligned} Q_i^{UPFC} = {} & V_iI_q + \\ & + V_iV_{se}\left[-g_{ij}\sin\left(\delta_i - \delta_{se}\right) + \left(b_{ij} + \frac{b}{2}\right)\cos\left(\delta_i - \delta_{se}\right)\right]; \end{aligned} \quad (20)$$

$$Q_j^{UPFC} = -V_jV_{se}\left[-g_{ij}\sin\left(\delta_i - \delta_{se}\right) + b_{ij}\cos\left(\delta_i - \delta_{se}\right)\right]. \quad (21)$$

Then, the NR power flow algorithm is expressed by the following relationship:

$$\begin{bmatrix} \Delta P \\ \Delta Q \end{bmatrix} = \begin{bmatrix} H_{new} & N_{new} \\ M_{new} & L_{new} \end{bmatrix}\begin{bmatrix} \Delta\delta \\ \Delta V \end{bmatrix}, \quad (22)$$

where the new error vectors are

$$\Delta P_i = P_i^{spec} + P_i^{UPFC} - P_i^{calc}; \quad (23)$$

$$\Delta Q_i = Q_i^{spec} + Q_i^{UPFC} - Q_i^{calc}, \quad (24)$$

where P_i^{spec} and Q_i^{spec} are the classical specified powers; P_i^{UPFC} and Q_i^{UPFC} are the power injection associated to the UPFC device; P_i^{calc} and Q_i^{calc} and are computed using the power flow equations.

And, the Jacobian matrix is modified to introduce new power injections that are functions of the bus voltages:

$$H_{new} = H + \frac{\partial P^{UPFC}}{\partial\delta}; \quad (25)$$

$$M_{new} = M + \frac{\partial P^{UPFC}}{\partial V}; \quad (26)$$

$$N_{new} = N + \frac{\partial Q^{UPFC}}{\partial\delta}; \quad (27)$$

$$L_{new} = L + \frac{\partial Q^{UPFC}}{\partial V}. \quad (28)$$

Applied methodology. To enhance the power system performance in terms of reduced transmission loss, improved voltage profile as well security margin, it is necessary to integrate the UPFC in an optimal location. Then, it is necessary to define an objective function that measures the «goodness» of a particular setting. This objective function is formulated by considering some performance indices under the conditions of different RES penetration and load levels.

Optimal location. Keeping system security is one of the most important tasks of power system operators. Due to economic reasons, a transmission network of a power system is mandatory to function near its security boundaries [23]. FACTS devices, mainly UPFC, should be placed to prevent congestion in transmission lines and maintain bus voltages far from voltage collapse condition. In this paper and in addition to optimization method, line stability index (LSI) and line loading index (LLI) are used for placement of UPFC.

1) LSI based location.

The dependency of voltage stability on reactive power reserve in the network is well highlighted fact in the literature. For a transmission line connected between bus *i* and bus *j*, LSI can be assessed by (29) [23-25]

$$LSI_{ij} = \frac{4x_{ij}Q_{ij}}{\left[V_i \sin\left(\theta_{ij} - \delta_i + \delta_j\right)\right]^2} \le 1, \qquad (29)$$

where Q_{ij} is the reactive power flow in line *i-j* and θ_{ij} is the impedance argument of the line.

If LSI_{ij} reaches or nearing to unity, it indicates that the line is losing its stability and voltage collapse will occur. For stable operation, the LSI should be less than 1 for all the lines. The LSI greater than 1 indicates the proximity of instability or voltage collapse. The stability or security margin improvement can be shown by decreasing the LSI of all the lines. By observing the parameters in LSI, it is directly proportional to reactive power flow through the line and inversely proportional to the square of the voltage magnitude. Since the UPFC device is able to control the reactive power flows as well as improve the voltage profile, the location which can moderate the LSI value of all the lines is selected as optimal location. An LSI index value away from 1 and close to zero indicates an improved system security.

Also, the stressful condition of the line from its LSI value can be used to identify/rank the critical lines in network. The lines with higher LSI are the weakest and critical lines and are chosen as candidates for installing UPFC. We exclude the lines which are having regulating transformers and those incidents to generator/synchronous condenser buses.

2) LLI based location.

The overloading of lines provides an indication about the power system reliability. In order to remove congestions of the lines and to distribute the load flows uniformly, the UPFC has to be placed in a line that may minimize the average loadability. This can be achieved by considering the line loading index (LLI) used for determining the congestion of the transmission lines and defined below [21, 26]

$$LLI_l = \left(\frac{S_l}{S_{l\max}}\right)^2, \qquad (30)$$

where LLI_l is the line loading index of the line; S_l is the actual MVA rating of the line; $S_{l\max}$ is the maximum MVA rating of the line.

LLI is proposed to rank the most severe lines to allocate the UPFC controller. The power transmission lines which have most amount of LLI are recognized as critical lines from the viewpoint of congestion phenomenon and are chosen as candidates for installing UPFC.

3) Optimization based location.

The optimization algorithm is utilized to decide the optimal location and parameters of UPFC. The algorithm is proposed to execute the optimization process. Here also, UPFC can be incorporated in any line excluding the lines which are incident to generator buses as well as those are having tap changing transformer.

The UPFC is situated between two buses so from location and to optimal location are distinguished.

Definition of the objective function. The definition of the objective function of problems related to allocation of control devices is usually associated with improvement of the efficiency and / or operational safety of the power [3]. Two objectives are considered in this study, reduction of the active power losses of transmission lines and voltage profile improvement.

1) Minimization of losses.

Active power line transmission losses are a very important factor to optimize in a power network. Minimizing losses of active power of the system implies a decrease in the use of system generators and optimization of the circulation of power in the electrical network. Power losses P_{loss} can be expressed as:

$$P_{loss} = \sum_{k=1}^{nl} g_k \left[V_i^2 + V_j^2 - 2V_iV_j\cos\left(\delta_i - \delta_j\right)\right], \qquad (31)$$

where g_k is the conductance of line *k* and *nl* the number of lines.

2) Voltage deviation.

Excessive high or low voltages can lead to an unacceptable service quality and can create voltage instability problems. UPFC connected at appropriate locations play a leading role in improving voltage profile thereby avoiding voltage collapse in the power system. To have a good voltage performance, the voltage deviation at each load bus must be made as small as possible in order to prevent the under or over voltages at network buses. The voltage deviation index to be minimized is as follows:

$$VD = \sum_k \left(V_k - V_{refk}\right)^2, \qquad (32)$$

where V_k is voltage magnitude of bus *k*; V_{refk} is the reference value for this voltage.

3) Aggregated objective.

The overall objective function is formulated to minimize voltage deviation and total real power loss simultaneously and expressed as

$$F = w_1\left[P_{loss}\right] + w_2\left[VD\right], \qquad (33)$$

where w_1 and w_2 are the weighting factors used for adjusting the network total active power loss and voltage deviation functions respectively. In this case, $w_1 = w_2 = 1$.

4) Vector of control variables.

The aim is then to minimize the voltage deviation and real power loss by optimizing the UPFC parameters considering RES integration. These objectives are highly dependent on adequate voltage profile. Hence, the vector of control variables consists of generator bus voltage magnitudes, tap-changer settings, eventual shunt MVAr injection, and control variables of UPFC device and generations at RES locations. For the UPFC, the associated control variables to be considered are: magnitude and voltage angle of the series controller and the shunt injected current of the device.

Consideration of renewable energy sources. The renewable energy is incorporated into the optimization problem and plays the role of negative loads in order to decrease the demand load. In general, any types of RES may not produce always at its maximum capacity due to dependency on various parameters involved in their operation. For example, wind turbine power is dependent on wind velocity and solar photovoltaic (PV) system generation is dependent on solar radiation etc.

Hence, it is assumed that the power generated by any RES is less than its maximum capacity. Then, a

random number $r_{int,i}$ will be considered for the RES at bus i in the range of ($0 \le r_{int,i} \le 1$) to simulate intermittency of this power source.

The power generation at a RES bus is then

$$P_{res,i} = r_{int,i} P_{res,i}^{\max}, \quad (34)$$

where $P_{res,i}^{\max}$ is the real power injection capability (maximum capacity) of RES installed at bus i.

The total RES intermittency in the network can be formulated as

$$r_{int} = \frac{\sum_i P_{res,i}}{\sum_i P_{res,i}^{\max}}. \quad (35)$$

Today PV inverters are working with very small values of reactive power. Then, the power factor (PF) is very close to the unit. So, the PV installations only inject active power into the grid. However, induction machines are mostly used as generators in wind power based generations and may draw reactive power from the system to which they are connected.

Consideration of operating conditions – load levels. Many studies do not consider operational variations in the allocation process, using, for example, a constant load condition. This can interfere inappropriately in the allocation of the FACTS controllers, since they must, obviously, have their performance adjusted to the different operating conditions of the system.

To overcome this possibility, we can represent the different load conditions of the system in levels. The levels are defined from the discretization of daily consumption averages at intervals of consumption. Seeking to reduce the computational effort required to carry out large studies such as the one that characterizes device allocation problems, a usual division of the loads' behavior is to represent them, at three levels consumption: light, medium and heavy [27]. The objective is to represent the effect of changes in consumption control devices acting on the electrical network and that should interfere with the allocation process. In the present work, we consider only the base case and a heavy one with overloading of 30 %.

System constraints.

1) Equality constraints.

As per load flow studies, the residual powers at any bus should be equal to generation minus demand. Power flow equations corresponding to both real and reactive power balance equations are the equality constraints that can be written, for all the buses expect UPFC incident buses, as

$$P_{Gi} - P_{Di} - P_i(\delta, V) = 0, \quad (36)$$

$$Q_{Gi} - Q_{Di} - Q_i(\delta, V) = 0, \quad (37)$$

where P_{Gi}, P_{Di}, Q_{Gi} and Q_{Di} are the real and reactive power generations and loads at bus i respectively.

The equality constraints represent the typical load flow equations as follows:

$$P_{Gi} - P_{Di} - V_i \sum_{j=1}^{nb} V_j \left[G_{ij} \cos(\delta_i - \delta_j) + B_{ij} \sin(\delta_i - \delta_j) \right] = 0, \quad (38)$$

$$Q_{Gi} - Q_{Di} - V_i \sum_{j=1}^{nb} V_j \left[G_{ij} \sin(\delta_i - \delta_j) - B_{ij} \cos(\delta_i - \delta_j) \right] = 0, \quad (39)$$

$$i = 1, \ldots, nb$$

where nb is the number of buses of the power system.

For buses with RES powers, generation is expressed in terms of conventional and RES powers

$$P_i = (P_{Gi} + r_{int} P_{Gi,r}) - P_{Di}; \quad (40)$$

$$Q_i = (Q_{Gi} + r_{int} Q_{Gi,r}) - Q_{Di}, \quad (41)$$

where r_{int} is the random numbers in the range of [0, 1] to represent the intermittence of the RES at bus i related to maximum real power $P_{Gi,r}$ and reactive power generations $Q_{Gi,r}$ respectively.

Similarly, for the UPFC incident buses, the real and reactive power balance equations can be written as,

$$P_i = P_{Gi} - (P_{Di} + P_{inj,i}); \quad (42)$$

$$Q_i = Q_{Gi} - (Q_{Di} + Q_{inj,i}), \quad (43)$$

where $P_{inj,i}$ and $Q_{inj,i}$ are the real and reactive power injections by UPFC device as given in equations (18)-(21) for incident buses.

2) Inequality constraints.

The inequality constraints represent the system operating limits like limits on reactive generation and bounds on tap settings of transformers.

Real power generation limits:

$$P_{G\min} \le P_G \le P_{G\max}. \quad (44)$$

Reactive power generation limits:

$$Q_{G\min} \le Q_G \le Q_{G\max}. \quad (45)$$

Bus voltage limits:

$$V_{i\min} \le V_i \le V_{i\max}. \quad (46)$$

Bus voltage phase angle limits:

$$\delta_{i\min} \le \delta_i \le \delta_{i\max}. \quad (47)$$

Tap-changers limits:

$$a_{i\min} \le a_i \le a_{i\max}. \quad (48)$$

Line power flow limits:

$$S_l \le S_{l\max}. \quad (49)$$

Optimization method. WOA is a new nature-inspired metaheuristic for optimization problems proposed in 2016 [28-30]. It mimics the hunting behavior of one of the biggest baleen whales called humpback whales. This kind of whales feeds a small prey as krill, herrings, and other small fishes near the surface. They have a special hunting method to find and hunt the prey called bubble-net feeding which is a complex and coordinated tactic for catching many fish at once. The hunt begins as the whales dive down and then start to create a ring of bubbles to encircle the fishes, which are too frightened to pass through the bubbles, in meantime the whales swim upward to the surface through the bubble net and swallowing a huge number of fishes in one swig.

In the optimization process, a population of whales (search agents) evolves to find the global optima after a specified number of iterations. WOA begins with the initialization of search agents randomly upon the interval bounds of the problem variables. After that, WOA evaluates the fitness score for each search agent by using the fitness function. The best solution is saved for further processing later.

Exploration phase: Searching for prey.

In the whale optimization algorithm, individual whales perform a random search through the positions of other individuals within the population to increase the exploration capability of the algorithm, and this behavior can be expressed by the following mathematical equation:

$$\vec{D} = \left| C \cdot \vec{X}_{rand} - \vec{X}_t \right|; \quad (50)$$

$$\vec{X}_{t+1} = \vec{X}_{rand} - A \cdot \vec{D}, \quad (51)$$

where t specifies the current iteration; X_t is the current individual; X_{rand} is the other randomly selected individuals within the population; D is the distance between the current individual and the randomly selected individuals.

The parameters A and C in (50) and (51) are coefficient vectors defined as follows:

$$A = 2a \cdot r - a; \quad (52)$$

$$C = 2 \cdot r, \quad (53)$$

where a is the parameter that decreases linearly with the number of iterations from 2 to 0; r is the uniformly distributed random number in the range of [0, 1].

Therefore, A is used with the random values $|A| > 1$ in order to guarantee the global search for the WOA algorithm. The position of every search agent is renewed according to a randomly chosen search agent.

Exploitation phase.

The local search performed by individual whales is realized by encircling predation and bubble net attack, respectively. These two behaviors can be simulated by the following mathematical model:

1) Encircling the prey.

After locating the prey, humpback whales circle around this prey to start hunting them. The WOA presumes that the current best candidate solution is the target prey or is close to the optimum. Accordingly, the overall search agents will update their new positions towards the best-determined search agent.

The following equations represent the encircling behavior:

$$\vec{D} = \left| C \cdot \overrightarrow{X^*} - \vec{X}_t \right|; \quad (54)$$

$$\vec{X}_{t+1} = \overrightarrow{X^*} - A \cdot \vec{D}, \quad (55)$$

where $\overrightarrow{X^*}$ is the position vector of the best solution obtained so far. The position of a search agent can be updated, according to the position of the current best record, by adjusting the values of A and C vectors.

2) Bubble-net attacking strategy: Spiral updating position.

After locating the prey and encircling them, humpback whales start the hunting step using the bubble-net mechanism. Two approaches to model the bubble-net demeanor of humpback whales are proposed as represented below.

The humpback whales swim around the prey within a shrinking circle and along a spiral path at the same time. To model this simultaneous behaviour, it is supposed that there is a probability of 50 % to choose the technique that will be used to update the position of whales during optimization.

The mathematical spiral equation for position update between whale and prey designed as follows:

$$\vec{D} = \left| \overrightarrow{X^*} - \vec{X}_t \right|; \quad (56)$$

$$\vec{X}_{t+1} = \vec{D} \cdot e^{bl} \cdot \cos(2\pi l) + \overrightarrow{X^*}, \quad (57)$$

where b is the constant that determines the shape of the spiral and l is the random number uniformly distributed in the range of [–1, 1].

$$l = (a_2 - 1) \cdot r + 1, \quad (58)$$

where a_2 is the linearly decreasing parameter from –1 to –2; r is the uniformly distributed random number in the range [0, 1].

When $|A| \geq 1$, the exploration phase is executed according to (50) and (51), and when $|A| < 1$, the encircling predation is executed according to (54) and (55). In addition a uniformly distributed hyper parameter p is set by which the WOA can switch between the two strategies of surround predation or bubble-net attack. Mathematically, it is modeled as follows:

$$\vec{X}_{t+1} = \begin{cases} \overrightarrow{X^*} - A \cdot \vec{D} & p < 0.5 \\ \vec{D} \cdot e^{bl} \cdot \cos(2\pi l) + \overrightarrow{X^*} & p \geq 0.5 \end{cases}. \quad (59)$$

Simulations and results. The proposed approach is applied on the standard IEEE 30 bus test system. The test system data is taken from [31]. The simulation studies were carried out in MATLAB environment. MATLAB programming codes for optimization algorithms and modified power flow algorithm to include UPFC are developed and incorporated together for the simulation purposes. In all simulation results quantities are in p.u. on a 100 MVA base.

Without RES integration. The IEEE-30 bus benchmark system consists of six generator buses, 24 load buses and 41 transmission lines. The system generator units are located at buses 1, 2, 5, 8, 11, and 13 of the network. Also, four tap-controlled transformers are connected between the transmission lines 6 to 9, 6 to 10, 4 to 12, and 27 to 28. In addition, the bus data and line data are detailed in [31]. Moreover, the voltage magnitudes of PV buses are limited from 0.9 to 1.1 (p.u.). Operating limits of the load buses are subjected from 0.9 to 1.1 (p.u.).

Initially, the system base case load flow analysis is done by the standard NR algorithm. It has real and reactive loads. The system is suffering with 17.52 MW real and 68.87 MVAr reactive power losses for a generation schedule of 40MW at bus 2 and the remaining load is supplied by slack bus 1. The components of the objective function for this operating condition are VD = 0.0222 and P_{loss} = 17.52 MW. The proposed methodology for finding optimal location of UPFC is then applied below.

For each loading condition LSI, LLI indices at each line and power losses are calculated. Based upon LSI or LLI index the critical line is identified i.e., the line with highest values of these indices and in that line UPFC is placed and again the above parameters are calculated.

1) LSI based optimal location.

At first, the LSI values are determined for all the lines and the lines are ranked in descending order. By excluding the lines which are incident to generator buses as well as those are having tap changing transformer, the top ranked lines as per LSI values associated with line number are given in Table 1 for the test system. Line # 34 (25–26) is ranked first with LSI value of 0.0493 and chosen for UPFC integration. The second is line # 38 (27–30) with LSI value of 0.0415 and so on. Considering the case of heavy load (130 %), the line (# 34) is still ranked first with respect to LSI values in descending order.

Table 1

LSI ranking

case	rank	1	2	3	4	5
Base load 100%	Line	**# 34 (25–26)**	#38 (27-30)	#18 (12-15)	#7 (4-6)	#27 (10-21)
	LSI	**0.0493**	0.0415	0.0368	0.0353	0.0323
Heavy load 130%	Line	**# 34 (25–26)**	#18 (12-15)	#33 (24-25)	#27 (10-21)	#19 (12-16)
	LSI	**0.0760**	0.0623	0.0533	0.0487	0.0482

2) LLI based optimal location.

In the same way, the LLI values are determined for all the lines and the lines are ranked in descending order. By excluding the lines which are incident to generator buses as well as those are having tap changing transformer, the top ranked lines as per LLI values associated with line number are given in Table 2 for the test system. Line # 7 (4–6) is ranked first with LLI value of 0.8253 and then chosen for UPFC integration. The same line is obtained for the case of heavy load.

Table 2

LLI ranking

case	rank	1	2	3	4	5
Base load 100 %	Line	**#7 (4-6)**	#18 (12-15)	#41 (6-28)	#27 (10-21)	#38 (27-30)
	LLI	**82.53**	60.04	59.46	57.97	45.52
Heavy load 130 %	Line	**#7 (4-6)**	#4 (3-4)	#18 (12-15)	#27 (10-21)	#41 (6-28)
	LLI	**111.13**	70.43	64.62	58.57	57.93

3) Optimal parameters of UPFC.

The WOA algorithm is applied for three cases: optimization of parameters of UPFC located according to LSI index, according to LLI index, and optimization of both location and parameters simultaneously by the optimizer. The WOA parameters considered are: number of populations is 30 and number of maximum iterations is 70.

In the optimization problem, variables are related to generator bus voltages, tap-changers, parameters in UPFC modeling and line location (depending on the case). The optimization results are summarized in Table 3.

Table 3

Optimization solution by WOA

	Base load (100 %)				Heavy load (130 %)			
Case / Variable	without UPFC	Line #34 LSI based location	Line #7 LLI based location	Line #41 WOA based location	without UPFC	Line #34 LSI based location	Line #7 LLI based location	Line #7 WOA based location
V_1	1.06	1.0796	1.0069	1.0423	1.06	1.1	1.068	1.0456
V_2	1.043	1.1	1.0046	0.9782	1.003	1.1	1.0398	1.0449
V_5	1.01	1.0064	0.9895	1.0177	0.93	1.0684	1.1	1.0183
V_8	1.01	0.9512	0.9721	1.0621	0.94	1.0438	1.1	1.0367
V_{11}	1.082	1.1	1.1	1.1000	1.032	1.0425	0.95	1.0459
V_{13}	1.071	1.1	1.1	1.1000	1.031	1.023	1.1	1.1
a_{11}	0.978	1.0924	1.1	1.1	0.978	0.9732	0.9622	1.1
a_{12}	0.969	0.9047	0.9	0.9	0.969	1.1	1.1	0.9
a_{15}	0.932	1.0243	1.0111	1.1	0.932	0.9848	1.0154	1.0047
a_{36}	0.968	0.9882	0.9597	0.9824	0.968	0.9943	0.9738	0.9577
V_{se}		0.2498	0.3	0.3		0.3	0.3	0.3
δ_{se}		3.1653	6.2832	6.2832		3.0381	6.2832	6.2832
I_q		0.0431	0.15	–0.1427		0.1023	–0.15	–0.15
P_{loss}	0.1752	0.1578	0.0495	0.0731	0.3345	0.2645	0.0873	0.0884
VD	0.0396	0.0044	0.0024	0.0065	0.0768	0.0091	0.0146	0.0059
$\sum LSI$	1.6749	1.1010	1.2823	1.3969	2.0972	1.1776	1.7657	1. 3385
$\sum LLI$	10.2120	10.5340	6.2287	11.3710	17.8972	16.5231	10.2989	9.9744

From these results, it is observed that LLI based case has provided better results than in all other cases. The optimal location based on the LLI index is line 4-6. Voltage deviation index and active losses which constitute the objective function are both minimized. The values of the control variables, voltage, turns ratios and UPFC settings are clearly shown in Table 3. LSI is decreased to 1.2823 from 1.6749 and LLI-index decreased from 10.2120 to 6.2287 for the base load. For the high load and UPFC placed in the same location, LSI is decreased to 1.3385 from 2.0972 and LLI index decreased to 9.9744 from 16.5231.

Figures 4, 5 show convergence performance for WOA method for the two loading conditions and compared with Particle Swarm Optimization (PSO) algorithm. The performance of WOA is outlined.

Then voltage profile and system losses without UPFC and with UPFC are presented in Fig. 6–9 respectively for both base load and heavy load. The voltage profiles at the network nodes depicted in Fig. 6, 7 clearly show its improvement. Figures 8, 9 indicate that globally the result based on LLI location gives losses lower for both normal load and heavy load cases.

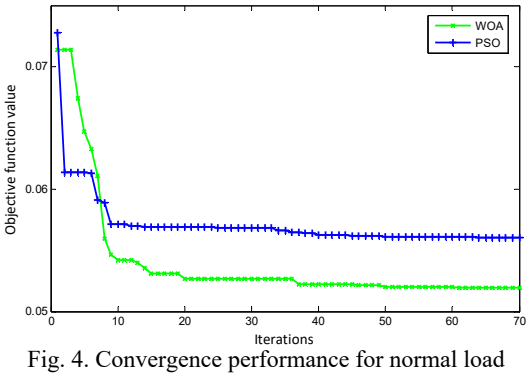

Fig. 4. Convergence performance for normal load

As the performance of UPFC has been tested on system with normal loading and 130 % loading conditions, we can notice that is providing good voltage profile as well as reduced the system losses which can be observed from the Table 3. But congestion or improved active power flow performance is better when UPFC is placed in line 4-6 than line 25-26 as well as voltage stability improvement is good when UPFC is in line 4-6 even if it is less than in line 25-26.

The results obtained from this comparative analysis prove the dominating performance of the optimization technique with the LLI based location.

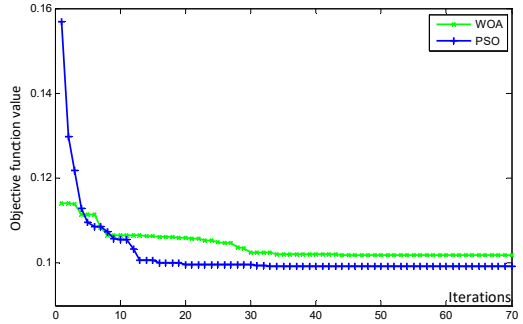

Fig. 5. Convergence performance for heavy load

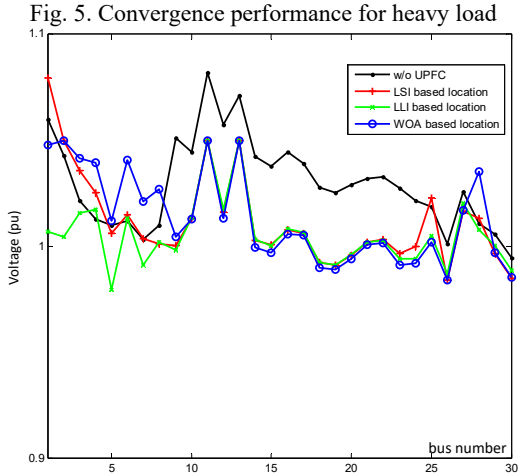

Fig. 6. Voltage profile under normal loading condition

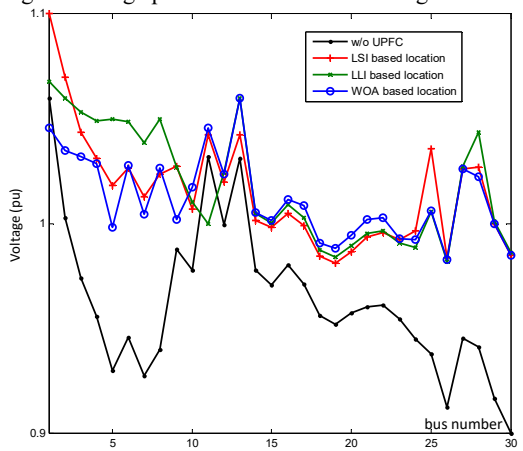

Fig. 7. Voltage profile under heavy loading condition

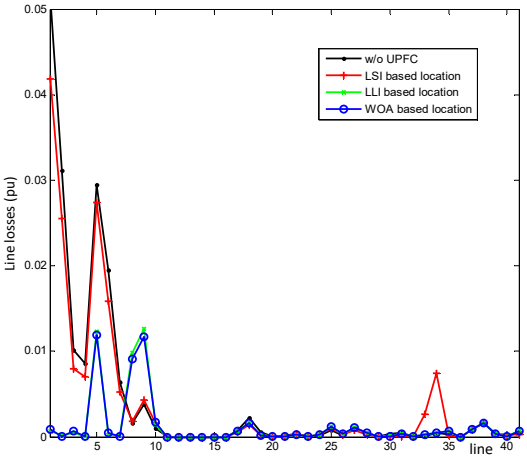

Fig. 8. Line losses under normal loading condition

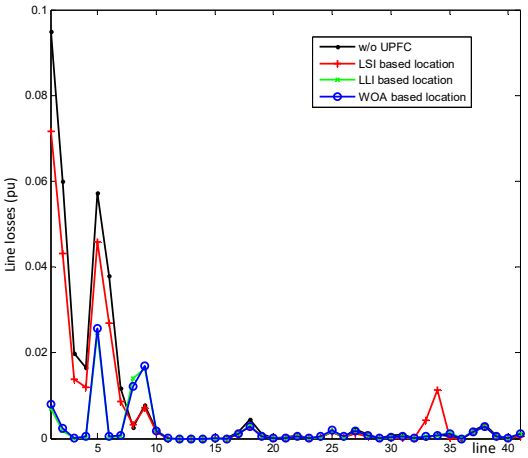

Fig. 9. Line losses under heavy loading condition

Integration of RES. In this case, the standard IEEE 30-bus system is considered by including two RES: wind farm located at bus numbers 24 and solar farm at bus 10. Moreover, the wind farms consist of several units of wind turbine generation (WTG) with a total capacity of 30 MW. The solar RES is also having a capacity of 30 MW. Unity power factor is considered for solar and 0.8 power factor for wind farm.

Their capacity will be considered as an input to the program for every case study. For different values of r_{int} ($0 \le r_{int} \le 1$), the total power supplied may or` not equal to RES installed capacity. The ratio of total RES generation to RES installed capacity is considered randomly to simulate the RES uncertainty.

The performance of UPFC integration in terms of *VD* and P_{loss} for IEEE 30-bus system under different RES intermittency conditions is shown Table 4.

The convergence performance of WOA for this case is given in Fig. 10 for moderate and heavy load. The results are summarized in Table 4. From this table, the locations obtained for the UPFC are the same as for the case without integration of RES but the set values of the voltages of the generators and the settings of the UPFC depend on the integration rate of the renewable power. Compared to the base case, the objective functions *VD* and P_{loss} are reduced for all levels of intermittency RES. Moreover, it can also be concluded that the effect of RES intermittency on the system performance is also significantly controlled by the UPFC controls by having reduced losses and improved voltage profile in all cases. This is clearly shown by voltage profile presented by Fig. 11, 12 and system losses depicted in Fig. 13, 14.

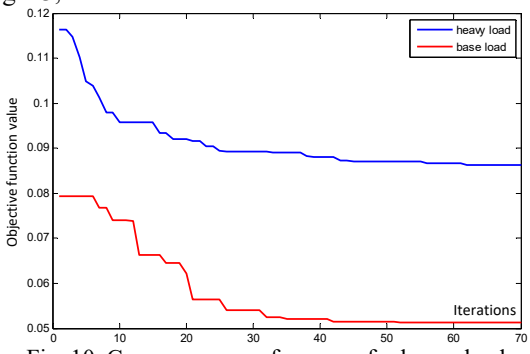

Fig. 10. Convergence performance for heavy load

Table 4

Optimization solution by WOA considering RES

	Base load (100 %)			Heavy load (130 %)		
Case	Line #34	Line #7	Line #7	Line #34	Line #7	Line #7
Variable	LSI based location	LLI based location	WOA based location	LSI based location	LLI based location	WOA based location
V_1	1.0599	1.0472	0.9982	1.1	1.0503	1.0511
V_2	1.0776	1.1	0.95	1.1	1.1	1.1
V_5	1.0252	1.009	0.95	1.0693	1.0031	1.0069
V_8	1.0595	1.0299	1.045	0.9843	1.0737	1.0532
V_{11}	0.9937	0.9551	1.0402	1.1	0.9500	0.9500
V_{13}	0.9831	1.0166	0.9507	1.0906	0.9679	0.95
a_{11}	1.0655	0.9872	10972	1.1	0.9776	1.0956
a_{12}	1.0738	1.0849	0.9	1.0077	1.1	0.9294
a_{15}	0.9629	1.0108	0.9234	1.0575	0.9614	0.9366
a_{36}	0.9563	0.9874	0.9728	1.1	0.9897	0.9873
V_{se}	0.1330	0.2311	0.2790	0.2203	0.3	0.3
δ_{se}	3.7511	0	0	3.4186	6.2832	0
I_q	–0.1058	–0.1447	0.15	0.15	–0.15	0.15
$r_{int,wind}$	0.9287	0.4854	0.3997	0.8524	0.7595	0.6039
$r_{int,solar}$	0.7920	0.3881	0.1402	0.9453	0.6983	0.7226
P_{loss}	0.1168	0.0461	0.0491	0.2004	0.0789	0.0771
VD	0.0069	0.0071	0.0023	0.0178	0.0074	0.0083
$\sum LSI$	1.5310	1.2192	1.2355	2.0247	1.4287	1.4920
$\sum LLI$	8.0148	4.5651	4.8779	14.5057	7.4804	7.5613

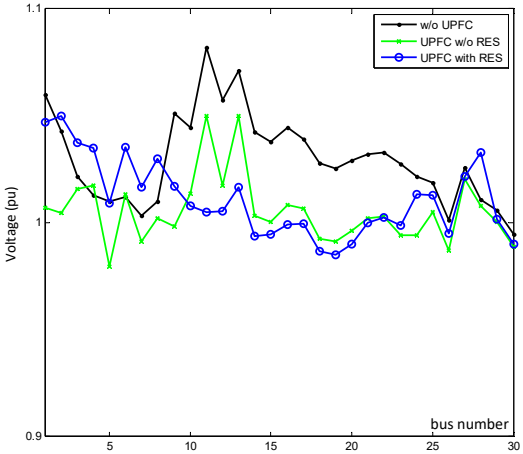

Fig. 11. Voltage profile under normal loading condition with RES

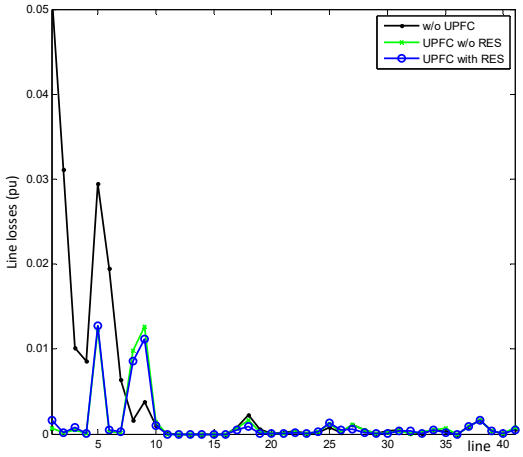

Fig. 13. Line losses under normal loading condition with RES

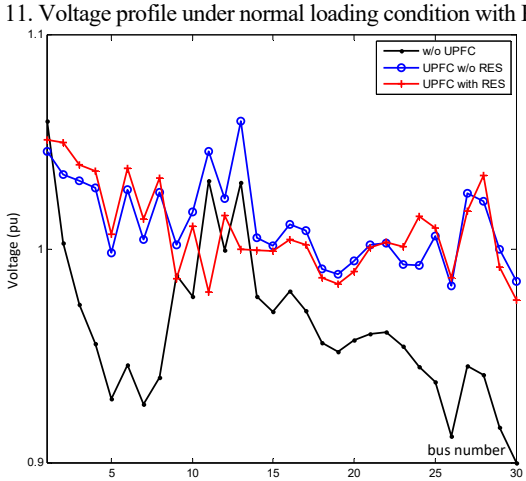

Fig. 12. Voltage profile under heavy loading condition with RES

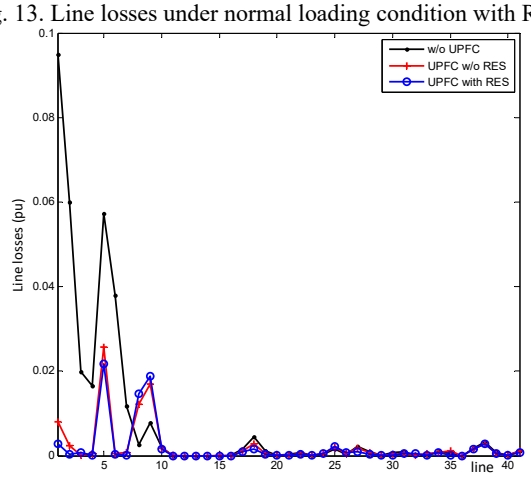

Fig. 14. Line losses under heavy loading condition with RES

Conclusions. In this work, a methodology was presented to evaluate the WOA meta-heuristic for the allocation of UPFC in electrical power systems where the penetration of renewable energy sources (RES) and their intermittency are considered. The location of UPFC device is determined by using line stability index (LSI) and line loading index (LLI) with combination of the meta-heuristic technique. The simulation studies on standard 30-bus system highlighted the effectiveness of the search process for the solution of the allocation problem of UPFC by providing improved voltage profile and reduced losses. The parameters involved in the optimization problem are optimized using WOA algorithm towards improved performance system. Indeed, the results showed that using the UPFC at optimal location in the network yields a significant reduction in power loss and minimization of voltage deviation while satisfying the network equality and inequality constraints.

On the other side, as power systems become more complex with deeper penetration of RES, the impact of RES uncertainty

was also analyzed indicating a significant influence on the overall transmission loss and voltage profile enhancements of the network. The performance of WOA was evaluated by comparison with PSO algorithm which indicates more efficiency.

Conflict of interest. The authors declare that they have no conflicts of interest.

REFERENCES

1. Mutegi M.A., Nnamdi N.I. Optimal Placement of FACTS Devices Using Filter Feeding Allogenic Engineering Algorithm. *Technology and Economics of Smart Grids and Sustainable Energy*, 2022, vol. 7, no. 1, art. no. 2. doi: https://doi.org/10.1007/s40866-022-00132-3.

2. Akumalla S.S., Peddakotla S., Kuppa S.R.A. A Modified Cuckoo Search Algorithm for Improving Voltage Profile and to Diminish Power Losses by Locating Multi-type FACTS Devices. *Journal of Control, Automation and Electrical Systems*, 2016, vol. 27, no. 1, pp. 93-104. doi: https://doi.org/10.1007/s40313-015-0219-x.

3. Govindaraghavan G., Varadarajan R. Hybrid KHSO Based Optimal Location and Capacity of UPFC for Enhancing the Stability of Power System. *Gazi University Journal of Science Part A: Engineering and Innovation*, 2018, vol. 5, no. 4, pp. 141-157.

4. Shehata A.A., Tolba M.A., El-Rifaie A.M., Korovkin N.V. Power system operation enhancement using a new hybrid methodology for optimal allocation of FACTS devices. *Energy Reports*, 2022, vol. 8, pp. 217-238. doi: https://doi.org/10.1016/j.egyr.2021.11.241.

5. Zahid M., Chen J., Li Y., Duan X., Lei Q., Bo W., Mohy-ud-din G., Waqar A. New Approach for Optimal Location and Parameters Setting of UPFC for Enhancing Power Systems Stability under Contingency Analysis. *Energies*, 2017, vol. 10, no. 11, art. no. 1738. doi: https://doi.org/10.3390/en10111738.

6. Kishore A.Y., Mohan B.G. Enhancement of Voltage stability and Transmission Congestion management with UPFC. *International Journal of Grid and Distributed Computing*, 2018, vol. 11, no. 6, pp. 15-26. doi: https://doi.org/10.14257/ijgdc.2018.11.6.02.

7. Kalyani Radha P. Nonlinear optimization approach for UPFC power flow control and voltage security: Sufficient system constraints for optimality. *Doctoral Dissertation*, 2007.

8. Abdo M., Kamel S., Ebeed M., Yu J., Jurado F. Solving Non-Smooth Optimal Power Flow Problems Using a Developed Grey Wolf Optimizer. *Energies*, 2018, vol. 11, no. 7, art. no. 1692. doi: https://doi.org/10.3390/en11071692.

9. Rao B.V. Sensitivity Analysis based Optimal Location and Tuning of Static VAR Compensator using Firefly Algorithm. *Indian Journal of Science and Technology*, 2014, vol. 7, no. 8, pp. 1201-1210. doi: https://doi.org/10.17485/ijst/2014/v7i8.15.

10. Vijay Kumar B., Srikanth N.V. Optimal location and sizing of Unified Power Flow Controller (UPFC) to improve dynamic stability: A hybrid technique. *International Journal of Electrical Power & Energy Systems*, 2015, vol. 64, pp. 429-438. doi: https://doi.org/10.1016/j.ijepes.2014.07.015.

11. AL Ahmad A., Sirjani R. Optimal placement and sizing of multi-type FACTS devices in power systems using metaheuristic optimisation techniques: An updated review. *Ain Shams Engineering Journal*, 2020, vol. 11, no. 3, pp. 611-628. doi: https://doi.org/10.1016/j.asej.2019.10.013.

12. Padma K., Maru Y.S. Comparative Analysis of a Performance of Metaheuristic Algorithms in Solving Optimal Power Flow Problems with UPFC Device in the Transmission System. *International Journal of Recent Technology and Engineering (IJRTE)*, 2021, vol. 9, no. 5, pp. 316-326. doi: https://doi.org/10.35940/ijrte.E5301.019521.

13. Abdullah Salman G., Hasan Ali M., Najim Abdullah A. Implementation Optimal Location and Sizing of UPFC on Iraqi Power System Grid (132 kV) Using Genetic Algorithm. *International Journal of Power Electronics and Drive Systems (IJPEDS)*, 2018, vol. 9, no. 4, pp. 1607-1615. doi: https://doi.org/10.11591/ijpeds.v9.i4.pp1607-1615.

14. Patil B., Karajgi S.B. Optimized placement of multiple FACTS devices using PSO and CSA algorithms. *International Journal of Electrical and Computer Engineering (IJECE)*, 2020, vol. 10, no. 4, pp. 3350-3357. doi: https://doi.org/10.11591/ijece.v10i4.pp3350-3357.

15. Kavuturu K.V.K., Narasimham P.V.R.L. Optimal Parameters of OUPFC and GUPFC Under Renewable Energy Power Variation Using Cuckoo Search Algorithm Variants. *Journal of Electrical Engineering & Technology*, 2020, vol. 15, no. 5, pp. 2079-2098. doi: https://doi.org/10.1007/s42835-020-00501-x.

16. Sunday Y.S., Ubeh O.P., Saidu A.A., Fahad A. Grey wolf optimizer based optimal placement of multiple facts devices in the transmission system under dynamic loading system. *Journal of Engineering Studies and Research*, 2021, vol. 27, no. 1, pp. 132-143. doi: https://doi.org/10.29081/jesr.v27i1.262.

17. Laifa A. Application of harmony search method for UPFC location for enhancing power system security. *2015 International Conference on Smart Grid and Clean Energy Technologies (ICSGCE)*, 2015, pp. 154-158. doi: https://doi.org/10.1109/ICSGCE.2015.7454288.

18. Vijay Kumar B. Optimal Location of Upfc to Improve Power System Voltage Stability Using Artificial Bee Colony Algorithm. *American Journal of Electrical Power and Energy Systems*, 2019, vol. 8, no. 2, pp. 42-49. doi: https://doi.org/10.11648/j.epes.20190802.11.

19. Abdul Hamid Z., Musirin I., Adli Nan M.A., Othman Z. Optimal Voltage Stability Improvement under Contingencies using Flower Pollination Algorithm and Thyristor Controlled Series Capacitor. *Indonesian Journal of Electrical Engineering and Computer Science*, 2018, vol. 12, no. 2, pp. 497-504. doi: https://doi.org/10.11591/ijeecs.v12.i2.pp497-504.

20. Rezaee Jordehi A. Brainstorm optimisation algorithm (BSOA): An efficient algorithm for finding optimal location and setting of FACTS devices in electric power systems. *International Journal of Electrical Power & Energy Systems*, 2015, vol. 69, pp. 48-57. doi: https://doi.org/10.1016/j.ijepes.2014.12.083.

21. Kavitha K., Neela R. Optimal Placement of UPFC to Enhance System Security Using BBO Technique. *World Applied Sciences Journal,* 2016, vol. 34, no. 10, pp. 1326-1337. doi: https://doi.org/10.5829/idosi.wasj.2016.1326.1337.

22. Nada Kh., Alrikabi M.A. Renewable energy types. *Journal of Clean Energy Technologies*, 2014, vol. 2, no. 1, pp. 61-64. doi: https://doi.org/10.7763/JOCET.2014.V2.92.

23. Vadivelu K.R., Marutheswar G.V. Fast voltage stabilty index based optimal reactive power planning using differential evolution. *Electrical and Electronics Engineering: An International Journal (ELELIJ)*, 2014, vol. 3, no. 1, pp. 51-60.

24. Samuel I.A., Katende J., Awosope C.O.A., Awelewa A.A. Prediction of voltage collapse in electrical power system networks using a new voltage stability index. *International Journal of Applied Engineering Research*, 2017, vol. 12, no. 2, pp. 190-199.

25. Bourzami A., Amroune M., Bouktir T. On-line voltage stability evaluation using neuro-fuzzy inference system and moth-flame optimization algorithm. *Electrical Engineering & Electromechanics*, 2019, no. 2, pp. 47-54. doi: https://doi.org/10.20998/2074-272X.2019.2.07.

26. Mishra A., Nagesh Kumar G.V. A Line Utilization Factor and Krill Herd Algorithm based Optimal Utilization of Interline Power Flow Controller for Congestion Management. *International Journal of Electrical and Electronics Research*, 2015, vol. 3, no. 3, pp. 58-65. doi: https://doi.org/10.37391/IJEER.030304.

27. Naganathan A., Ranganathan V. Improving Voltage Stability of Power System by Optimal Location of FACTS Devices Using Bio-Inspired Algorithms. *Circuits and Systems*, 2016, vol. 07, no. 06, pp. 805-813. doi: https://doi.org/10.4236/cs.2016.76069.

28. Mirjalili S., Lewis A. The Whale Optimization Algorithm. *Advances in Engineering Software*, 2016, vol. 95, pp. 51-67. doi: https://doi.org/10.1016/j.advengsoft.2016.01.008.

29. Shahbudin I.S., Musirin I., Suliman S.I., Harun A.F., Syed Mustaffa S.A., Suyono H., Md Ghani N.A. FACTS device installation in transmission system using whale optimization algorithm. *Bulletin of Electrical Engineering and Informatics*, 2019, vol. 8, no. 1, pp. 30-38. pp. https://doi.org/10.11591/eei.v8i1.1442.

30. Mehdi M.F., Ahmad A., Ul Haq S.S., Saqib M., Ullah M.F. Dynamic economic emission dispatch using whale optimization algorithm for multi-objective function. *Electrical Engineering & Electromechanics*, 2021, no. 2, pp. 64-69. doi: https://doi.org/10.20998/2074-272X.2021.2.09.

31. Available at: http://www.ee.washington.edu/research/pstca/pf30/pg_tca30bus.htm (Accessed 3 May 2022).

Received 22.09.2022
Accepted 17.12.2022
Published 07.03.2023

Abdelaziz Laifa[1], *Doctor of Science,*
Bilel Ayachi[1], *Doctor of Science,*
[1] Department of Electrical Engineering,
University of August 20, 1955, Skikda, Algeria,
e-mail: a.laifa@univ-skikda.dz (Corresponding Author);
b.ayachi@univ-skikda.dz

How to cite this article:
Laifa A., Ayachi B. Application of whale algorithm optimizer for unified power flow controller optimization with consideration of renewable energy sources uncertainty. *Electrical Engineering & Electromechanics*, 2023, no. 2, pp. 69-78. doi: https://doi.org/10.20998/2074-272X.2023.2.11

UDC 621.3 https://doi.org/10.20998/2074-272X.2023.2.12

M. Manohara, V.C. Veera Reddy, M. Vijaya Kumar

Exploration and mitigation of power quality problems in radial distribution system by placing distributed generation through voltage stability index

Introduction. *Distributed generation has played an important role in many aspects of sustainability, such as improving voltage profiles and reducing power losses, in the distribution network.* ***Problem.*** *Frequent variation of loads causes many complications while placing and sizing of distributed generation in the radial distribution network, via quality of supply, and stability of the system.* ***Goal*** *of the paper is to investigate and mitigate the power quality issues towards stabilizing the system during distributed generations placed in the system under various loading conditions.* ***Methodology.*** *The line voltage stability index analyses and enhances the performance of the radial distribution network by effective sizing and location of distributed generation towards the objective function.* ***Practical value.*** *A standard test system IEEE-69 bus radial distribution network is used to understand through MATLAB environment.* References 38, table 4, figures 11.

Key words: **voltage stability index, distribution system, voltage sag, power quality, distributed generation.**

Вступ. *Розподілена генерація відіграла важливу роль у багатьох аспектах стійкості, таких як покращення профілів напруги та зниження втрат електроенергії у розподільній мережі.* ***Проблема***. *Часті коливання навантаження викликають безліч складнощів при розміщенні та визначенні розміру розподіленої генерації в радіальній розподільній мережі через якість постачання та стабільність системи.* ***Мета*** *статті полягає в тому, щоб дослідити та пом'якшити проблеми з якістю електроенергії для стабілізації системи під час розподіленої генерації, розміщеної у системі за різних умов навантаження.* ***Методологія.*** *Індекс стабільності лінійної напруги аналізує та підвищує продуктивність радіальної розподільної мережі за рахунок ефективного визначення розміру та розташування розподіленої генерації щодо цільової функції.* ***Практична цінність***. *Для розуміння використовується стандартна тестова система радіальної розподільної мережі IEEE-69 за допомогою середовища MATLAB.* Бібл. 38, табл. 4, рис. 11.

Ключові слова: **індекс стабільності напруги, розподільна система, провали напруги, якість електроенергії, розподілена генерація.**

Introduction. Regardless of enhancement value in the active power and the developments of transmission and distribution system, ongoing development of touchy loads and utilizing them in modern and medical clinic places, the quality issue of power is significant. Power quality issues like voltage sag are because by some reasons like shortcomings, abrupt burden increment, and an enormous increase in the consumption of electrical appliances. Voltage droop in modern delicate burdens emerges because of short out in various pieces of the organization. Voltage dip under basic worth in these heaps causes malfunctioning of electrical hardware and efficient misfortunes, accordingly, an answer for this issue ought to be found.

Distributed generation (DG) additionally increments the age limit and to ease public worries about contamination, conveyed age plants have been presented in circulation organizations. By expanding the short-out limit, the establishment of DG assets can forestall voltage hang in touchy burdens. The extent of voltage list after issue exceptionally relies upon the way between the issue area and delicate loads just as short out limits such that the DG and reconfiguration of the network can be implemented. Changing the geography of the organization won't improve the circumstance; in addition, other organization imperatives might restrict the execution of every single arrangement. Besides, to acquire the benefit of the DG assets, a few boundaries, like the finest area, no. and limit of the DGs are required. Another issue is while fusing them for a huge scope for example glitches of assurance circuits, recurrence deviation, voltage profile rising, and dependability issues; in this manner, every one of referenced strategies is powerful however numerous limitations are being used every one of them independently [1-5].

DG assets designation is likewise a muddled improvement issue for which various techniques were utilized to tackle before. Viral and Khatod completed an exhaustive audit of various strategies, for example, scientific, meta-heuristic, man-made reasoning, and hereditary calculations crossover draws near. In scientists applied the affectability examination for DG assets distribution; besides, reconfiguration and DG assets portion cooperatively diminish misfortune at three diverse burdens [6-9]. DG assets assignment for further developing power quality lists is another point that is introduced by a couple of analysts of late. Hamedi and Gandomkar thought about the power quality due to DG assets. Though utilizing DG assets for further developing voltage lists is worthwhile, it isn't sufficient in substantial burdens or extreme deficiencies; in addition, as referenced previously, fusing DG assets for a huge scope would prompt genuine results. In this manner, it is strongly prescribed to apply different strategies, for example, reconfiguration alongside utilizing DG assets [10-24].

As previously stated, to improve voltage sag induced by failures, reconfiguration and DG resource placement have been explored separately. The fundamental idea of this work is to use both reconfiguration and DG resource placement at the same time to improve voltage sag while still achieving the main goal of reconfiguration (loss reduction) [25-30]. The ideal DG resource capacity and network design can be accomplished by inserting the DG resource in one of the distribution network buses and a trade-off between power quality indices and system power loss. The BPSO algorithm is used for optimization because of its simplicity and great efficiency in reconfiguration situations. The proposed method is highly effective at reducing voltage sag, as evidenced by the results [31-35].

Problem formulation. In the operation and control of Radial Distribution Network (RDN), minimization of real power loss is one of the major goals. This can be achieved mainly by improving the voltage profile across the network, and consequently, the loss can reduce by

having reduced current flow through each branch/element. In addition, an improved voltage profile can result in enhanced voltage stability.

Objective function. The primary objective is to consider loss minimization in the feeder by having maximum PV penetration at appropriate locations. The real power loss of a branch in a distribution system is given by:

$$\min f(P_{loss}) = \sum_{mn} r_{(mn)} I^2_{(mn)}, \quad (1)$$

where P_{loss} is the total real power loss in the feeder distribution; mn is the branch index; $P(n)$, $Q(n)$, $|V(n)|$ are the real, reactive power loads and voltage magnitude of the n^{th} bus.

The following bus voltage, branch current, DG active, and reactive power compensation constraints are considered in solving the proposed objective function:

$$|V_i|_{\min} \le |V_i| \le |V_i|_{\max} \quad i = 1,2,...,nb, \quad (2)$$

$$|I_i| \le |I_i|_{\max} \quad i = 1,2,...,nl, \quad (3)$$

$$Q_{cb(T)} \le Q_{load(T)}. \quad (4)$$

Enhancement of power quality. There are many quality issues that arise at the end user because of load variations. The major focus is to minimize the voltage sag and voltage swell. The system voltage profile must be increased to voltage sag limits 0.9 to 1.

Mathematical model. The huge R/X ratio in RDNs leads traditional load flow algorithms to fail to converge. A single-line diagram of a balanced RDN can be used to depict the network. So, at the distribution operating voltage, line shunt capacitances are highly malleable and may thus be ignored [5, 36]. The i-node apparent power is calculated for i^{th} node is given by

$$S_i = V_i (LI)^*_i = P_i + jQ_i. \quad (5)$$

Branch current calculations:

$$I_{brj} = \sum_{i=1}^{n} |LI_i| \cos\theta_i + j \sum_{i=1}^{n} |LI_i| \sin\theta_i = \mathrm{Re}(I_{brj}) + \mathrm{Im}(I_{brj}). \quad (6)$$

Receiving end voltage calculations are [37, 38]:

$$V_r = V_s - I_{br} Z_{br}; \quad (7)$$

$$V_r \angle\theta_r = V_s \angle\theta_s - I_{br} \angle\theta_r Z_{br} \angle\theta_r. \quad (8)$$

Equations (6)-(8) are used to compute branch currents as well as the bus voltages. The active and reactive power at each bus is estimated from the above I_{br} and V_{br}.

Line voltage stability index. Voltage instability is the result of the power system's inability to handle the additional demand brought on by the growing load. However, studies of this kind don't typically produce stability or sensitivity data. So, dynamic simulations can only be used to study certain types of voltage collapse, like sudden or transient voltage collapse, and to make sure that protection and control are working together.

Voltage stability requirements were created based on a paradigm for power transmission on a single line. By reducing a linked system to a single-line network, the overall stability of the system is evaluated. Using the same idea, a stability requirement is constructed and applied to every network line. The line voltage stability index (LVSI) is given by (9)

$$LVSI = \frac{4XQ_r}{[V_s \sin(\theta - \delta)]^2} \le 1. \quad (9)$$

In an interconnected network that connects two bus bars, the stability criteria known as LVSI are utilized to determine the stability index for each line. Line stability indices can be used to predict voltage collapse with accuracy. As long as the stability index is less than 1, the system is stable. However, if it exceeds 1, the system as a whole loses stability, leading to voltage collapse.

Distributed generation. Depending on the different powers available, the DG is classified into four types [3].

Type 1: This form of DG can only supply active electricity, such as photovoltaic (PV), microturbines, and fuel cells, and is connected to the main grid via converters/inverters.

Type 2: Only reactive power may be delivered via DG. Gas turbines and capacitor banks are examples of synchronous compensators, which perform at zero power factors.

Type 3: DG can supply real power while also using reactive power. This category mostly includes induction generators used in wind farms. However, like synchronous generators, doubly-fed induction generators devices can utilize or create reactive power.

Type 4: Both active and reactive electricity can be delivered via DG. This category includes synchronous machine-based DG units (cogeneration, gas turbine, and so on).

Static mathematical model of DG. The real and reactive power at the i^{th} bus is modeled as below [4]:

$$P_i = P_{DG_i} - P_{D_i}; \quad (10)$$

$$Q_i = Q_{DG_i} - Q_{D_i} = \alpha_i \times P_{DG_i} - Q_{D_i}; \quad (11)$$

$$\alpha_i = \tan(\cos^{-1} PF_{DG});$$

where P_{DG} is the real power at DG; Q_{DG} is the reactive power at DG; P_D is the real power demand; Q_D is the reactive power demand; PF_{DG} is the power factor.

The power factor is determined by the kind of DG and the DG unit's working state:

Type 1 – $PF_{DGi} = 1$;

Type 2 – PFDGi = 0;

Type 3 – $0 < PF_{DGi} < 1$ and sign = –1;

Type 4 – $0 < PF_{DGi} < 1$ and sign = +1.

DG in load flow analysis. DG as load bus. PQ buses made up of DGs can be treated as passive loads or negative loads. The quantity of DG produced reduces the total burden.

DG units as PV bus. The modeling of DGs managed like PV buses are more difficult than that of PQ buses. The compensating approach from [7] is used to modulate the voltage of PV nodes.

Impacts of DG installation. The system with DG is shown in Fig. 1, where Z_3 is the impedance between PCC and DG resources, while Z_4 is the DG resources' transient reactance. As the capacity of DG resources grows, branch-power flow decreases, voltage drops decrease, and V_p approaches 1 p.u. as a typical value. As a result, the voltage of the sensitive load increases by 1. Furthermore, the placement of DG resources has an impact on Z_3, and raising Z_3 sensitive load voltage might increase Z_3.

The magnitude of the sag is calculated as:

$$V_{sag} = 1 - \left[\frac{Z_4}{Z_3 + Z_4} \cdot (1 - V_{PCC}) \right]; \quad (12)$$

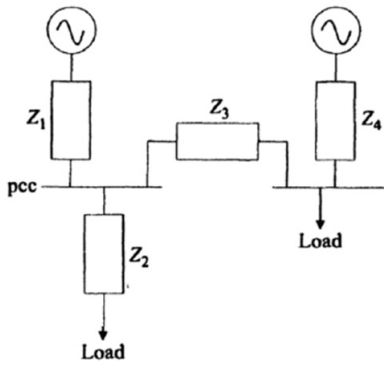

Fig. 1. A simple system representing the load

Computational aspects to reach the objective.

Step-I: Read the system data and set all node voltages and branch currents to 1.0 p. u. (per unit) at the beginning.

Step-II: Calculate the branch currents.

Step-III: Update the bus voltages with branch currents as in step II.

Step-IV: Calculate the power and power losses at each bus.

Step-V: Identify the candidate bus using LVSI analysis.

Step-VI: Estimate the voltage sag and swell by comparing the voltage values from the results.

Step-VII: Select and calculate the size of DG, and place it randomly at each bus to minimize the losses.

Step VIII: Again, repeat Step IV, if it is in constraints then go to the next step else go to Step II.

Step IX: Stop.

Proposed algorithm. The schematic representation of the proposed algorithm flow toward the theme as shown in Fig. 2.

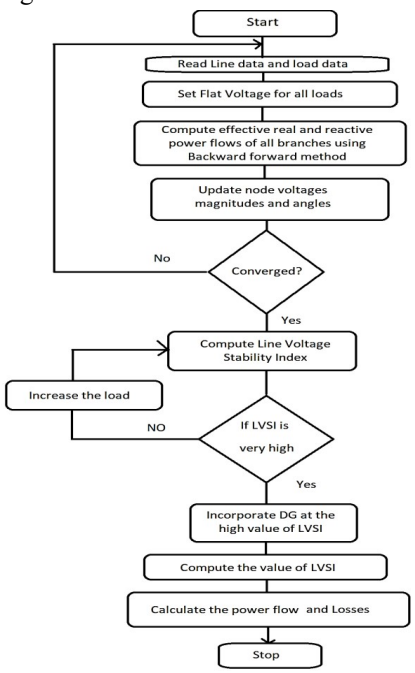

Fig. 2. Flowchart of the proposed algorithm

Test system and simulation results. To comprehend the suggested algorithm, a simulation of the IEEE-69 radial distribution system is taken into account. There are 48 load buses and 68 lines in this system. Table 1 lists the load buses that were taken into account when analyzing the IEEE-69 bus system. As bus number one is regarded as the generator bus in the radial distribution network, only 48 of the 69 buses are load buses, and the rest are not connected to any loads.

Table 1

Considered load buses for analysis in IEEE-69 bus system

S. No.	Bus No.	S. No.	Bus No.	S. No.	Bus No.	S. No.	Bus No.
1	6	13	20	25	37	37	53
2	7	14	21	26	39	38	54
3	8	15	22	27	40	39	55
4	9	16	24	28	41	40	59
5	10	17	26	29	43	41	61
6	11	18	27	30	45	42	62
7	12	19	28	31	46	43	64
8	13	20	29	32	48	44	65
9	14	21	33	33	49	45	66
10	16	22	34	34	50	46	67
11	17	23	35	35	51	47	68
12	18	24	36	36	52	48	69

Comparative analysis of distribution load flows for 69 bus system. In Table 2 describe and analyzed the 69-bus system during composite load models and figures out its behaviour with critical buses and voltage profile. In fact, in many cases, it is noticed that the system reaches sag conditions.

Table 2

Comparative analysis of 69-bus system

Type of load	P, kW	Q, kVAR	P losses, kW	Q losses, kVAR	V_{min}, p.u.	Bus numbers
DLF	3033.43	2275.07	123.94	56.386	0.93155	6, 7, 57, 58, 59, 60, 61, 66
Constant P Model	3825.02	2635.20	317.19	143.49	0.87549	6, 7, 57, 58, 59, 60, 61, 66
Constant I Model	3567.15	2469.34	245.93	112.97	0.89139	6, 7, 57, 58, 59, 61, 66
Constant Z Model	3337.11	2319.30	192.44	89.98	0.90492	6, 7, 57, 58, 66

The voltage sag condition without DG for the load variation is shown in Fig. 3 for conditions ranging from 50 % system loading to 150 % system loading. The voltage on each individual bus drops as the load rises. Without adding DG to the system, the lowest voltage for 50 %, 100 %, and 150 % system loading conditions is at bus numbers 63 and 27. For 50 %, 100 %, and 150 % system loads, bus numbers 28 and 36 have maximum voltages of 1, 0.99, 0.999, and 0.999, respectively.

The active power flow and the reactive power flow in the system without DG are shown in Fig. 4, 5 for the load variation from a 50 % system loading state to a 150 % system loading condition. Figures 6, 7 display the active power and reactive power loss in the system.

Table 3 shows the voltage profile for different loading scenarios without DG in the system. The voltage sag observed through the index value is presented in Table 3. The high value of the index at a particular bus is considered to have voltage sag at that bus. Compared to all the load buses available in the system, bus no. 6 is the most complex load bus with the maximum sag.

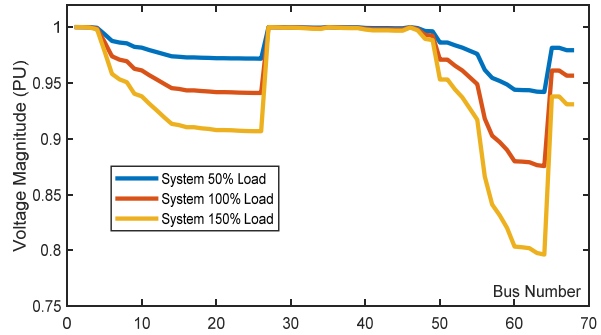

Fig. 3. Voltage sag condition without DG in IEEE-69 bus system

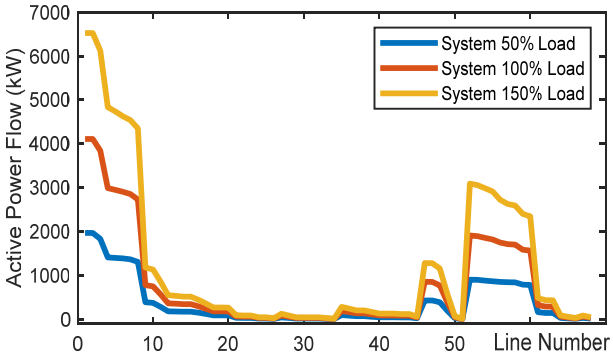

Fig. 4 Active power flow without DG in IEEE-69 bus system

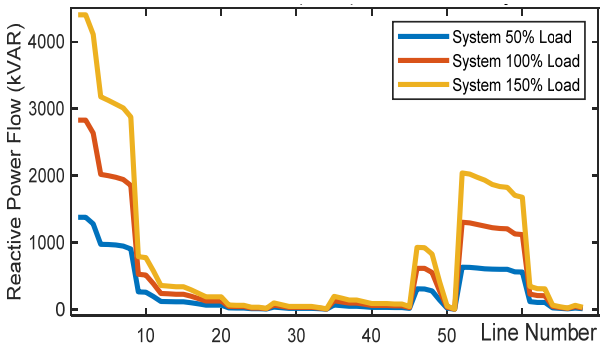

Fig. 5. Reactive power flow without DG in IEEE-69 bus system

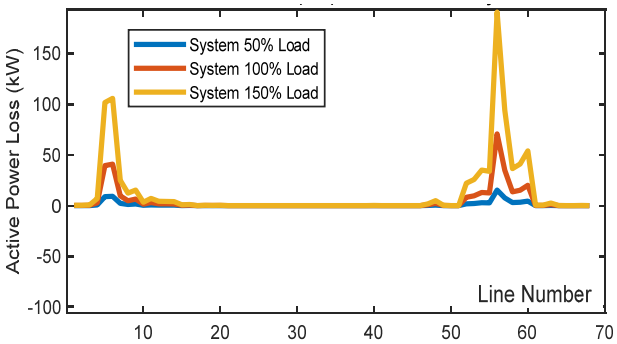

Fig. 6. Active power loss without DG in IEEE-69 bus system

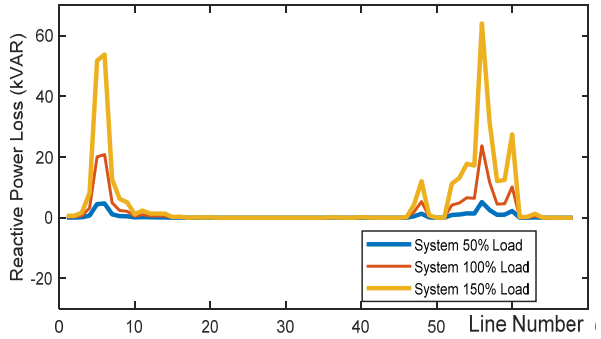

Fig. 7. Reactive power loss without DG in IEEE-69 bus system

Table 3
Identification of voltage sag through line voltage stability index

Bus. no.	Index value		
	50 % system loading	100 % system loading	150 % system loading
6	0.0289	0.0598	0.0936
7	0.0301	0.0623	0.0976
8	0.0072	0.015	0.0237
9	0.0037	0.0077	0.0122
10	0.024	0.049	0.0752
11	0.0054	0.011	0.017
12	0.0153	0.0313	0.0483
13	0.0138	0.0283	0.0437
14	0.0137	0.0281	0.0435
16	0.0025	0.0052	0.0081
17	0.0042	0.0086	0.0133
18	0	0.0001	0.0001
20	0.0015	0.0031	0.0048
21	0.0024	0.005	0.0078
22	0	0.0001	0.0001
24	0.0008	0.0016	0.0025
26	0.0004	0.0007	0.0011
27	0.0001	0.0002	0.0003
28	0	0	0
29	0.0001	0.0003	0.0004
33	0.0013	0.0026	0.0039
34	0.0017	0.0034	0.0051
35	0.0003	0.0007	0.001
36	0	0.0001	0.0001
37	0.0003	0.0007	0.001
39	0.0001	0.0002	0.0003
40	0	0	0
41	0.0014	0.0028	0.0042
43	0.0001	0.0002	0.0002
45	0.0002	0.0004	0.0006
46	0	0	0
48	0.0024	0.0049	0.0074
49	0.0075	0.0151	0.0226
50	0.0011	0.0021	0.0032
51	0.0001	0.0002	0.0004
52	0	0.0001	0.0002
53	0.0091	0.0191	0.0305
54	0.0106	0.0222	0.0355
55	0.0146	0.0306	0.0489
59	0.0211	0.0449	0.0731
61	0.0244	0.052	0.0847
62	0.001	0.0021	0.0034
64	0.0063	0.0135	0.0222
65	0.0019	0.0041	0.0067
66	0.0003	0.0006	0.001
67	0	0	0
68	0.0017	0.0034	0.0053
69	0	0	0

The DG is located at bus number 35, and it has the same power loss as other DGs of similar capacity when placed in other buses. Its size is 0.035 MW. As the load increases, the voltage at each bus drops. Since DG was incorporated into the system, the voltage sag at each individual load bus has improved. For three system loading scenarios, the maximum voltage is at bus nos. 28, and 36, respectively.

Figures 8, 9 depict the active power flow and reactive power flow in the system with DG for the load fluctuation from 50 % system loading condition to 150 % system loading condition. Figures 10, 11 show the system's reduced active and reactive power with DG in place.

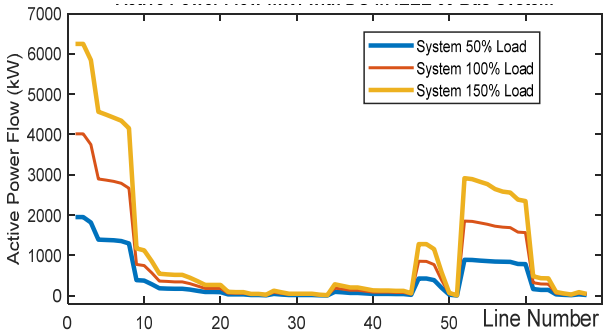

Fig. 8. Active power flow with DG in IEEE-69 bus system

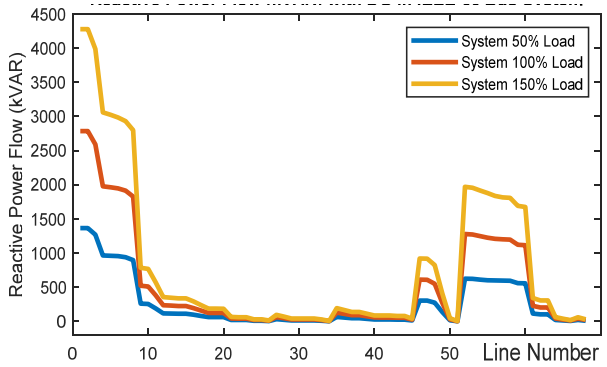

Fig. 9. Reactive power flow with DG in IEEE-69 bus system

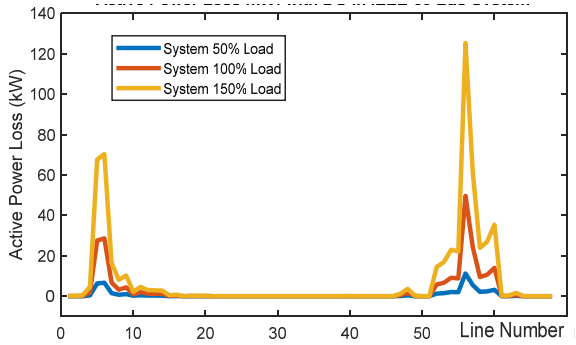

Fig. 10. Active power loss with DG in IEEE-69 bus system

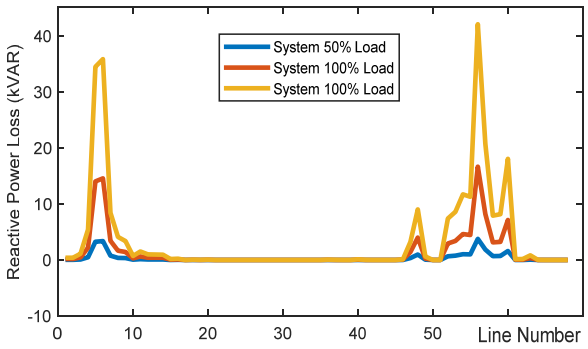

Fig. 11. Reactive power loss with DG in IEEE-69 bus system

Table 4 presents the improvement of voltage sag incorporating DG in the system. The minimum voltage is at bus no. 26 and 27 and is 0.9855, 0.9705, 0.9553 for 50 %, 100 %, and 150 % system loading condition respectively. The maximum voltage is at the bus no. 36 for 50 %, 100 %, and 150 % system loading condition respectively. The voltage sag with DG in the system has been enhanced compared without DG in the system. The change in the voltage in the system can also be observed.

Table 4

Improvement of voltage sag incorporating DG in the system

Bus. no.	Index value		
	50% system loading	100% system loading	150% system loading
6	0.0215	0.0439	0.0677
7	0.0224	0.0457	0.0705
8	0.0053	0.011	0.017
9	0.0027	0.0056	0.0087
10	0.0173	0.0352	0.0536
11	0.0039	0.0079	0.0121
12	0.0109	0.0221	0.0338
13	0.0103	0.021	0.0322
14	0.0102	0.0209	0.032
16	0.0019	0.0039	0.0059
17	0.0031	0.0064	0.0098
18	0	0.0001	0.0001
20	0.0011	0.0023	0.0036
21	0.0018	0.0037	0.0057
22	0	0.0001	0.0001
24	0.0006	0.0012	0.0019
26	0.0003	0.0005	0.0008
27	0.0001	0.0002	0.0002
28	0	0	0
29	0.0001	0.0002	0.0003
33	0.001	0.0019	0.0029
34	0.0013	0.0026	0.0039
35	0.0002	0.0005	0.0007
36	0	0	0.0001
37	0.0003	0.0005	0.0008
39	0.0001	0.0001	0.0002
40	0	0	0
41	0.0011	0.0021	0.0032
43	0.0001	0.0001	0.0002
45	0.0001	0.0003	0.0004
46	0	0	0
48	0.0018	0.0037	0.0056
49	0.0057	0.0114	0.0171
50	0.0008	0.0016	0.0024
51	0.0001	0.0002	0.0003
52	0	0.0001	0.0001
53	0.0068	0.014	0.0219
54	0.0079	0.0163	0.0255
55	0.0109	0.0225	0.0352
59	0.0157	0.0328	0.0518
61	0.0182	0.038	0.06
62	0.0007	0.0015	0.0024
64	0.0047	0.0098	0.0156
65	0.0014	0.003	0.0047
66	0.0002	0.0005	0.0007
67	0	0	0
68	0.0006	0.0013	0.002
69	0	0	0

Discussions.

1. The IEEE-69 bus system performance is analyzed during composite and different loading conditions.

2. The location and sizing of DG is estimated to mitigate the power quality issues.

3. LVSI indices provide the system stability with and without DG at each location.

4. Enhancement of RDS performance by appropriate DG placement with the LVSI method.

Conclusions.

The effectiveness of the IEEE-69 bus radial distribution system is examined under various loading scenarios. This leads to system instability, which lowers voltage and improves power losses, both of which have an effect on the supply's quality. The right size and placement of typical DG solutions to reduce quality problems and improve the voltage profile in the system. The stability analysis at each load bus provides unambiguous estimations of the precise position of the DG to prevent outages and quality problems. In this, the system is examined and its performance is improved based on LVSI indices, without the use of any meta-heuristic techniques.

Conflict of interest. The authors declare that they have no conflicts of interest.

REFERENCES

1. Baran M.E., Wu F.F. Network reconfiguration in distribution systems for loss reduction and load balancing. *IEEE Transactions on Power Delivery*, 1989, vol. 4, no. 2, pp. 1401-1407. doi: https://doi.org/10.1109/61.25627.

2. Balamourougan V., Sidhu T.S., Sachdev M.S. Technique for online prediction of voltage collapse. *IEE Proceedings – Generation, Transmission and Distribution*, 2004, vol. 151, no. 4, pp. 453-460. doi: https://doi.org/10.1049/ip-gtd:20040612.

3. Olamaei J., Niknam T., Gharehpetian G. Application of particle swarm optimization for distribution feeder reconfiguration considering distributed generators. *Applied Mathematics and Computation*, 2008, vol. 201, no. 1–2, pp. 575-586. doi: https://doi.org/10.1016/j.amc.2007.12.053.

4. Shih-An Yin, Chan-Nan Lu. Distribution Feeder Scheduling Considering Variable Load Profile and Outage Costs. *IEEE Transactions on Power Systems*, 2009, vol. 24, no. 2, pp. 652-660. doi: https://doi.org/10.1109/TPWRS.2009.2016300.

5. Patne N.R., Thakre K.L. Effect of transformer on stochastic estimation of voltage sag due to faults in the power system: a PSCAD/EMTDC simulation. *Turkish Journal of Electrical Engineering and Computer Sciences*, 2010, vol. 18, no. 1, pp. 43-58. doi: https://doi.org/10.3906/elk-0802-6.

6. Mohammadi Nodushan M., Ghadimi A.A., Salami A. voltage sag improvement in radial distribution networks using reconfiguration simultaneous with DG placement. *Indian Journal of Science and Technology*, 2013, vol. 6, no. 7, pp. 1-8. doi: https://doi.org/10.17485/ijst/2013/v6i7.4.

7. Jain S., Agnihotri G., Kalambe S., Kamdar R. Siting and Sizing of DG in Medium Primary Radial Distribution System with Enhanced Voltage Stability. *Chinese Journal of Engineering*, 2014, pp. 1-9. doi: https://doi.org/10.1155/2014/518970.

8. Hamouda A., Zehar K. Efficient Load Flow Method for Radial Distribution Feeders. *Journal of Applied Sciences*, 2006, vol. 6, no. 13, pp. 2741-2748. doi: https://doi.org/10.3923/jas.2006.2741.2748.

9. Ramana T., Ganesh V., Sivanagaraju S. Simple and Fast Load Flow Solution for Electrical Power Distribution Systems. *International Journal on Electrical Engineering and Informatics*, 2013, vol. 5, no. 3, pp. 245-255. doi: https://doi.org/10.15676/ijeei.2013.5.3.1.

10. Ram M.V.S., Srinivasa Rao G. Load Flow analysis for Radial Distribution Network with Network Topology Method, *International journal of engineering research & technology (IJERT) ETE*, 2016, vol. 4, no. 07. doi: https://doi.org/10.17577/IJERTCONV4IS07010.

11. Murugananthan B., Gnanadass R., Padhy N.P. Performance analysis and comparison of load flow methods in a practical distribution system. *2016 National Power Systems Conference (NPSC)*, 2016, pp. 1-6. doi: https://doi.org/10.1109/NPSC.2016.7858848.

12. Issicaba D., Coelho J. Rotational Load Flow Method for Radial Distribution Systems. *International Journal of Electrical and Computer Engineering (IJECE)*, 2016, vol. 6, no. 3, pp. 1344-1352. doi: https://doi.org/10.11591/ijece.v6i3.10083.

13. Reddy P.D.P., Reddy V.C.V., Manohar T.G. An Efficient Distribution Load Flow Method for Radial Distribution Systems with Load Models. *International Journal of Grid and Distributed Computing*, 2018, vol. 11, no. 3, pp. 63-78. doi: https://doi.org/10.14257/ijgdc.2018.11.3.06.

14. Bernstein A., Wang C., Dall'Anese E., Le Boudec J.-Y., Zhao C. Load Flow in Multiphase Distribution Networks: Existence, Uniqueness, Non-Singularity and Linear Models. *IEEE Transactions on Power Systems*, 2018, vol. 33, no. 6, pp. 5832-5843. doi: https://doi.org/10.1109/TPWRS.2018.2823277.

15. Venkata Krishna B., Padma Srinivasu N. A Direct Method for Distribution System Load Flow Solutions. *International Journal of Engineering and Advanced Technology*, 2019, vol. 8, no. 6S3, pp. 749-753. doi: https://doi.org/10.35940/ijeat.F1138.0986S319.

16. Abd-rabou A.M., Soliman A.M., Mokhtar A.S. Impact of DG different types on the grid performance. *Journal of Electrical Systems and Information Technology*, 2015, vol. 2, no. 2, pp. 149-160. doi: https://doi.org/10.1016/j.jesit.2015.04.001.

17. Pradeepa H., Ananthapadmanabha T., Rani D.N., Sandhya Bandhavya C. Optimal Allocation of Combined DG and Capacitor Units for Voltage Stability Enhancement. *Procedia Technology*, 2015, vol. 21, pp. 216-223. doi: https://doi.org/10.1016/j.protcy.2015.10.091.

18. Bohre A.K., Agnihotri G., Dubey M. Optimal sizing and sitting of DG with load models using soft computing techniques in practical distribution system. *IET Generation, Transmission & Distribution*, 2016, vol. 10, no. 11, pp. 2606-2621. doi: https://doi.org/10.1049/iet-gtd.2015.1034.

19. Prakash D.B., Lakshminarayana C. Multiple DG Placements in Distribution System for Power Loss Reduction Using PSO Algorithm. *Procedia Technology*, 2016, vol. 25, pp. 785-792. doi: https://doi.org/10.1016/j.protcy.2016.08.173.

20. Mezhoud N., Ayachi B., Amarouayache M. Multi-objective optimal power flow based gray wolf optimization method. *Electrical Engineering & Electromechanics*, 2022, no. 4, pp. 57-62. doi: https://doi.org/10.20998/2074-272X.2022.4.08.

21. Remha S., Chettih S., Arif S. Optimal placement of different DG units type in distribution networks based on voltage stability maximization and minimization of power losses. *2016 8th International Conference on Modelling, Identification and Control (ICMIC)*, 2016, pp. 867-873. doi: https://doi.org/10.1109/ICMIC.2016.7804237.

22. Sambaiah K.S. A review on optimal allocation and sizing techniques for DG in distribution systems. *International Journal of Renewable Energy Research*, 2018, vol. 8, no. 3, pp. 1236-1256. doi: https://doi.org/10.20508/ijrer.v8i3.7344.g7424.

23. Dinakara Prasasd Reddy P., Veera Reddy V.C., Gowri Manohar T. Ant Lion optimization algorithm for optimal sizing of renewable energy resources for loss reduction in distribution systems. *Journal of Electrical Systems and Information Technology*, 2018, vol. 5, no. 3, pp. 663-680. doi: https://doi.org/10.1016/j.jesit.2017.06.001.

24. Suresh M.C.V., Belwin E.J. Optimal DG placement for benefit maximization in distribution networks by using Dragonfly algorithm. *Renewables: Wind, Water, and Solar*, 2018, vol. 5, no. 1, art. no. 4. doi: https://doi.org/10.1186/s40807-018-0050-7.

25. Dinakara Prasad Reddy P., Veera Reddy V.C., Gowri Manohar T. Optimal renewable resources placement in distribution networks by combined power loss index and whale optimization algorithms. *Journal of Electrical Systems and Information Technology*, 2018, vol. 5, no. 2, pp. 175-191. doi: https://doi.org/10.1016/j.jesit.2017.05.006.

26. Mehta P., Bhatt P., Pandya V. Optimal selection of distributed generating units and its placement for voltage stability enhancement and energy loss minimization. *Ain Shams Engineering Journal*, 2018, vol. 9, no. 2, pp. 187-201. doi: https://doi.org/10.1016/j.asej.2015.10.009.

27. Salmani M., Pasupuleti J., Ramachandaramurthy V.K. Optimal Placement and Sizing of Multiple DG in Microgrid Systems. *International Journal of Recent Technology and Engineering (IJRTE)*, 2019, vol. 8, no. 4, pp. 6230-6235. doi: https://doi.org/10.35940/ijrte.D5145.118419.
28. Selim A., Kamel S., Mohamed A.A., Elattar E.E. Optimal Allocation of Multiple Types of Distributed Generations in Radial Distribution Systems Using a Hybrid Technique. *Sustainability*, 2021, vol. 13, no. 12, art. no. 6644. doi: https://doi.org/10.3390/su13126644.
29. Tan Z., Zeng M., Sun L. Optimal Placement and Sizing of Distributed Generators Based on Swarm Moth Flame Optimization. *Frontiers in Energy Research*, 2021, vol. 9, pp. 1-8. doi: https://doi.org/10.3389/fenrg.2021.676305.
30. Nivetha D., Karunakaran M. A Review on Power Quality Analysis, Techniques, Methods and Controlling. *International Journal of Advanced Research in Electrical, Electronics and Instrumentation Engineering*, 2016, vol. 5, no. 3, pp. 2049-2054. doi: https://doi.org/10.15662/IJAREEIE.2015.0503143.
31. Bhende C.N., Kalam A., Malla S.G. Mitigation of Power Quality Problems in Grid-Interactive Distributed Generation System. *International Journal of Emerging Electric Power Systems*, 2016, vol. 17, no. 2, pp. 165-172. doi: https://doi.org/10.1515/ijeeps-2015-0163.
32. Hossain E., Tur M.R., Padmanaban S., Ay S., Khan I. Analysis and Mitigation of Power Quality Issues in Distributed Generation Systems Using Custom Power Devices. *IEEE Access*, 2018, vol. 6, pp. 16816-16833. doi: https://doi.org/10.1109/ACCESS.2018.2814981.
33. Bhavani R., Ananthakumaran D.S. Development of Real Time Power Quality (RTPQ) Analyzer using Lab-VIEW. *International Journal of Recent Technology and Engineering (IJRTE)*, 2019, vol. 8, no. 3, pp. 458-464. doi: https://doi.org/10.35940/ijrte.C4192.098319.
34. Minh Khoa N., Van Dai L. Detection and Classification of Power Quality Disturbances in Power System Using Modified-Combination between the Stockwell Transform and Decision Tree Methods. *Energies*, 2020, vol. 13, no. 14, art. no. 3623. doi: https://doi.org/10.3390/en13143623.
35. Kumar M., Uqaili M.A., Memon Z.A., Das B. Mathematical Modeling of THD Mitigation Using HAPF for UPS System with Experimental Analysis via Hybrid Interface of Optical USB and Power Quality Meter. *Mathematical Problems in Engineering*, 2021, pp. 1-15. doi: https://doi.org/10.1155/2021/3981287.
36. Manohara M., Deepika K. Optimal placement of DSTATCOM and load flow analysis of radial distribution network. *International Journal of Engineering Science and Technology* (IJEST), 2012, vol. 4, no. 6, pp. 2967-2980.
37. Manohara M., Vinod Kumar K., Devaraju T. Implementation of Dynamic Voltage Restorer for Mitigation of Voltage Sag. *International Journal of Engineering Research and Applications (IJERA)*, 2013, vol. 3, no. 4, pp. 123-128.
38. Manohara M., S Siva Sasthri. Power quality improvement in grid connected wind energy conversion systems by using custom power device. *International Research Journal of Engineering and Technology (IRJET)*, 2017, vol. 4, no. 6, pp. 3254-3259.

Received 19.09.2022
Accepted 15.12.2022
Published 07.03.2023

M. Manohara [1]*, M. Tech.,*
V.C. Veera Reddy [2]*, PhD, Professor,*
M. Vijaya Kumar [3]*, PhD, Professor,*
[1] Research Scholar, Jawaharlal Nehru Technological University Anantapur, Ananthapuramu, India,
e-mail: muppirimanohar@yahoo.com (Corresponding Author)
[2] Department of Electrical and Electronics Engineering,
Sri Padmavati Mahila Visvavidyalayam, Tirupati, India,
e-mail: veerareddy_vc@yahoo.com
[3] JNTUA College of Engineering, Ananthapuramu, Constituent College of Jawaharlal Nehru Technological University Anantapur, Ananthapuramu, India,
e-mail: mvk_2004@rediffmail.com

How to cite this article:
Manohara M., Veera Reddy V.C., Vijaya Kumar M. Exploration and mitigation of power quality problems in radial distribution system by placing distributed generation through voltage stability index. *Electrical Engineering & Electromechanics*, 2023, no. 2, pp. 79-85. doi: https://doi.org/10.20998/2074-272X.2023.2.12

UDC 621.3 https://doi.org/10.20998/2074-272X.2023.2.13

O. Oualah, D. Kerdoun, A. Boumassata

Super-twisting sliding mode control for brushless doubly-fed reluctance generator based on wind energy conversion system

Introduction. *Recently, wind power generation has grown at an alarming rate in the past decade and will continue to do so as power electronic technology continues to advance.* ***Purpose.*** *Super-twisting sliding mode control for brushless doubly-fed reluctance generator based on wind energy conversion system.* ***Methods.*** *This paper deals with the robust power control of a grid-connected brushless doubly-fed reluctance generator driven by the variable speed wind turbine using a variable structure control theory called sliding mode control. The traditional sliding mode approach produces an unpleasant chattering phenomenon that could harm the system. To eliminate chattering, it is necessary to employ a high-order sliding mode controller. The super-twisting algorithm is one type of nonlinear control presented in order to ensure the effectiveness of the control structure we tested these controllers in two different ways reference tracking, and robustness.* ***Results.*** *Simulation results using MATLAB/Simulink have demonstrated the effectiveness and robustness of the super-twisting sliding mode controller.* References 31, figures 14.
Key words: **wind power, brushless doubly-fed reluctance generator, maximum power point tracking, vector control, super-twisting algorithm**.

Вступ. *В останнє десятиліття виробництво вітрової енергії зростало загрозливими темпами і продовжуватиме зростати у міру розвитку технологій силової електроніки.* ***Мета.*** *Управління ковзним режимом суперскручування для реактивного безщіткового генератора з подвійним живленням на основі системи перетворення енергії вітру.* ***Методи.*** *У цій статті розглядається надійне керування потужністю підключеного до мережі безщіткового реактивного генератора з подвійним живленням, що приводиться в дію вітряною турбіною зі змінною швидкістю, з використанням теорії управління зі змінною структурою, яка називається керуванням в ковзному режимі. Традиційний підхід зі ковзним режимом створює неприємне явище вібрації, що може зашкодити системі. Для усунення вібрації необхідно використовувати регулятор ковзного режиму високого порядку. Алгоритм суперскручування - це один із типів нелінійного управління, представлений для забезпечення ефективності структури управління. Ми протестували ці контролери двома різними способами: відстеженням посилань та надійністю.* ***Результати*** *моделювання з використанням MATLAB/Simulink продемонстрували ефективність та надійність контролера ковзного режиму суперскручування.* Бібл. 31, рис. 14.
Ключові слова: **енергія вітру, безколекторний реактивний генератор з подвійним живленням, відстеження точки максимальної потужності, векторне управління, алгоритм суперкручування.**

Introduction. Researchers have long been looking for alternative form of energy production driven by the environmental concerns and the operational cost. This led to an increased study on renewable form of energy in recent years [1]. The first wind turbine (WT) was developed to generate electricity. Wind power was remarked as one of the promising renewable energy sources in the decade 1980-1990 [2]. The use of wind energy does not cause harmful emissions like greenhouse gases during its operating period and, without any surprise, worldwide wind power is one of the rapidly growing renewable energy sources. According to the World Wind Association, wind capacity over the world has reached up to 744 GW in 2020 [3], which was 318 MW in 2013 [4].

The brushless doubly-fed reluctance machine (BDFRM) has been investigated during the last decade as a potential alternative to the existing solutions in variable speed applications with narrow speed range [5]. The brushless doubly-fed induction machine (BDFIM) and the BDFRM are the two main competitors attracting most of the attention from researchers [6].

The following are the main benefits of BDFRM [7, 8]:

- maintenance free operation due to sturdy construction (no brushes or sliding rings) and great dependability, as opposed to the classic doubly-fed induction machine (DFIM);
- implicitly medium speed functioning enables the use of a two stage gearbox rather than a susceptible three stage equivalent with DFIMs, providing improved mechanical robustness and reduced failure rates, resulting in obvious cost savings;
- a lower capacity power electronics converter (about 25-30 % of the machine rated) for WTs and pump motors with a typical speed range of 2:1;
- operating mode flexibility as it can operate as a classical induction machine, or as a fixed/adjustable speed synchronous turbo machine, enabling high speed, field-weakened traction applications as well as high-frequency generators.

The brushless doubly-fed reluctance generator (BDFRG) has two three-phase windings in its stator: primary (or power) winding and secondary (or control) winding and have different pole pairs. So, a reluctance rotor, which the number of its salient poles is equal with sum of the primary and secondary pole pairs, provides coupling between the windings [9]. The primary winding is connected to the grid and the secondary to an inverter. These two windings always have different pole numbers [10]. Various control methodologies have been investigated for the BDFRM including: scalar control [11], vector control or field oriented control [12-14], control without a shaft position [15] or sensorless speed control [16] and direct power control [17]. These controllers are not robust against parameters variations, model uncertainties and external perturbations and are able to give an asymptotic convergence. Their main appeal is the rather low computational cost along with their simple implementation.

The linear control encountered difficulties since variable speed wind turbine (VSWT) system is a complex and highly non-linear system with strong coupling features and uncertainty in both the aerodynamic and the electrical parts. Thus, various non-linear control methods on VSWTs have been proposed, such as H_∞ control, robust control, feedback linearization technique, neural networks [18] control model reference adaptive system [19], model predictive [20], sliding mode control (SMC)

[14], synergetic-super-twisting algorithms [21], fuzzy model-based multivariable predictive regulator [22].

Apart from these non-linear controller, variable structure SMC has gained increased attention for the BDFRG-based wind energy conversion system (WECS) owing to its robust nature against both modeled and unmodeled external disturbance, fault scenarios, parameter variations, simple structure, low parameter sensitivity and easy implementation for wind extraction a number of SMC techniques have been proposed in the literature [23].

The traditional sliding mode approach produces an unpleasant chattering effect, which could be detrimental to the system. Thus, it is suitable to explore the use of second-order sliding mode algorithms which inherit all the properties of SMC and attenuates chattering or high frequency vibrations in controlled quantity thus reducing mechanical stresses in the system [24], in [14] the author compared between SMC and vector control of a BDFRG based on WECS.

Recently, nonlinear super-twisting sliding mode techniques have become an interesting option to be used in several kinds of systems. SMC guaranties the robustness and finite time convergence of a nonlinear system if the attractiveness condition is verified. Several works have been published using this technique, for example in [25].

The grid side converter (GSC) of the BDFRG is limited to proportional-integral (PI) control. The strategy of the BDFRG based on WECS control mainly consist two separate controls: *a*) stator side converter; *b*) grid side converter (GSC). In this paper, an active and reactive power of the stator of BDFRG is employed in a control winding side converter where its input is presented for the GSC; however, the GSC is managed by traditional PI based control strategy. The suggested control strategy is based on the famous, super complicated algorithm, this latter guarantees more reliable chatter free transient response of the BDFRG parameters in comparison to the traditional PI.

WECS modeling. WT model. The mechanical power extracted by the turbine from the wind is defined as [26]:

$$P_t = \frac{1}{2}\cdot\rho\cdot A\cdot C_p(\lambda)\cdot V^3\,, \tag{1}$$

where ρ is the air density; $A = \pi R^2$ is the rotor swept area; R is the turbine radius; C_p is the power coefficient; λ is the tip speed ratio; V is the wind speed.

The power coefficient C_p represents the aerodynamic efficiency of the WT. It is determined by the tip speed ratio λ and the blade pitch angle β. The tip speed ratio is expressed as:

$$\lambda = \frac{\Omega_t\cdot R}{V}, \tag{2}$$

where Ω_t is the turbine speed; β is the blade pitch angle.

For our example, the power coefficient C_p is

$$C_p(\lambda,\beta) = 0.5176\cdot\left(\frac{116}{\lambda_x} - 0.4\beta - 5\right)e^{-\frac{21}{\lambda_x}} + 0.0068\lambda\,, \tag{3}$$

where

$$\frac{1}{\lambda_x} = \frac{1}{\lambda + 0.08\beta} - \frac{0.035}{\beta^3 + 1}. \tag{4}$$

The C_p curve is shown in Fig. 1, from which there is an optimum λ at which the power coefficient C_p is maximal.

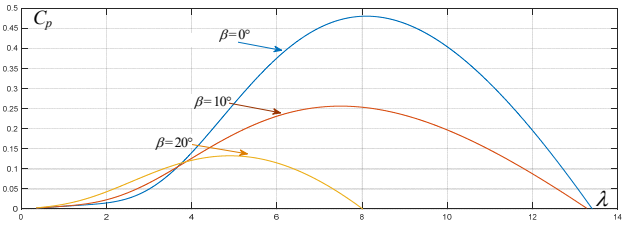

Fig. 1. Characteristics of the WT power coefficient with the tip speed ratio λ at different values of the blade pitch angle β

The maximum value of $C_p = 0.48$ is for $\beta = 0°$ and for $\lambda = 8.1$.

The turbine torque can be written as:

$$T_t = P_t/\Omega_t\,. \tag{5}$$

The mechanical speed of the generator and the torque of the turbine referred to the generator are given by:

$$\begin{cases}\Omega_{mec} = \Omega_t\cdot G;\\ T_m = T_t/G,\end{cases} \tag{6}$$

where G is the gearbox ratio.

The mechanical equation of the system can be characterized by:

$$J\frac{\mathrm{d}\Omega mec}{\mathrm{d}t} = T_m - T_{em} - f\cdot\Omega_{mec}\,, \tag{7}$$

where J is the equivalent total inertia of the generator shaft; f is the equivalent total friction coefficient; T_{em} is the electromagnetic torque.

To extract the maximum power from the WT, the electromagnetic torque command of the BDFRG, $T_{e\text{-}ref}$ should be determined at the optimal value of the tip speed ratio and the corresponding maximum value of WT power coefficient C_p.

Mathematical model of BDFRG. The electrical equations of the BDFRG in the *d–q* Park reference frame are given by:

$$\begin{cases} Vpd = R_P I_{pd} + \dfrac{d\Phi_{pd}}{dt} - \omega_p\cdot\Phi_{pq};\\ Vpq = R_P I_{pq} + \dfrac{d\Phi_{pq}}{dt} + \omega\cdot\Phi_{pd};\\ Vsd = R_s I_{sd} + \dfrac{d\Phi_{sd}}{dt} - (\omega_r - \omega)\cdot\Phi_{sq};\\ Vsq = R_s I_{sq} + \dfrac{d\Phi_{sq}}{dt} + (\omega_r - \omega)\cdot\Phi_{sd};\end{cases} \tag{8}$$

$$\begin{cases}\Phi_{pd} = L_P I_{pd} + L_m I_{sd};\\ \Phi_{pq} = L_P I_{pq} - L_m I_{sq};\\ \Phi_{sd} = L_s I_{sd} + L_m I_{pd};\\ \Phi_{sq} = L_s I_{sq} - L_m I_{pq}.\end{cases} \tag{9}$$

The electromagnetic torque is expressed as:

$$T_e = \frac{3P_R L_m}{2L_P}\left(V_{pd}I_{sq} + V_{pq}I_{sd}\right). \tag{10}$$

The active and reactive powers equations at the primary stator, the secondary stator, and the grid are, respectively, written as:

$$\begin{cases} P_p = \dfrac{3}{2}\left(V_{pd}I_{pd} + V_{pq}I_{pq}\right);\\ Q_p = \dfrac{3}{2}\left(V_{pq}I_{pd} - V_{pd}I_{pq}\right);\end{cases} \tag{11}$$

$$\begin{cases} P_s = \dfrac{3}{2}\left(V_{sd} I_{sd} + V_{sq} I_{sq}\right); \\ Q_s = \dfrac{3}{2}\left(V_{sq} I_{sd} - V_{sd} I_{sq}\right); \end{cases} \tag{12}$$

$$\begin{cases} P_g = P_p + P_s; \\ Q_g = Q_p + Q_s, \end{cases} \tag{13}$$

where: V_{sd}, V_{sq} are the d-q axis control winding voltages; V_{pd}, V_{pq} are the d-q axis power winding voltages; R_p, R_s are the power and control winding resistances; L_p is the leakage inductance of power winding; L_s is the leakage inductance of control winding; L_m is the mutual inductance between power and control windings; I_{sd}, I_{sq} are the d-q axis control winding currents; I_{pd}, I_{pq} are the d-q axis power winding currents; ω_p is the angular frequencies of power windings; ω_s is the angular frequencies of control windings; ω_r is the BDFRG mechanical rotor angular speed; Φ_s is the d-q axis control winding flux linkages; Φ_p is the d-q axis power winding flux linkages.

GSC modeling and control. The grid-side converter maintains a constant DC-link voltage and satisfies the reactive power requirement in accordance with grid rules. Utilizing grid V_{OC}, active and reactive power may be easily regulated by d-axis and q-axis current. Two cascaded loops are used in this control approach. The inner loop controls grid current, while the outer loop controls DC-link voltage and reactive power for the GSC. The active power has a strong influence on the DC-link voltage [27].

The relationship between the grid and the converter are:

$$\begin{cases} L_f \dfrac{\mathrm{d}I_{fd}}{\mathrm{d}t} = -R_f I_{fd} + L_f \omega_s I_{fq} + V_{fd} - V_{sd}; \\ L_f \dfrac{\mathrm{d}I_{fq}}{\mathrm{d}t} = -R_f I_{fq} + L_f \omega_s I_{fd} + V_{fq} - V_{sq}. \end{cases} \tag{14}$$

As for the continuous side:

$$\frac{\mathrm{d}V_{dc}}{\mathrm{d}t} = \frac{1}{C}\left(I_s - I_l\right). \tag{15}$$

The forms of the grid active and reactive powers are as follow:

$$\begin{cases} P_s = \dfrac{3}{2}\left(V_{sd} I_{fd} + V_{sq} I_{fq}\right); \\ Q_s = \dfrac{3}{2}\left(V_{sq} I_{fd} - V_{sd} I_{fq}\right), \end{cases} \tag{16}$$

where V_{sd}, V_{sq} are the grid and converter voltage respectively; I_{fd}, I_{fq} are the grid and converter currents; R_f is the equivalent resistance of the grid filter; L_f is the inductance of the grid filter.

By orienting the inverter voltage on the grid side ($V_{sd} = 0$ and $V_{sq} = V$) we found:

$$\begin{cases} P_s = \dfrac{3}{2} V_{sq} I_{fq} = V_{dc} I_{dc}; \\ Q_s = \dfrac{3}{2} V_{sq} I_{fd}; \end{cases} \tag{17}$$

$$\begin{cases} V_{fd} = L_f \dfrac{\mathrm{d}I_{fd}}{\mathrm{d}t} + R_f I_{fd} - e_q^{'}; \\ V_{fq} = L_f \dfrac{\mathrm{d}I_{fq}}{\mathrm{d}t} + R_f I_{fq} - e_d^{'}; \end{cases} \text{with} \begin{cases} e_{fq} = -L_f \omega_s I_{fq}; \\ e_{fd} = -L_f \omega_s I_{fd} + V. \end{cases} \tag{18}$$

Figure 2 shows the block diagram of the control of the GSC.

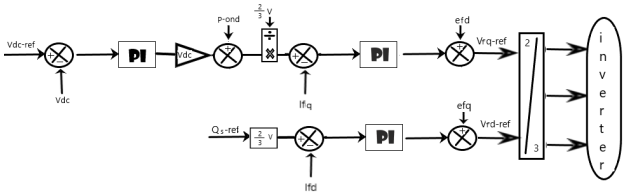

Fig. 2. Block diagram of grid side control

Vector control of the BDFRG. In order to decouple the stator active and reactive powers, the primary stator flux vector will be aligned with *d*-axis φ_{pd} ($\varphi_{pd} = \varphi_p$ and $\varphi_{pq} = 0$), and the stator voltages will be expressed by:

$$\begin{cases} V_{pd} = 0; \\ V_{pq} = V_P = \omega_p \cdot \Phi_p. \end{cases} \tag{19}$$

The expressions of the primary stator currents are written as:

$$\begin{cases} I_{pd} = \dfrac{\Phi_{pd} - L_m I_{sd}}{L_p}; \\ I_{pq} = \dfrac{L_m I_{sq}}{L_p}. \end{cases} \tag{20}$$

By replacing these currents in the secondary stator fluxes equations, we obtain:

$$\begin{cases} \Phi_{sd} = L_s \sigma I_{sd} + \dfrac{L_m}{L_p} \Phi_{pd}; \\ \Phi_{sq} = \sigma L_s I_{sq}, \end{cases} \tag{21}$$

with σ is the leakage coefficient, defined by:

$$\sigma = 1 - \frac{{L_m}^2}{L_p L_s}. \tag{22}$$

The secondary stator voltages can be written according to the secondary stator currents as:

$$\begin{cases} V_{sd} = R_s I_{sd} + L_s \sigma \dfrac{\mathrm{d}I_{sd}}{\mathrm{d}t} + eq; \\ V_{sq} = R_s I_{sq} + L_s \sigma \dfrac{\mathrm{d}I_{sq}}{\mathrm{d}t} + ed + e\varphi, \end{cases} \tag{23}$$

with

$$\begin{cases} eq = -\omega_s \sigma L_s I_{sq}; \\ ed = \omega_s \sigma L_s I_{sd}; \\ e\varphi = \omega_s \dfrac{L_m}{L_p} \Phi_p, \end{cases} \tag{24}$$

the active and reactive stator powers of the BDFRG are expressed by:

$$\begin{cases} P_p = \dfrac{3 V_{pq} L_m}{2 L_P} I_{sq}; \\ Q_p = \dfrac{3}{2} \dfrac{{V_{pq}}^2}{\omega_p L_p} - \dfrac{3}{2} V_{pq} \dfrac{L_m}{L_p} I_{sd}, \end{cases} \tag{25}$$

where *s* is the slip of the BDFRG.

The electromagnetic torque can be written as:

$$T_e = \frac{3 P_r L_m}{2 L_p} I_{pd} I_{sq}. \tag{26}$$

For relatively weak sleep values and by neglecting the voltage drops, the grid active and reactive powers are simplified into:

$$\begin{cases} P_g = \dfrac{3(1-s)V_{pq}L_m}{2L_P} I_{sq}; \\ Q_g = \dfrac{3}{2}\dfrac{V_{pq}^{\ 2}}{\omega_p L_p} - \dfrac{3(1-s)}{2} V_{pq}\dfrac{L_m}{L_p} I_{sd}. \end{cases} \quad (27)$$

From (27) we have:

$$\begin{cases} I_{sq} = \dfrac{2L_p}{3(1-s)V_{pq}L_m} P_g; \\ I_{sd} = \left(\dfrac{3V_{pq}^2}{2w_p L_p} - Q_g\right)\dfrac{2L_p}{3(1-s)V_{pq}L_m}. \end{cases} \quad (28)$$

Substitute (28) in (23) we obtain:

$$\begin{cases} \dot{P}_g = \dfrac{V_{sq}}{AL_s\sigma} - \dfrac{R_s}{L_s\sigma}P_g - \dfrac{ed}{AL_S\sigma} - \dfrac{e\varphi}{AL_S\sigma}; \\ \dot{Q}_g = \dfrac{-V_{sd}}{AL_s\sigma} - \dfrac{R_s}{L_s\sigma}Q_g + \dfrac{eq}{AL_S\sigma} + \dfrac{ev}{AL_S\sigma}, \end{cases} \quad (29)$$

with:

$$\begin{cases} A = \dfrac{2L_p}{3(1-s)V_{pq}L_m}; \\ ev = AR_s\dfrac{3V_{pq}^2}{2\omega_p L_p}. \end{cases} \quad (30)$$

In order to capture the optimal mechanical power, the control of the mechanical speed is applied as shown on Fig. 3.

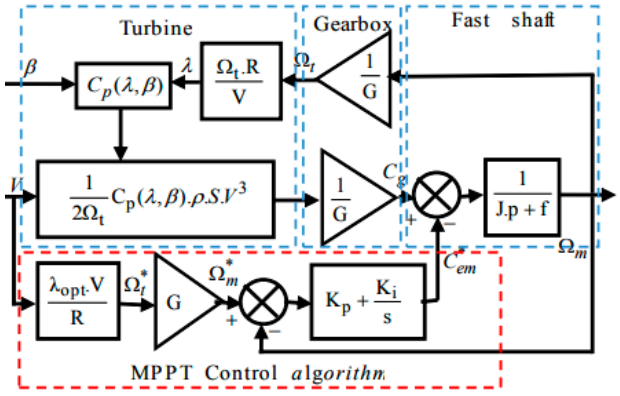

Fig. 3. MPPT with the control of the speed

The reference value of the active power exchanged between the wind generator and the grid is generated by maximum power point tracking (MPPT) control, and it's given by:

$$P_{g-ref} = T_{em-ref} \cdot \Omega_{mec}. \quad (31)$$

The reference grid reactive power, $Q_{g\text{-}ref}$ is fixed to zero value to maintain the power factor at unity. The detailed scheme of the studied system is illustrated in Fig. 4 and presents a general schematic diagram of the BDFRG using super-twisting algorithm with GSC control.

High-order SMC. Control with high uncertainty is one of the most difficult control challenges. While there are a variety of advanced ways, such as adaptation based on identification and observation or perfect stability

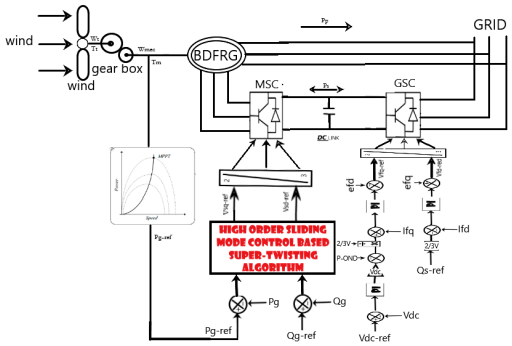

Fig. 4. The scheme of BDFRG using super-twisting algorithm with GSC control

techniques, the most apparent solution to engage with uncertainty is to «brutally enforce» some limitations. Therefore, any carefully maintained equality eliminates one «uncertainty dimension». The simplest technique to maintain a constraint is to respond instantly to any divergence of the system by stirring it back to the restriction with a suitably intense effort. When implemented directly, the method results in so-called sliding modes, which have become the primary operation modes in virtual switching system (VSS). They have demonstrated their great precision and resilience in the face of diverse internal and external disturbances [28].

The main drawbacks of the traditional SMC are chattering effect and discontinuous high-frequency switching control which is impractical. To overcome these problems, super-twisting controller is used. A single-dimensional motion of a unit mass system [29].

Second order SMC can only attenuate this problem. Twisting and super-twisting algorithms are the standard second order algorithms reported [25]. Today, the super-twisting method is preferred over the traditional sliding mode, since it eliminates the chattering phenomenon [24].

Super-twisting algorithm. To eliminate chattering in VSS, a super-twisting control method was proposed. It is a continuous controller which insures all the properties of the first order SMC for the system with matched bounded uncertainties/disturbances [30, 31].

For the dynamic system, the super-twisting control consists of two parts, a discontinuous part and a continuous part:

$$u = u_1 + u_2,$$

with

$$\begin{cases} u_1 = -\alpha|S|^{\tau} sign(S); \\ \dot{u}_2 = -\beta sign(S); \end{cases} \quad \tau \in 0{,}0.5; \quad (32)$$

where α, β checking for the following inequalities [24]:

$$\begin{cases} S(x,t) = \left(\dfrac{\mathrm{d}}{\mathrm{d}t} + \lambda\right)^{n-1} e; \\ \alpha^2 > \dfrac{4C_0K_m(\alpha + C_0)}{K_m^{\ 3}(\alpha - C_0)}; \\ \beta > \dfrac{C_0}{K_m}, \end{cases} \quad (33)$$

where S is called the sliding surface; $x = [x, \dot{x}, \ddot{x}, ..., x^{n-1}]$ is the state vector; $x^d = [x^d, \dot{x}^d, \ddot{x}^d, ..., x^d]$ is the desired state vector; $e = x^d - x = [e, \dot{e}, \ddot{e}, ..., e^{n-1}]$ is the error vector; λ is the positive coefficient; n is the system order; C_0, K_m are the positive constants.

High-order SMC of active and reactive powers. The switching surfaces of the stator powers are given by:

$$\begin{cases} S(P_g) = e(P_g) = P_g - P_{g-ref}; \\ S(Q_g) = e(Q_g) = Q_g - Q_{g-ref}. \end{cases} \quad (34)$$

Then, we have:

$$\begin{cases} \dot{S}(P_g) = \dot{P}_g - \dot{P}_{g-ref}; \\ \dot{S}(Q_g) = \dot{Q}_g - \dot{Q}_{g-ref}. \end{cases} \quad (35)$$

From (29) we have:

$$\begin{cases} \dot{P}_g = \dfrac{V_{sq}}{AL_s\sigma} - \dfrac{R_s}{L_s\sigma}P_g - \dfrac{ed}{AL_S\sigma} - \dfrac{e\varphi}{AL_S\sigma}; \\ \dot{Q}_g = \dfrac{-V_{sd}}{AL_s\sigma} - \dfrac{R_s}{L_s\sigma}Q_g + \dfrac{eq}{AL_S\sigma} + \dfrac{ev}{AL_S\sigma}. \end{cases} \quad (36)$$

Now consider the following command:

$$\begin{cases} V_{sd} = u_2 + \alpha_1 |S(Q_g)|^{\tau} sign(S(Q_g)); \\ \dot{u}_2 = \beta_1 sign(S(Q_g)); \\ V_{sq} = w_2 + \alpha_2 |S(P_g)|^{\tau} sign(S(P_g)); \\ \dot{w}_2 = \beta_2 sign(S(P_g)); \\ \tau \in]0, 0.5[. \end{cases} \quad (37)$$

where the error $S(P)$ and $S(Q)$ are the sliding variables and constant gains α_1, α_2, β_1, β_2 verify the stability conditions in (33).

Results and discussion. The control technique suggested in this paper has been approved by the MATLAB/Simulink software. The generator used in this simulation is 4.5 kW. This generator is connected directly to the grid through its primary stator and controlled through its secondary stator. Rated parameters [5] are: R_p = 3.781 Ω; R_s = 2.441 Ω; L_p = 0.41 H; L_s = 0.316 H; L_m = 0.3 H; J = 0.2 kg·m^2; P_r = 4. WT parameters are: R (blade radius) = 4 m, gearbox ratio G = 7.5; turbine inertia 1.5 kg·m^2, air density ρ = 1.225 kg/m^3; number of blades – 3.

Figure 5 indicates the speed of the wind, and Fig. 6 – the generator speed. The mechanical speed generated by the turbine is similar to the wind profile applied to the turbine. The stator active power reference $P_{g\text{-}ref}$ corresponding at its maximum is obtained by the WT with MPPT control. The reference value $P_{g\text{-}ref}$ determined by (31), and the reference of the reactive power is maintained at zero to guarantee unity power factor.

The active and reactive powers follow perfectly and clearly their references with super-twisting algorithm without overshoot or dynamic errors.

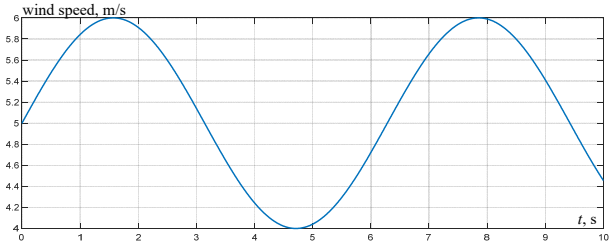

Fig. 5. Wind speed

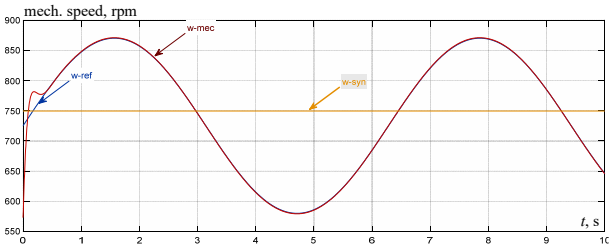

Fig. 6. Turbine mechanical speed

The simulation results illustrated in Fig. 7, 8 show the effectiveness of the control used for the control of the active and reactive powers, a good tracking is observed with a remarkable speed and precision. This chattering phenomenon is reduced with super-twisting controller [14].

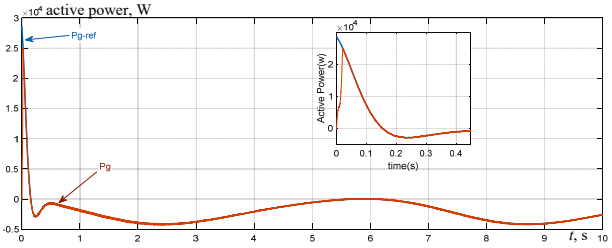

Fig. 7. Active power control

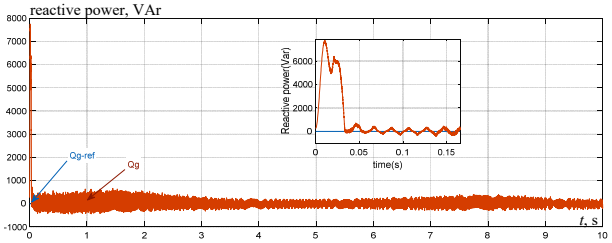

Fig. 8. Reactive power control

Figures 9, 10 present the winding currents in which we observe that both the frequency and the amplitude of these control currents (secondary currents I_s) change during the period of variation of active and reactive powers. Frequency of the current of the supply winding (primary currents I_p) remains constant to be adapted to the supply frequency of the grid, so when the reference of the active power is changed, the amplitude of the current also is changed.

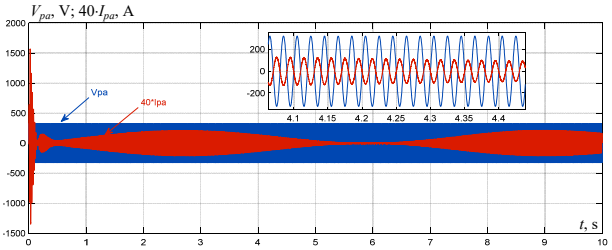

Fig. 9. Phase power winding current and voltage

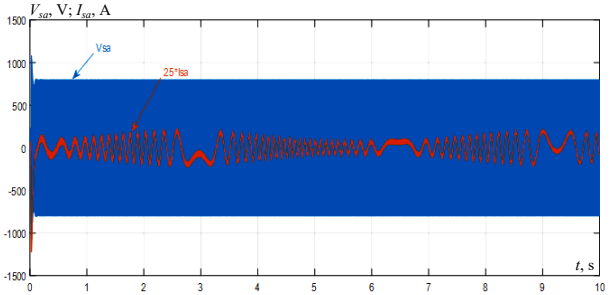

Fig. 10. Phase control winding current and voltage

Figure 11 demonstrates the voltage through the capacitor (direct voltage) throughout the shifting of power. It is clear that its pace follows well the reference (600 V).

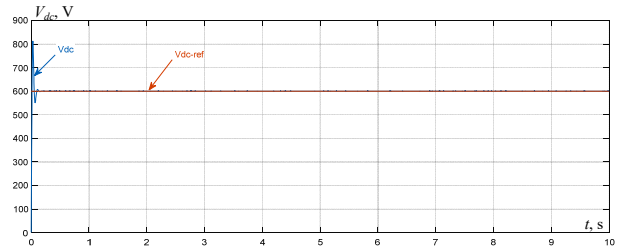

Fig. 11. DC bus voltage

Figure 12 demonstrates that the grid side reactive power fellow her reference clearly on zero a good tracking so the unit power factor is ensured by the proposed controller.

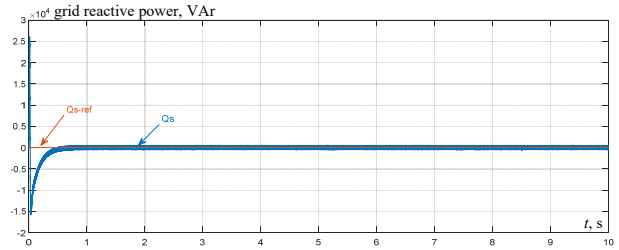

Fig. 12. Grid side reactive power control

Robustness test. The internal parameters of the BDFRG are dependent on variations caused by different physical parameters like temperature increase, saturation and skin effect, so our controller must provide good results against parameters variations of the generator.

In this test we have changed the values of the generator parameters (Fig. 13). Figure 14 demonstrates a tracking response of the reference value of the stator's active and reactive powers.

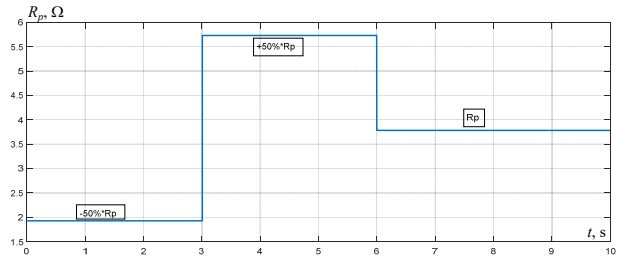

Fig. 13. Parameter variations (primary stator resistance variation)

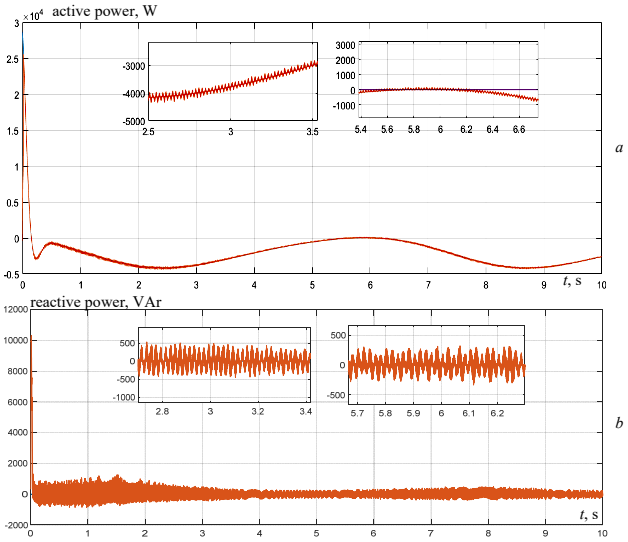

Fig. 14. Stator active and reactive power response

Conclusions. This paper has presented a super-twisting (second order sliding mode control) applied in wind energy system (variable speed wind turbine) to achieve the objectives of maximum power extraction and regulating the stator reactive power to follow grid requirements.

We have presented the wind turbine modeling and its maximum power point tracking control then we have provided the brushless doubly-fed reluctance generator modeling and its vector control. Super-twisting algorithm and its application to the brushless doubly-fed reluctance generator are described in order to ensure the effectiveness of the control structure we tested these controllers in two different ways reference tracking, and robustness.

Simulation results show the optimized performances of the super-twisting sliding mode controller. We observe high performances in terms of response time and reference tracking without overshoots through the response characteristics. The decoupling, the stability, and the convergence towards the equilibrium are assured. Furthermore, this regulation presents a high dynamic response, and it is more robust against parameter variation of the brushless doubly-fed reluctance generator.

Conflict of interest. The authors declare that they have no conflicts of interest.

REFERENCES

1. Fateh L., Ahmed O., Amar O., Abdelhak D., Lakhdar B. Modeling and control of a permanent magnet synchronous generator dedicated to standalone wind energy conversion system. *Frontiers in Energy*, 2016, vol. 10, no. 2, pp. 155-163. doi: https://doi.org/10.1007/s11708-016-0410-1.

2. Sami I., Ullah S., Ali Z., Ullah N., Ro J.-S. A Super Twisting Fractional Order Terminal Sliding Mode Control for DFIG-Based Wind Energy Conversion System. *Energies*, 2020, vol. 13, no. 9, art. no. 2158. doi: https://doi.org/10.3390/en13092158.

3. *Wind power capacity worldwide reaches 744 GW, 147 GW added in 2019*. Available at. https://wwindea.org/information-2/statistics-news/ (Accessed 11 May 2022).

4. Ullah N., Asghar Ali M., Ibeas A., Herrera J. Adaptive Fractional Order Terminal Sliding Mode Control of a Doubly Fed Induction Generator-Based Wind Energy System. *IEEE Access*, 2017, vol. 5, pp. 21368-21381. doi: https://doi.org/10.1109/ACCESS.2017.2759579.

5. Ademi S., Jovanovic M. Vector control strategies for brushless doubly-fed reluctance wind generators. *2012 2nd International Symposium On Environment Friendly Energies And Applications*, 2012, pp. 44-49. doi: https://doi.org/10.1109/EFEA.2012.6294084.

6. Hopfensperger B., Atkinson D.J. Doubly-fed AC machines: classification and comparison. *European Power Electronics Conference*, 2001, vol. 200, no. 1.

7. Ademi S., Jovanovic M.G. Vector Control Methods for Brushless Doubly Fed Reluctance Machines. *IEEE Transactions on Industrial Electronics*, 2015, vol. 62, no. 1, pp. 96-104. doi: https://doi.org/10.1109/TIE.2014.2327564.

8. Jovanovic M. Sensored and sensorless speed control methods for brushless doubly fed reluctance motors. *IET Electric Power Applications*, 2009, vol. 3, no. 6, pp. 503-513. doi: https://doi.org/10.1049/iet-epa.2008.0227.

9. Moazen M., Kazemzadeh R., Azizian M.-R. Mathematical proof of BDFRG model under unbalanced grid voltage condition. *Sustainable Energy, Grids and Networks*, 2020, vol. 21, art. no. 100327. doi: https://doi.org/10.1016/j.segan.2020.100327.

10. Betz R.E., Jovanovic M.G. Theoretical analysis of control properties for the brushless doubly fed reluctance machine. *IEEE Transactions on Energy Conversion*, 2002, vol. 17, no. 3, pp. 332-339. doi: https://doi.org/10.1109/TEC.2002.801997.

11. Jovanovic M. Control of Brushless Doubly-Fed Reluctance Motors. *Proceedings of the IEEE International Symposium on Industrial Electronics (ISIE 2005)*, 2005, pp. 1667-1672. doi: https://doi.org/10.1109/ISIE.2005.1529182.
12. Ademi S., Jovanovic M. Vector control strategies for brushless doubly-fed reluctance wind generators. *2012 2nd International Symposium On Environment Friendly Energies And Applications*, 2012, pp. 44-49. doi: https://doi.org/10.1109/EFEA.2012.6294084.
13. Ademi S., Jovanovic M.G., Hasan M. Control of Brushless Doubly-Fed Reluctance Generators for Wind Energy Conversion Systems. *IEEE Transactions on Energy Conversion*, 2015, vol. 30, no. 2, pp. 596-604. doi: https://doi.org/10.1109/TEC.2014.2385472.
14. Oualah O., Kerdoun D., Boumassata A. Comparative study between sliding mode control and the vector control of a brushless doubly fed reluctance generator based on wind energy conversion systems. *Electrical Engineering & Electromechanics*, 2022, no. 1, pp. 51-58. doi: https://doi.org/10.20998/2074-272X.2022.1.07.
15. Jovanovic M., Ademi S., Llano D.X. Control of Doubly-Fed Reluctance Machines without a Shaft Position or Speed Sensor. *2018 International Symposium on Power Electronics, Electrical Drives, Automation and Motion (SPEEDAM)*, 2018, pp. 1245-1250. doi: https://doi.org/10.1109/SPEEDAM.2018.8445405.
16. Kumar M., Das S., Sinha A.K. Sensorless speed control of brushless doubly-fed reluctance machine for pump storage and wind power application. *2018 IEEMA Engineer Infinite Conference (ETechNxT)*, 2018, pp. 1-6. doi: https://doi.org/10.1109/ETECHNXT.2018.8385316.
17. Zhu L., Zhang F., Jin S., Ademi S., Su X., Cao W. Optimized Power Error Comparison Strategy for Direct Power Control of the Open-Winding Brushless Doubly Fed Wind Power Generator. *IEEE Transactions on Sustainable Energy*, 2019, vol. 10, no. 4, pp. 2005-2014. doi: https://doi.org/10.1109/TSTE.2018.2877439.
18. Liu X., Han Y., Wang C. Second-order sliding mode control for power optimisation of DFIG-based variable speed wind turbine. *IET Renewable Power Generation*, 2017, vol. 11, no. 2, pp. 408-418. doi: https://doi.org/10.1049/iet-rpg.2015.0403.
19. Kiran K., Das S., Sahu A. Sensorless speed estimation and control of brushless doubly-fed reluctance machine drive using model reference adaptive system. *2016 IEEE International Conference on Power Electronics, Drives and Energy Systems (PEDES)*, 2016, pp. 1-6. doi: https://doi.org/10.1109/PEDES.2016.7914480.
20. Kiran K., Das S., Singh D. Model predictive field oriented speed control of brushless doubly-fed reluctance motor drive. *2018 International Conference on Power, Instrumentation, Control and Computing (PICC)*, 2018, pp. 1-6. doi: https://doi.org/10.1109/PICC.2018.8384760.
21. Benbouhenni H., Lemdani S. Combining synergetic control and super twisting algorithm to reduce the active power undulations of doubly fed induction generator for dual-rotor wind turbine system. *Electrical Engineering & Electromechanics*, 2021, no. 3, pp. 8-17. doi: https://doi.org/10.20998/2074-272X.2021.3.02.
22. Babes B., Hamouda N., Kahla S., Amar H., Ghoneim S.S.M. Fuzzy model based multivariable predictive control design for rapid and efficient speed-sensorless maximum power extraction of renewable wind generators. *Electrical Engineering & Electromechanics*, 2022, no. 3, pp. 51-62. doi: https://doi.org/10.20998/2074-272X.2022.3.08.
23. Oualah O., Kerdoun D., Boumassata A. Comparison between sliding mode and traditional PI controllers in a speed control of a brushless doubly fed reluctance machine. *1st International Conference on Scientific and Academic Research (ICSAR 2022)*, December 10-13, 2022, Konya, Turkey, pp. 1-6.
24. Boubzizi S., Abid H., El hajjaji A., Chaabane M. Comparative study of three types of controllers for DFIG in wind energy conversion system. *Protection and Control of Modern Power Systems*, 2018, vol. 3, no. 1, art. no. 21. doi: https://doi.org/10.1186/s41601-018-0096-y.
25. Kelkoul B., Boumediene A. Stability analysis and study between classical sliding mode control (SMC) and super twisting algorithm (STA) for doubly fed induction generator (DFIG) under wind turbine. *Energy*, 2021, vol. 214, art. no. 118871. doi: https://doi.org/10.1016/j.energy.2020.118871.
26. Boumassata A., Kerdoun D., Oualah O. Maximum power control of a wind generator with an energy storage system to fix the delivered power. *Electrical Engineering & Electromechanics*, 2022, no. 2, pp. 41-46. doi: https://doi.org/10.20998/2074-272X.2022.2.07.
27. Zhou D., Song Y., Blaabjerg F. Control of Wind Turbine System. *In Book: Control of Power Electronic Converters and Systems*, 2018, pp. 269-298. doi: https://doi.org/10.1016/B978-0-12-805245-7.00010-X.
28. Levant A. *Introduction to high-order sliding modes*. School of Mathematical Sciences, Israel, 2003. 55 p.
29. Durga Rao R. Implementation of fuzzy based power control of BDFIG with super-twisting sliding mode control. *JAC : A Journal of Composition Theory (JCT)*, 2020, vol. 13, no. 3, pp. 454-461.
30. Shiralkar A., Kurode S. Generalized super-twisting algorithm for control of electro-hydraulic servo system. *IFAC-PapersOnLine*, 2016, vol. 49, no. 1, pp. 742-747. doi: https://doi.org/10.1016/j.ifacol.2016.03.145.
31. Mahgoun M.S., Badoud A.E. New design and comparative study via two techniques for wind energy conversion system. *Electrical Engineering & Electromechanics*, 2021, no. 3, 18-24. doi: https://doi.org/10.20998/2074-272X.2021.3.03.

Received 25.08.2022
Accepted 06.12.2022
Published 07.03.2023

O. Oualah [1]*, PhD,*
D. Kerdoun [1]*, Doctor of Electrotechnical, Professor,*
A. Boumassata [2]*, Doctor of Electrotechnical,*
[1] LGEC Research Laboratory,
Department of Electrical Engineering,
Brothers Mentouri University Constantine 1, Algeria,
e-mail: oussama.oulha@umc.edu.dz (Corresponding Author),
Kerdjallel@yahoo.fr
[2] National Polytechnic School Constantine, Algeria,
e-mail: a_boumassata@umc.edu.dz

How to cite this article:
Oualah O., Kerdoun D., Boumassata A. Super-twisting sliding mode control for brushless doubly fed reluctance generator based on wind energy conversion system. *Electrical Engineering & Electromechanics*, 2023, no. 2, pp. 86-92. doi: https://doi.org/10.20998/2074-272X.2023.2.13

UDC 621.3 https://doi.org/10.20998/2074-272X.2023.2.14

Y. Tami, K. Sebaa, M. Lahdeb, O. Usta, H. Nouri

Extended mixed integer quadratic programming for simultaneous distributed generation location and network reconfiguration

Introduction. *To minimise power loss, maintain the voltage within the acceptable range, and improve power quality in power distribution networks, reconfiguration and optimal distributed generation placement are presented. Power flow analysis and advanced optimization techniques that can handle significant combinatorial problems must be used in distribution network reconfiguration investigations. The optimization approach to be used depends on the size of the distribution network. Our* ***methodology*** *simultaneously addresses two nonlinear discrete optimization problems to construct an intelligent algorithm to identify the best solution. The proposed work is* ***novel*** *in that it the Extended Mixed-Integer Quadratic Programming (EMIQP) technique, a deterministic approach for determining the topology that will effectively minimize power losses in the distribution system by strategically sizing and positioning Distributed Generation (DG) while taking network reconfiguration into account. Using an efficient Quadratic Mixed Integer Programming (QMIP) solver (IBM ®), the resulting optimization problem has a quadratic form. To ascertain the range and impact of various variables, our methodology outperforms cutting-edge algorithms described in the literature in terms of the obtained power loss reduction, according to extensive numerical validation carried out on typical IEEE 33- and 69-bus systems at three different load factors.* ***Practical value****. Examining the effectiveness of concurrent reconfiguration and DG allocation versus sole reconfiguration is done using test cases. According to the findings, network reconfiguration along with the installation of a distributed generator in the proper location, at the proper size, with the proper loss level, and with a higher profile, is effective.* References 24, table 4, figures 14.

Key words: **active distribution networks, distribution system reconfiguration, distributed generation, mixed-integer quadratic programming, power loss.**

Вступ*. Для мінімізації втрат потужності, підтримки напруги в допустимому діапазоні та покращення якості електроенергії у розподільчих мережах представлена реконфігурація та оптимальне розміщення розподіленої генерації. При дослідженнях реконфігурації розподільної мережі необхідно використовувати аналіз потоку потужності та передові методи оптимізації, які можуть вирішувати серйозні комбінаторні проблеми. Підхід до оптимізації, що використовується, залежить від розміру розподільної мережі. Наша* ***методологія*** *одночасно вирішує дві задачі нелінійної дискретної оптимізації, щоби побудувати інтелектуальний алгоритм для визначення найкращого рішення. Пропонована робота є* ***новою****, оскільки вона використовує метод розширеного змішано-цілочисельного квадратичного програмування (EMIQP), детермінований підхід до визначення топології, що ефективно мінімізує втрати потужності в системі розподілу за рахунок стратегічного визначення розмірів та позиціонування розподіленої генерації (DG) з урахуванням реконфігурації мережі. При використанні ефективного солвера Quadratic Mixed Integer Programming (QMIP) (IBM®) результуюча задача оптимізації має квадратичну форму. Щоб з'ясувати діапазон та вплив різних змінних, наша методологія перевершує передові алгоритми, описані в літературі, з точки зору одержаного зниження втрат потужності, згідно з великою числовою перевіркою, проведеною на типових системах з шинами IEEE 33 і 69 при трьох різних коефіцієнтах навантаження.* ***Практична цінність****. Вивчення ефективності одночасної реконфігурації та розподілу DG у порівнянні з єдиною реконфігурацією проводиться з використанням тестових прикладів. Відповідно до результатів, реконфігурація мережі разом із установкою розподіленого генератора в потрібному місці, належного розміру, з належним рівнем втрат і з більш високим профілем є ефективною.* Бібл. 24, табл. 4, рис. 14.

Ключові слова: **активні розподільчі мережі, реконфігурація системи розподілу, розподілена генерація, змішано-цілочисельне квадратичне програмування, втрати потужності.**

Introduction. The last power system supply stage is the electrical distribution network, where the electricity is distributed to individual customers. At the distribution level, the energy could be lost in the form of heat caused by current flow (I^2R). The total power losses of a network could be pretty high for large-scale distribution networks. According to [1] power losses on transmission and sub-transmission lines accounted for 30 % of total power losses, whereas losses in a distribution network may account for 70 % of total power losses. The loss of power directly affects the operating cost of an electrical network. Technically, power losses could also cause a system's voltage profile to change, especially in systems that are heavily loaded.

The power losses in the distribution network can be minimised either by reconfiguring the network or by using (placement and size) multiple distributed generators (DGs). Although these techniques have the capability of loss reduction, their simultaneous combination and implementation will improve the system performance tremendously. Network reconfiguration changes the switches states, which can be normally open (tie switches) or closed (sectionalizing switches). The tie switches are used for the reconfiguration, while the sectionalizing switches isolate the faulted part. These switches help to isolate failed subnets, thus preventing discontinuity and supplying the whole network. The topological structure of the network is changed by closing open switches and vice versa, reducing power losses and improving the overall voltage profile. This will transfer the load to less loaded feeders, which will decrease the overall power loss. Further reductions in power losses can be achieved through the insertion of distributed generation (DG).

DGs are classified into renewable energy resources (RES) and non-RES DGs [2]. On the one hand, some of the RES DGs can only inject active power, such as photovoltaic cells and fuel cells (type P) or inject active and reactive power. Others can inject active power and consume reactive power, such as wind turbines (PQ-type). On the other hand, some non-RES DGs can inject both active and reactive power, such as combined combustion technology (PQ+-type), the internal combustion engine, and combined cycle DGs. Non-RES systems are characterized by the minimization of active and reactive losses, while their main disadvantage is that they have a weak effect on reducing the total cost of production and lead to an increase in global warming [3].

If DG is added to distribution networks in a place that isn't ideal, it will cause more power loss and voltage changes.

Therefore, a strategy for selecting the optimal placement and sizing of the DG must be developed to ensure an optimal configuration. If the distributed generators are correctly installed at optimal locations and if the units are correctly coordinated, they will improve the voltage profile and reduce power losses. The impacts of the reconfiguration and DG allocation techniques are summarized in Table 1 [4].

Table 1

Impacts of reconfiguration, DG allocation techniques

Impacts on techniques	Network reconfiguration	DG allocation
• Voltage support	x	x
• Loss minimization	x	x
• Cost saving		x
• Reliability	x	
• Load balancing		x
THD reduction		
• Demand side management	x	x
• Affects protection system coordination	x	x
• Green energy		x

Several studies use DG placements and network reconfiguration separately to minimise active power losses and improve the voltage profile in distribution networks [5-7]. However, very few offer network reconfiguration to be used in parallel with the location and sizing of DGs for a further reduction in power losses. [8-10].

As more research is done, meta-heuristic, heuristic, hybrid, and analytical techniques for solving functions with one or more objectives are created subject of investigations [11-14].

In [15] proposes a meta-heuristic harmony search algorithm to reconfigure and identify the optimal locations for installing DG units. In [12] presents a new integration technique for optimal network reconfiguration and DG placement. They use the fireworks algorithm, which is a swarm intelligence-based optimization algorithm that is based on how fireworks work to find the best place for the sparks. It is used to reconfigure and assign the best DG units in a distribution network at the same time.

A feeder reconfiguration problem in the presence of distributed generators to minimise the system power loss while satisfying operating constraints using the Hyper Cube-Ant Colony Optimization algorithm has been suggested in [16]. Because the implementation of the Ant Colony Optimization algorithm in the Hyper-Cube framework has the advantage of scaling the value of the objective function, allowing the rapid discovery of reasonable solutions and rapid optimal convergence.

In [17] used the modified plant growth simulation algorithm to minimize the actual power loss. This algorithm does not require barrier factors or crossing rates, as the objectives and constraints are treated separately. From [17], the main advantages of this algorithm are the continuous guided search and the shift target function, as the power of the distributed generation is constantly varying, which can be applied for real-time applications with the necessary modifications. These authors have come up with a way to find the best place to put multiple DGs and the right size for each one to reduce losses and improve voltage profiles.

In [18], a combination of the evolutionary algorithm Strength Pareto Evolutionary Algorithm 2 and the theories of spanning trees are also proposed to optimise several objective functions, providing optimal Pareto solutions, where the network manager can select an option. The results prove that reconfiguring the network with simultaneous placement and sizing of several solar DGs is more beneficial in improving the quality of energy than with a single solar DG. A new technique has been proposed in [19]. A Selective Optimization of Particle Swarms algorithm is used to obtain a reconfigured distribution network and an analytical technique to solve the DG and capacitor placement problem. They proposed a new constant, the power voltage sensitivity constant, for determining the location and size of the candidate bus and a new index, which incorporates the penetration index of the DG and the percentage reduction in actual power losses.

In this work, the Extended Mixed-Integer Quadratic Programming (EMIQP) method minimizes the power losses in a distribution network, including several DG's. EMIQP is applied to simultaneously determine network reconfiguration, DG allocation, and sizing, which can reduce power loss and improve the test profile of the distribution network.

The paper makes a contribution by extending the Taylor formulation [20] to the simultaneously DGs allocation, sizing, and reconfiguration problem.

Three test cases were considered to verify the proposed method, consisting of a distribution network with and without DGs. The results prove the proposed method's ability to produce minimal losses by finding an optimal system topology, DG locations, and adequate sizes.

Problem formulation. Power flow equations. The study of power flow is an essential step in any serious analysis of an electrical network. Indeed, it allows us to calculate the magnitudes of a balanced steady-state network, namely the modules and phases of the voltages at any network point. From these, one can calculate the currents in the lines; the transited active and reactive powers, and the power losses caused during the transport of electrical energy. This analysis is very important for the study, planning, and operation of an electrical network.

The quadratic terms in the DistFlow branch equations represent the losses on the branches; hence, they are much smaller than the branch power terms. The power flow in a radial distribution network can be expressed by a set of recursive equations called distribution flow branch equations (Fig. 1) created by [15]

$$\sum_{k:(i,k)\in E} p_{ik} = p_{ji} - r_{ji}\frac{p_{ji}^2 + q_{ji}^2}{v_j^2} - p_i^L; \quad (1)$$

$$\sum_{k:(i,k)\in E} q_{ik} = q_{ji} - x_{ij}\frac{p_{ji}^2 + q_{ji}^2}{v_j^2} - p_i^L; \quad (2)$$

$$v_i^2 = v_j^2 - 2\left(r_{ij}p_{ji} + x_{ij}q_{ji}\right) + \left(r_{ij}^2 + x_{ij}^2\right)\frac{p_{ji}^2 + q_{ji}^2}{v_j^2}; \quad (3)$$

where p_{ij} and q_{ij} are the active and reactive powers of bus i to bus j; v_i is the voltage magnitude; p_i^L, q_i^L are the real and reactive loads at bus i. Note that p_{ij} and q_{ij} do not equal p_{ji} and q_{ji}. Since v_i does not appear in our formulation, we consider v_i^2 is considered as a variable itself. Let V represent all the buses and E the set of lines, and r_{ij}, x_{ij}, represent the resistance and the reactance of the

line, respectively. Single-index constraints represent all (i) in V, and double-index constraints represent all (i, j) in E.

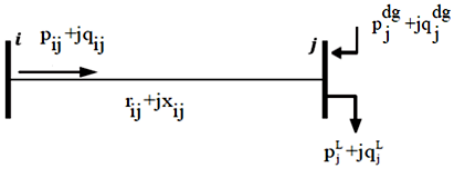

Fig. 1. Simple distribution line

Extended Mixed-Integer Quadratic Programming (EMIQP). The quadratic terms in the equations (1)–(3) represent the line losses which are smaller compared to line power p_{ji} and q_{ji}. Therefore, by removing the second order terms, power flow equations can be simplified [20, 21]. Let E^S be the subset of E with switches, V^F be the subset of V which are substations, p_i^F and q_i^F, $i \in V^F$, be the real and reactive powers from the substations, and M be the sufficiently large disjunctive parameter and α, λ are the aggregate coefficient. Note that the set V^F may contain multiple substations, each of which will be connected to exactly one tree with no other substations attached to it. An EMIQP is obtained for loss minimization by coupling the quadratic objective:

$$\min_{p,q,p^{dg},q^{dg},y,z,h} \sum_{(i,j)} r_{ij}\left(p_{ij}^2+q_{ij}^2\right)+\alpha\sum_{k=1}^{N_{bus}}\left(p_k^{dg}+q_k^{dg}\right)..+ \\ +\lambda\sum_{k=1}^{N_{bus}} h_k; \tag{4}$$

And the set of linear constraints:

$$\sum_{j:(i,j)\in E} p_{ji}-p_{ij}=p_i^L,\quad i\in V/V^F; \tag{5}$$

$$\sum_{j:(i,j)\in E} q_{ji}-q_{ij}=q_i^L,\quad i\in V/V^F; \tag{6}$$

$$\sum_{j:(i,j)\in E} p_{ij}=p_i^F,\quad i\in V^F; \tag{7}$$

$$\sum_{j:(i,j)\in E} q_{ij}=q_i^F,\quad i\in V^F. \tag{8}$$

The radiality constraint has represented by two variables z_{ij} and z_{ji} which are assigned to each line indicating which direction, if any, the flow can travel. Each switched line is associated with a single binary variable y_{ij}, which will be equal to zero if the switch is open and equal to one if closed

$$0\le p_{ij}\le Mz_{ij}; \tag{9}$$

$$0\le q_{ij}\le Mz_{ij}; \tag{10}$$

$$z_{ij}\ge 0; \tag{11}$$

$$z_{if}=0,\quad f\in V^F; \tag{12}$$

$$z_{ij}+z_{ji}=1,\quad (i,j)\in E/E^S; \tag{13}$$

$$z_{ij}+z_{ji}=y_{ij},\quad (i,j)\in E^S; \tag{14}$$

$$\sum_{j:(i,j)\in E} z_{ji}=1,\quad i\in V/V^F; \tag{15}$$

$$y_{ij}\in\{0,1\},\quad (i,j)\in E^S. \tag{16}$$

Three decision variables are added, p_i^{dg}, q_i^{dg} which are the continuous variables designates the size of the DG's, and h_i is the discrete variable (binary) which designates whether the i^{th} DG is installed or not. It is assumed that the bus where the DG is installed is considered a feeder. Therefore, we have two new constraints (17) and (18), which replace constraints (5) and (6) to simultaneously determine network reconfiguration with siting and sizing of distributed generation (DG)

$$\sum_{j:(i,j)\in V^{DG}} p_{ij}-p_{ji}=h_i\cdot p_i^{dg},\quad i\in V^{DG}; \tag{17}$$

$$\sum_{j:(i,j)\in V^{DG}} q_{ij}-q_{ji}=h_i\cdot q_i^{dg},\quad i\in V^{DG}; \tag{18}$$

$$\sum_{i=1}^{N_{dg}} h_i=N_{DG},\quad i\in V^{DG}. \tag{19}$$

Size of DG units should be within specific limits:

$$\begin{cases} p_{i,\min}^{dg}\le p_i^{dg}\le p_{i,\max}^{dg}; \\ q_{i,\min}^{dg}\le q_i^{dg}\le q_{i,\max}^{dg}; \end{cases} \quad i\in V^{DG}, \tag{20}$$

where $p_{i,\max}^{dg}$, $q_{i,\max}^{dg}$ and $p_{i,\min}^{dg}$, $q_{i,\min}^{dg}$ are the maximum and minimum power supplied by DG, respectively.

The convex optimization problem defined by (4)– (18) is an EMIQP as the objective function (4) is convex quadratic, and the constraint functions are affine [22, 23], but the constraints (17) and (18) are nonlinear; we can replace them by another's linear constraints (21) and (22) using the big M method:

$$\begin{cases} \sum_{j:(i,j)\in E} p_{ij}-p_{ji}\le p_i^{dg},\quad i\in V^{DG}; \\ p_i^{dg}\le M\cdot h_i; \end{cases} \tag{21}$$

$$\begin{cases} \sum_{j:(i,j)\in E} q_{ij}-q_{ji}\le q_i^{dg},\quad i\in V^{DG}; \\ q_i^{dg}\le M\cdot h_i; \end{cases} \tag{22}$$

When h_i is equal to one, (21) and (22) are disabled, otherwise p_i^{dg} and q_i^{dg} are set to zero

$$nDG^{\min}\le\sum_{k=1}^{nBus} h_k\le nDG^{\max}, \tag{23}$$

where $nDG^{\min}$, $nDG^{\max}$ are respectively the minimum and the maximum allowed number of DGs. On the grounds that the number DG should be within a specific rang, therefore (23) is added.

In this study, in addition to active power, we are also limiting reactive power because the non-RES DG's (PQ+-type) can inject both active and reactive power. In addition, the radial nature of the distribution network must be maintained, and all loads must be supplied. If one of the above constraints is not respected, the resulting solution will be rejected. Three different scenarios at three different load factors: $\beta=0.5$ (light), $\beta=1.0$ (nominal), and $\beta=1.5$ (heavy), are considered to simulate and analyse the performance of the proposed method. These are:

Scenario 1: this base scenario is a power flow solution to the problem.

Scenario 2: this scenario only considers the reconfiguration of the active distribution networks.

Scenario 3: this scenario looks at the reconfiguration of the system as well as the placement and size of three DGs.

Computer simulation and performance analysis studies. The performance analysis of the proposed method was carried out using the two IEEE standard radial distribution system models (IEEE 33-bus and 69-bus) [6], and tolerable results were obtained. The network models of 33 and 69-bus distribution systems, including network reconfiguration, DG allocation, and DG sizing, are implemented in MATLAB. For all these radial systems, the substation voltage was examined as one p.u. The EMIQP models were solved via CPLEX (the CPLEX Optimizer was named for the simplex method implemented in the C programming language) [20, 21]. The numerical computations are carried out on an Intel Core I7-6500U CPU at 2.5 GHz with 8 GB of RAM. Although most of the previous studies focused only on active power injection into the network, the effect of active and reactive power injection of DG units is also considered. The obtained results are verified using other metaheuristics methods.

Case study 1: Using the IEEE 33-Bus Test System. The IEEE 33-Bus System consists of 37 switches, 32 sectionalism switches; and five tie switches. Switch numbers 33, 34, 35, 36, and 37 are normally open for the original network, while the other switches are typically closed, as shown in Fig. 2. The total real load demand is 3715 kW, while the system voltage is 12.66 kV.

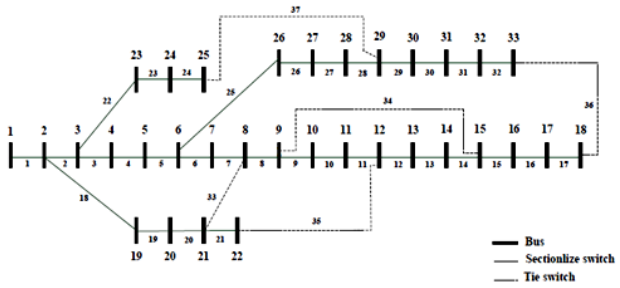

Fig. 2. IEEE 33-bus distribution network before reconfiguration and DG allocation process

The base value of the apparent power is 100 MVA. When the network was first set up, it lost 202.69 kW of power, and the lowest bus voltage was 0.9131 p.u.

The substation (bus 1) voltage is considered as one p.u. All the tie and sectionalising switches are candidate switches for reconfiguration and DG locations. The results obtained from the computer simulation studies are summarised in Table 2. This summary includes the proposed method's performance for three different scenarios, and the results are validated using the metaheuristic algorithms PSO, GWO, and hybrid PSO-GWO [24]. The initial values from the power flow analysis of the 33-bus network are used in Scenario 1.

Table 2

Comparison of simulation results of a 33-bus system

Scenarios		Proposed method (EMIQP)	GWO-PSO [24]	GWO [24]	PSO [24]
Scenario 1	Switches opened	33,34,35,36,37	33,34,35,36,37	33, 34, 35, 36, 37	33, 34, 35, 36, 37
	P loss (kW)	**202.69**	202.67	202.67	202.67
	Q loss (kVAr)	**135.18**	135.14	135.14	135.14
Scenario 2	Switches opened	7,9,14,32,37	7,9,14,32,37	7, 9, 14, 32, 37	7, 9, 14, 32, 37
	P loss (kW)	**139.55**	139.55	139.55	139.55
	Q loss (kVAr)	**102.32**	102.31	102.3	102.3
	Reduction % P loss	31.15 %	31.14 %	31.14 %	31.14 %
	Reduction % Q loss	24.30 %	24.29 %	24.29 %	24.29 %
	V_{min} (p.u.)	**0.93782**	0.93782	–	–
Scenario 3	Switches opened	06,13,17,21,22	05,11,13,15,23	05, 11, 13, 15, 26	07, 16, 21, 25, 34
	DG size in MVA (bus)	1.075 + j 0.510 (09) 0.930 + j 0.450 (24) 1.010 + j 0.990 (30)	1.0975 + j 0.5593 (08) 1.1523 + j 0.8047 (25) 0.7491 + j 0.5620 (32)	1.0818 + j 0.5138 (8) 1.1327 + j 0.8311 (25) 0.7528 + j 0.5720 (32)	0.7826 + j 0.3752 (12) 0.9533 + j 0.4627 (24) 1.1959 + j 1.0738 (30)
	P loss (kW)	**10.102**	8.916	8.954	10.846
	Q loss (kVAr)	**8.2211**	7.4668	7.53	8.79
	Reduction % P loss	**95.01 %**	95.60 %	95.58 %	94.64 %
	Reduction % Q loss	**93.92 %**	94.47 %	94.42 %	93.49 %
	V_{min} (p.u.)	**0.9932**	0.97344	–	–
	CPU time (s)	**7,040.3**	12,184.33	26,054.34	23,909.09

From Table 2, it is first observed that the base case power loss of 202.69 kW was reduced to 139.55 kW and 10.102 kW in scenarios 2 and 3, respectively. The percentage reduction in power loss is 31.15 % and 95.01 % in Scenarios 2 and 3, respectively.

Table 2 also shows that the minimum voltage magnitude of the system is improved impressively from 0.9131p.u. up to 0.93782 p.u. and 0.9932 p.u. for scenarios 2 and 3, respectively. It can be seen that the least amount of power is lost in scenario three, where the size and location of the DGs are optimized and the network configuration is optimized.

In this scenario, the real power loss reduction has its lowest value. Figure 3 shows the voltage profile of the 33-bus network. The most flattering voltage profile is achieved in scenario 3, where the minimum voltage magnitude of the network is 0.9131 p.u. and is improved to 0.9378 and 0.9932 for scenarios 2 and 3, respectively. Figure 4 shows the voltage profiles of the network under different case conditions.

These are cases 1 with one DG unit, case 2 with two DG units, and case 3 with three DG units. From this figure, we see that the tension profile of the system is improved for several DGs equal to 3. It can be seen that the integration of several DGs in different places results in a better reduction of the voltage deviation in the distribution network.

Figure 5 indicates active power losses under operating conditions such as Scenario 1, Scenario 2 and 3.

It can be seen that the reduction of the power loss is the highest for scenario three, including PQ+-type DG units.

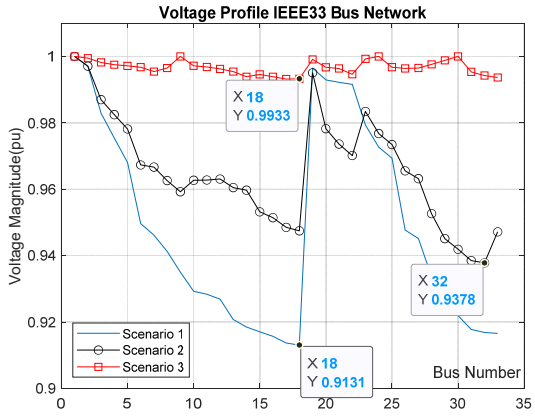

Fig. 3. Bus voltage profile of the networks for 3 scenarios

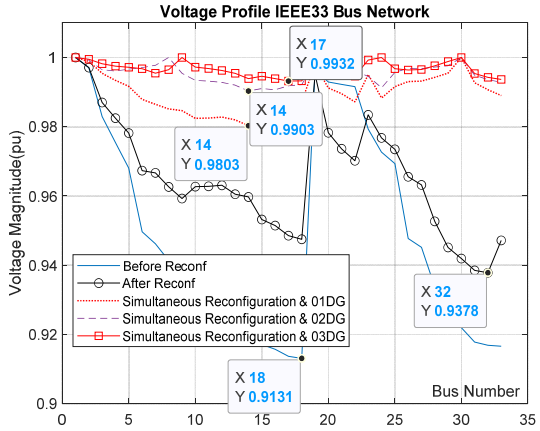

Fig. 4. Bus voltage profile of the 33-bus networks for different network conditions

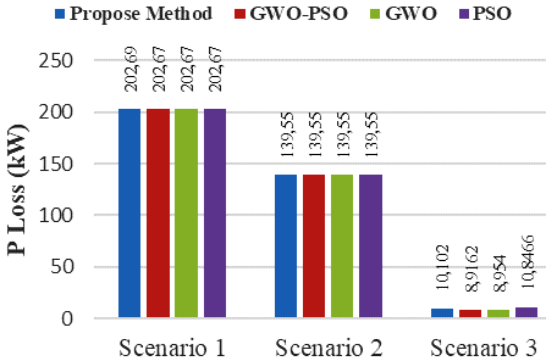

Fig. 5. Power loss of a 33-bus system for 3 different scenarios

From Fig. 6, base case reactive loss is 135.18 kVAr, reduced to 102.32 and 8.2211 for scenarios 2 and 3, respectively, using the proposed technique.

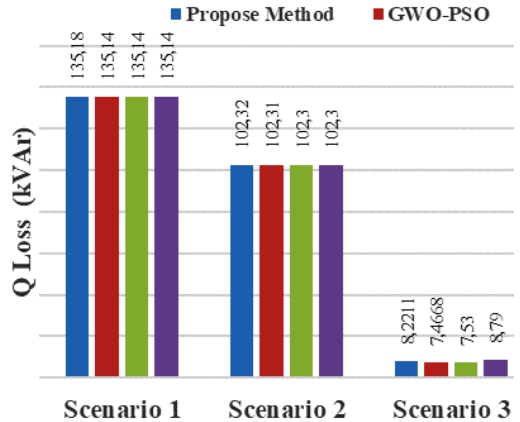

Fig. 6. Reactive loss of a 33-bus system for 3 different scenarios

It has been seen that injecting both active and reactive power at the same time as reconfiguring the system reduces reactive power losses. The proposed technique also improves both the optimal solution and the speed of convergence the most.

Case study 2. Using the IEEE 69-Bus Test System. The 69-bus distribution system includes 69 nodes and 73 branches. There are five tie switches, as shown in Fig. 7. The system load is (3.8 + j2.69) MVA, and the initial active power loss before reconfiguration is 225.04 kW and 102.18 kVAr. The normally open switches are 69, 70, 71, 72, and 73. The system's base capacity is 100 MVA, and the base voltage is 12.66 kV.

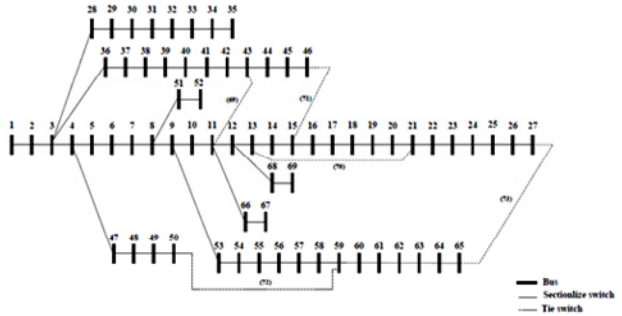

Fig. 7. IEEE 69-bus distribution network before reconfiguration and DG allocation process

Similar to Case Study 1, this case is also simulated for three scenarios, and the results are presented in Table 3. The same observations as in the 33-bus network can be seen regarding the integration of several DGs in multiple locations (Fig. 8), resulting in a better reduction in the power loss and the voltage deviation in the distribution network. From Table 3,the base case power loss is 225.04 kW, reduced to 84.803 and 3.6608 using scenarios 2 and 3, with a percentage reduction of 62.32 % and 98.37 %, respectively, by the integration of DG with PQ+-type and system reconfiguration simultaneously. The minimum voltage magnitude of the network is 0.9131 (p.u.), which is improved to 0.94948 and 0.99588 for scenarios 2 and 3, respectively, using the proposed algorithm. As with the 33-bus test system, the voltage profile of the 69-bus test system for Scenario 3 is seen to be the best (Fig. 9).

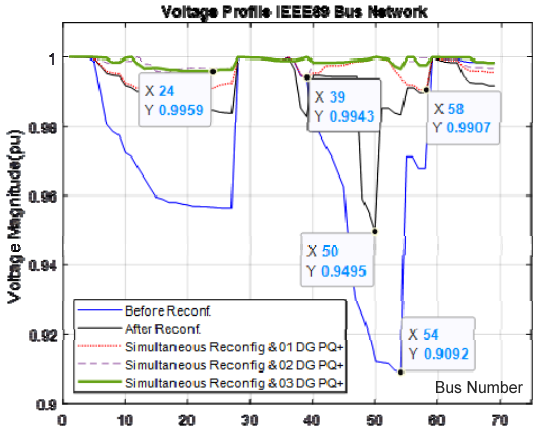

Fig. 8. Bus voltage profiles of the 69-bus network for different network conditions

From Fig. 10, base case active loss is 225.04 kW, which is reduced to 84.803 and 3.6608 using scenarios 2 and 3, respectively, and also, from Fig. 11, base case reactive loss is 102.18 kVAr, which is reduced to 82.623 and 2.1806 using scenarios 2 and 3, respectively.

Table 3

Comparison of simulation results of a 69-bus system

Scenarios		Proposed method (EMIQP)	GWO-PSO [24]	GWO [24]	PSO [24]
Scenario 1	Switches opened	69,70,71,72,73	69,70,71,72,73	69, 70, 71, 72, 73	69, 70, 71, 72, 73
	P loss (kW)	**225.04**	224.93	224.9295	224.9295
	Q loss (kVAr)	**102.18**	102.15	102.14	102.14
Scenario 2	Switches opened	14, 44, 50, 69, 70	14, 57, 61, 69, 70	14, 57, 61, 69, 70	14, 57, 61, 69, 70
	P loss (kW)	**84.803**	98.569	98.5687	98.5687
	Q loss (kVAr)	**82.623**	92.024	92.02	92.02
	Reduction % P loss	62.32 %	56.17 %	56.17 %	56.17 %
	Reduction % Q loss	19.14 %	9.90 %	9.91 %	9.91 %
	V_{min} (p.u.)	**0.94948**	0.94947	–	–
Scenario 3	Switches opened	07, 13, 18, 24, 35	14, 16, 41, 55, 64	8, 13, 20, 24, 55	12, 21, 40, 53, 70
	DG size in MVA (bus)	1.004 + j 0.697 (11) 0.848 + j 0.605 (39) 1.714 + j 1.224 (50)	0.4319 + j 0.2913 (21) 0.5897 + j 0.4161 (11) 1.6770 + j 1.1979 (61)	0.0887 + j 0.5722 (2) 0.8475 + j 0.5899 (11) 1.7651 + j 1.2605 (61)	1.7298 + j 1.2346 (61) 0.7649 + j 0.5493 (50) 0.7791 + j 0.5339 (43)
	P loss (kW)	**3.6608**	3.7132	5.4798	4.40472
	Q loss (kVAr)	**2.1806**	5.6053	6.54	2.79
	Reduction % P loss	98.37 %	98.34 %	97.56 %	98.04 %
	Reduction % Q loss	97.87 %	94.51 %	93.59 %	97.26 %
	V_{min} (p.u.)	**0.99588**	0.99486	–	–

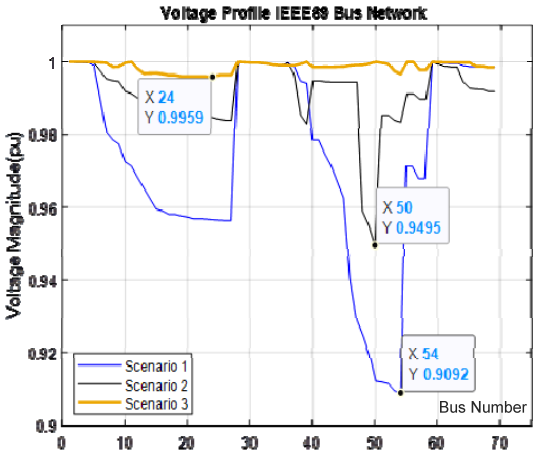

Fig. 9. Bus voltage profiles of the networks for 3 scenarios

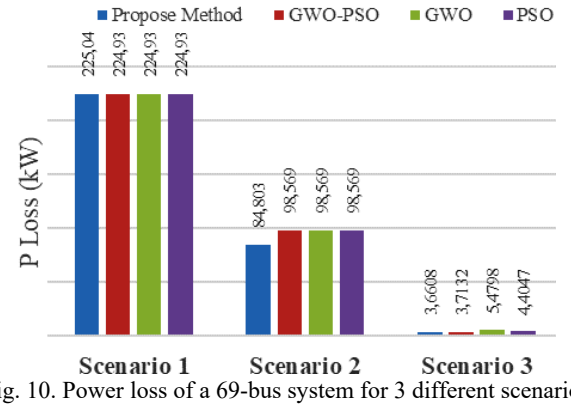

Fig. 10. Power loss of a 69-bus system for 3 different scenarios

Table 3 and Fig. 9 show that the proposed algorithm performs nearly identically to the metaheuristic algorithms PSO, GWO, and hybrid PSO-GWO [24] in terms of solution quality in all scenarios; additionally, the proposed technique offers the best improvement in convergence speed.

Sensitivity analysis. A sensitivity analysis is carried out to determine the range and impact of different variables, and to verify the proposed method's ability to find the optimal solution under different load conditions. Each scenario takes into account three different load factors: light (β = 0,5), nominal (β = 1), and heavy (β = 1,5). Although the heavy load (overload) occurs in emergency conditions.

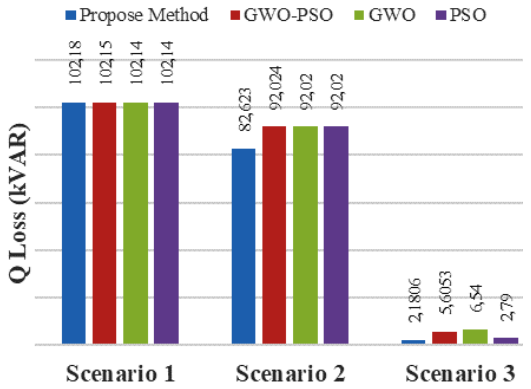

Fig. 11. Reactive loss of a 69-bus system for 3 different scenarios

Table 4 shows that at load factor β = 1.0 (nominal load level), the active power losses in the network with scenario 1 (base case) is 202.69, which is reduced to 139.55 and 10.10 using scenarios 2, and 3, respectively. The percentage reduction in active power losses for scenarios 2 and 3 is 31.15 and 95.02, respectively. Similarly, under load factors β = 0.5 (light) and β = 1.5 (heavy), the percent reduction in active power losses for Scenarios 2 and 3 is 29.32 and 95.37; 33.88 and 95.48, respectively.

It can also be seen from Table 4 that, at all load factors, the magnitude of the minimum voltage of the system is impressively improved in all three scenarios. Under the light, nominal, and high load conditions, the magnitude of the minimum voltage (in p.u.) is improved from 0.9131, 0.9583, and 0.8528 to 0.9968, 0.9932, and 0.9891 in scenarios 1, 2, and 3, respectively (Fig. 12 – Fig. 14).

It is observed that at three load factors, the values of the active and reactive power losses and the minimum voltage are the highest using scenario 3, which proves the superiority of the proposed technique. The improvement in the percentage reduction of active and reactive power losses and the magnitude of the minimum voltage is greater in scenario 3. This shows that changing the network and where the DGs are located at the same time (scenario 3) is better for the quality of the solutions than the other scenarios that were looked at.

Table 4

Performance analysis of proposed method on 33-bus system at different load factors

Scenario	Item	Load level		
		Light (β =0.5)	Nominal (β =1.0)	Heavy (β =1.5)
Base case (scenario I)	Switches opened	33-34-35-36-37	33-34-35-36-37	33-34-35-36-37
	$P_{T,Loss}$ (kW)	47.072	202.69	575.4
	$Q_{T,Loss}$ (kVAr)	31.358	135.18	384.37
	V_{min} in p.u.	**0.95826**	**0.91308**	**0.85281**
	(Bus no)	18	18	18
Only reconfiguration (scenario II)	Switches opened	7-9-14-32-37	7-9-14-32-37	7-9-14-32-37
	$P_{T,Loss}$ (kW)	33.269	139.55	380.45
	$Q_{T,Loss}$ (kVAr)	24.388	102.32	279.02
	V_{min} in p.u.	**0.96978**	**0.93782**	**0.89667**
	(Bus no)	32	32	32
	% P_{Loss} reduction	**29.32**	**31.15**	**33.88**
Simultaneous reconfiguration and DG installation (scenario III)	Switches opened	5-13-15-20-23	6-13-17-21-22	6-13-17-21-22
	DG size in MW (candidate bus)	0.582 +j 0.277 (8)	1.075 + j 0.510 (09)	1.720 +j 0.816 (9)
		0.540 +j 0.257 (25)	0.930 + j 0.450 (24)	1.488 +j 0.720 (24)
		0.415 +j 0.445 (31)	1.010 + j 0.990 (30)	1.616 +j 1.584 (30)
	$P_{T,Loss}$ (kW)	2.1795	10.102	26.0004
	$Q_{T,Loss}$ (kVAr)	1.8406	8.2211	21.166
	V_{in} in p.u.	**0.99684**	**0.9932**	**0.98907**
	(Bus no)	13	17	17
	% P_{Loss} reduction	**95.37**	**95.02**	**95.48**

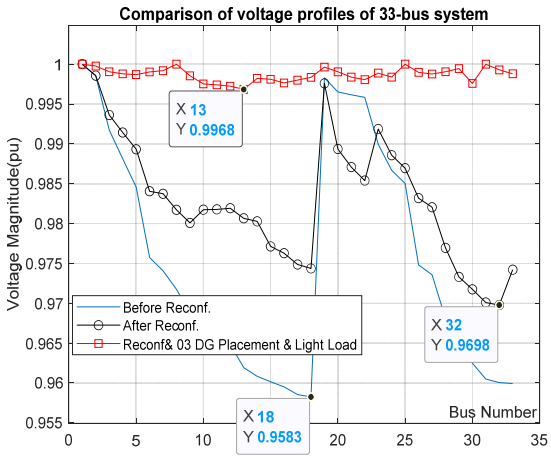

Fig. 12. Comparison of voltage profiles of 33 bus system at light load conditions

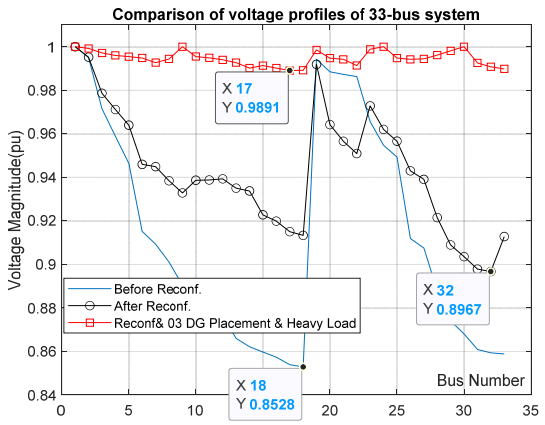

Fig. 13. Comparison of voltage profiles of 33 bus system at nominal load conditions

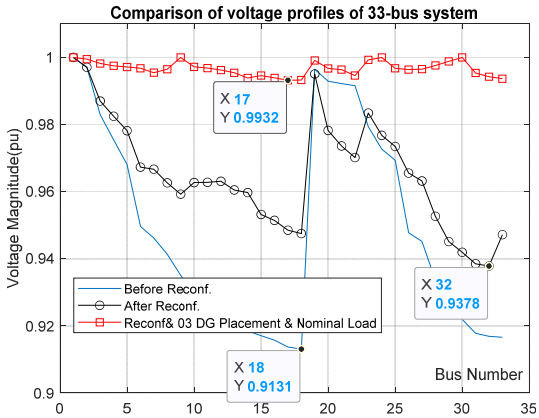

Fig. 14. Comparison of voltage profiles of 33 bus system at heavy load conditions

Conclusions. In this work, an extension of mixed integer quadratic programming (EMIQP) has been successfully applied to the 33 and 69-bus radial systems at different load factors to minimize the power loss, improve the system voltage profile and improve power quality in the active distribution network. Three different scenarios were considered, namely base case, reconfiguration, and simultaneous reconfiguration, with DG's units' location and sizing at three different load factors: β = 0.5 (light), β = 1.0 (nominal), and β = 1.5 (heavy) to analyze the performance of the proposed algorithm. In addition, the proposed method is verified using the metaheuristic algorithms PSO and GWO individually and in a hybrid PSO-GWO. The results indicate that scenario 3 (network reconfiguration with simultaneous DG installation) is more effective in minimising the loss of power and improving the voltage profile compared to the other scenarios considered. Thus, we observe that the proposed algorithm leads to precise results like the other metaheuristic algorithms PSO, GWO, and hybrid PSO-GWO in terms of power losses and voltage profile improvement.

The proposed algorithm outperforms the other metaheuristic algorithms in terms of convergence speed. In addition, this study provides the network manager with a robust tool for technically optimising the distribution network. Future work will be devoted to solving the current optimisation problem for the number of different renewable DG technologies. The goal is to solve this complicated problem by taking into account both the intermittent nature of the power made by renewable DGs and the load.

Conflict of interest. The authors declare no conflict of interest.

REFERENCES

1. Wu Y.-K., Lee C.-Y., Liu L.-C., Tsai S.-H. Study of reconfiguration for the distribution system with distributed generators. *IEEE Transactions on Power Delivery*, 2010, vol. 25, no. 3, pp. 1678-1685. doi: https://doi.org/10.1109/TPWRD.2010.2046339.

2. Kansal S., Kumar V., Tyagi B. Optimal placement of different type of DG sources in distribution networks. *International Journal of Electrical Power & Energy Systems*, 2013, vol. 53, pp. 752-760. doi: https://doi.org/10.1016/j.ijepes.2013.05.040.

3. Esmaeilian H.R., Fadaeinedjad R. Energy Loss Minimization in Distribution Systems Utilizing an Enhanced Reconfiguration Method Integrating Distributed Generation. *IEEE Systems Journal*, 2015, vol. 9, no. 4, pp. 1430-1439. doi: https://doi.org/10.1109/JSYST.2014.2341579.

4. Sambaiah K.S., Jayabarathi T. Loss minimization techniques for optimal operation and planning of distribution systems: A review of different methodologies. *International Transactions on Electrical Energy Systems*, 2020, vol. 30, no. 2, pp. 1-48. doi: https://doi.org/10.1002/2050-7038.12230.

5. Bayat A., Bagheri A., Noroozian R. Optimal siting and sizing of distributed generation accompanied by reconfiguration of distribution networks for maximum loss reduction by using a new UVDA-based heuristic method. *International Journal of Electrical Power & Energy Systems*, 2016, vol. 77, pp. 360-371. doi: https://doi.org/10.1016/j.ijepes.2015.11.039.

6. Lotfipour A., Afrakhte H. A discrete Teaching–Learning-Based Optimization algorithm to solve distribution system reconfiguration in presence of distributed generation. *International Journal of Electrical Power & Energy Systems*, 2016, vol. 82, pp. 264-273. doi: https://doi.org/10.1016/j.ijepes.2016.03.009.

7. Tebbakh N., Labed D., Labed M.A. Optimal size and location of distributed generations in distribution networks using bald eagle search algorithm. *Electrical Engineering & Electromechanics*, 2022, no. 6, pp. 75-80. doi: https://doi.org/10.20998/2074-272X.2022.6.11.

8. Taher S.A., Karimi M.H. Optimal reconfiguration and DG allocation in balanced and unbalanced distribution systems. *Ain Shams Engineering Journal*, 2014, vol. 5, no. 3, pp. 735-749. doi: https://doi.org/10.1016/j.asej.2014.03.009.

9. Dogan A., Alci M. Simultaneous Optimization of Network Reconfiguration and DG Installation Using Heuristic Algorithms. *Elektronika Ir Elektrotechnika*, 2019, vol. 25, no. 1, pp. 8-13. doi: https://doi.org/10.5755/j01.eie.25.1.22729.

10. Esmaeili M., Sedighizadeh M., Esmaili M. Multi-objective optimal reconfiguration and DG (Distributed Generation) power allocation in distribution networks using Big Bang-Big Crunch algorithm considering load uncertainty. *Energy*, 2016, vol. 103, pp. 86-99. doi: https://doi.org/10.1016/j.energy.2016.02.152.

11. Jasthi K., Das D. Simultaneous distribution system reconfiguration and DG sizing algorithm without load flow solution. *IET Generation, Transmission & Distribution*, 2018, vol. 12, no. 6, pp. 1303-1313. doi: https://doi.org/10.1049/iet-gtd.2017.0338.

12. Mohamed Imran A., Kowsalya M., Kothari D.P. A novel integration technique for optimal network reconfiguration and distributed generation placement in power distribution networks. *International Journal of Electrical Power & Energy Systems*, 2014, vol. 63, pp. 461-472. doi: https://doi.org/10.1016/j.ijepes.2014.06.011.

13. Nguyen T.T., Truong A.V., Phung T.A. A novel method based on adaptive cuckoo search for optimal network reconfiguration and distributed generation allocation in distribution network. *International Journal of Electrical Power & Energy Systems*, 2016, vol. 78, pp. 801-815. doi: https://doi.org/10.1016/j.ijepes.2015.12.030.

14. Sambaiah K.S., Jayabarathi T. Optimal reconfiguration and renewable distributed generation allocation in electric distribution systems. *International Journal of Ambient Energy*, 2021, vol. 42, no. 9, pp. 1018-1031. doi: https://doi.org/10.1080/01430750.2019.1583604.

15. Rao R.S., Ravindra K., Satish K., Narasimham S.V.L. Power Loss Minimization in Distribution System Using Network Reconfiguration in the Presence of Distributed Generation. *IEEE Transactions on Power Systems*, 2013, vol. 28, no. 1, pp. 317-325. doi: https://doi.org/10.1109/TPWRS.2012.2197227.

16. Nayak M.R. Optimal Feeder Reconfiguration of Distribution System with Distributed Generation Units using HC-ACO. *International Journal on Electrical Engineering and Informatics*, 2014, vol. 6, no. 1, pp. 107-128. doi: https://doi.org/10.15676/ijeei.2014.6.1.8.

17. Rajaram R., Sathish Kumar K., Rajasekar N. Power system reconfiguration in a radial distribution network for reducing losses and to improve voltage profile using modified plant growth simulation algorithm with Distributed Generation (DG). *Energy Reports*, 2015, vol. 1, pp. 116-122. doi: https://doi.org/10.1016/j.egyr.2015.03.002.

18. Hamida I.B., Salah S.B., Msahli F., Mimouni M.F. Simultaneous Distribution Network Reconfiguration and Optimal Distributed Generations Integration using a Pareto Evolutionary Algorithm. *International Journal of Renewable Energy Research*, 2018, vol. 8, no. 1, pp. 345-356. doi: https://doi.org/10.20508/ijrer.v8i1.6789.g7309.

19. Nawaz S., Singh S., Awasthi S. Power Loss Minimization in Radial Distribution System using Network Reconfiguration and Multiple DG Units. *European Journal of Scientific Research*, 2018, vol. 148, no. 4, pp. 474-483.

20. Tami Y., Sebaa K., Lahdeb M., Nouri H. Mixed-Integer Quadratic Constrained Programming versus Quadratic Programming Methods for Distribution Network Reconfiguration. *2019 International Conference on Advanced Electrical Engineering (ICAEE)*, 2019, pp. 1-5. doi: https://doi.org/10.1109/ICAEE47123.2019.9015181.

21. Rosseti G.J.S., de Oliveira E.J., de Oliveira L.W., Silva I.C., Peres W. Optimal allocation of distributed generation with reconfiguration in electric distribution systems. *Electric Power Systems Research*, 2013, vol. 103, pp. 178-183. doi: https://doi.org/10.1016/j.epsr.2013.05.017.

22. Taylor J.A., Hover F.S. Convex Models of Distribution System Reconfiguration. *IEEE Transactions on Power Systems*, 2012, vol. 27, no. 3, pp. 1407-1413. doi: https://doi.org/10.1109/TPWRS.2012.2184307.

23. Boyd S., Vandenberghe L. *Convex Optimization*. New York, Cambridge University Press, 2004. 716 p.

24. Abd El-salam M., Beshr E., Eteiba M. A New Hybrid Technique for Minimizing Power Losses in a Distribution System by Optimal Sizing and Siting of Distributed Generators with Network Reconfiguration. *Energies*, 2018, vol. 11, no. 12, art. no. 3351. doi: https://doi.org/10.3390/en11123351.

Received 18.10.2022
Accepted 22.12.2022
Published 07.03.2023

Youcef Tami[1], *PhD*,
Karim Sebaa[1], *Professor*,
Mohamed Lahdeb[2], *Doctor*,
Omer Usta[3], *Professor*,
Hassan Nouri[4], *Professor*,
[1] LSEA, University of Medea, Algeria,
e-mail: tamiyoucef1973@gmail.com (Corresponding Author);
sebaa.karim@univ-medea.dz
[2] LaACoSE, Electriques,
University of Laghouat, Algeria,
e-mail: m.lahdeb@lagh-univ.dz
[3] Department of Electrical Engineering,
Istanbul Technical University, Turkey,
e-mail: ustao@itu.edu.tr
[4] Department of Engineering, Design and Mathematics,
University of the West of England, United Kingdom,
e-mail: hassan.nouri@uwe.ac.uk

How to cite this article:
Tami Y., Sebaa K., Lahdeb M., Usta O., Nouri H. Extended mixed integer quadratic programming for simultaneous distributed generation location and network reconfiguration. *Electrical Engineering & Electromechanics*, 2023, no. 2, pp. 93-100. doi: https://doi.org/10.20998/2074-272X.2023.2.14

Матеріали приймаються за адресою:
Кафедра "Електричні апарати", НТУ "ХПІ", вул. Кирпичева, 2, м. Харків, 61002, Україна
Електронні варіанти матеріалів по e-mail: a.m.grechko@gmail.com

Довідки за телефонами: +38 067 359 46 96 Гречко Олександр Михайлович

Передплатний індекс: 01216